MODULE-LEVEL AUTONOMOUS SETTING-LESS PROTECTION AND MONITORING OF STANDALONE AND GRID CONNECTED PHOTOVOLTAIC ARRAY SYSTEMS USING QUADURATIC INTEGRATION MODELING

A Dissertation
Presented to
The Academic Faculty

By

Aniemi Moffat Umana

In Partial Fulfillment
Of the Requirements for the Degree
Doctor of Philosophy in the
School of Electrical and Computer Engineering

Georgia Institute of Technology
December, 2015

MODULE-LEVEL AUTONOMOUS SETTING-LESS PROTECTION AND MONITORING OF STANDALONE AND GRID CONNECTED PHOTOVOLTAIC ARRAY SYSTEMS USING QUADURATIC INTEGRATION MODELING

Approved by:

Dr. A. P. Sakis Meliopoulos, Advisor
School of Electrical and Computer Engineering
Georgia Institute of Technology

Dr. Ajeet Rohatgi
School of Electrical and Computer Engineering
Georgia Institute of Technology

Dr. Thomas Habetler
School of Electrical and Computer Engineering
Georgia Institute of Technology

Dr. Maryam Saeedifard
School of Electrical and Computer Engineering
Georgia Institute of Technology

Dr. Andy Sun
School of Industrial and Systems Engineering
Georgia Institute of Technology

Date Approved: [September 29, 2015]

To my dear wife, Uduak Umana:

Thank you for your support and for always being there.

I could not have done it without you.

To my beloved children, Andiong, Akeel, Menimel and Ufanel.

To my beloved mother, Bernadette Umana:

Thank you for believing in me.

To my sisters, Nsisong and Ima-Eka:

Thank you for your prayers.

ACKNOWLEDGEMENTS

I want to start by giving glory to my God and King, for making this journey come to a successful end. My journey through Georgia Tech has been an exciting and rewarding one. Though exciting, this journey was not without ups and downs, because I had my fair share of them. I am just very grateful to have wonderful friends and family, who stood by my side, and held me up through this journey.

I remember my first semester in Georgia Tech when I took five classes, was a teaching assistant, and also had to study for the preliminary exam. This was by far my most difficult semester at Georgia Tech. On two separate occasions, I spent a full week in school sleeping on the desk in the lab and going to the gymnasium in the mornings for showers. Looking back, it was all worth it, as these experiences played an important role in equipping me to bring my Ph.D. program to a finish.

I want to specifically thank my professor, Dr. Sakis Meliopoulos, for his support, and for not just being my advisor, but also a mentor. His leadership and counsel were instrumental in the completion of my research at Georgia Tech. I also want to thank him for being patient with me, and addressing all the questions I had during my research. I could not have asked for a better advisor. A special thank you goes to Dr. George Cokkinides, who always made time out of his busy schedule to address questions and issues I had during my research.

Furthermore, I want to thank my thesis committee members, namely, Dr. Ajeet Rohatgi, Dr. Thomas Habetler, Dr. Maryam Saeedifard, and Dr. Andy Sun, for their guidance and willingness to serve on my committee. If I were to select my committee

members all over, I would choose all of you again. I also want to thank Dr. Yongnam Cho, Dr. Sungyan Choi, Dr. Renke Huang, Dr. Yonghee Lee, Dr. Dongbo Zhao, Sanghun Choi, Lianyi Sun, Zhenyu Tan, Rui Fan, Evangelos Polymeneas, Thamer Alquthami, Stella Kampezidou, Liu Yu and the other power system automation laboratory students for their support through my research years at Georgia Tech.

In addition, I want to thank Bath Engineering for giving me some time-off to finish the documentation of my research. I also want to thank the Niger Delta Development Commission for their support.

Lastly, I want to thank my dear wife, Uduak, for her support during this journey. I also want to thank my mother and my children for being so supportive while I spent several hours in school working on my research. I love you Andiong, Akeel, Menimel and Ufanel. Your support gave me the strength and motivation to keep going on.

TABLE OF CONTENTS

LIST OF TABLES

LIST OF FIGURES

xiii

SUMMARY

In this research, a recently developed protection scheme - the setting-less protection, has been applied, for the first time, to the field of photovoltaic (PV) arrays. At this point, the proposed protection algorithm has been implemented on traditional protection zones for individual power system devices, but this research extends this protection to a microgrid, specifically, a system of PV network composed of several PV modules. Several illustrative examples have been provided to demonstrate the effectiveness of this protection scheme even in the presence of changing atmospheric conditions and with the operation of maximum power point tracking (MPPT) equipped dc-dc converters. The contributions of this research to the field of PV array modeling, protection and control are as follows:

- the development of the model of a PV module using Quadratic Integration (QI) modeling,

- the steps for extracting parameters of a PV module,

- the application and extension of the setting-less protection scheme to the protection of an integrated system of devices, namely, the PV modules,

- a method to determine the location of a faulted PV module within an array

- a scheme for providing condition-based monitoring of PV array systems.

A two-diode PV model has been developed using QI modeling. This modeling applies a scaling factor to the Taylor series expansion of the exponential terms of the model of the PV module. Then the higher order terms of the Taylor series expansion are reduced to at most second order terms using the quadratization technique. By applying

the scaling factor, the resulting model of the PV module becomes more accurate than if the scaling factor were not used. The order of accuracy of this scaling factor over the same Taylor series expansion without the scaling factor has been demonstrated to be in the order of 10^{-9} . The significance of this PV model is that its accuracy will aid in performing accurate PV array system state estimation, reliable condition-based monitoring of the PV array, accurate load flow analysis, and other microgrid/power system-based analytical studies.

The accuracy of the model of the PV module is only realized when correct parameters of the PV module have been determined. Therefore, for this research a novel approach to extract the PV parameters, namely, the ideality constants, leakage currents, PV module internal current, shunt resistance and series resistances has been presented. A comparison was performed between numerically generated data using the determined PV module parameters and data measurements from a physical PV module. It was shown that the maximum error from this comparison was below 0.12A for the PV modules used for this research. This contribution is important because accurate PV module parameters are required to adequately model the PV module. Besides, the presented PV protection approach for this research requires an accurate model of the protected system; therefore, these extracted parameters ensure an accurate PV model is used in the PV array protection.

Up to this point, the recently developed setting-less protection has only been implemented on traditional zones of protection for individual power system equipment. This research extends this protection to a system of PV array. Demonstrative examples have been provided to show the protection of the system of PV arrays. On the

significance of this contribution, by implementing the PV array protection as a system, one relay can be used to protect the entire PV system without loss of sensitivity for cell-level anomalies within PV modules. The significance of this contribution is that the PV array is adequately protected against various anomalies that PV array systems are subjected to. Thereby, ensuring the designed lifespan of the PV array system is realized.

The residual data from the PV array protection scheme has been used to develop a method for identifying the location of faulted PV modules. The significance of this contribution is that it saves the PV operator a tremendous amount of time in the inspection of various PV modules to determine the faulted module. The time savings becomes more significant in larger PV installations. By quickly determining the location of the faulted PV module, steps can be taken to isolate and/or replace the faulted module and re-energize the PV array system. This quick PV array system restoration and reconnection to the power network, reduces the downtime of the PV array. Besides, reducing the downtime of the PV array ensures the lost revenue incurred by the PV owner is minimized.

Condition-based monitoring of the PV array system has also been presented with examples. From the PV array system monitoring, the shading and underperformance of a PV module are identified and brought to the attention of the PV system operator. This information is invaluable to a PV system operator, and is a significant contribution in the PV industry because it maximizes the power yield of the PV array. The power yield is maximized because the PV operator has enough PV array information to perform maintenance and/or replacement of underperforming PV modules. This

maintenance/replacement ultimately extends the life of the PV array and maximizes its output power yield, which consequently maximizes the revenue to the PV owner.

This research was based on an actual system that is comprised of 10 identical series connected PV modules. Therefore, the developed PV array system for this research was developed to match this system. However, this protection has not been performed on data from a physical series, parallel PV array system. As a follow up to this research, the developed integrated system of PV array will need to be extended to a physically installed series, parallel PV array system.

Furthermore, under this research, one set of PV parameter was used to form the system of PV array. The use of one set of PV parameter was because the PV modules for this research were identical. In general, PV module parameters in a larger PV array installation may be different, and have slightly different characteristics. The system integration method outlined in this research will need to be modified to accept and use different sets of parameters to reconstruct the integrated PV system model. This integrated PV system will now be comprised of dissimilar PV modules. Additionally, the scheme for detecting an underperforming PV module will need to be modified to include PV array systems with dissimilar PV modules. A modification of this underperformance scheme is required because, given the parameter differences among the PV modules, the PV system voltages may not be evenly distributed across a set of series connected PV modules.

The protection and demonstration discussed in this research uses a personal computer for its computation. Another area of future work is the development of a protective relay hardware, a physical PV array relay. This relay would contain the

necessary computer processor and the input terminals for accepting and calibrating the various PV array measurements. These measurements include voltage, current, temperature and irradiance measurements. Also, this relay should have the required communication infrastructure for the PV operator to download PV event reports. This equipment will then become a standalone hardware that can be used within the microgrid for the protection of PV arrays.

1 INTRODUCTION

The capacity of installed photovoltaic (PV) array systems continues to increase over the years. Some currently installed PV arrays have reached high capacities, such as, the Topaz solar farm in California with a capacity of 500MW. With such high capacity installations, it behooves PV protection engineers to adequately protect the PV array from various anomalies that could occur in the PV system. The PV array, however, has an electrical characteristic that is different from traditional power generation systems such as fossil fuel generators. This difference in characteristics gives rise to challenges in the protection of the PV array system. In this chapter the problem statement for this thesis is discussed. Also, the objective and outline of this research is addressed.

1.1 Problem Statement

The unique characteristic of the PV array poses a challenge in its protection method. PV arrays have been predicted to constitute a significant percentage of new generation connected to the power system [1]. China has published its plans to develop large scale PV integration into the high voltage-level grid of western China in the near future [2]. Therefore, it is important that an effective PV protection philosophy is established that addresses the prevalent faults that might occur within the PV array system. In a conventional power system with PV arrays, the currently used protection philosophies have some drawbacks in protecting PV arrays. During fault conditions in a PV array, the fault current magnitude is usually very close to the nominal load current magnitude. This similarity in current magnitude makes it difficult for the traditional protection devices to differentiate between load and fault currents. Furthermore, using traditional protection systems, it is challenging to detect fault conditions, such as, a high

impedance fault between the PV module terminals and ground, a line to line fault on the terminals of PV modules, or faults during low solar irradiance. If these faults within the PV system are not quickly isolated, these faults can lead to a fatality or fire hazard on the panels as seen in [3].

In a PV array that has a series connected diode, only the reverse current of the diode can flow from an external system to a faulted PV array. The location of this fault is assumed to be behind the series diode. The reverse current is typically in the order of $10^{-9}A$, and too small to be detected by traditional overcurrent devices. Therefore, the fault within the PV array could continue to circulate, posing a safety threat to the equipment and personnel working around the PV system. Consequently, in this research, a recently developed protection philosophy, the setting-less protection [4], has been extended to the PV system to address these drawbacks of traditional protective devices. An added benefit of extending this protection scheme to the PV system is the ability to determine the location of a faulted PV module, and providing preventative diagnostics for the system of PV array.

The setting-less protection of the PV module is a model-based state estimation protection approach, where an accurate model of the PV module is required for the PV protection. With this setting-less protection approach, internal parameter of the PV, such as, the internal voltage can be estimated and made available to the system operator. In contrast to the currently used protection philosophy, where fuses are used for line-line faults, and ground fault detectors are used to detect PV array ground faults, the setting-less protection embodies both functionalities of detecting line-line faults and ground faults. Moreover, the setting-less protection is able to detect high impedance faults where

the current magnitude would typically be too low for traditional PV protection systems to detect.

At the system level, the integration of renewable generation such as PV arrays has brought concerns on the security and stability of the electrical system. The output of a PV array is intermittent and depends on external factors such as irradiance and temperature; consequently, on a cloudy day, the output of the PV system is greatly affected. Therefore, at a large-scale PV level, most PV systems have devices to extract the maximum power from the PV array even during cloudy days. For this research a dc-dc booster equipped with MPPT has been modeled using the quadratic integration technique [5]. Quadratic integration (QI) modeling method is a time-domain based numerical integration method which performs better than other popular numerical integration methods, such as trapezoidal integration (TI). The TI has an accuracy of order two, compared to the order 6 accuracy of QI [6]. A comparison between QI, TI and cubic integration methods was done in [6]. In this comparison, it was demonstrated that the QI method is more robust, and does not suffer from numerical oscillation as the trapezoidal and cubic integration methods. This robustness makes the QI method suitable for complex power system modeling, and is the reason why the QI method was selected for this research.

1.2   Objective of Research

The objective of this research is to introduce a recently developed power systems protection approach to Microgrids by implementing and demonstrating this protection method in the PV array. This research extends this protection approach beyond a component-level protection to the protection of an integrated system of components, namely, a system of PV arrays. In addition to offering a system-level protection, this

scheme, at the same time, also offers a module-level PV protection with the added benefit of detecting the location of faulted PV modules. To adequately protect the PV array system, accurate PV parameters such as series and shunt resistances, ideality constants and leakage currents have to be determined. Therefore, this research outlines a novel way of extracting the PV module parameters via estimation methods. The parameter extraction is done using the data from the PV module datasheet and an additional PV module data measurement. The additional data measurement can be obtained from the PV module curve provided from manufacturer, or from physical measurements. Furthermore, the PV array interfaces with various power system devices to connect to the power grid. Therefore, to demonstrate this protection scheme, quadratic integration modeling of microgrid components used for this research, has been performed. These microgrid components include the lead-acid battery, the PV module, an MPPT-equipped dc-dc converter, and a single-phase inverter.

The microgrid is comprised of components that have different fault current characteristics, and are interfaced with inverters which are typically designed to limit fault currents from the microgrid. An additional complexity is the fact that when the microgrid is interconnected with the main power grid, the fault current from the main grid may be much higher than the fault contribution from the microgrid components. This higher fault contribution from the main grid makes it difficult to detect and clear faults at microgrid circuits. The basic approach of this research project is to introduce and demonstrate the setting-less protection of the PV array, both at a system and module level, while providing condition based monitoring of the PV array. As discussed in the

subsequent chapters, this setting-less protection scheme is a dynamic state estimation (DSE)-based protection which requires an accurate PV model.

1.3   Outline of Thesis

The remainder of this thesis is organized as follows: in chapter 2, the literature survey that was performed in relation to the challenge of protecting PV arrays is addressed. Furthermore, current state of the art designs and previous work proposed on dc-dc boosters with MPPT functionality is also addressed.

In chapter 3, QI modeling and validation of the PV module is discussed. The developed model of PV modules is used to formulate the system-level model of the entire PV array. The system-level model is used to demonstrate the protection of the PV array systems.

In chapter 4, the method for extracting the parameters of the PV module is presented. The parameter extraction is performed using the data provided on the datasheet of the PV, such as, the open circuit voltage, the maximum power voltage and current, and the short circuit current. Also, the methods used for the parameter extraction, namely, the Steepest Descent numerical method, and the Fibonacci search method, is discussed.

In chapter 5, the various microgrid components that have been modelled are listed and integrated into a system. It is on this integrated system that the protection method and monitoring of the PV system is demonstrated.

The formulation of the setting-less protection algorithm as it relates to the protection of the PV array system is discussed in chapter 6. As was noted, this protection

method requires an accurate model of the PV. The developed model of chapter 3 is used for the protection formulation.

The demonstration of the formulated protection scheme of chapter 6 is presented in chapter 7. This demonstration is by means of numerical simulations and comprises fault conditions, such as, the line to ground and high impedance faults. In this chapter, it will also be shown that this protection method is not affected by normal changes in atmospheric conditions, such as changes in temperature and solar irradiance.

In chapter 8, the setting-less protection algorithm is applied on data that was obtained from an actual PV installation, thereby, further validating the efficacy of this protection scheme. The events that were tested on the actual PV installation included high and low impedance fault conditions.

The use of this protection scheme to perform condition-based monitoring of the PV array, and the detection of the shading effect on the PV array system is discussed and demonstrated in chapter 9.

In chapter 10, conclusions of this research, including the contributions of this research are discussed. Also discussed in this chapter is the significance of each contribution, and the potential future work for this research.

This dissertation has six appendices. Appendix A, Appendix B, Appendix C and Appendix D, cover the modeling of the lead-acid battery, dc-dc converter, single phase inverter, and single phase load respectively. The models in the appendices are the ones used in the integrated system of chapter 5. Appendix E lists the data measurements for a PV module, and groups them under different measurement types. Appendix F consists of several simulation results, which illustrate the presented protection scheme.

2 LITERATURE SURVEY

In this chapter, the challenges in protecting the PV array system, along with current state-of-the-art systems in protecting the PV array is covered. Also, the drawbacks of these traditional PV protection systems are discussed.

Fault currents of PV arrays are usually quite close in magnitude to the nominal load current. However, it is essential that these fault currents are interrupted to prevent damage to the solar cells and to ensure personnel safety. Different protection methods are currently used in commercial PV systems, and several other protection methods have been proposed. While a lot of these protection methods have some merits, some of these methods make assumptions that are specific to a particular PV configuration. For example, some of these methods rely on the absence of a series connected blocking diodes to the PV array. The absence of this blocking diode leads to a higher fault current contribution from the power system to operate the PV array protective device, the series fuse. Therefore, these traditional PV protection methods do not address a general PV system configuration, and typically do not operate during certain types of faults within the PV system, such as, high impedance faults.

2.1 Traditional PV Fault Detection systems and their drawbacks

Most traditional systems use overcurrent devices for the protection of the PV array against line-to-line faults, as demonstrated in [7]. However, the overcurrent device, which is typically a fuse, is only able to detect and isolate the fault if the solar irradiation is high. At high irradiation, a large PV currents magnitude is generated. This high current magnitude could fall within the operating curve region of the fuse, as compared with lower irradiation conditions. When the fault current is low due to reduced irradiation, the

fuse will be unable to detect the fault currents, because the current magnitude is much lower than the operational range of the fuse. Moreover, in [7], a resistive grounding system is used to detect ground faults in the PV system, but it was also demonstrated that a double ground fault in the PV system would by-pass the ground detection system and go unnoticed.

Furthermore, it has been demonstrated that fault currents are not easily detected in the presence of blocking diodes [8]. The blocking diodes are used to prevent current reversal from the storage battery in a stand-alone system. This inability to detect fault currents results because the blocking diode only permits the reverse current to go through the series fuse of the PV array. Besides, the reverse current will usually be much smaller than the rating of the fuse. Therefore, it was proposed that the blocking diodes be removed to mimic commercial grid-connected PV systems in [8]. While the removal of this blocking diode may be a possible solution for commercial systems, this solution does not work for the protection of stand-alone systems. Furthermore, the blocking diode removal only avoids, rather than solves, the "inability to detect faults in the presence of blocking diodes" issue.

Other challenges with overcurrent protection devices have been investigated in [8]. In addition to the difficulty for the fault current to be noticed during low irradiance, it has been shown that in the presence of MPPT, faults that occur during low irradiance may never be detected even when the irradiance becomes high enough. This inability to detect the fault is due to the optimization of the MPPT to get the maximum power, thereby, keeping the fault current lower than it would have been without MPPT. The MPPT fault-current-level-reduction scenario is buttressed in [9], which avers that faults in PV systems

8

at night can also go unnoticed throughout the day. The fault current can go unnoticed because, as the irradiation increases during the day, the MPPT continues to operate to draw the maximum power from the PV system, thereby, preventing the current from getting high enough to be detected by the fuse.

A differential method of protection is proposed in [10], where the current going out of the positive terminal of the PV equals the current coming into the negative terminal. Although the focus of the protection is on distributed generation, the drawback of this protection is its dependence solely on current quantities. For example, if a line to line fault occurs shorting out a set of PV modules, the current going out of the array will be equal to that coming in. In this scenario, the line-to-line fault may never be detected by the differential protection.

Moreover, even though fuses and blocking diodes alone cannot adequately protect a PV system, research has shown that eliminating these devices from the PV installation can lead to extensive damages during ground faults [11]. These fuses have been shown to not only be effective during high irradiance faults, but also in situations where fault currents come from the utility grid to a fault located within the PV system. Fault currents from the utility will usually be high enough to melt the fuse; therefore, the fuse is still a useful device for protecting the PV system against faults. Furthermore, in the presence of the blocking diode, not only is current reversal from the battery bank inhibited, fault current contribution from the battery and ac system is limited to the amount of reverse current permitted by the blocking diode. Besides, if the blocking diode fails, since it fails to a shorted position [11], the higher currents can then be detected and interrupted by the series fuse.

Another issue of concern in the protection of PV systems is the amount of down time of the PV systems due to the melting of a fuse. It was reported in [12] that blown fuses and alarm related shut down accounted for over half of the system down time in a Hesperia PV system. It was recommended that the fuses be replaced with DC circuit breakers with an ampacity of at least 1.25 times that of the short circuit current. This approach can shorten the time taken to put the PV system back in service after the cause of the fault has been identified and addressed. The reduction in the PV array down time comes from only having to switch the DC breakers back to the on-state, as compared with the time it would take to replace damaged fuses. The drawback to this approach is that the DC breakers are not capable of identifying various faults to which the PV system may be subjected, such as a high impedance fault.

Additionally, in a PV system, there can be leakage currents in various locations, such as surge protection devices, wiring circuits, and interconnected arrays, which when added up, can appear as a ground fault [13]. In this scenario, since the fault does not follow a fixed path, neither the DC breaker proposed in [12] nor the generally used fuses will be able to detect this kind of fault. The method proposed in [7] may be able to detect this kind of ground fault. In [7], the PV system is connected to ground through a resistor with a ground fault detector (GFD), such that any ground fault current would establish a voltage across the grounding resistor, thereby, causing the GFD to activate. The assumption is that the return path of the current will be strictly through the grounding resistor. However, in the presence of multiple grounds, this ground-fault detector may never operate.

Another challenge of the currently used protection schemes for PV systems is the inability to detect arcing faults. Studies have shown that arcs as low as 200 watts with an arc length of 10 mm can ignite most plastics in a matter of 4 seconds [14]. This ignition implies that not only will the wire or circuit under the fault condition be damaged, but also, other wires in the vicinity of the arc are subjected to damage as well. In a PV system protected primarily with fuses, the operation of the fuse is dependent on the fault current level. An arcing fault in a PV array will alter the resistance of the PV system and will affect the current seen by fuse. If the presence of the arcing fault is such that the PV current magnitude is lowered, the fuse may not be able to detect the presence of a fault. Besides, even if the fault current were high enough to be detected by the fuse, depending on the magnitude of the fault current, the time it takes for the fuse to operate may be longer than is required to prevent damage to the PV systems, due to the generated heat energy from the arc. The resulting temperature from the generated heat can be as high as 6000K to 7000K [14]. Therefore, the presence of an arcing fault calls for a protection scheme that is guaranteed to operate in a high enough speed that will prevent extensive damage to the PV array system.

2.2 Proposed PV Fault Detection system

In light of the drawbacks of existing and currently proposed methods, it is essential to develop a protection system that is robust enough to detect various types of anomalies such as line to line faults, ground faults and shading conditions in PV systems. This protection system should be expected to operate irrespective of the changes in irradiation, the presence of blocking diodes, or the operation of MPPT. Therefore, in this research, a new protection system to the PV industry is proposed, namely the module-level setting-

less protection of PV systems and is applicable to both standalone and grid-connected PV systems. The PV model used for this research and the PV protection algorithm is discussed in subsequent chapters.

2.3   PV Parameter Extraction Methods

An essential part in the modeling of a PV module is the extraction of the PV module parameters. A lot of work has been done in the area of PV parameter extraction for both the one-diode and two-diode PV models. In [15], the PV parameters are determined for a one-diode model via computation rather than simulation. The maximum error obtained using this method is close to 0.2A. The one-diode model is also used in [16], where the shunt resistance is maximized while the series resistance is minimized. In this method of parameter extraction, zero values are often obtained for the series resistance. Also, the maximization of the shunt resistance is supposed to be done using an equation that has several unknowns. This method of PV extraction obtained good results, however there are no steps on how the resistance values are obtained.

Another PV extraction method is presented in [17], where the series and shunt resistances are computed as a pair. This method selects a series and shunt resistance pair, with a fixed ideality constant, and from these three parameters, the rest of the PV parameters are determined. At the start of this method, the optimum series resistance value is unknown. The optimum series resistance value is obtained by varying its value from zero to an upper limit. The series resistance value that results in the least PV power deviation from the maximum PV power, as documented on the PV datasheet, is considered the optimum series resistance value. The selected ideality constant, which was held constant to find the optimum series resistance, is later adjusted to improve the

obtained result. This parameter extraction method also yields good results, but has the drawback of performing several functional evaluations as the value of the series resistance is varied from zero to its upper limit.

The approach in [18], [19], and [20] use a two-diode PV model approach, with simplifications that make the set of equations solvable, given the initial four equations with seven unknowns. The approach in [18] is based on a linear fitting of the PV data, with the assumption that the data used is accurate. In other words, spurious data could weaken the effectiveness of this approach. In [19], a simplification that is common in the extraction of PV parameters is done. This simplification assumes that the leakage current through the two diodes in the PV model are of a small magnitude. Furthermore, at this small magnitude, the values of these two leakage currents are assumed to be of the same value. This simplification eliminates the need of computing the two leakage currents separately, as they are effectively the same. The simplifications done in [20] are that the two leakage currents have the same value, similar to the assumption in [19], besides, the values selected for the ideality constants are chosen arbitrarily.

All these methods attempt to extract the PV parameters from limited information from the manufacturer. In this research the PV parameter is extracted by introducing an extra equation from a data measurement from the PV module. Next the Steepest Descent numerical method is used in conjunction with the Fibonacci optimization search method to extract the PV parameters. It should be noted that no simplifications, such as the leakage currents being the same, have been made, and the ideality constants are determined sequentially. The end result of the proposed method is that it produces PV parameters that closely match the measured PV data curves for this research.

2.4   MPPT-equipped DC-DC converters

On the topic of dc-dc converters for PV arrays, several methods have been proposed. Simulation results from a pulse width modulation (PWM) controller with a switching frequency of 100 kHz and another simulation that uses a hysteresis controller have been presented in [21]. While the techniques for these controls are effective, without an MPPT algorithm, the PV inverter may be operational but not extracting the maximum power from the PV system.

Others have proposed MPPT that uses an open loop system [22]. The control method outlined in [22] was used to demonstrate the extraction of the maximum power at a given solar irradiation and temperature. In this method of control, the maximum power point voltage (V_{mp}) is approximated as a constant factor of the open circuit voltage (V_{oc}), given as

$$V_{mp} = \alpha V_{oc}.$$
(2.1)

To determine the open circuit voltage for the PV array using this method, a separate PV cell is installed in the vicinity of the PV array. The assumption is that the PV cell is subjected to the same weather conditions as the PV array. The sole purpose of the additionally installed PV cell is to measure the V_{oc} of the PV cell, which is considered a factor of the open circuit voltage of the PV array, and used to determine V_{mp}. The assumption that the open circuit voltage of the PV cell is the same as that of the PV array appears to be ideal for a small PV installation. For a large PV array, there could be a high additional cost of installing the additional PV cells just to determine V_{oc}. Besides, in large PV systems, different segments of the PV array could be subjected to different levels of shading and surface temperature that will affect the overall V_{oc}. Therefore, using only the

data from the additionally installed PV cells may not offer accurate values to guarantee the extraction of maximum power from the PV system. From the foregoing, the effectiveness of this method is limited to smaller PV systems, perhaps at the residential level.

Another approach is adopted in [23], where the actual power that is drawn from the PV system, at a given voltage, is compared to a reference power. The reference power was obtained from predetermined power versus voltage curves at different insolation levels. Therefore, for a given voltage, the corresponding power at the selected insolation indicated the potential maximum power that could be extracted from the PV system. The error obtained from the extracted power – reference power comparison is applied to a proportional-integral (PI) regulator, which ultimately generates the required control signal required for the switches (e.g., IGBT's) to extract the maximum power from the PV system. With this approach, not much information is given on how the control of the dc-dc booster is obtained. To obtain the maximum power from the PV system, the insolation level will have to be determined, so that the voltage level that corresponds to that maximum power can be determined and operated at. Therefore, it is not clear how the implementation of this approach can be achieved, since the voltage level alone is just a piece of the bigger solution.

Other publications have stated that the stability level of the PV systems can be improved by adopting a distributed MPPT approach on each panel, rather than using a central MPPT [24]. In this method, the incremental conductance is used, which is based on the fact that at the maximum power point of the PV, the slope of the PV power is zero. Therefore, the following can be said,

$$\frac{dP}{dV} = \frac{dIV}{dV} = V\frac{dI}{dV} + I\frac{dV}{dV},$$

$$\cong V\frac{\Delta I}{\Delta V} + I.$$
(2.2)

At the maximum power point, the change in power with respect to the change in voltage is zero, therefore,

$$\frac{dP}{dV} = 0 = V\frac{\Delta I}{\Delta V} + I.$$
(2.3)

From the foregoing, at the maximum power point, the change in current with respect to the change in voltage is given as

$$-\frac{I}{V} = \frac{\Delta I}{\Delta V}.$$
(2.4)

From (2.4), the incremental conductance control method is implemented to generate the required duty cycle for the switch to attain the maximum power point. The approach in [24] shows acceptable results in using the distributed MPPT approach. The only drawback in using this distributed method is that in a large PV installation, the improved stability of the system comes at the expense of an increase in installation cost, from installing MPPT devices at individual PV modules.

2.5 Modeling of MPPT-equipped dc-dc converter

From the foregoing, it is essential to develop an MPPT equipped dc-dc boosters with sufficient operational speed to function under changing power system conditions, while offering improved stability and retaining cost effectiveness.

MPPT-equipped dc-dc converters ensure that the connected PV arrays operate at an operational point that supplies the maximum power to the power network. This MPPT

function becomes invaluable during varying atmospheric conditions, where the operating condition at a given atmospheric condition may not be the optimum operational point at a different atmospheric condition.

The MPPT control algorithm that is used for the QI-modeled dc-dc booster for this research is the Perturb and Observe (P&O) method which has a low-medium implementation complexity compared with other MPPT control algorithms as outlined in [25]. Besides, by performing QI modeling, the MPPT equipped dc-dc converter will not only yield results void of numerical oscillations, but yield results with a higher order of accuracy as discussed in chapter 1. This MPPT implementation is used to demonstrate the efficacy of the proposed PV protection system. Also, the proposed PV protection scheme has been demonstrated to function properly in the presence of the MPPT algorithm of the dc-dc converter.

3 DEVELOPMENT OF PV MODEL

In this chapter, the mathematical model for the PV module is derived. This model is used for the setting-less protection of the PV as discussed in chapter 6. The model of the PV module that is modeled in this chapter is the two-diode model. The two-diode model is a common scheme that is used in several of similar modeling as seen in [17]-[19]. This model of the PV module is modeled using QI.

3.1 Quadratic Integration Modeling

The modeling technique used for this research project is the quadratic integration modeling method. This modeling method is a numerical integration method which is based on the assumption that over an integration time step, the numerically integrated function varies quadratically. The accuracy of this modeling method has been verified in [5] and [26] and when compared to other modeling techniques, such as the TI numerical method, the QI modeling yields more accurate results of order 10^{-6} [6]. There are other modeling methods that yield more accurate results than the QI such as the cubic numerical method. However, the cubic method may create fictitious oscillations which QI does not suffer from.

3.2 Two-Diode PV Model

In this section, the modeling of a PV module is discussed using the two-diode PV schematic given in Figure 3.1. First, the compact form of the PV model is derived, then the quadratized model which has at most second order terms.
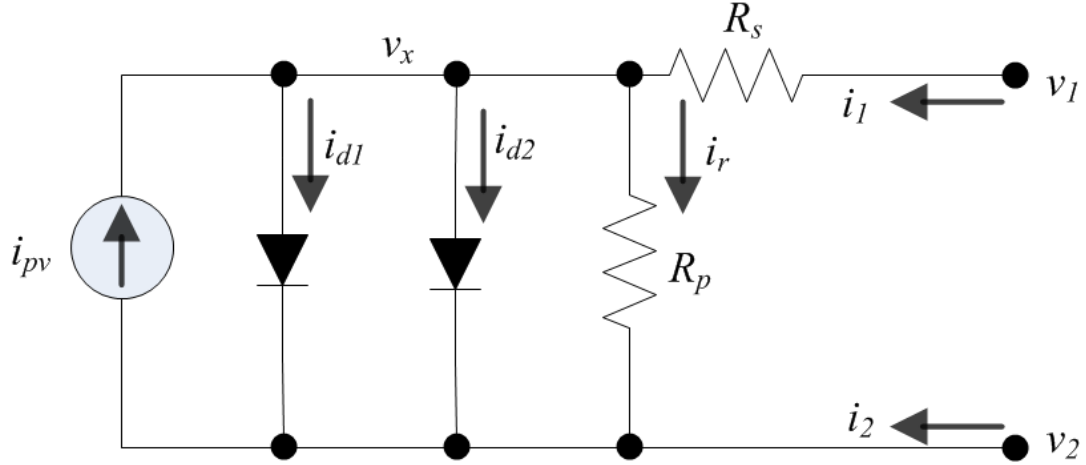
Figure 3.1:   Schematic for photovoltaic module.

3.2.1   Compact Model of a PV Module

From Figure 3.1, the mathematical equations that characterize the operation of a PV module are obtained, and these mathematical equations are discussed next. Assuming the series and parallel conductance of Figure 3.1 are given as $G_s = 1/R_s$ and $G_p = 1/R_p$ respective, then the mathematical model is as follows:

$$i_1 = G_s\left(v_1 - v_x\right),\tag{3.1}$$

$$i_2 = -G_s\left(v_1 - v_x\right),\tag{3.2}$$

$$0 = -G_s(v_1 - v_x) + G_p\left(v_x - v_2\right) + i_{d1} + i_{d2} - i_{pv},\tag{3.3}$$

where

i_{d1} = diode current due to diffusion in the p-n junction, and

i_{d2} = diode current due to recombination.

The expression for the current through a diode is a known expression, and for the two diodes in Figure 3.1, are given as

19

$$i_{d1} = I_{o1}\left[\exp[(v_x - v_2)/aN_sV_T]-1\right], \tag{3.4}$$

$$i_{d2} = I_{o2}\left[\exp[(v_x - v_2)/nN_sV_T]-1\right], \tag{3.5}$$

where:

I_{01} = leakage current 1, through diode 1 of Figure 3.1,

I_{02} = leakage current 2, through diode 1 of Figure 3.1,

V_T = thermal voltage constant, which is given by $\frac{kT}{q}$, $k = 1.381x10^{-23}\frac{J}{K}$, $q = 1.6x10^{-19}eV$, $and\ T$ is temperature which is 300K at room temperature.

a = ideality constant for diode 1,

n = ideality constant for diode 2,

N_S = number of series connected PV cells within a PV module, found on the PV module datasheet.

The expression for i_{pv} in (3.3) depends on temperature change and solar irradiance and is given as:

$$i_{pv} = \left(I_{pv,n} + k_1\Delta_T\right)\frac{S}{S_n}, \tag{3.6}$$

where:

$I_{pv,n}$ = light generated current under STC,

k_1 = temperature coefficient for the current, found on the PV datasheet,

Δ_T = currently measured temperature – nominal temperature, $(T - T_n)$,

S = solar irradiance on the PV surface measured in (W/m^2),

S_n = Nominal solar irradiance $(1000\ W/m^2)$.

The open circuit voltage of the PV module is also temperature dependent, and has a relationship given as

$$v_{oc} = \left(v_{oc,n} + k_2 \Delta_T\right),$$ (3.7)

where k_2 is the temperature coefficient for the voltage of the PV module.

Some of the parameters in (3.1) – (3.6), such the terminal voltage v_1 and v_2, the PV temperature, T, and the solar irradiance, S, can be directly measured. Other parameters such as the number of series connected PV cells, N_s, and the PV module current and voltage temperature coefficients k_1 and k_2 respectively, are provided on the datasheet of the PV module. There are seven parameters that are neither provided on the manufacturer's datasheet nor can they be directly measured. These unknown parameters are i_{pv}, I_{01}, I_{02}, R_s, R_p, a, and n, and are determined in chapter 4.

The equations obtained so far are summarized as follows:

$$i_1 = G_s v_1 - G_s v_x,$$ (3.8)

$$i_2 = -G_s v_1 + G_s v_x,$$ (3.9)

$$0 = -G_s v_1 - G_p v_2 + \left(G_p + G_s\right) v_x + I_{o1}\left[\exp\{(v_x - v_2)/aN_sV_T\} - 1\right]$$
$$+ I_{o2}\left[\exp\{(v_x - v_2)/nN_sV_T\} - 1\right] - i_{pv},$$ (3.10)

and can be written in a compact form as,

$$\begin{bmatrix} I \\ 0 \end{bmatrix} = M \begin{bmatrix} V \\ Y \end{bmatrix} + N,$$ (3.11)

where $I = \begin{bmatrix} i_1 i_2 \end{bmatrix}^T$,

$V = \begin{bmatrix} v_1 v_2 \end{bmatrix}^T$,

$Y = \begin{bmatrix} v_x \end{bmatrix}$,

$$M = \begin{bmatrix} G_s & 0 & -G_s \\ -G_s & 0 & G_s \\ -G_s & -G_p & (G_p + G_s) \end{bmatrix}, \text{ and}$$

$$N = \begin{bmatrix} 0 \\ 0 \\ I_{o1}\left[\exp[(v_x - v_2)/aN_sV_T]-1\right] + I_{o2}\left[\exp[(v_x - v_2)/nN_sV_T]-1\right] - i_{pv} \end{bmatrix}.$$

3.2.2 Quadratized Model of a PV Array

In this section, three PV models are considered, namely: the piecewise linear approximation model, which approximates the exponential term of (3.10); the exponential model, which expresses the exponential term of (3.10) as a Taylor series expansion; and an approximation that scales the exponential term of (3.10).

3.2.2.1 *Quadratized Piecewise Linear Model of a PV Module*

The first exponential term in (3.10) is expressed as a Taylor series expansion as follows:

$$\exp[(v_x - v_2)/aN_sV_T] = 1 + \frac{v_x - v_2}{aN_sV_T} + \frac{(v_x - v_2)^2}{2a^2N_s^2V_T^2} + \frac{(v_x - v_2)^3}{6a^3N_s^3V_T^3} + \cdots HOT, \quad (3.12)$$

however, during simulations, the solution for this expression may not converge quickly for operating conditions that are close to the open circuit voltage. This is because, as the value of the quantity, $(v_x - v_2)/aN_sV_T$ increases, higher terms of the Taylor series expansion are required to bring the curve closer to the actual exponential curve. Furthermore, as the result of the exponential term evaluation increases beyond 15 to 17 digits, it was noticed that the precision of the exponential term decreased as compared to

the actual exponential curve. In the presence of MPPT converter, where the PV operates primarily at the maximum power point (MPP), the slow convergence in the exponential modeling no longer becomes a significant issue. Besides, when the PV module operates at the MPP, it is operating away from the open circuit voltage. The exponential model that is used for the demonstrated the protection algorithm for this research is covered in section 3.2.2.4. To ensure convergence is achieved for the entire PV voltage operating domain, a piecewise linear model, which is an approximation model, has been developed in this section. Considering only the first exponential of (3.10), the approximation model commences with the equation

$$\exp[(v_x - v_2)/aN_sV_T] = A(1+x).$$
(3.13)

Consequently, the following are obtained:

$$(v_x - v_2)/aN_sV_T = \ln(A) + \ln(1+x),$$
(3.14)

$$\ln(1+x) = x - \frac{x^2}{2} + \frac{x^3}{3} - \frac{x^4}{4} + \frac{x^5}{5} - \frac{x^6}{6} + ...HOT,$$
(3.15)

where $(-1 \le x \le 1)$.

From the foregoing, i_{d1} in (3.4) is given as:

$$i_{d1} = I_{01}\left[A(1+x)-1\right] = I_{01}(A + Ax - 1),$$
(3.16)

and by writing a similar expression for the second exponential of (3.10), combining (3.13) through (3.16) and substituting in (3.10) gives

$$0 = -G_s(v_1 - v_x) + G_p(v_x - v_2) + I_{01}(A + Ax - 1) + I_{02}(B + By - 1) - i_{pv},$$
(3.17)

where A is substituted with B, x substituted with y, and a substituted with n to derive the corresponding expression for the second exponential term of (3.10).

Equation (3.15) has non-linear terms of degree 6, and the objective of the quadratization process of this section is to reduce the high-order, non-linear terms to at most a second order term, hence forming a quadratic equation. This order reduction is achieved by the introduction of new state variables, as follows:

$$0 = z_1 - x^2, \tag{3.18}$$

$$0 = z_2 - z_1^2. \tag{3.19}$$

By substituting (3.18) and (3.19) in (3.15) and substituting the result in (3.14) gives,

$$0 = \frac{(v_x - v_2)}{aN_sV_T} - \ln(A) - x + \frac{z_1}{2} - \frac{z_1 x}{3} + \frac{z_2}{4} - \frac{z_2 x}{5} + \frac{z_1 z_2}{6} - \cdots HOT. \tag{3.20}$$

The summary of equations obtained from the quadratization process is given as follows:

$$i_1 = G_s v_1 - G_s v_x, \tag{3.21}$$

$$i_2 = -G_s v_1 + G_s v_x, \tag{3.22}$$

$$0 = -G_s v_1 - G_p v_2 + \left(G_p + G_s\right)v_x + I_{01}Ax + I_{02}By + I_{01}\left(A - 1\right) + I_{02}\left(B - 1\right) - i_{pv}, \tag{3.23}$$

$$0 = z_1 - x^2, \tag{3.24}$$

$$0 = z_2 - z_1^2, \tag{3.25}$$

$$0 = z_3 - y^2, \tag{3.26}$$

$$0 = z_4 - z_3^2, \tag{3.27}$$

$$0 = \frac{-v_2}{aN_sV_T} + \frac{v_x}{aN_sV_T} - x + \frac{z_1}{2} + \frac{z_2}{4} - \frac{z_1 x}{3} - \frac{z_2 x}{5} + \frac{z_1 z_2}{6} - \ln(A), \tag{3.28}$$

$$0 = \frac{-v_2}{nN_sV_T} + \frac{v_x}{nN_sV_T} - y + \frac{z_3}{2} + \frac{z_4}{4} - \frac{z_3 y}{3} - \frac{z_4 y}{5} + \frac{z_3 z_4}{6} - \ln(B), \tag{3.29}$$

where (3.26), (3.27), and (3.29) are contributions from the second exponential term of (3.10). The PV equations (3.21) - (3.29) are cast into a standard matrix form for autonomous operation, and the standard matrix form is given as

$$
\begin{bmatrix} i_1 \\ i_2 \\ 0 \\ 0 \\ 0 \\ 0 \\ 0 \\ 0 \\ 0 \end{bmatrix} = [Yeq] \begin{bmatrix} v_1 \\ v_2 \\ v_x \\ x \\ y \\ z_1 \\ z_2 \\ z_3 \\ z_4 \end{bmatrix} + \begin{bmatrix} v_1 \\ v_2 \\ v_x \\ x \\ y \\ z_1 \\ z_2 \\ z_3 \\ z_4 \end{bmatrix}^T [Meq] \begin{bmatrix} v_1 \\ v_2 \\ v_x \\ x \\ y \\ z_1 \\ z_2 \\ z_3 \\ z_4 \end{bmatrix} - [Beq],
\tag{3.30}
$$

where Yeq is expressed as

$$
Y_{eq} = \begin{bmatrix}
G_s & 0 & -G_s & 0 & 0 & 0 & 0 & 0 & 0 \\
-G_s & 0 & G_s & 0 & 0 & 0 & 0 & 0 & 0 \\
-G_s & -G_p & G_p+G_s & I_{01}A & I_{02}B & 0 & 0 & 0 & 0 \\
0 & 0 & 0 & 0 & 0 & 1 & 0 & 0 & 0 \\
0 & 0 & 0 & 0 & 0 & 0 & 1 & 0 & 0 \\
0 & 0 & 0 & 0 & 0 & 0 & 0 & 1 & 0 \\
0 & 0 & 0 & 0 & 0 & 0 & 0 & 0 & 1 \\
0 & \dfrac{-1}{aN_sV_T} & \dfrac{1}{aN_sV_T} & -1 & 0 & \dfrac{1}{2} & \dfrac{1}{4} & 0 & 0 \\
0 & \dfrac{-1}{nN_sV_T} & \dfrac{1}{nN_sV_T} & 0 & -1 & 0 & 0 & \dfrac{1}{2} & \dfrac{1}{4}
\end{bmatrix},
\tag{3.31}
$$

25

Meq expressed as

$$M_{eq} = \begin{bmatrix} Feq_0 \\ Feq_1 \\ Feq_2 \\ Feq_3 \\ Feq_4 \\ Feq_5 \\ Feq_6 \\ Feq_7 \\ Feq_8 \end{bmatrix}, \tag{3.32}$$

with

$$Feq_0 = Feq_1 = Feq_2 = \begin{bmatrix} 0 & 0 & 0 & 0 & 0 & 0 & 0 & 0 & 0 \\ 0 & 0 & 0 & 0 & 0 & 0 & 0 & 0 & 0 \\ 0 & 0 & 0 & 0 & 0 & 0 & 0 & 0 & 0 \\ 0 & 0 & 0 & 0 & 0 & 0 & 0 & 0 & 0 \\ 0 & 0 & 0 & 0 & 0 & 0 & 0 & 0 & 0 \\ 0 & 0 & 0 & 0 & 0 & 0 & 0 & 0 & 0 \\ 0 & 0 & 0 & 0 & 0 & 0 & 0 & 0 & 0 \\ 0 & 0 & 0 & 0 & 0 & 0 & 0 & 0 & 0 \\ 0 & 0 & 0 & 0 & 0 & 0 & 0 & 0 & 0 \end{bmatrix}, \tag{3.33}$$

and

$$Feq_3 = \begin{bmatrix} 0 & 0 & 0 & 0 & 0 & 0 & 0 & 0 & 0 \\ 0 & 0 & 0 & 0 & 0 & 0 & 0 & 0 & 0 \\ 0 & 0 & 0 & 0 & 0 & 0 & 0 & 0 & 0 \\ 0 & 0 & 0 & -1 & 0 & 0 & 0 & 0 & 0 \\ 0 & 0 & 0 & 0 & 0 & 0 & 0 & 0 & 0 \\ 0 & 0 & 0 & 0 & 0 & 0 & 0 & 0 & 0 \\ 0 & 0 & 0 & 0 & 0 & 0 & 0 & 0 & 0 \\ 0 & 0 & 0 & 0 & 0 & 0 & 0 & 0 & 0 \\ 0 & 0 & 0 & 0 & 0 & 0 & 0 & 0 & 0 \end{bmatrix}, \tag{3.34}$$

$$Feq_4 = \begin{bmatrix} 0 & 0 & 0 & 0 & 0 & 0 & 0 & 0 & 0 \\ 0 & 0 & 0 & 0 & 0 & 0 & 0 & 0 & 0 \\ 0 & 0 & 0 & 0 & 0 & 0 & 0 & 0 & 0 \\ 0 & 0 & 0 & 0 & 0 & 0 & 0 & 0 & 0 \\ 0 & 0 & 0 & 0 & 0 & 0 & 0 & 0 & 0 \\ 0 & 0 & 0 & 0 & 0 & -1 & 0 & 0 & 0 \\ 0 & 0 & 0 & 0 & 0 & 0 & 0 & 0 & 0 \\ 0 & 0 & 0 & 0 & 0 & 0 & 0 & 0 & 0 \\ 0 & 0 & 0 & 0 & 0 & 0 & 0 & 0 & 0 \end{bmatrix}, \tag{3.35}$$

$$Feq_5 = \begin{bmatrix} 0 & 0 & 0 & 0 & 0 & 0 & 0 & 0 & 0 \\ 0 & 0 & 0 & 0 & 0 & 0 & 0 & 0 & 0 \\ 0 & 0 & 0 & 0 & 0 & 0 & 0 & 0 & 0 \\ 0 & 0 & 0 & 0 & 0 & 0 & 0 & 0 & 0 \\ 0 & 0 & 0 & 0 & -1 & 0 & 0 & 0 & 0 \\ 0 & 0 & 0 & 0 & 0 & 0 & 0 & 0 & 0 \\ 0 & 0 & 0 & 0 & 0 & 0 & 0 & 0 & 0 \\ 0 & 0 & 0 & 0 & 0 & 0 & 0 & 0 & 0 \\ 0 & 0 & 0 & 0 & 0 & 0 & 0 & 0 & 0 \end{bmatrix}, \tag{3.36}$$

$$Feq_6 = \begin{bmatrix} 0 & 0 & 0 & 0 & 0 & 0 & 0 & 0 & 0 \\ 0 & 0 & 0 & 0 & 0 & 0 & 0 & 0 & 0 \\ 0 & 0 & 0 & 0 & 0 & 0 & 0 & 0 & 0 \\ 0 & 0 & 0 & 0 & 0 & 0 & 0 & 0 & 0 \\ 0 & 0 & 0 & 0 & 0 & 0 & 0 & 0 & 0 \\ 0 & 0 & 0 & 0 & 0 & 0 & 0 & 0 & 0 \\ 0 & 0 & 0 & 0 & 0 & 0 & 0 & 0 & 0 \\ 0 & 0 & 0 & 0 & 0 & 0 & 0 & -1 & 0 \\ 0 & 0 & 0 & 0 & 0 & 0 & 0 & 0 & 0 \end{bmatrix}, \tag{3.37}$$

$$
Feq_7 = \begin{bmatrix}
0 & 0 & 0 & 0 & 0 & 0 & 0 & 0 & 0 \\
0 & 0 & 0 & 0 & 0 & 0 & 0 & 0 & 0 \\
0 & 0 & 0 & 0 & 0 & 0 & 0 & 0 & 0 \\
0 & 0 & 0 & 0 & 0 & 0 & 0 & 0 & 0 \\
0 & 0 & 0 & 0 & 0 & 0 & 0 & 0 & 0 \\
0 & 0 & 0 & -\dfrac{1}{3} & 0 & 0 & \dfrac{1}{6} & 0 & 0 \\
0 & 0 & 0 & -\dfrac{1}{5} & 0 & 0 & 0 & 0 & 0 \\
0 & 0 & 0 & 0 & 0 & 0 & 0 & 0 & 0 \\
0 & 0 & 0 & 0 & 0 & 0 & 0 & 0 & 0
\end{bmatrix},
\tag{3.38}
$$

$$
Feq_8 = \begin{bmatrix}
0 & 0 & 0 & 0 & 0 & 0 & 0 & 0 & 0 \\
0 & 0 & 0 & 0 & 0 & 0 & 0 & 0 & 0 \\
0 & 0 & 0 & 0 & 0 & 0 & 0 & 0 & 0 \\
0 & 0 & 0 & 0 & 0 & 0 & 0 & 0 & 0 \\
0 & 0 & 0 & 0 & 0 & 0 & 0 & 0 & 0 \\
0 & 0 & 0 & 0 & 0 & 0 & 0 & 0 & 0 \\
0 & 0 & 0 & 0 & 0 & 0 & 0 & 0 & 0 \\
0 & 0 & 0 & 0 & -\dfrac{1}{3} & 0 & 0 & 0 & \dfrac{1}{6} \\
0 & 0 & 0 & 0 & -\dfrac{1}{5} & 0 & 0 & 0 & 0
\end{bmatrix},
\tag{3.39}
$$

and lastly, *Beq* is expressed as

$$Beq = \begin{bmatrix} 0 \\ 0 \\ -[I_{01}(A-1) + I_{02}(B-1) - i_{pv}] \\ 0 \\ 0 \\ 0 \\ 0 \\ \ln(A) \\ \ln(B) \end{bmatrix}. \tag{3.40}$$

3.2.2.2 Quadratized Exponential Model of a PV Array

The Taylor series expansion for the PV model was given in (3.12). This series expansion has been rewritten as

$$\exp(\frac{x}{aN_sV_T}) = 1 + \frac{x}{aN_sV_T} + \frac{x^2}{2a^2N_s^2V_T^2} + \frac{x^3}{6a^3N_s^3V_T^3} + \frac{x^4}{24a^4N_s^4V_T^4}$$
$$+ \frac{x^5}{120a^5N_s^5V_T^5} + H.O.T, \tag{3.41}$$

where x is the voltage difference of (3.12) given as

$$x = v_x - v_2. \tag{3.42}$$

Equation (3.41) has high-order terms and by following the same approach in section 3.2.2.1, (3.41) can be made at most, a second order equation by introducing new state variables as follows:

$$x^2 - y_1 = 0, \tag{3.43}$$

$$y_1^2 - y_2 = 0. \tag{3.44}$$

With the newly introduced state variables, (3.41) can be expressed as:

$$\exp\{\frac{v_x - v_2}{aN_sV_T}\} = \exp(\frac{x}{c_1}) = 1 + \frac{x}{c_1} + \frac{y_1}{c_2} + \frac{xy_1}{c_3} + \frac{y_2}{c_4} + \frac{xy_2}{c_5} + H.O.T, \quad (3.45)$$

where

$$aN_sv_T = c_1,$$

$$2a^2N_s^2v_T{}^2 = c_2,$$

$$6a^3N_s^3v_T{}^3 = c_3, \quad (3.46)$$

$$24a^4N_s^4v_T{}^4 = c_4,$$

$$120a^5N_s^5v_T{}^5 = c_5.$$

Similarly, by substituting c with d, and a with n in (3.46), the expression for the second

exponential in (3.10) is given as

$$\exp\{\frac{v_x - v_2}{nN_sV_T}\} = \exp(\frac{x}{d_1}) = 1 + \frac{x}{d_1} + \frac{y_1}{d_2} + \frac{xy_1}{d_3} + \frac{y_2}{d_4} + \frac{xy_2}{d_5} + H.O.T, \quad (3.47)$$

Therefore, the PV exponential mathematical model is summarized as follows:

$$i_1 = G_s v_1 - G_s v_x, \quad (3.48)$$

$$i_2 = -G_s v_1 + G_s v_x, \quad (3.49)$$

$$0 = -G_s v_1 - G_p v_2 + (G_s + G_p)v_x + I_{01}[\frac{x}{c_1} + \frac{y_1}{c_2} + \frac{y_2}{c_4} + \frac{xy_1}{c_3} + \frac{xy_2}{c_5}]$$

$$+ I_{02}[\frac{x}{d_1} + \frac{y_1}{d_2} + \frac{y_2}{d_4} + \frac{xy_1}{d_3} + \frac{xy_2}{d_5}] - i_{pv}, \quad (3.50)$$

$$0 = -v_2 + v_x - x, \quad (3.51)$$

$$0 = x^2 - y_1, \quad (3.52)$$

$$0 = y_1^2 - y_2. \quad (3.53)$$

30

Next, (3.48) through (3.53) are cast into the standard quadratized matrix form as was done in section 3.2.2.1, is given as

$$
\begin{bmatrix} i_1 \\ i_2 \\ 0 \\ 0 \\ 0 \\ 0 \end{bmatrix} = Yeq \begin{bmatrix} v_1 \\ v_2 \\ v_x \\ x \\ y_1 \\ y_2 \end{bmatrix} + \begin{bmatrix} v_1 \\ v_2 \\ v_x \\ x \\ y_1 \\ y_2 \end{bmatrix}^T Meq \begin{bmatrix} v_1 \\ v_2 \\ v_x \\ x \\ y_1 \\ y_2 \end{bmatrix} - Beq,
\tag{3.54}
$$

where Yeq is expressed as:

$$
Yeq = \begin{bmatrix}
G_s & 0 & -G_s & 0 & 0 & 0 \\
-G_s & 0 & G_s & 0 & 0 & 0 \\
-G_s & -G_p & G_p + G_s & \dfrac{I_{01}}{c_1} + \dfrac{I_{02}}{d_1} & \dfrac{I_{01}}{c_2} + \dfrac{I_{02}}{d_2} & \dfrac{I_{01}}{c_4} + \dfrac{I_{02}}{d_4} \\
0 & -1 & 1 & -1 & 0 & 0 \\
0 & 0 & 0 & 0 & -1 & 0 \\
0 & 0 & 0 & 0 & 0 & -1
\end{bmatrix},
\tag{3.55}
$$

Meq as

$$
M_{eq} = \begin{bmatrix} Feq_0 \\ Feq_1 \\ Feq_2 \\ Feq_3 \\ Feq_4 \\ Feq_5 \end{bmatrix},
\tag{3.56}
$$

where

$$
Feq_0 = Feq_1 = Feq_3 = \begin{bmatrix}
0 & 0 & 0 & 0 & 0 & 0 \\
0 & 0 & 0 & 0 & 0 & 0 \\
0 & 0 & 0 & 0 & 0 & 0 \\
0 & 0 & 0 & 0 & 0 & 0 \\
0 & 0 & 0 & 0 & 0 & 0 \\
0 & 0 & 0 & 0 & 0 & 0
\end{bmatrix},
\tag{3.57}
$$

$$Feq_2 = \begin{bmatrix} 0 & 0 & 0 & 0 & 0 & 0 \\ 0 & 0 & 0 & 0 & 0 & 0 \\ 0 & 0 & 0 & 0 & 0 & 0 \\ 0 & 0 & 0 & 0 & \dfrac{I_{01}}{c_3}+\dfrac{I_{02}}{d_3} & \dfrac{I_{01}}{c_5}+\dfrac{I_{02}}{d_5} \\ 0 & 0 & 0 & 0 & 0 & 0 \\ 0 & 0 & 0 & 0 & 0 & 0 \end{bmatrix}, \tag{3.58}$$

$$Feq_4 = \begin{bmatrix} 0 & 0 & 0 & 0 & 0 & 0 \\ 0 & 0 & 0 & 0 & 0 & 0 \\ 0 & 0 & 0 & 0 & 0 & 0 \\ 0 & 0 & 0 & 1 & 0 & 0 \\ 0 & 0 & 0 & 0 & 0 & 0 \\ 0 & 0 & 0 & 0 & 0 & 0 \end{bmatrix}, \tag{3.59}$$

$$Feq_5 = \begin{bmatrix} 0 & 0 & 0 & 0 & 0 & 0 \\ 0 & 0 & 0 & 0 & 0 & 0 \\ 0 & 0 & 0 & 0 & 0 & 0 \\ 0 & 0 & 0 & 0 & 0 & 0 \\ 0 & 0 & 0 & 0 & 1 & 0 \\ 0 & 0 & 0 & 0 & 0 & 0 \end{bmatrix}, \tag{3.60}$$

and

$$Beq = \begin{bmatrix} 0 \\ 0 \\ i_{pv} \\ 0 \\ 0 \\ 0 \end{bmatrix}. \tag{3.61}$$

3.2.2.3 Hybrid PV Model – The Two-Diode Model

From the already developed model of sections 3.2.2.1 and 3.2.2.2, a new model is developed, which is a combination of the two models based in the operation point of the PV model. The model developed in 3.2.2.1, for a given set of parameter, conforms to the actual PV model as the operation point of the PV moves beyond the MPP towards open circuit voltage conditions. The model outlined in section 3.2.2.2 conforms to the PV module characteristics between the short circuit and maximum power point operation regions. For a seamless transition between the models in sections 3.2.2.1 and 3.2.2.2, the two models were developed to have the same number of state variables and non-linear terms. The extension of the model in section 3.2.2.2, which has six state variables, to match the nine state variable count of section 3.2.2.1 is discussed next.

Equation (3.45) is rewritten as

$$
\begin{aligned}
\exp\{\frac{v_x - v_2}{aN_sV_T}\} &= \exp(\frac{x}{c_1}) \\
&= 1 + \frac{x}{c_1} + \frac{y_1}{c_2} + \frac{y_2}{c_3} + \frac{y_3}{c_4} + \frac{y_4}{c_5} + \frac{y_5}{c_6} + \frac{y_2 y_3}{c_7} + \frac{y_2 y_4}{c_8} + \frac{y_2 y_5}{c_9} \\
&\quad + \frac{y_3 y_5}{c_{10}} + \frac{y_4 y_5}{c_{11}} + H.O.T \ ,
\end{aligned}
\tag{3.62}
$$

where c_1 to c_5 is the same is (3.46) and the additional terms are given as

$$
\begin{aligned}
6!a^6 N_s^6 v_T^6 &= c_6, \\
7!a^7 N_s^7 v_T^7 &= c_7, \\
8!a^8 N_s^8 v_T^8 &= c_8, \\
9!a^9 N_s^9 v_T^9 &= c_9, \\
10!a^{10} N_s^{10} v_T^{10} &= c_{10}, \\
11!a^{11} N_s^{11} v_T^{11} &= c_{11},
\end{aligned}
\tag{3.63}
$$

$$0 = x^2 - y_1, \tag{3.64}$$

$$0 = xy_1 - y_2, \tag{3.65}$$

$$0 = y_1^2 - y_3, \tag{3.66}$$

$$0 = y_1 y_2 - y_4, \tag{3.67}$$

$$0 = y_1 y_3 - y_5. \tag{3.68}$$

Performing a similar substitution for the second exponential as was performed in section 3.2.2.2 yields

$$
\exp\{\frac{v_x - v_2}{nN_s V_T}\} = \exp(\frac{x}{d_1})
$$

$$
= 1 + \frac{x}{d_1} + \frac{y_1}{d_2} + \frac{y_2}{d_3} + \frac{y_3}{d_4} + \frac{y_4}{d_5} + \frac{y_5}{d_6} + \frac{y_2 y_3}{d_7} + \frac{y_2 y_4}{d_8} + \frac{y_2 y_5}{d_9}
$$

$$
+ \frac{y_3 y_5}{d_{10}} + \frac{y_4 y_5}{d_{11}} + H.O.T, \tag{3.69}
$$

where d_1 to d_9 are obtained by a substitution of the ideality constant a with n in (3.46) and (3.63). Therefore, the summary of equations for the exponential portion of the hybrid model is give as follows:

$$i_1 = G_s v_1 - G_s v_x, \tag{3.70}$$

$$i_2 = -G_s v_1 + G_s v_x, \tag{3.71}$$

$$
0 = -i_{pv} - G_s v_1 - G_p v_2 + \left(G_p + G_s\right) v_x
$$

$$
+ I_{01}[\frac{x}{c_1} + \frac{y_1}{c_2} + \frac{y_2}{c_3} + \frac{y_3}{c_4} + \frac{y_4}{c_5} + \frac{y_5}{c_6} + \frac{y_2 y_3}{c_7} + \frac{y_2 y_4}{c_8} + \frac{y_2 y_5}{c_9} + \frac{y_3 y_5}{c_{10}} + \frac{y_4 y_5}{c_{11}}]
$$

$$
+ I_{02}[\frac{x}{d_1} + \frac{y_1}{d_2} + \frac{y_2}{d_3} + \frac{y_3}{d_4} + \frac{y_4}{d_5} + \frac{y_5}{d_6} + \frac{y_2 y_3}{d_7} + \frac{y_2 y_4}{d_8} + \frac{y_2 y_5}{d_9} + \frac{y_3 y_5}{d_{10}} + \frac{y_4 y_5}{d_{11}}], \tag{3.72}
$$

$$0 = -v_2 + v_x - x, \tag{3.73}$$

$$0 = x^2 - y_1, \tag{3.74}$$

$$0 = xy_1 - y_2, \tag{3.75}$$

$$0 = y_1^2 - y_3, \tag{3.76}$$

$$0 = y_1 y_2 - y_4, \tag{3.77}$$

$$0 = y_1 y_3 - y_5, \tag{3.78}$$

Equations (3.70) - (3.78) can be cast into the standard quadratized matrix form, which has the form shown in (3.79):

$$
\begin{bmatrix} i_1 \\ i_2 \\ 0 \\ 0 \\ 0 \\ 0 \\ 0 \\ 0 \\ 0 \\ 0 \end{bmatrix} = Yeq \begin{bmatrix} v_1 \\ v_2 \\ v_x \\ x \\ y_1 \\ y_2 \\ y_3 \\ y_4 \\ y_5 \end{bmatrix} + \begin{bmatrix} v_1 \\ v_2 \\ v_x \\ x \\ y_1 \\ y_2 \\ y_3 \\ y_4 \\ y_5 \end{bmatrix}^T Meq \begin{bmatrix} v_1 \\ v_2 \\ v_x \\ x \\ y_1 \\ y_2 \\ y_3 \\ y_4 \\ y_5 \end{bmatrix} - Beq. \tag{3.79}
$$

A comparison of (3.30) and (3.79) confirms that they both have the same number of state variables. Also, this comparison also shows the two models have the same number of non-linear terms. Therefore, in the hybrid model, the exponential model formed in this section is used for an operation from short circuit to the maximum power point operation region. The model is switched to the approximation model for operating regions beyond maximum power point and up to the open-circuit condition. Using the hybrid model, the current versus voltage (I-V) and power versus voltage (P-V) curves of Figure 3.2 and Figure 3.3 are obtained.
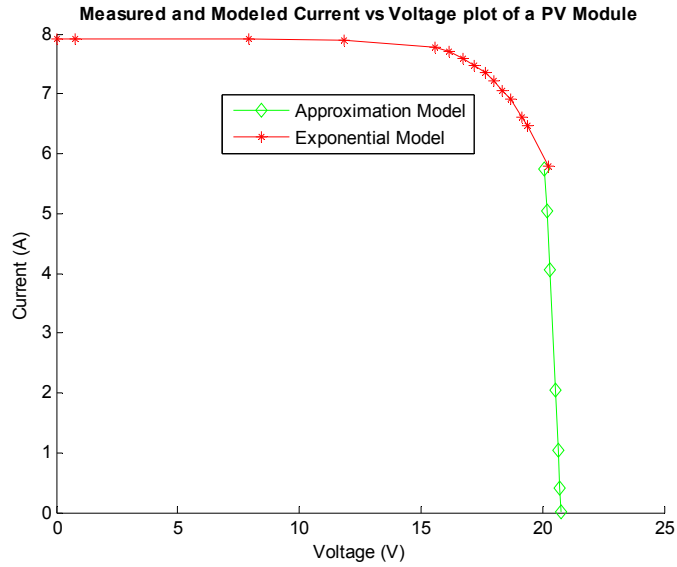
Figure 3.2:   **PV current-voltage hybrid model plot.**
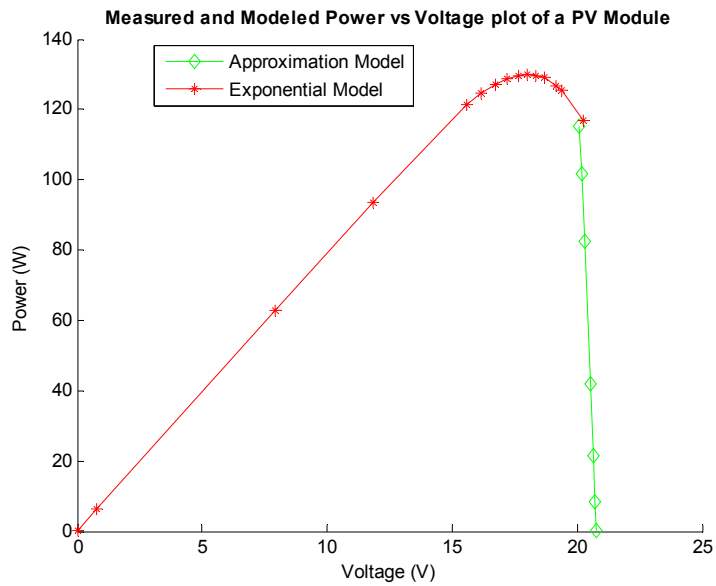
Figure 3.3:   **PV power-voltage hybrid model plot.**

3.2.2.4   Photovoltaic Model with Taylor Series Scaling

The models developed in the preceding sections had some limitations. These limitations were either in relation to the accuracy, or the difficulty in seamlessly transitioning from one operational point to another. For instance, in [27], a comparison

was performed between the method proposed in this section, the method proposed in section 3.2.2.2, and the actual exponential term. From the comparison, it was demonstrated that as the operation point of the PV module moved toward the open circuit voltage of the PV module, the error using the method in section 3.2.2.2, was in the order of 10^9. Therefore, a novel model was developed to ensure the modeled PV module seamlessly transitioned from one operational point to another, without sacrificing its accuracy. This proposed model of the PV module requires the scaling of the Taylor series expansion as described in [27]. With the introduction of the scaling factor, g, the following substitutions are made:

$$0 = -\lambda_1 a N_s V_T g + v_x - v_2, \tag{3.80}$$

$$0 = -\exp[\frac{(v_x - v_2)g}{a N_s V_T g}] + e^{\lambda_1 g}, \tag{3.81}$$

$$0 = -e^{\lambda_1} + \gamma_1, \tag{3.82}$$

$$0 = -\exp[\frac{(v_x - v_2)}{a N_s V_T}] + \gamma_1^{g}, \tag{3.83}$$

$$0 = -\gamma_1 + 1 + \lambda_1 + \frac{\lambda_1^2}{2!} + \frac{\lambda_1^3}{3!} + \frac{\lambda_1^4}{4!} + \frac{\lambda_1^5}{5!} + \frac{\lambda_1^6}{6!} + \frac{\lambda_1^7}{7!} + \frac{\lambda_1^8}{8!} + \frac{\lambda_1^9}{9!} + \frac{\lambda_1^{10}}{10!} + \frac{\lambda_1^{11}}{11!}. \tag{3.84}$$

And by setting the g scaling factor to 40, (3.10) is written as

$$0 = -G_s(v_1 - v_x) + G_{sh}(v_x - v_2) + I_{o1}\left[\gamma_1^{40} - 1\right] + I_{o2}\left[\gamma_2^{40} - 1\right] - i_{pv}, \tag{3.85}$$

where γ_2 is the substitution due to the second exponential of (3.10). By using the quadratization method described in the preceding sections, the system of PV module equations as described in [27] are as follows:

$$i_1 = G_s v_1 - G_s v_x, \tag{3.86}$$

37

$$i_2 = -G_s v_1 + G_s v_x, \tag{3.87}$$

$$0 = -G_s v_1 - G_{sh} v_2 + \left(G_{sh} + G_s\right) v_x + I_{o1}\left[c_1^2 - 1\right] + I_{o2}\left[d_1^2 - 1\right] - i_{pv}, \tag{3.88}$$

$$0 = -c_1 + \alpha_4^2, \tag{3.89}$$

$$0 = -\alpha_4 + \alpha_1 \alpha_3, \tag{3.90}$$

$$0 = -\alpha_3 + \alpha_2^2, \tag{3.91}$$

$$0 = -\alpha_2 + \alpha_1^2, \tag{3.92}$$

$$0 = -\alpha_1 + \gamma_1^2, \tag{3.93}$$

$$0 = -\gamma_1 + 1 + \lambda_1 + \frac{y_1}{2!} + \frac{y_2}{3!} + \frac{y_3}{4!} + \frac{y_4}{5!} + \frac{y_5}{6!} + \frac{y_2 y_3}{7!} + \frac{y_2 y_4}{8!} + \frac{y_2 y_5}{9!} + \frac{y_3 y_5}{10!} + \frac{y_4 y_5}{11!}, \tag{3.94}$$

$$0 = -40\lambda_1 a N_s V_T + v_x - v_2, \tag{3.95}$$

$$0 = \lambda_1^2 - y_1, \tag{3.96}$$

$$0 = \lambda_1 y_1 - y_2, \tag{3.97}$$

$$0 = y_1^2 - y_3, \tag{3.98}$$

$$0 = y_1 y_2 - y_4, \tag{3.99}$$

$$0 = y_1 y_3 - y_5. \tag{3.100}$$

$$0 = -d_1 + \beta_4^2, \tag{3.101}$$

$$0 = -\beta_4 + \beta_1 \beta_3, \tag{3.102}$$

$$0 = -\beta_3 + \beta_2^2, \tag{3.103}$$

$$0 = -\beta_2 + \beta_1^2, \tag{3.104}$$

$$0 = -\beta_1 + \gamma_2^2, \tag{3.105}$$

38

$$0 = -\gamma_2 + 1 + \lambda_2 + \frac{z_1}{2!} + \frac{z_2}{3!} + \frac{z_3}{4!} + \frac{z_4}{5!} + \frac{z_5}{6!} + \frac{z_2 z_3}{7!} + \frac{z_2 z_4}{8!} + \frac{z_2 z_5}{9!} + \frac{z_3 z_5}{10!} + \frac{z_4 z_5}{11!}, \qquad (3.106)$$

$$0 = -40\lambda_2 n N_s V_T + v_x - v_2, \qquad (3.107)$$

$$0 = \lambda_2^2 - z_1, \qquad (3.108)$$

$$0 = \lambda_2 z_1 - z_2, \qquad (3.109)$$

$$0 = z_1^2 - z_3, \qquad (3.110)$$

$$0 = z_1 z_2 - z_4, \qquad (3.111)$$

$$0 = z_1 z_3 - z_5, \qquad (3.112)$$

and can be shown in a compact form as given in (3.113),

$$
\begin{bmatrix} i_1 \\ i_2 \\ 0 \\ 0 \\ 0 \\ 0 \\ 0 \\ 0 \\ 0 \\ 0 \\ 0 \\ 0 \\ 0 \\ 0 \\ 0 \\ 0 \\ 0 \\ 0 \\ 0 \\ 0 \\ 0 \\ 0 \\ 0 \\ 0 \\ 0 \\ 0 \\ 0 \\ 0 \end{bmatrix}
= [Yeq]
\begin{bmatrix} v_1 \\ v_2 \\ v_x \\ c_1 \\ \lambda_1 \\ \gamma_1 \\ \alpha_1 \\ \alpha_2 \\ \alpha_3 \\ \alpha_4 \\ y_1 \\ y_2 \\ y_3 \\ y_4 \\ y_5 \\ d_1 \\ \lambda_2 \\ \gamma_2 \\ \beta_1 \\ \beta_2 \\ \beta_2 \\ \beta_3 \\ z_1 \\ z_2 \\ z_3 \\ z_4 \\ z_5 \end{bmatrix}
+
\begin{bmatrix} v_1 \\ v_2 \\ v_x \\ c_1 \\ \lambda_1 \\ \gamma_1 \\ \alpha_1 \\ \alpha_2 \\ \alpha_3 \\ \alpha_4 \\ y_1 \\ y_2 \\ y_3 \\ y_4 \\ y_5 \\ d_1 \\ \lambda_2 \\ \gamma_2 \\ \beta_1 \\ \beta_2 \\ \beta_2 \\ \beta_3 \\ z_1 \\ z_2 \\ z_3 \\ z_4 \\ z_5 \end{bmatrix}^T
[Meq]
\begin{bmatrix} v_1 \\ v_2 \\ v_x \\ c_1 \\ \lambda_1 \\ \gamma_1 \\ \alpha_1 \\ \alpha_2 \\ \alpha_3 \\ \alpha_4 \\ y_1 \\ y_2 \\ y_3 \\ y_4 \\ y_5 \\ d_1 \\ \lambda_2 \\ \gamma_2 \\ \beta_1 \\ \beta_2 \\ \beta_2 \\ \beta_3 \\ z_1 \\ z_2 \\ z_3 \\ z_4 \\ z_5 \end{bmatrix}
- [Beq], \qquad (3.113)
$$

where Yeq, Meq, and Beq are as previously described. This PV module model is validated in section 3.3.

3.3 Validation of Photovoltaic Model

In sections 3.2, the mathematical models for the PV module were developed. These models require the entry of PV parameters for numerical simulations. Therefore a PV graphical user interface (GUI) for entering these parameters was developed. These PV mathematical models were implemented in a software environment called WinIGS. The GUI for the PV model is given on Figure 3.4, and allows the user to enter the data that are available from the PV datasheet such as the open circuit voltage, short circuit current, current and voltage temperature coefficients, and the maximum power point voltage and current.
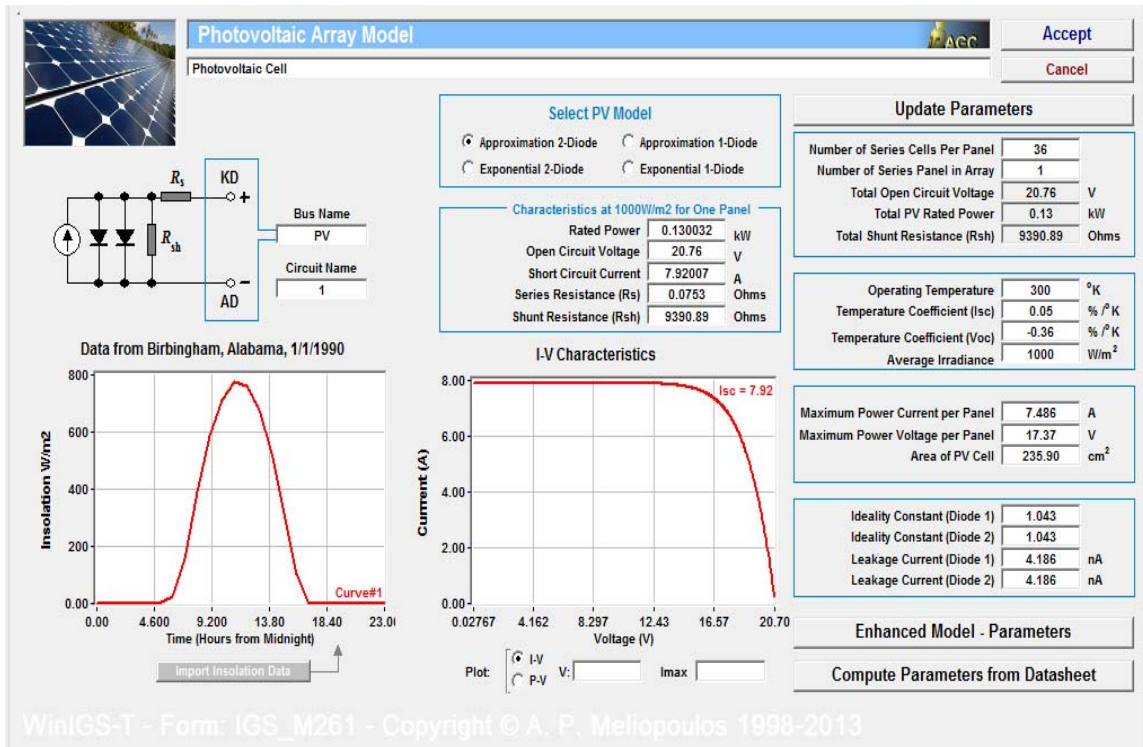
Figure 3.4: **GUI for PV model.**

Furthermore, the GUI gives the user the flexibility of the using the PV model as either the model of a PV module, or as a single PV cell, by changing the number of series connected cells in the top right portion of the interface in Figure 3.4. Although the method to obtain the values for the PV nominal current, leakage currents, resistor values and ideality constants has not been discussed, the values in Figure 3.4 have been selected to validate the developed PV model. The method for obtaining the PV parameters is covered in chapter 4.

To validate the PV model, the I-V and P-V curves for the PV module is generated using the model from section 3.2.2.4. It is expected that the resulting plots will agree with actual measurements that were taken from a physical PV module. The voltage and current quantities were obtained from this model by building a simple PV module- resistor series circuit in WinIGS. The schematic for this circuit is shown on Figure 3.5.
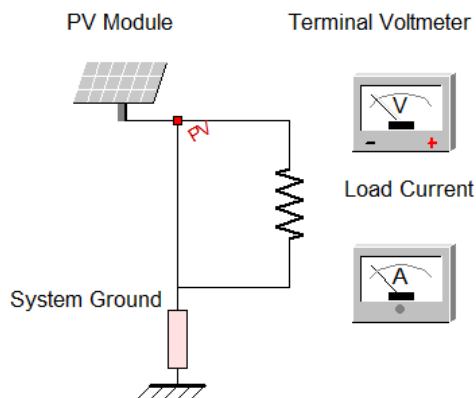
Figure 3.5:   **PV-resistor validation circuit [27].**

For this simulation, the resistor on Figure 3.5 was varied from a short circuit condition with a resistance value of 0.1Ω, to an open circuit condition with a resistor value of 10kΩ. The current and voltage values were measured and documented during each variation in resistance value. The resulting plot for the I-V and P-V curves are given

in Figure 3.6 and Figure 3.7. Due to the accuracy of the proposed model in section 3.2.2.4, only one model of the PV module was required for a seamless transition from one operational point to the next.
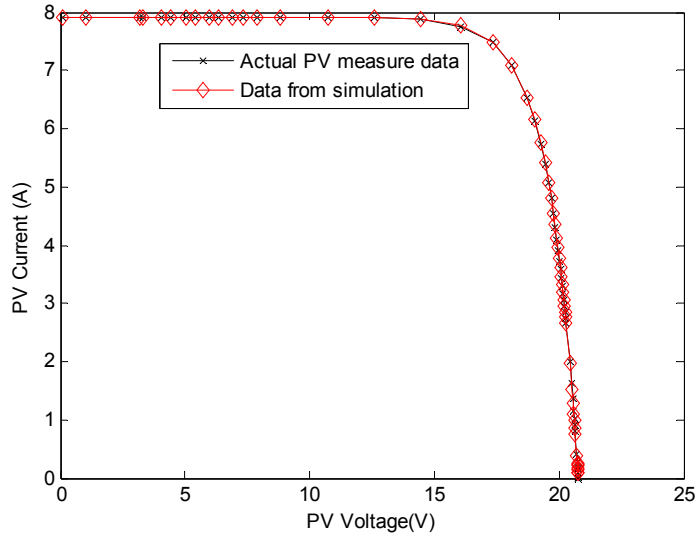
Figure 3.6:   **Photovoltaic module current-voltage plot compared to measured data [27].**
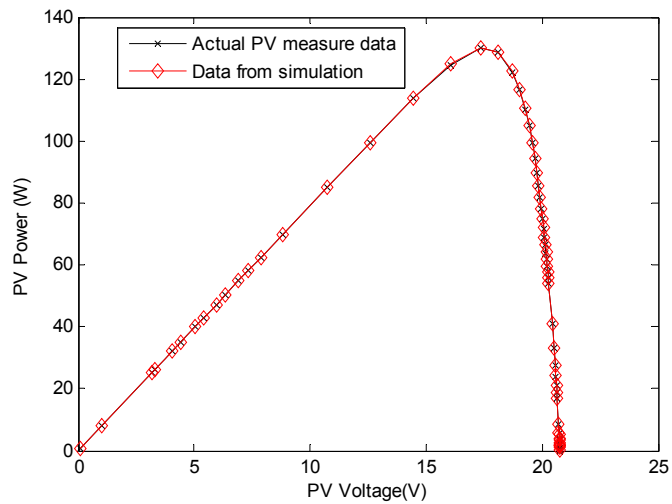
Figure 3.7:   **Photovoltaic module power-voltage plot compared to measured data [27].**

To further validate the PV model, the system in Figure 3.5 is modified by adding a switch that will short the PV module to ground, as shown in Figure 3.8. The aim of this

simulation is to ascertain that the operation of this PV model is consistent with expected results during normal and short circuit conditions of the PV module.
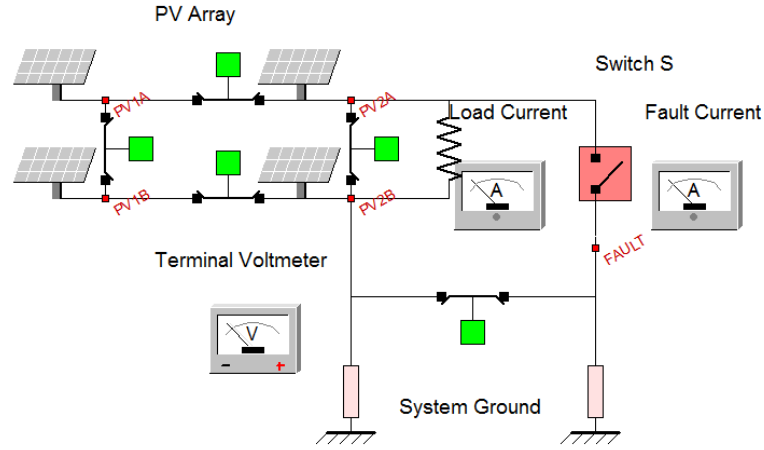
Figure 3.8:   Validation of PV model under fault condition [27].
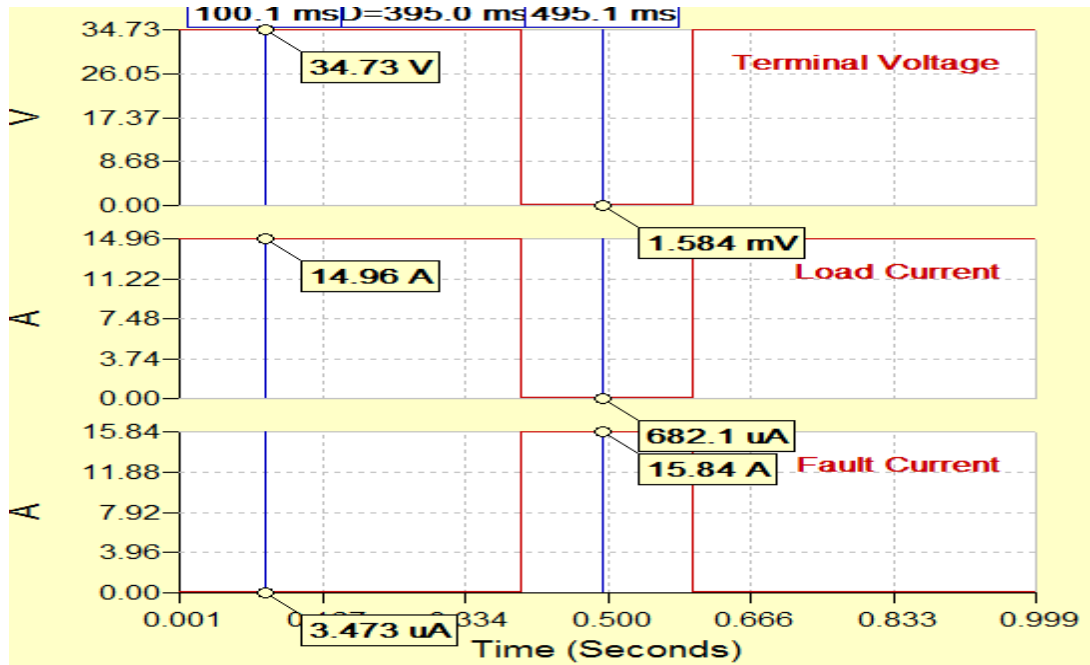
Figure 3.9:   Simulation result of PV model under fault condition [27].

At time $t = 0$ seconds the PV module is energized and approximately 520 watts is delivered to the connected load, modelled here as a resistor. At time $t = 0.4$ seconds the switch 'S' is closed, thereby, shorting the PV terminal to ground and diverting the

load current through the fault path to ground. Therefore, the fault current which was originally zero, goes up to the PV array short circuit value of 15.84A. At time $t =$ 0.6 seconds, the fault is cleared and the system goes back to the pre-fault condition. This PV array operation is consistent with the expect behavior of the combined PV module under loading and short circuit condition. The developed model in section 3.2.2.4 is used in the formulation of the model for a system of PV array. The formulation of the system of PV array using the model of section 3.2.2.4 is described in [28]. Therefore, a similar explanation is outlined in section 3.4, but using the model in section 3.2.2.2. The rational for using the model in section 3.2.2.2 is to demonstrate that the outlined array formulation method in 3.4 can be extended to any model of the PV module with the form given in (3.113).

3.4   Formulation of Photovoltaic Array Model

In the preceding sections for this chapter, the emphasis was on defining an accurate model for the PV module. However, in PV systems, the PV array is composed of interconnections of several PV modules to form an array. While the protection method discussed in this research is on the protection of the PV system at a module-level, the protection will use the model of the completely integrated PV array. Therefore, in this chapter, the model of the entire PV array used for this project, which can be extended to any size of PV installation, is formulated next. The formulation of the model of the PV array system has been formulated in [28]. The model formulation in [28] uses the model in section 3.2.2.4. The same method in [28] is used in this section, but using the model in section 3.2.2.2. Consequently, this method of developing the PV array model is applicable to any model of the PV module.

Given a PV array formed by integrating *n* individual PV modules, such as shown on Figure 3.10, the objective is to form a system of state variables from the states of the individual modules. This formulated system of state variables is used for the protection of the entire PV system, down to the PV module-level.

The steps for forming the integrated PV system model for the protection of the array are as follows:

- define the global PV array nodes

- define a connectivity matrix for individual PV modules

- map individual PV modules state variables to global state variables

- form a system model for the PV array for module-level protection
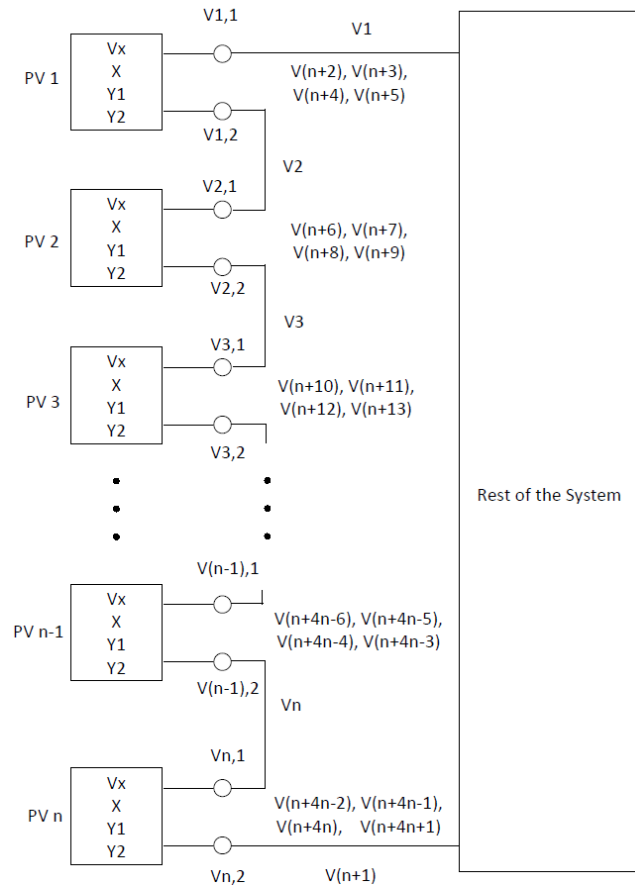
Figure 3.10:   **Formation of PV system from individual modules.**

3.4.1 Define Global PV Array Nodes

Using the exponential PV model of section 3.2.2.2, the PV module is comprised of twelve state variables, six of the state variables are for time t, and the other six for the half integration time step t_m. This global node definition is illustrated using two series connected PV modules, each having 12 states. Connecting the two PV modules form a global set of nodes shown in red on Figure 3.11.
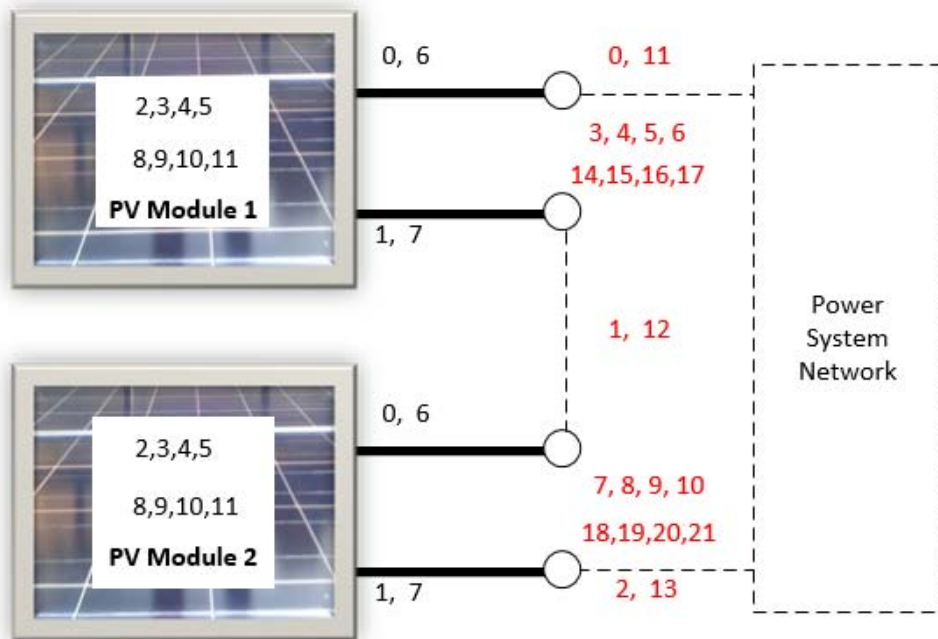
Figure 3.11:   Global node formation for PV modules connection.

By estimating the global states, not only are the states of both the PV modules also determined, but the estimation of the states is done efficiently. If the estimation of the PV modules state variables were done on an individual PV module bases, then the global terminal nodes 1 and 12 would have been estimated twice. The estimation would be done once for PV module 1 (nodes 1 and 7), and another for PV module 2 (nodes 0 and 6). These nodes are boxed in red dashed lines in Figure 3.12.
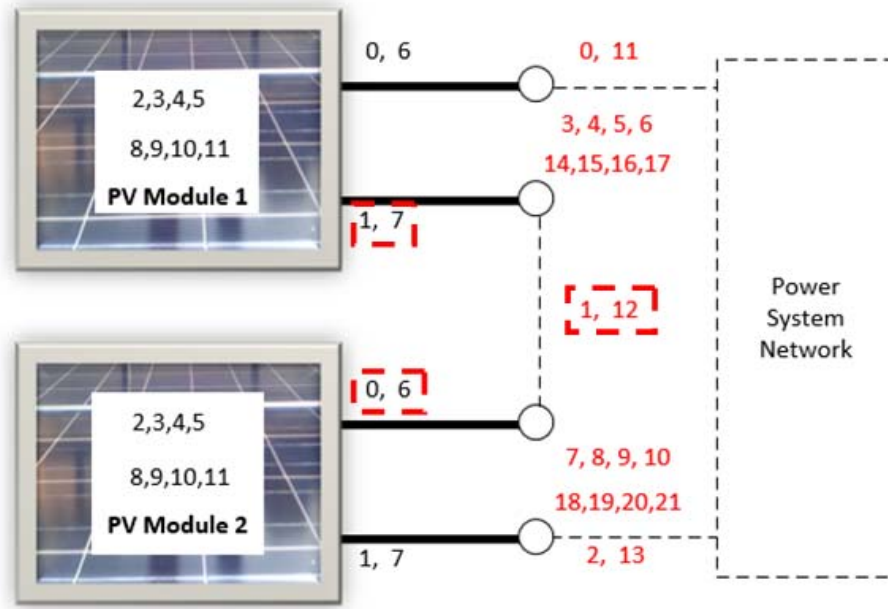
Figure 3.12: Individual PV module nodes forming a global node.

The computational time saved by using this method becomes more obvious in a system of PV comprised of a lot more PV modules. From Figure 3.12 the external PV states, which are the PV nodes that are connected to other PV modules, are assigned one global node. The other states of the PV modules, that is, the internal state variables, are moved to the global level as shown in red in Figure 3.12.

3.4.2 Defining Connectivity Matrix and Mapping to Global States

After assigning a global node for the PV system, a connectivity matrix is established. This connectivity matrix is made of an $i \times j$ matrix for each PV module, where i corresponds to PV global states and j represents the individual PV module states. Therefore, given a connectivity matrix $M_{i,j}^k$, i and j are as were just defined, and k is the PV module number. An example of the PV module number is "PV module 1" as shown on Figure 3.12. The same exercise is performed for "PV module 2" of Figure 3.12, and in

a larger PV array installation, such as the one for this research, the same procedure is repeated for all the PV modules. The matrix on Figure 3.13 is formulated by assigning a one, highlighted in yellow, if the PV node and global node are connected, and a zero otherwise.

PV Module 1 and PV Module 2 state variable indices (Section 3.2.2.2 Model)

	0	1	2	3	4	5	6	7	8	9	10	11	12	13	14	15	16	17	18	19	20	21	22	23
0	1	0	0	0	0	0	0	0	0	0	0	0	0	0	0	0	0	0	0	0	0	0	0	0
1	0	1	0	0	0	0	0	0	0	0	0	0	1	0	0	0	0	0	0	0	0	0	0	0
2	0	0	0	0	0	0	0	0	0	0	0	0	0	1	0	0	0	0	0	0	0	0	0	0
3	0	0	1	0	0	0	0	0	0	0	0	0	0	0	0	0	0	0	0	0	0	0	0	0
4	0	0	0	1	0	0	0	0	0	0	0	0	0	0	0	0	0	0	0	0	0	0	0	0
5	0	0	0	0	1	0	0	0	0	0	0	0	0	0	0	0	0	0	0	0	0	0	0	0
6	0	0	0	0	0	1	0	0	0	0	0	0	0	0	0	0	0	0	0	0	0	0	0	0
7	0	0	0	0	0	0	0	0	0	0	0	0	0	0	1	0	0	0	0	0	0	0	0	0
8	0	0	0	0	0	0	0	0	0	0	0	0	0	0	0	1	0	0	0	0	0	0	0	0
9	0	0	0	0	0	0	0	0	0	0	0	0	0	0	0	0	1	0	0	0	0	0	0	0
10	0	0	0	0	0	0	0	0	0	0	0	0	0	0	0	0	0	1	0	0	0	0	0	0
11	0	0	0	0	0	0	1	0	0	0	0	0	0	0	0	0	0	0	0	0	0	0	0	0
12	0	0	0	0	0	0	0	1	0	0	0	0	0	0	0	0	0	0	1	0	0	0	0	0
13	0	0	0	0	0	0	0	0	0	0	0	0	0	0	0	0	0	0	0	1	0	0	0	0
14	0	0	0	0	0	0	0	0	1	0	0	0	0	0	0	0	0	0	0	0	0	0	0	0
15	0	0	0	0	0	0	0	0	0	1	0	0	0	0	0	0	0	0	0	0	0	0	0	0
16	0	0	0	0	0	0	0	0	0	0	1	0	0	0	0	0	0	0	0	0	0	0	0	0
17	0	0	0	0	0	0	0	0	0	0	0	1	0	0	0	0	0	0	0	0	0	0	0	0
18	0	0	0	0	0	0	0	0	0	0	0	0	0	0	0	0	0	0	0	0	1	0	0	0
19	0	0	0	0	0	0	0	0	0	0	0	0	0	0	0	0	0	0	0	0	0	1	0	0
20	0	0	0	0	0	0	0	0	0	0	0	0	0	0	0	0	0	0	0	0	0	0	1	0
21	0	0	0	0	0	0	0	0	0	0	0	0	0	0	0	0	0	0	0	0	0	0	0	1

System of two PV modules global Indices (Figure 3.12)

Figure 3.13: PV connectivity matrix for PV module 1 and PV module 2 series connections.

3.4.3   Mapping to Global node and forming a System Model for the PV Array

After defining the connectivity matrix of each PV module, the individual PV modules are now ready to be mapped to the global states. By mapping these individual PV module state variables to the global states, the system model of the PV array is formulated. This system model formulation is discussed next.

The model of the individual PV module from (3.54) is simplified as shown on (3.114),

$$I^k = Yeq^k V^k + \left(V^k\right)^T Feq^k V^k - b^k, \qquad (3.114)$$

where k is the PV module number, such as 1 or 2, as in the case of "PV module 1" and "PV module 2" of Figure 3.11. To map the individual models of (3.114) to the system of PV array, the connectivity matrices for the individual PV modules are used to transform the individual models to a system model. For a linear device model, (3.114) would be given as

$$I^k = Yeq^k V^k - b^k, \qquad (3.115)$$

and to convert this individual level model to the system model, (3.115) is multiplied by the connectivity matrix resulting in

$$M^k I^k = M^k Yeq^k V^k - M^k b^k. \qquad (3.116)$$

Furthermore, the individual level state variable V^k is transformed to the system model using the relationship in (3.117),

$$V^k = \left(M^k\right)^T V, \qquad (3.117)$$

where V is the system state variable. Substituting (3.117) in (3.116) gives

$$M^k I^k = M^k Yeq^k \left(M^k\right)^T V - M^k b^k. \qquad (3.118)$$

The PV model, however, is non-linear, therefore, the contribution from the non-linear segment of the model is appended to (3.118). The non-linear segment of the individual level PV model is given as $(V^k)^T Feq^k V^k,$ and after substituting (3.117) yields

$$M^k I^k = M^k Yeq^k \left(M^k\right)^T V + \left(\left(M^k\right)^T V\right)^T Feq^k \left(M^k\right)^T V - M^k b^k. \qquad (3.119)$$

49

Equation (3.119) is further simplified to (3.120).

$$M^k I^k = M^k Yeq^k \left(M^k\right)^T V + V^T M^k Feq^k \left(M^k\right)^T V - M^k b^k. \tag{3.120}$$

Therefore, to obtain the PV system level model, the individual model of (3.120) are summed up to yield

$$I = YV + V^T FV - b, \tag{3.121}$$

where

$$I = \sum_{k=1}^{n} \left(M^k I^k\right), \tag{3.122}$$

$$Y = \sum_{k=1}^{n} \left(M^k Yeq^k \left(M^k\right)^T\right), \tag{3.123}$$

$$F = \sum_{k=1}^{n} \left(M^k Feq^k \left(M^k\right)^T\right), \tag{3.124}$$

$$b = \sum_{k=1}^{n} \left(M^k b^k\right), \tag{3.125}$$

and n in the summations of (3.122) – (3.125) is the number of PV modules integrated to form the system of PV array. As an illustration, (3.123) is formulated for the system on Figure 3.11, and results in a Y matrix partially shown on Figure 3.14. On Figure 3.14, the black-text Y matrix entries are contribution from PV module 1, while the red-text entries are contributions from PV module 2. Also, the bottom right half of Figure 3.14 is not shown, but is identical to Figure 3.14.

	0	1	2	3	4	5	6	7	8	9	10
0	G_s	0	0	$-G_s$	0	0	0	0	0	0	0
1	$-G_s$	G_s	0	G_s	0	0	0	$-G_s$	0	0	0
2	0	$-G_s$	0	0	0	0	0	G_s	0	0	0
3	$-G_s$	$-G_p$	0	$(G_p + G_s)$	$\frac{I_{01}}{c_1}+\frac{I_{02}}{d_1}$	$\frac{I_{01}}{c_2}+\frac{I_{02}}{d_2}$	$\frac{I_{01}}{c_4}+\frac{I_{02}}{d_4}$	0	0	0	0
4	0	-1	0	1	-1	0	0	0	0	0	0
5	0	0	0	0	0	1	0	0	0	0	0
6	0	0	0	0	0	0	1	0	0	0	0
7	0	$-G_s$	$-G_p$	0	0	0	0	$(G_p + G_s)$	$\frac{I_{01}}{c_1}+\frac{I_{02}}{d_1}$	$\frac{I_{01}}{c_2}+\frac{I_{02}}{d_2}$	$\frac{I_{01}}{c_4}+\frac{I_{02}}{d_4}$
8	0	0	-1	0	0	0	0	1	-1	0	0
9	0	0	0	0	0	0	0	0	0	-1	0
10	0	0	0	0	0	0	0	0	0	0	-1

Figure 3.14:   **Top left half of Y matrix for Figure 3.11.**

3.5 Summary

In this chapter, the system-level model of the PV array system has been derived. With the formulated system-level PV model, the protection of the entire PV system can be performed. Furthermore, since the individual states of each of the PV modules have been mapped to the global states, the status of the individual PV modules is known. This status information is later used for the protection and diagnosis of the PV array, which is covered in chapters 6 and 9 respectively.

.

4 EXTRACTION OF PARAMETERS FOR PV MODEL

The PV model was developed in the chapter 3, however, the procedure for obtaining the parameters for the PV model had not been determined. These parameters, which include the series and shunt resistances, the ideality constants and the leakage currents, are derived in this chapter. The extraction method in this chapter follows the method described in [29].

The parameters to be determined in this section are shown in red on Figure 4.1, and the extraction of these parameters originate from the PV system equation which was derived in section 3.2 and has been rewritten in (4.1).

$$0 = -I_{out} + I_{pv} - I_{d1} - I_{d2} - \frac{v_{12} + I_{out}R_s}{R_{sh}} \, , \qquad (4.1)$$

where

$$v_{12} = v_1 - v_2, \qquad (4.2)$$

$$I_{d1} = I_{o1} \left[\exp\left(\frac{v_{12} + I_{out}R_s}{aNV_t} \right) - 1 \right], \qquad (4.3)$$

$$I_{d2} = I_{o2} \left[\exp\left(\frac{v_{12} + I_{out}R_s}{nNV_t} \right) - 1 \right]. \qquad (4.4)$$
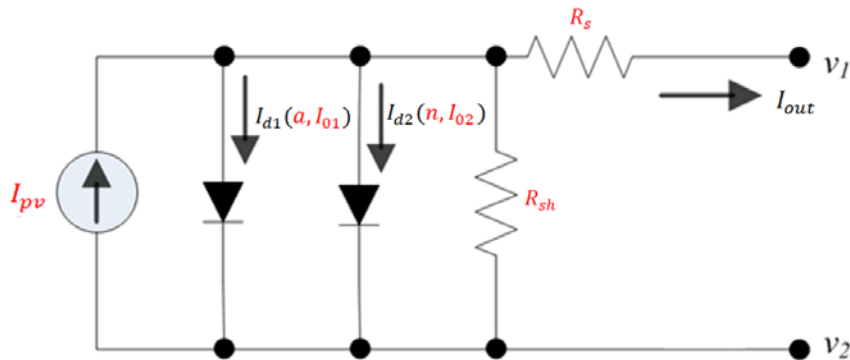
Figure 4.1:   Unknown PV parameters to be determined [29].

The datasheet of PV modules usually contain PV data, such as, the open circuit voltage, short circuit current, maximum power voltage and current obtained at STC. Using the information from the datasheet four equations can be derived from the (4.1). These four equations are discussed next.

i) Open circuit condition

When the PV module is in the open circuit condition, the PV module operates at the right extreme of its characteristic curve as shown with the arrow on Figure 4.2.
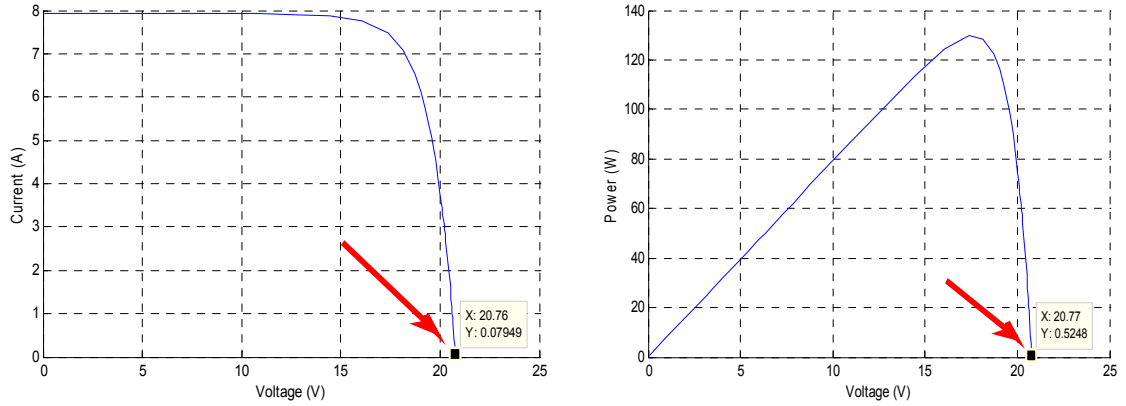
Figure 4.2: **PV operating point during open circuit conditions.**

Therefore, the output current $I_{out} = 0$, and equation (4.1) is reduced to

$$0 = I_{pv} - I_{o1}\left[\exp\left(\frac{V_{oc}}{aNV_t}\right) - 1\right] - I_{o2}\left[\exp\left(\frac{V_{oc}}{nNV_t}\right) - 1\right] - \frac{V_{oc}}{R_{sh}} . \tag{4.5}$$

ii) Short circuit condition

During a short circuit condition of a PV module, the PV module operates at the left extreme of Figure 4.3, as indicated with the arrow. Therefore the PV terminal voltage, which is the voltage from terminal v_1 to v_2 of Figure 4.1, approaches zero,

depending on the fault impedance. Conversely, the output current I_{out} becomes the short circuit current of the PV module.
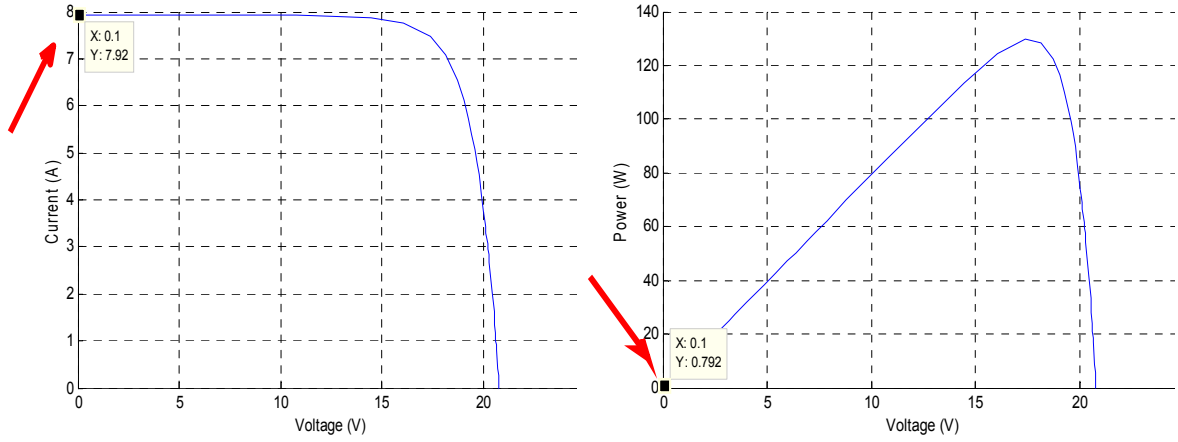
Figure 4.3:   **PV operating point during a short circuit conditions.**

Therefore (4.1) is modified as follows:

$$0 = -I_{sc} + I_{pv} - I_{o1}\left[\exp\left(\frac{I_{sc}R_s}{aNV_t}\right) - 1\right] - I_{o2}\left[\exp\left(\frac{I_{sc}R_s}{nNV_t}\right) - 1\right] - \frac{I_{sc}R_s}{R_{sh}} . \qquad (4.6)$$

iii) Maximum power point condition

When the PV module is operating at the maximum power point, which is the peak of the power-voltage curve as indicated with the arrow in Figure 4.4, the corresponding voltage-current pair constitutes the maximum power point voltage and current. Substituting these voltage and current quantities in (4.1) gives

$$0 = -P_{mp} + V_{mp}I_{pv} - V_{mp}I_{o1}\left[\exp\left(\frac{V_{mp} + I_{mp}R_s}{aNV_t}\right) - 1\right]$$
$$-V_{mp}I_{o2}\left[\exp\left(\frac{V_{mp} + I_{mp}R_s}{nNV_t}\right) - 1\right] - \frac{V_{mp}}{R_{sh}}\left(V_{mp} + I_{mp}R_s\right), \qquad (4.7)$$

54

where P_{mp} is the maximum power point and V_{mp} and I_{mp} are the corresponding voltage and currents at the maximum power point, which are available on the PV datasheet.
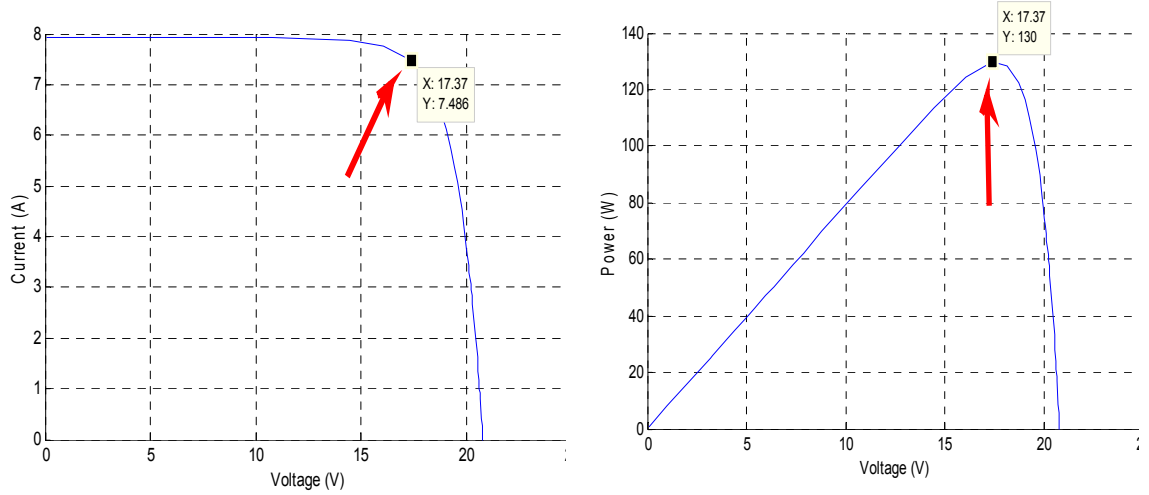
Figure 4.4: **PV operating point during maximum power point operation.**

iv) Derivative at maximum power point

At the maximum power point shown on Figure 4.4, the derivative of the power with respect to voltage is zero, therefore, (4.7) is differentiated with respect to V_{mp} and equated to zero to obtain

$$
\begin{aligned}
0 = I_{pv} &- I_{o1}\left[\exp\left(\frac{V_{mp}+I_{mp}R_s}{aNV_t}\right)-1\right] - \frac{I_{o1}V_{mp}}{aNV_t}\left[\exp\left(\frac{V_{mp}+I_{mp}R_s}{aNV_t}\right)\right] \\
&- I_{o2}\left[\exp\left(\frac{V_{mp}+I_{mp}R_s}{nNV_t}\right)-1\right] - \frac{I_{o2}V_{mp}}{nNV_t}\left[\exp\left(\frac{V_{mp}+I_{mp}R_s}{nNV_t}\right)\right] - \frac{V_{mp}}{R_{sh}} - \frac{V_{mp}+I_{mp}R_s}{R_{sh}} .
\end{aligned} \tag{4.8}
$$

From the foregoing, four equations, (4.5)-(4.8), are available to solve seven unknowns.

The validation of the PV parameters typically involves the comparison of the PV curves obtained from the computed parameters, against the curves from the measured data under STC. In the parameter extraction method used for this research, a measurement point from the PV measurement data set is used to form a fifth equation.

55

The measurement point is a voltage-current pair between the maximum power point and open circuit voltage point, which is then substituted in (4.1). Let the voltage-current pair obtained be the data measurement (V_α, I_α), the resulting equation is given in (4.9).

$$0 = -I_\alpha + I_{pv} - I_{o1}\left[\exp\left(\frac{V_\alpha + I_\alpha R_s}{aNV_t}\right) - 1\right] - I_{o2}\left[\exp\left(\frac{V_\alpha + I_\alpha R_s}{nNV_t}\right) - 1\right] - \frac{(V_\alpha + I_\alpha R_s)}{R_{sh}}. \quad (4.9)$$

The location of this data point used for this research is given in Figure 4.5. However, any other point between the open circuit and maximum power point operating conditions could have been selected, with points around the midpoint of these limits preferred.
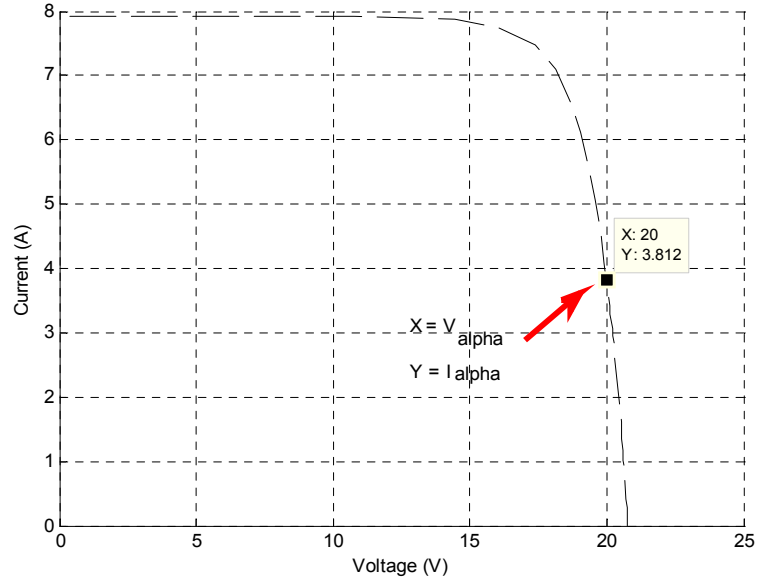
Figure 4.5: **PV measured point for additional equation.**

Therefore, there are now five equations to solve seven PV unknown parameters. The parameter determination method for this research project assumes we know the values for the ideality constants a and n, therefore, only five unknowns are left to be solved using five equations. Given the values of a and n, the five PV parameters: R_s, R_{sh}, I_{01}, I_{02}, and I_{pv} are found using the Steepest Descent numerical method [30]. The

use of the Steepest Descent method to determine the five unknown PV parameters is discussed in section 4.1. In section 4.2, an explanation of the method for determining the two known parameters, a and n is given, and in section 4.3, a comparison between the PV module curve generated using the computed PV parameters and the curves from the actual PV module measurements is performed.

4.1 Steepest Descent Numerical Method

The Steepest Descent numerical method was chosen for this research project because its convergence is global in nature. Other numerical methods, such as Newton Raphson's method, while effective, requires an accurate initial condition especially for non-linear functions such as (4.5)-(4.9). The Steepest Descent method does not require such accurate initial conditions and will give convergence from nearly any starting point [30].

The summary of equations used for the computation of the PV parameters is as follows:

$$f_0 = I_{pv} - I_{o1}\left[\exp\left(\frac{\gamma_1 V_{oc}}{NV_t}\right) - 1\right] - I_{o2}\left[\exp\left(\frac{\gamma_2 V_{oc}}{NV_t}\right) - 1\right] - G_{sh}V_{oc} \ , \tag{4.10}$$

$$f_1 = -I_{sc} + I_{pv} - I_{o1}\left[\exp\left(\frac{\gamma_1 I_{sc}R_s}{NV_t}\right) - 1\right] - I_{o2}\left[\exp\left(\frac{\gamma_2 I_{sc}R_s}{NV_t}\right) - 1\right] - G_{sh}I_{sc}R_s, \tag{4.11}$$

$$f_2 = -P_{mp} + V_{mp}I_{pv} - V_{mp}I_{o1}\left[\exp\left(\frac{\gamma_1(V_{mp} + I_{mp}R_s)}{NV_t}\right) - 1\right]$$

$$-V_{mp}I_{o2}\left[\exp\left(\frac{\gamma_2\left(V_{mp} + I_{mp}R_s\right)}{NV_t}\right) - 1\right] - V_{mp}G_{sh}\left(V_{mp} + I_{mp}R_s\right), \tag{4.12}$$

$$f_3 = I_{pv} - I_{o1}\left[\exp\left(\frac{\gamma_1(V_{mp} + I_{mp}R_s)}{NV_t}\right) - 1\right] - \frac{\gamma_1 I_{o1} V_{mp}}{NV_t}\left[\exp\left(\frac{\gamma_1(V_{mp} + I_{mp}R_s)}{NV_t}\right)\right]$$

$$- I_{o2}\left[\exp\left(\frac{\gamma_2(V_{mp} + I_{mp}R_s)}{NV_t}\right) - 1\right] - \frac{\gamma_2 I_{o2} V_{mp}}{NV_t}\left[\exp\left(\frac{\gamma_2(V_{mp} + I_{mp}R_s)}{NV_t}\right)\right] \quad (4.13)$$

$$- G_{sh}V_{mp} - G_{sh}\left(V_{mp} + I_{mp}R_s\right),$$

$$f_4 = -I_\alpha + I_{pv} - I_{o1}\left[\exp\left(\frac{\gamma_1(V_\alpha + I_\alpha R_s)}{NV_t}\right) - 1\right] - I_{o2}\left[\exp\left(\frac{\gamma_2(V_\alpha + I_\alpha R_s)}{NV_t}\right) - 1\right] - G_{sh}\left(V_\alpha + I_\alpha R_s\right), \quad (4.14)$$

where $G_{sh} = R_{sh}^{-1}$, $a = \gamma_1^{-1}$, $n = \gamma_2^{-2}$, and $f_0 = f_1 = f_2 = f_3 = f_4 = 0$.

As the state variables of (4.10)-(4.14) converge to the solution, it is possible to obtain values that are not practical, such as a negative resistance or a current direction in the reverse direction than shown in Figure 4.1. Therefore, additional equations and state variables have been introduced to ensure the PV parameters are in the correct domain.

The minimum value of the shunt resistance R_{sh_min} is generally computed from the PV curve segment between the short circuit condition and the maximum power operating point. R_{sh-min} is therefore computed as the ratio of the voltage and current differences between these points, and is given as

$$-R_{sh-min} = \frac{V_{mp} - V_{short\ circuit}}{I_{mp} - I_{short\ circuit}}. \quad (4.15)$$

The voltage at short circuit condition is assumed to be zero, which reduces (4.15) to

$$R_{sh-min} = \frac{-V_{mp}}{I_{mp} - I_{short\ circuit}}. \quad (4.16)$$

With the shunt resistance being limited as shown in (4.16), the values for G_{sh} are restricted between zero and G_{sh-max}, which has a value of $\frac{1}{R_{sh-min}}$. Therefore, the following equation is obtained:

$$f_5 = \left(G_{sh} - G_0\right)^2 + \tau^2 - G_{sh-radius}^2 . \tag{4.17}$$

In (4.17), the value of τ is not important for this problem, and is only used to define the domain of G_{sh} as demonstrated pictorially on Figure 4.6.
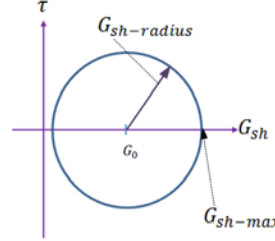
Figure 4.6: **Restriction of PV module shunt resistance value.**

Similarly, to ensure that the leakage currents I_{01} and I_{02} are positive numbers, two equations are added to the set of equations as follows:

$$f_6 = K_1 I_{01} - \zeta^2 , \tag{4.18}$$

$$f_7 = K_2 I_{02} - \phi^2 , \tag{4.19}$$

where K_1 and K_2 are constants in the order of 10^0 to 10^1, and the terms ζ^2 and ϕ^2 are to ensure these terms are positive numbers. The leakage currents I_{01} and I_{02} are generally of a small magnitude in the order of 10^{-7}. Therefore, by multiplying them by the constants K_1 and K_2, it is guaranteed that a positive number in the order of 10^0 minus another positive number (ζ^2 and ϕ^2) results in a zero valued solution f_6 and f_7. If the constants K_1 and K_2 were not used, negative valued solution in the order of 10^{-9} for f_6 and f_7 in (4.18) and (4.19) respectively, could be obtained, and deemed close enough to the required zero value. Therefore, the following addition equations are added to $f_{0,1,2,3,4}\left(I_{01}, G_{sh}, R_s, I_{pv}, I_{02}\right)$ of $(4.10) - (4.14)$,

$$f_5 = \left(G_{sh} - G_0\right)^2 + \tau^2 - G_{sh-radius}, \qquad (4.20)$$

$$f_6 = K_1 I_{01} - \zeta^2, \qquad (4.21)$$

$$f_7 = K_2 I_{02} - \phi^2, \qquad (4.22)$$

where, $f_5 = f_6 = f_7 = 0$.

Let x be given as the state variable set $[I_{01}, G_{sh}, R_s, I_{pv}, \tau, I_{02}, \zeta, \phi]$, then

$$F(x) = \begin{bmatrix} f_0(x) \\ f_1(x) \\ f_2(x) \\ f_3(x) \\ f_4(x) \\ f_5(x) \\ f_6(x) \\ f_7(x) \end{bmatrix}, \qquad (4.23)$$

and the Jacobian matrix for $(4.10) - (4.14)$ and $(4.20) - (4.22)$ is given as

$$J(x) = \begin{bmatrix}
\dfrac{\delta f_0(x)}{\delta I_{01}} & \dfrac{\delta f_0(x)}{\delta G_{sh}} & \dfrac{\delta f_0(x)}{\delta R_s} & \dfrac{\delta f_0(x)}{\delta I_{pv}} & \dfrac{\delta f_0(x)}{\delta \tau} & \dfrac{\delta f_0(x)}{\delta I_{02}} & \dfrac{\delta f_0(x)}{\delta \zeta} & \dfrac{\delta f_0(x)}{\delta \phi} \\[2mm]
\dfrac{\delta f_1(x)}{\delta I_{01}} & \dfrac{\delta f_1(x)}{\delta G_{sh}} & \dfrac{\delta f_1(x)}{\delta R_s} & \dfrac{\delta f_1(x)}{\delta I_{pv}} & \dfrac{\delta f_1(x)}{\delta \tau} & \dfrac{\delta f_1(x)}{\delta I_{02}} & \dfrac{\delta f_1(x)}{\delta \zeta} & \dfrac{\delta f_1(x)}{\delta \phi} \\[2mm]
\dfrac{\delta f_2(x)}{\delta I_{01}} & \dfrac{\delta f_2(x)}{\delta G_{sh}} & \dfrac{\delta f_1(x)}{\delta R_s} & \dfrac{\delta f_2(x)}{\delta I_{pv}} & \dfrac{\delta f_2(x)}{\delta \tau} & \dfrac{\delta f_2(x)}{\delta I_{02}} & \dfrac{\delta f_2(x)}{\delta \zeta} & \dfrac{\delta f_2(x)}{\delta \phi} \\[2mm]
\dfrac{\delta f_3(x)}{\delta I_{01}} & \dfrac{\delta f_3(x)}{\delta G_{sh}} & \dfrac{\delta f_3(x)}{\delta R_s} & \dfrac{\delta f_3(x)}{\delta I_{pv}} & \dfrac{\delta f_3(x)}{\delta \tau} & \dfrac{\delta f_3(x)}{\delta I_{02}} & \dfrac{\delta f_3(x)}{\delta \zeta} & \dfrac{\delta f_3(x)}{\delta \phi} \\[2mm]
\dfrac{\delta f_4(x)}{\delta I_{01}} & \dfrac{\delta f_4(x)}{\delta G_{sh}} & \dfrac{\delta f_4(x)}{\delta R_s} & \dfrac{\delta f_4(x)}{\delta I_{pv}} & \dfrac{\delta f_4(x)}{\delta \tau} & \dfrac{\delta f_4(x)}{\delta I_{02}} & \dfrac{\delta f_4(x)}{\delta \zeta} & \dfrac{\delta f_4(x)}{\delta \phi} \\[2mm]
\dfrac{\delta f_5(x)}{\delta I_{01}} & \dfrac{\delta f_5(x)}{\delta G_{sh}} & \dfrac{\delta f_5(x)}{\delta R_s} & \dfrac{\delta f_5(x)}{\delta I_{pv}} & \dfrac{\delta f_5(x)}{\delta \tau} & \dfrac{\delta f_5(x)}{\delta I_{02}} & \dfrac{\delta f_5(x)}{\delta \zeta} & \dfrac{\delta f_5(x)}{\delta \phi} \\[2mm]
\dfrac{\delta f_6(x)}{\delta I_{01}} & \dfrac{\delta f_6(x)}{\delta G_{sh}} & \dfrac{\delta f_6(x)}{\delta R_s} & \dfrac{\delta f_6(x)}{\delta I_{pv}} & \dfrac{\delta f_6(x)}{\delta \tau} & \dfrac{\delta f_6(x)}{\delta I_{02}} & \dfrac{\delta f_6(x)}{\delta \zeta} & \dfrac{\delta f_6(x)}{\delta \phi} \\[2mm]
\dfrac{\delta f_7(x)}{\delta I_{01}} & \dfrac{\delta f_7(x)}{\delta G_{sh}} & \dfrac{\delta f_7(x)}{\delta R_s} & \dfrac{\delta f_7(x)}{\delta I_{pv}} & \dfrac{\delta f_7(x)}{\delta \tau} & \dfrac{\delta f_7(x)}{\delta I_{02}} & \dfrac{\delta f_7(x)}{\delta \zeta} & \dfrac{\delta f_7(x)}{\delta \phi}
\end{bmatrix}, \qquad (4.24)$$

The components of the Jacobian matrix are as follows:

$$\frac{\delta f_0(x)}{\delta I_{01}} = -\exp\left(\frac{\gamma_1 V_{oc}}{NV_t}\right) + 1.0, \tag{4.25}$$

$$\frac{\delta f_0(x)}{\delta G_{sh}} = -V_{oc}, \tag{4.26}$$

$$\frac{\delta f_0(x)}{\delta I_{pv}} = 1.0, \tag{4.27}$$

$$\frac{\delta f_0(x)}{\delta I_{02}} = -\exp\left(\frac{\gamma_2 V_{oc}}{NV_t}\right) + 1.0, \tag{4.28}$$

$$\frac{\delta f_1(x)}{\delta I_{01}} = -\exp\left(\frac{\gamma_1 I_{sc} R_s}{NV_t}\right) + 1.0, \tag{4.29}$$

$$\frac{\delta f_1(x)}{\delta G_{sh}} = -I_{sc} R_s, \tag{4.30}$$

$$\frac{\delta f_1(x)}{\delta R_s} = -\frac{\gamma_1 I_{sc} I_{o1}}{NV_t} \exp\left(\frac{\gamma_1 I_{sc} R_s}{NV_t}\right) - \frac{\gamma_2 I_{sc} I_{o2}}{NV_t} \exp\left(\frac{\gamma_2 I_{sc} R_s}{NV_t}\right) - G_{sh} I_{sc}, \tag{4.31}$$

$$\frac{\delta f_1(x)}{\delta I_{pv}} = 1.0, \tag{4.32}$$

$$\frac{\delta f_1(x)}{\delta I_{02}} = -\exp\left(\frac{\gamma_2 I_{sc} R_s}{NV_t}\right) + 1.0, \tag{4.33}$$

$$\frac{\delta f_2(x)}{\delta I_{01}} = -V_{mp}\left[\exp\left(\frac{\gamma_1 (V_{mp} + I_{mp} R_s)}{NV_t}\right) - 1.0\right], \tag{4.34}$$

$$\frac{\delta f_2(x)}{\delta G_{sh}} = -V_{mp}\left(V_{mp} + I_{mp} R_s\right), \tag{4.35}$$

$$\frac{\delta f_2(x)}{\delta R_s} = -\frac{V_{mp} I_{o1} \gamma_1 I_{mp}}{NVt} \exp\left(\frac{\gamma_1 (V_{mp} + I_{mp} R_s)}{NV_t}\right) - \frac{V_{mp} I_{o2} \gamma_2 I_{mp}}{NVt} \exp\left(\frac{\gamma_2 (V_{mp} + I_{mp} R_s)}{NV_t}\right) - V_{mp} G_{sh} I_{mp}, \tag{4.36}$$

$$\frac{\delta f_2(x)}{\delta I_{pv}} = V_{mp},$$ (4.37)

$$\frac{\delta f_2(x)}{\delta I_{02}} = -V_{mp}\left[\exp\left(\frac{\gamma_2\left(V_{mp} + I_{mp}R_s\right)}{NV_t}\right) - 1.0\right],$$ (4.38)

$$\frac{\delta f_3(x)}{\delta I_{01}} = -\exp\left(\frac{\gamma_1(V_{mp} + I_{mp}R_s)}{NV_t}\right) + 1 - \frac{\gamma_1 V_{mp}}{NV_t}\exp\left(\frac{\gamma_1(V_{mp} + I_{mp}R_s)}{NV_t}\right),$$ (4.39)

$$\frac{\delta f_3(x)}{\delta G_{sh}} = -2V_{mp} - I_{mp}R_s,$$ (4.40)

$$\frac{\delta f_3(x)}{\delta R_s} = -\frac{I_{o1}\gamma_1 I_{mp}}{NV_t}\exp\left(\frac{\gamma_1(V_{mp} + I_{mp}R_s)}{NV_t}\right) - \frac{\gamma_1^2 I_{mp}I_{o1}V_{mp}}{\left(NV_t\right)^2}\exp\left(\frac{\gamma_1(V_{mp} + I_{mp}R_s)}{NV_t}\right)$$
$$- \frac{I_{02}\gamma_2 I_{mp}}{NV_t}\exp\left(\frac{\gamma_2(V_{mp} + I_{mp}R_s)}{NV_t}\right) - \frac{\gamma_2^2 I_{mp}I_{o2}V_{mp}}{\left(NV_t\right)^2}\exp\left(\frac{\gamma_2(V_{mp} + I_{mp}R_s)}{NV_t}\right) - G_{sh}I_{mp},$$ (4.41)

$$\frac{\delta f_3(x)}{\delta I_{pv}} = 1.0,$$ (4.42)

$$\frac{\delta f_3(x)}{\delta I_{02}} = -\exp\left(\frac{\gamma_2(V_{mp} + I_{mp}R_s)}{NV_t}\right) + 1.0 - \frac{\gamma_2 V_{mp}}{NV_t}\left[\exp\left(\frac{\gamma_2(V_{mp} + I_{mp}R_s)}{NV_t}\right)\right],$$ (4.43)

$$\frac{\delta f_4(x)}{\delta I_{01}} = -\exp\left(\frac{\gamma_1(V_\alpha + I_\alpha R_s)}{NVt}\right) + 1.0,$$ (4.44)

$$\frac{\delta f_4(x)}{\delta G_{sh}} = -V_\alpha - I_\alpha R_s,$$ (4.45)

$$\frac{\delta f_4(x)}{\delta R_s} = -\frac{I_{o1}\gamma_1 I_\alpha}{NV_t}\exp\left(\frac{\gamma_1(V_\alpha + I_\alpha R_s)}{NV_t}\right) - \frac{I_{o2}\gamma_2 I_\alpha}{NV_t}\exp\left(\frac{\gamma_2(V_\alpha + I_\alpha R_s)}{NV_t}\right) - G_{sh}I_\alpha,$$ (4.46)

$$\frac{\delta f_4(x)}{\delta I_{pv}} = 1.0,$$ (4.47)

$$\frac{\delta f_4(x)}{\delta I_{02}} = -\exp\left(\frac{\gamma_2(V_\alpha + I_\alpha R_s)}{NVt}\right) + 1.0, \tag{4.48}$$

$$\frac{\delta f_5(x)}{\delta G_{sh}} = 2G_{sh} - 2G_0, \tag{4.49}$$

$$\frac{\delta f_5(x)}{\delta \tau} = 2\tau, \tag{4.50}$$

$$\frac{\delta f_6(x)}{\delta I_{01}} = K_1, \tag{4.51}$$

$$\frac{\delta f_6(x)}{\delta \zeta} = -2\zeta, \tag{4.52}$$

$$\frac{\delta f_7(x)}{\delta I_{02}} = K_2, \tag{4.53}$$

$$\frac{\delta f_7(x)}{\delta \phi} = -2\phi. \tag{4.54}$$

All the other derivatives not listed in (4.25)-(4.54), have a value of zero.

Assuming a solution to the set of equations, $f_0 - f_7$, has been determined, and is given by

$x = [I_{01}, G_{sh}, R_s, I_{pv}, \tau, I_{02}, \zeta, \phi]^T$, then the function g which has the form

$$g(x) = [F(x)]^T [F(x)], \tag{4.55}$$

has a minimal value of zero at this solution x. To find this solution, however, an initial guess is needed. For this research, the initial guess was given as follows:

$$
\mathbf{x}_0 = \begin{bmatrix} I_{01} \\ G_{sh} \\ R_s \\ I_{pv} \\ \tau \\ I_{02} \\ \zeta \\ \phi \end{bmatrix} = \begin{bmatrix} 10^{-9} \\ 10^{-4} \\ 10^{-3} \\ I_{short\ circuit} = 7.92 \\ 10^{-2} \\ 10^{-9} \\ \sqrt{I_{01}} \\ \sqrt{I_{02}} \end{bmatrix}, \tag{4.56}
$$

where the quantities are given in their basic units. The resulting $g(\mathrm{x})$ in (4.55), given as $g(x_0)$ is computed. If x_0 is the solution of this non-linear system of equations, then the gradient $\nabla g(\mathrm{x}_0)$, given as

$$
\nabla g\left(\mathrm{x}_0\right) = 2\left[J\left(\mathrm{x}_0\right)\right]^T F\left(\mathrm{x}_0\right), \tag{4.57}
$$

has a value of zero and a relative minimum is reached. If x is not the solution to the system of equations, which is most often the case after the initial guess, then the state variable set, x_0, needs to be moved in a direction such that $g(\mathrm{x})$ is decreased the most.

The direction of move that yields the greatest decrease of $g(x)$ occurs in the direction of $-\nabla g(x)$. Therefore, the initial guess x_0 is moved in the direction of $-\nabla g(\mathrm{x}_0)$ as follows:

$$
\mathrm{x}_1 = \mathrm{x}_0 - \alpha z, \tag{4.58}
$$

where α is a positive integer selected in such a manner that ensures $g(\mathrm{x}_1)$ is less than $g(\mathrm{x}_0)$, and z is the unit vector of $\nabla g(x_0)$ given as:

$$
z = \frac{1}{\sqrt{\left[\nabla g\left(x_0\right)\right]^T \left[\nabla g\left(x_0\right)\right]}} \nabla g\left(x_0\right). \tag{4.59}
$$

To find the appropriate value for α in (4.58), x_1 is evaluated at three α points, $\alpha_1, \alpha_2, \alpha_3$, where $\alpha_1 < \alpha_2 < \alpha_3$. This research follows the method in [30], where $\alpha_1 = 0$ and

$\alpha_3 = 1$. If $g(x_1|\alpha_3) > g(x_1|\alpha_1)$, a new value of α_3 is determined by dividing the current

α_3 by 2 until an α_3 that yields $g(x_1|\alpha_3) < g(x_1|\alpha_1)$ is obtained. Then α_2 is selected to be

the midpoint between $[\alpha_1, \alpha_3]$.

As previously stated, the method of obtaining the ideality constants a and n is

discussed in the subsequent section. However, for this illustration, assuming the values of

the inverse of the ideality constants are given as

$$\gamma_1 = \gamma_2 = 0.7236, \tag{4.60}$$

where γ_1 and γ_2 are the inverse of a and n respectively, the following are obtained:

Table 4.1:   Results from x_0 parameter computation [29].

Variable	Simulation Value
$\dfrac{1}{\sqrt{\left[\nabla g(x_0)\right]^T \left[\nabla g(x_0)\right]}} =$	$1.3197 \, x10^{-9}$
$z =$	$\begin{bmatrix} -0.70711 \\ -7.2414\,x10^{-6} \\ -5.9795\,x10^{-9} \\ 3.90901\,x10^{-7} \\ 5.14736\,x10^{-15} \\ -0.70711 \\ -1.6692\,x10^{-17} \\ -1.6692\,x10^{-17} \end{bmatrix}$
$\alpha_1 =$	0.0
$\alpha_3 =$	$9.5367\,x10^{-7}$
$\alpha_2 =$	$4.7684\,x10^{-7}$
$g(x_0|\alpha_1) = g_1(\alpha_1) =$	186.0589
$g(x_0|\alpha_3) = g_3(\alpha_3) =$	184.884
$g(x_0|\alpha_2) = g_2(\alpha_2) =$	5.1021

From the data obtained, the Newton's forward divided-difference interpolation formula is used to form a polynomial, which can be used to compute any α_i between the end points $[\alpha_1, \alpha_3]$. This polynomial is given as

$$P(\alpha) = g[\alpha_1] + g[\alpha_1, \alpha_2](\alpha - \alpha_1) + g[\alpha_1, \alpha_2, \alpha_3](\alpha - \alpha_1)(\alpha - \alpha_2), \qquad (4.61)$$

where

$$g[\alpha_1] = g(\alpha_1), \qquad (4.62)$$

$$g[\alpha_1, \alpha_2] = \frac{g(\alpha_2) - g(\alpha_1)}{\alpha_2 - \alpha_1} = h_1, \qquad (4.63)$$

$$g[\alpha_1, \alpha_2, \alpha_3] = \frac{g[\alpha_2, \alpha_3] - g[\alpha_1, \alpha_2]}{\alpha_3 - \alpha_1} = \frac{h_2 - h_1}{\alpha_3 - \alpha_1} = h_3, \qquad (4.64)$$

and

$$g[\alpha_2, \alpha_3] = h_2 = \frac{g(\alpha_3) - g(\alpha_2)}{\alpha_3 - \alpha_2}. \qquad (4.65)$$

By making substitutions using the newly introduced terms of (4.62)-(4.65), (4.61) is rewritten as

$$P(\alpha) = g(\alpha_1) + h_1(\alpha - \alpha_1) + h_3(\alpha - \alpha_1)(\alpha - \alpha_2), \qquad (4.66)$$

which is reduced to

$$P(\alpha) = g(\alpha_1) + h_1\alpha + h_3\alpha(\alpha - \alpha_2), \qquad (4.67)$$

by substituting the value for α_1 From Table 4.1. The derivative $\dfrac{\delta P(\alpha)}{\delta \alpha}$, evaluated at $\alpha = \alpha_0$, has a value of zero when

$$\alpha_0 = \frac{h_3\alpha_2 - h_1}{2h_3}. \qquad (4.68)$$

66

Consequently, $g(\alpha_0)$ is evaluated and selected if it leads to the most decrease in $g(x)$, as compared with the values on Table 4.1 From the foregoing, the following additional values have been obtained for this research as shown on Table 4.2.

Table 4.2:   **Additional results from x_0 parameter computation [29].**

Variable	Simulation Value
$h_1 =$	$-3.79\,x10^8$
$h_2 =$	$3.77\,x10^8$
$h_3 =$	$7.93\,x10^{14}$
$\alpha_0 =$	$4.7761x10^{-7}$
$g(x_0 \mid \alpha_0) = g_0(\alpha_0) =$	5.10167

A comparison of Table 4.1 and Table 4.2 shows that α_0 reduces $g(x)$ the most, therefore (4.58) is evaluated as

$$x_1 = x_0 - \alpha_0 z = \begin{bmatrix} 3.387\,x10^{-9} \\ 10^{-4} \\ 10^{-3} \\ 7.92007 \\ 10^{-2} \\ 3.387\,x10^{-7} \\ 3.162\,x10^{-5} \\ 3.162\,x10^{-5} \end{bmatrix}. \tag{4.69}$$

The next set of states that reduces $g(x)$ is determined by solving (4.58) for x_2 as follows:

$$x_2 = x_1 - \alpha z, \tag{4.70}$$

with z updated using the values from x_1. The final solution for the given ideality constants are as follows:

$$
\mathbf{x} = \begin{bmatrix} I_{01} \\ G_{sh} \\ R_s \\ I_{pv} \\ \tau \\ I_{02} \\ \zeta \\ \phi \end{bmatrix} = \begin{bmatrix} 3.81x10^{-7} \\ 0.0056 \\ 0.00572 \\ 7.92053 \\ 0.01 \\ 3.81x10^{-7} \\ 3.162x10^{-5} \\ 3.162x10^{-5} \end{bmatrix} , \tag{4.71}
$$

all given in basic units. Absolute values of G_{sh} and R_s were used for this research with the assumption that if these parameters were negative values, their absolute value will yield non-optimum results and be discarded. The discarding of the non-optimum results is discussed in section 4.2.

As previously discussed, to determine the value of R_s, in a single diode model approach, the value of R_s was increased in small increments in [17]. The R_s variation continued till an R_s value that resulted in the maximum power was obtained at a given ideality constant value. The ideality factor was later adjusted to match the experimental PV curve. In this research, by varying the ideality constant n, and keeping the ideality constant a and the other PV module parameters of (4.71) fixed, (4.1) is computed numerically to determine the maximum power. From the maximum power obtained at each variation of the ideality constant n, Figure 4.7 has been generated.

PV Deviation from Maximum Power with Changing Ideality Constant
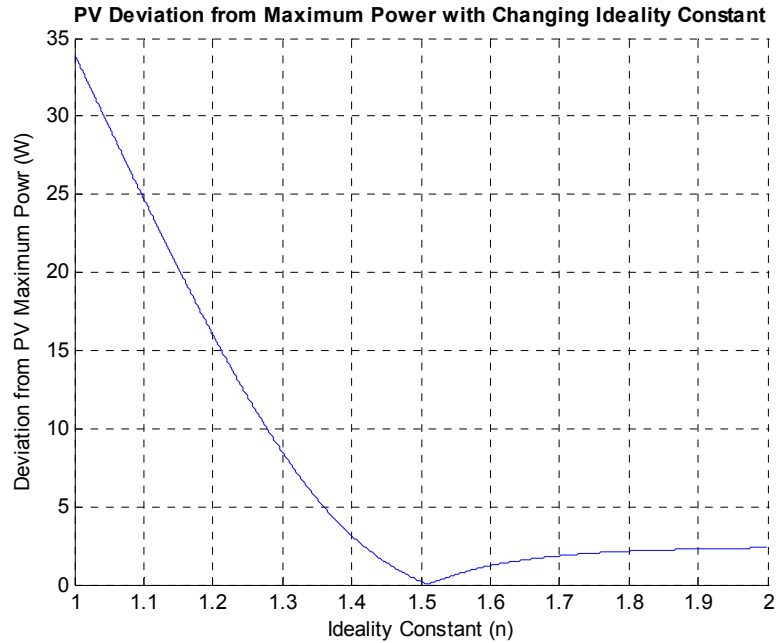
Figure 4.7:   **Maximum power deviation versus change in n.**

By using the method in [17], depending on how small of an increment n is allowed to vary, the computational time to arrive at the desired values can be substantial. Recognizing that Figure 4.7 is a unimodal function, an optimization search method, the Fibonacci method, is employed in this research and is discussed in section 4.2.

It should be noted, however, that although the value of $n = 1.51$ yielded a maximum power quite close to the desired value of 130.032W, this value is not the desired solution. In fact, $\gamma_1 = 0.7236$ and $\gamma_2 = 1/n = 1.51$, along with the set of solution in (4.71) are not the desired solution. This is easily demonstrated by comparing the curves generated by this set of solution with the experimentally measured data as shown on Figure 4.8 and Figure 4.9.

In the subsequent section, the method of determining a and n is discussed. The advantage of this method is that the whole set of solution is recomputed for the selected a

and *n* values, rather than holding some parameters fixed to vary another variable as performed in [17].
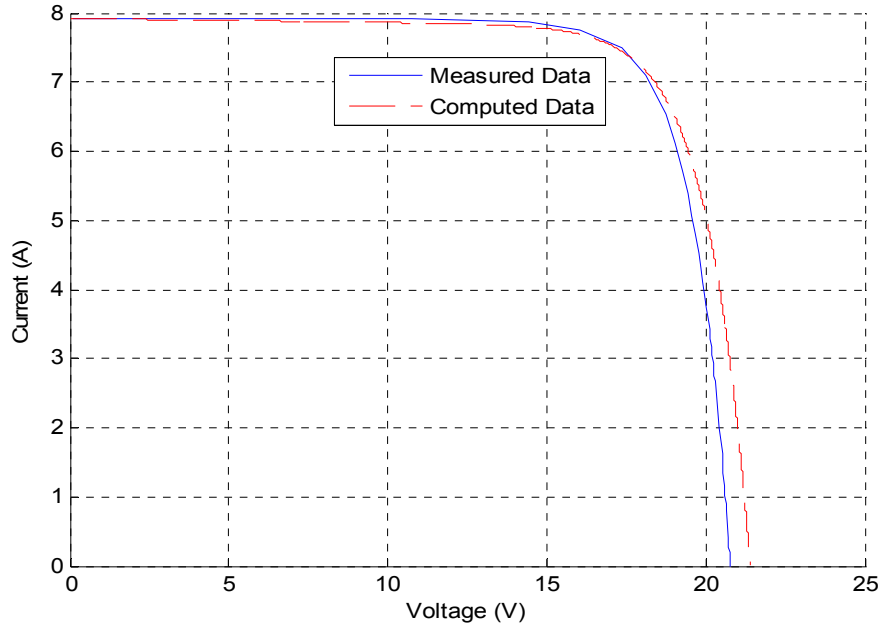

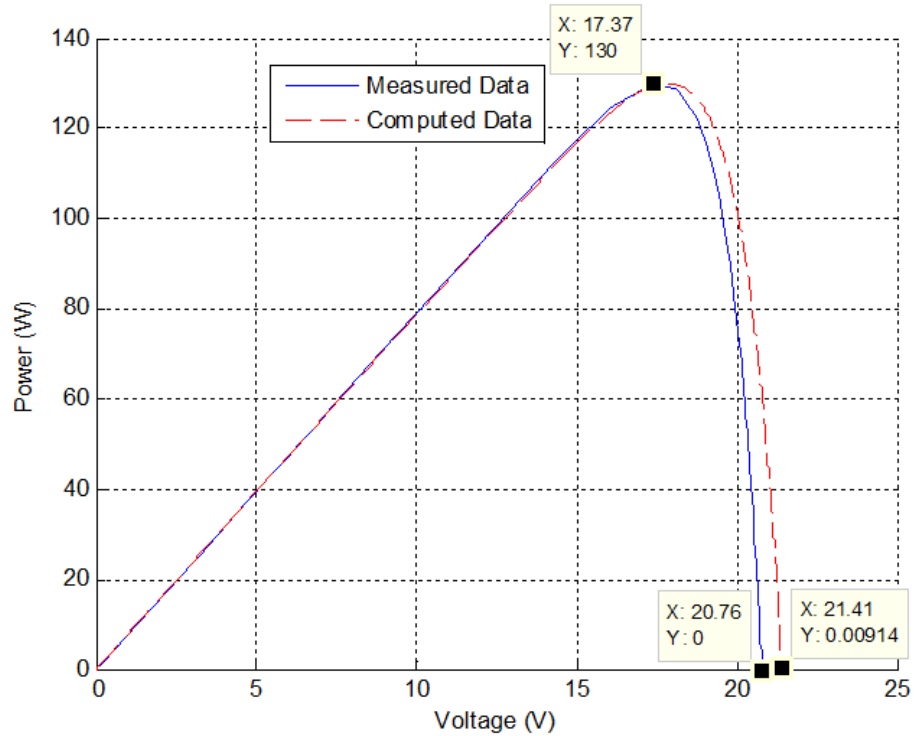**Figure 4.8:**   PV module voltage-current curve comparison with a =1.38 and n=1.51.

Figure 4.9:   PV module power-voltage curve comparison with a=1.38 and n=1.51

4.2 Fibonacci Parameter Search Method

The Fibonacci search method is effective with unimodal functions, which as previously discussed, the parameters of interest (ideality constants a and n) fall under this category. The Fibonacci method was chosen for this research project because when compared to other search methods such as dichotomous search and equal interval search, be it a three-point or four-point interval search, the Fibonacci method arrives at the solution quicker. The Fibonacci search method is quicker because it performs lesser functional evaluations for a given interval of uncertainty. Specifically, after the two initial functional evaluations, the Fibonacci search only requires one functional evaluation per Fibonacci search step [31].

4.2.1 One-dimensional Fibonacci Parameter Search

In this section, the Fibonacci search method is used to determine the value for the ideality constant n, given the value of a. Therefore, assuming the value for the ideality constant a is given as $a = 1.38$, as was used in section 4.1, the steps for determining the optimal value for the ideality constant n are as follows:

i)   Establish the interval of uncertainty for the search,

ii)   Establish an initial search boundary for the ideality constant,

iii)   Adjust the search boundary until the desired interval of uncertainty is attained.

These steps are discussed in the subsequent paragraphs

i) Establish interval of uncertainty

The interval of uncertainty is the level of accuracy desired, and for this research project, an interval of uncertainty of less than 10^{-3} has been selected. With larger interval of uncertainty, the computational time to arrive at the optimized solution

becomes faster, when compared to a lesser degree of certainty. However, this larger degree of uncertainty will result in a less accurate optimized solution. For a less than 10^{-3} interval of uncertainty, the Fibonacci series factors are given on Table 4.3.

Table 4.3:   Fibonacci Series Factors

Fibonacci Factors, k	0	1	2	3	4	$\cdots$	13	14	15	16
Series, F_k	1	1	2	3	5	$\cdots$	377	610	987	1597
Degree of Uncertainty $\frac{1}{F_k}$	1	1	0.5	0.33	0.2	$\cdots$	0.003	0.002	0.00101	0.0006

where

$$F_0 = F_1 = 1, \tag{4.72}$$

$$F_k = F_{k-1} + F_{k-2}, \forall k \geq 2. \tag{4.73}$$

As confirmed on Table 4.3, the smaller the interval of uncertainty, the more accurate the solution. However, this accuracy comes at a price of performing more iterations before arriving at the optimized the solution. From Table 4.3, the interval of uncertainty for the research project is $0.6 \ x \ 10^{-3}$.

ii) Establish the initial search boundary for n

The search boundary selected for this ideality constant search is consistent with typical values listed in various publications. The value of the ideality constant typically falls between 1 and 2 [19], [20], [32], and these are the boundaries used for this research.

The difference between the upper and lower bounds, 1 and 2 respectively, becomes the search domain within which the optimized value is found.

iii) Validation and adjustment of search boundaries

Given the other PV parameters, namely $(I_{01}, I_{02}, R_p, R_s, I_{pv}, a)$, the function $f(I_{out}, v_{12})$ given as

$$f\left(I_{out}, v_{12}\right) = -I_{out} + I_{pv} - I_{o1}\left[\exp\left(\frac{v_{12} + I_{out}R_s}{aNV_t}\right) - 1\right] - I_{o2}\left[\exp\left(\frac{v_{12} + I_{out}R_s}{nNV_t}\right) - 1\right] - \frac{v_{12} + I_{out}R_s}{R_{sh}}, \quad (4.74)$$

is evaluated to obtain the maximum PV module power, by varying v_{12} from zero to v_{oc}. The numerical method used for this evaluation is the Newton Raphson's iterative method, with an n value of n_1 given on Table 4.4. This evaluation process is repeated for an n value of n_2. Both n_1 and n_2 are located Δn_2 away from the lower and upper boundary points, where $n_1 < n_2$. The value of Δn is given as follows:

$$\Delta n = \left(upb - lwb\right) * \frac{F_{k-2}}{F_k}, \quad (4.75)$$

where $k \geq 2$. The term, k, is the Fibonacci factor (or Fibonacci iteration) that is currently being evaluated, and for the first Δn computation for this research, k has a starting value of 16. The terms lwb and upb are the lower and upper boundaries respectively, for the ideality factor n at the given Fibonacci iteration. For this research, the values of the Fibonacci parameters at the first iteration are given on Table 4.4. It is from the value of n_1 from Table 4.4, that the initial values for γ_1 and γ_2, given as $1/n_1$ in (4.60), were selected. To evaluate (4.74), v_{12} is varied from the short circuit voltage, $v_{12} = 0$, to the open circuit voltage while computing the power from the (I_{out}, v_{12}) pair to determine the maximum power at the given n value.

73

Table 4.4:   **Fibonacci terms at first iteration.**

Variable	Value
$k =$	16
$lwb =$	1
$upb =$	2
$\Delta n_2 = 1 \, x \dfrac{610}{1597} =$	0.382
$n_1 = lwb + \Delta n_2 =$	1.382
$n_2 = upb - \Delta n_2 =$	1.618

It is expected that the maximum power at the optimized n ($P_{max,n}$) be the same as the maximum measured PV module power at STC ($P_{max,STC}$). Therefore,

$$f(n) = |P_{max,n} - P_{max,STC}|, \tag{4.76}$$

approaches zero as n gets closer to the optimized value. For the n_1 and n_2 values of Table 4.4 (4.76) is computed as follows

$$f(n_1) = f(1.382) = |125.6473 - 130.032| = 4.3847, \tag{4.77}$$

$$f(n_2) = f(1.618) = |129.7772 - 130.032| = 0.2548. \tag{4.78}$$

Next, a comparison is done between f(n_1) and f(n_2). If f(n_1) < f(n_2), this means that n_1 is closer to the desired value of n. Therefore, n_1 minimizes the function $f(n)$ in (4.76) better than the value of n_2. Also, for $f(n_1) < f(n_2)$, the lower limit of the search interval remains unchanged while the upper limit is moved to the value of n_2, and (4.76) is re-evaluated at a new n, n_3, given as $n_3 = lwb + \Delta n_3$.

From (4.77) and (4.78), $f(n_1) > f(n_2)$, therefore the upper limit remains unchanged while the lower limit is moved to the value of n_1. In other words, the boundary points are adjusted as follows:

$$lwb = n_1 = 1.382, \tag{4.79}$$

$$upb = upb = 2.0, \tag{4.80}$$

resulting in a smaller search domain.

After these initial functional evaluations, only one function evaluation per Fibonacci step is performed. For the next Fibonacci step, a new n value, n_3, is selected which is Δn_3 away from the boundary that remained unchanged. In the above example, the unchanged boundary was upb, as given in (4.80), therefore, n_3 is given as

$$n_3 = upb - \Delta n_3. \tag{4.81}$$

The term, Δn_3, is computed by substituting the new boundary values of (4.79) and (4.80) in (4.75), with $k = 15$. Using these new boundary points with the current k value, Table 4.4 is updated as shown on Table 4.5.

Table 4.5: Fibonacci terms at second iteration [29].

Variable	Value
$k =$	15
$lwb =$	1.382
$upb =$	2.00
$\Delta n_3 = 0.618\,x\dfrac{377}{987} =$	0.2361
$n_3 = upb - \Delta n_3 =$	1.7634

The function $f(n_3)$ is computed next, and has a value of

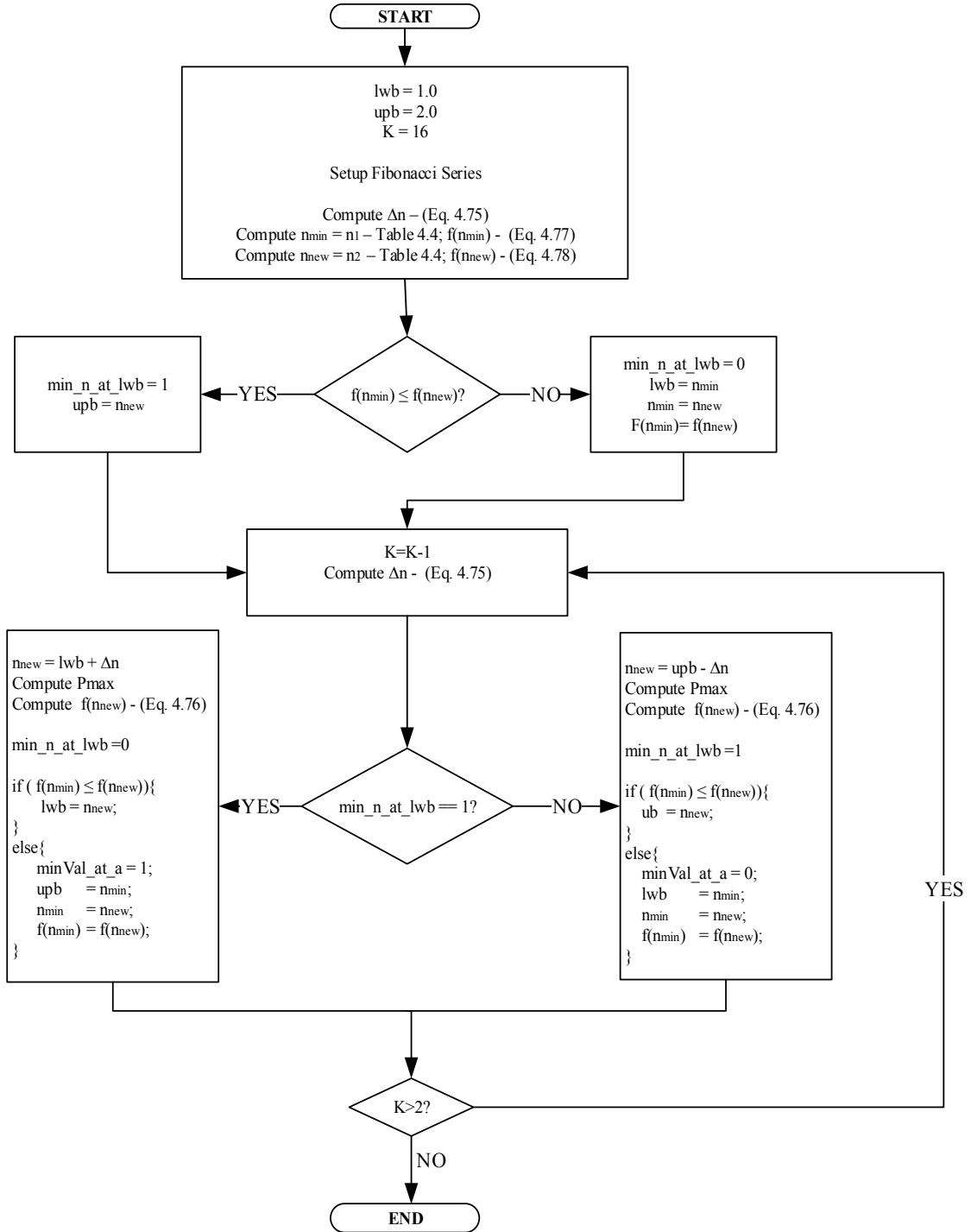$$f(n_3) = f(1.7634) = |129.695 - 130.032| = 0.337, \tag{4.82}$$

which is then compared against $f(n_2)$. For this step, only $f(upb - \Delta n_3) = f(n_3)$ was computed, not $f(lwb + \Delta n_3)$ as well. The quantity $f(lwb + \Delta n_3)$ is not computed

because it was already computed in the previous step. That is, $\left(lwb + \Delta n_3\right) = 1.618$, was already computed in (4.76). In fact, $f\left(lwb + \Delta n_3\right) = f\left(n_2\right)$ which is the second parameter being compared against in this step. This corroborates the claim that only one function evaluation is required at each Fibonacci step.

From the comparison between $f\left(n_2\right)$ and $f\left(n_3\right)$, $f\left(n_3\right)$ has a higher value, therefore the upper boundary is moved to n_3 while lwb remains unchanged at 1.38. Equation (4.75) is evaluated next, with $k = 14$, and a new n value, n_4, is determined. This procedure continues till the desired level of accuracy is attained, which occurs at $k = 2$. This process has been automated in C++ for this research. The table showing the computations for each Fibonacci step and A flow chart showing the procedure are shown on Table 4.6 and Figure 4.10 and respectively.

Table 4.6:   Results of Fibonacci steps.

k	14	13	12	11	10	9	$\cdots$	2
lwb	1.3820	1.3820	1.4721	1.5279	1.5279	1.5492	$\cdots$	1.56356
upb	1.7639	1.6180	1.6180	1.6180	1.5836	1.5836	$\cdots$	1.56481
Δn	0.1450	0.09017	0.0557	0.03444	0.02129	0.01315	$\cdots$	0.00063
n_{new}	1.5279	1.4721	1.5623	1.5836	1.5492	1.5704	$\cdots$	1.5642
$f\left(n_{new}\right)$	0.2519	0.2645	0.2498	0.2504	0.2501	0.2499	$\cdots$	0.24979
$f\left(n_{min}\right)$	0.2548	0.2519	0.2519	0.2498	0.2498	0.2498	$\cdots$	0.24979
n_{min}	1.6180	1.5279	1.5279	1.5623	1.5623	1.5623	$\cdots$	1.56418

START

lwb = 1.0
upb = 2.0
K = 16

Setup Fibonacci Series

Compute Δn – (Eq. 4.75)
Compute $n_{min} = n_1$ – Table 4.4; $f(n_{min})$ - (Eq. 4.77)
Compute $n_{new} = n_2$ – Table 4.4; $f(n_{new})$ - (Eq. 4.78)

$f(n_{min}) \leq f(n_{new})$?

YES

min_n_at_lwb = 1
upb = n_{new}

NO

min_n_at_lwb = 0
lwb = n_{min}
$n_{min} = n_{new}$
$F(n_{min}) = f(n_{new})$

K=K-1
Compute Δn - (Eq. 4.75)

$n_{new} = lwb + \Delta n$
Compute Pmax
Compute $f(n_{new})$ - (Eq. 4.76)

min_n_at_lwb =0

if ($f(n_{min}) \leq f(n_{new})$){
    lwb = n_{new};
}
else{
    minVal_at_a = 1;
    upb   = n_{min};
    n_{min} = n_{new};
    $f(n_{min})$ = $f(n_{new})$;
}

YES

min_n_at_lwb == 1?

NO

$n_{new} = upb - \Delta n$
Compute Pmax
Compute $f(n_{new})$ - (Eq. 4.76)

min_n_at_lwb =1

if ($f(n_{min}) \leq f(n_{new})$){
    ub = n_{new};
}
else{
    minVal_at_a = 0;
    lwb   = n_{min};
    n_{min} = n_{new};
    $f(n_{min})$ = $f(n_{new})$;
}

YES

K>2?

NO

END

Figure 4.10: **Flow chart for determining ideality constant *n* using Fibonacci search.**

Therefore, using the Fibonacci method, the search interval for the ideality constant n that minimizes (4.76) has been reduced to the interval $n = [1.56418, 1,56481]$. The obtained search interval is due to the interval of uncertainty of less than 10^{-3} that was selected. It should be noted that for each new ideality constant n, on Table 4.6, a new set of parameters were computed using the method in section 4.1. Therefore, given an ideality constant of $a = 1.38$, and employing the method in section 4.1, the best set of solution to minimize (4.76) is given as:

$$x = \begin{bmatrix} I_{01} \\ I_{02} \\ R_s \\ R_{sh} \\ I_{pv} \\ a \\ n \end{bmatrix} = \begin{bmatrix} 1.104\,x10^{-6}\,A \\ 2.311\,x10^{-5}\,A \\ 0.001\Omega \\ 10002.6\Omega \\ 7.92007A \\ 1.38 \\ 1.564 \end{bmatrix}, \tag{4.83}$$

In the subsequent section, the method for determining the ideality constant a which results in the optimum solution for the PV system is discussed.

4.2.2 Two-dimensional Fibonacci Parameter Search

In section 4.2.1, the Fibonacci search method was used to determine the value for the ideality constant n. However, the evaluation of (4.76) was performed under the assumption that the value for the ideality constants a was already known. In this section, the optimal value of the ideality constant a is determined using a two-dimensional Fibonacci search.

The two-dimensional Fibonacci search follows the same method described in section 4.2.1, to form a cascading search scheme. Specifically, for each selected ideality

constant a_i, which follows the same selection process as section 4.2.1, the optimal ideality constant n_i for that a_i is determined and $f(a)$ is evaluated as,

$$f(a) = |P_{max,a} - P_{max,STC}|. \tag{4.84}$$

This process is repeated until the desired interval of uncertainty is attained. For this research, the same interval of uncertainty as that of section 4.2.1 was selected.

Therefore, the process starts by defining the boundary points for the ideality constant a, which has been selected to be the same as the ideality constant n in section 4.2.1. The first set of parameters for the determination of a is given on Table 4.7.

Table 4.7: Fibonacci terms at first iteration for ideality constant a.

Variable	Value
$k =$	16
$lwb =$	1
$upb =$	2
$\Delta a_2 = 1x\dfrac{610}{1597} =$	0.382
$a_1 = lwb + \Delta a_2 =$	1.382
$a_2 = upb - \Delta a_2 =$	1.618

Next, (4.84) is evaluated using the ideality constants a_1 and a_2 to compute $(P_{max,a})$, by solving (4.74) numerically. In the evaluation of $P_{max,a}$, the corresponding optimal n values, determined in section 4.2.1, is used. As was previously stated, for these ideality constant values a_1 and a_2, the corresponding n ideality constants, n_i and n_{ii}, using section 4.2.1, are determined. These n ideality constants are the optimal n values that minimize (4.84) the most, specifically for a_1 and a_2 respectively. The evaluations of (4.84) for these ideality constants are given as

$$f(a_1) = f(1.382) = |129.782 - 130.032| = 0.2497, \tag{4.85}$$

$$f(a_2) = f(1.618) = |129.789 - 130.032| = 0.2433. \tag{4.86}$$

Comparing $f(a_1)$ and $f(a_2)$ shows the value of a_2 is closer to the desired value of a. The value of a_2 is closer to the desired value because a_2 minimizes $f(a)$ in (4.84) better than a_1 as seen in (4.85) and (4.86). Therefore, following the steps of section 4.2.1, *upb* remains unchanged while *lwb* is moved as follows:

$$lwb = a_1 = 1.382, \tag{4.87}$$

$$upb = upb = 2.0, \tag{4.88}$$

Next, a new a value is selected for evaluation and has the value

$$a_3 = upb - \Delta a_3, \tag{4.89}$$

where

$$\Delta a_3 = (2.0 - 1.382) * \frac{F_{15-2}}{F_{15}} = 0.2361. \tag{4.90}$$

Therefore, it is from the Fibonacci steps of this section that sections 4.2.1 and 4.2.2 get the a ideality constant value for evaluating (4.74). Consequently, the two sections, sections 4.2.1 and 4.2.2, form a two-dimensional Fibonacci parameter search scheme. The rest of the steps follow the description in section 4.2.1, and results in the solution sets given on Table 4.8, at each Fibonacci step.

Table 4.8: PV Parameters at each two-dimensional Fibonacci search.

k	16	15	14	13	12	11	10	⋯	2
a	1.618	1.7639	1.8541	1.9098	1.9098	1.8885	1.8754	⋯	1.8804
n	1.333	1.2166	1.07263	1.18159	1.2116	1.1408	1.0626	⋯	1.1077
I_{01}	1.15e-6	2.64E-6	1.01E-5	6.16E-6	4.57E-6	8.05E-6	1.13E-5	⋯	9.49E-6
I_{02}	4.79e-7	7.69E-8	5.99E-9	4.67E-8	7.72E8	2.28E-8	4.98E-9	⋯	1.22E-8
R_s	0.001	0.001	0.001	0.001	0.001	0.001	0.001	⋯	0.001
R_{sh}	10000.3	10044.5	10064.5	10545.9	10259.6	10250.9	10073.1	⋯	10074.3
I_{pv}	7.92007	7.92007	7.92007	7.92007	7.92007	7.92007	7.92007	⋯	7.92007
$f(a)$	0.24337	0.21367	0.06778	4.27E-4	4.27E-4	8.27E-5	4.14E-5	⋰	2.31E-5

As mentioned in section 4.2.1, this procedure has been automated using C++ an implemented within the WinIGS software. The user interface for the PV model was given in Figure 3.4. At the bottom right corner of the interface is the option: "Compute Parameters from Datasheet," which is also indicated on Figure 4.11.
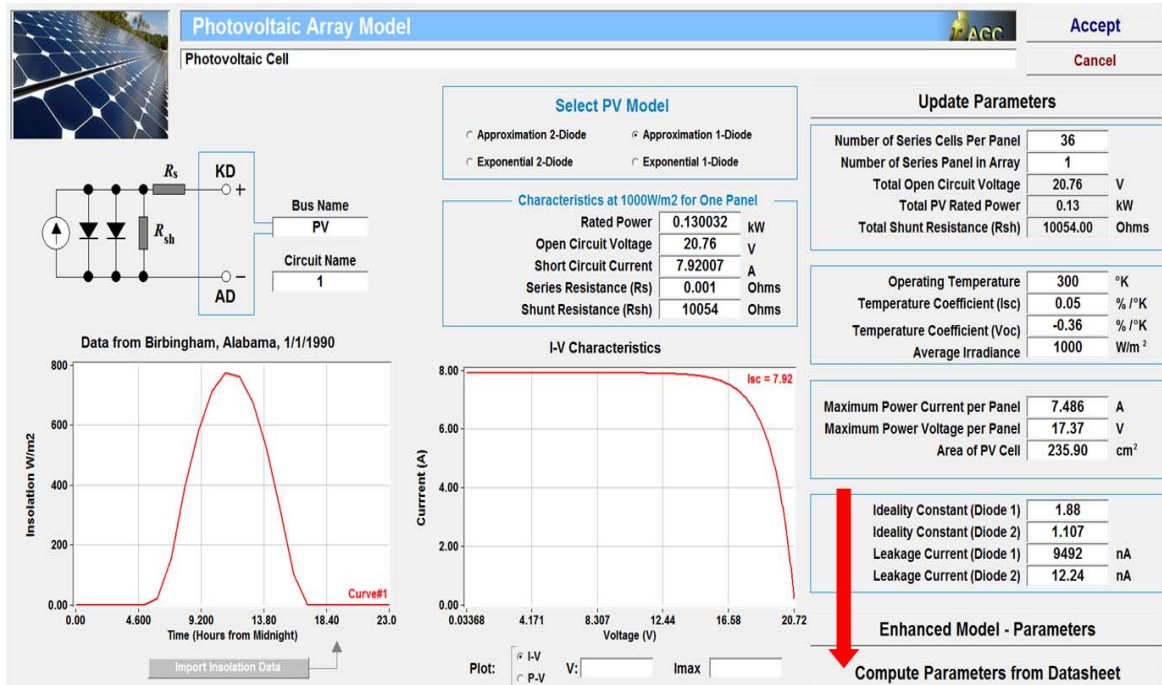
Figure 4.11: Initiation of PV parameter computation process.

Selecting this "Compute Parameters from Datasheet" option opens up an interface for entering the boundary limits for the ideality constant, the desired interval of uncertainty and initial parameter guesses as shown on Figure 4.12.

Figure 4.12: User interface for PV module parameter computation.

When the "Compute" button is selected, the procedures in sections 4.1 and 0 are initiated with the percent completion of the process displayed. When the computation process is completed, the result is shown on a message box. The message box contains the computed series resistance, shunt resistance, ideality constants, leakage currents and PV source currents. The result obtained for this research is shown on Figure 4.13.

Figure 4.13: Result of the PV module parameter computation.

From the foregoing, the optimized parameters for the PV module for this research project is given as

$$x = \begin{bmatrix} a \\ n \\ I_{01} \\ I_{02} \\ R_s \\ R_{sh} \\ I_{pv} \end{bmatrix} = \begin{bmatrix} 1.8804 \\ 1.1077 \\ 9.492424x10^{-6}\,A \\ 1.224311x10^{-8}\,A \\ 0.001\Omega \\ 10074.2596\Omega \\ 7.92007A \end{bmatrix},$$
(4.91)

which as shown on Table 4.8 has minimized (4.84) to the order of 10^{-5}. In section 4.3, the validity of this solution set is discussed.

It should be noted that the initial V_α, I_α pair selected from the measurement curve produced a computed v_{oc} value that was less than the actual v_{oc} for the PV module. Increasing the value of I_α to 5.60A, as shown on Figure 4.12, brought the computed v_{oc} value to the desired value of 20.76V.

4.3 PV Module Parameter Extraction Result

The PV modules used for this research project is the SPM 130P Solartech Power, PV modules. The PV modules are all identical and the specification of the module is given as follows:

Table 4.9:   PV module specifications

Datasheet parameter	Value
Short circuit current	7.92A
Open circuit voltage	20.76V
Maximum power point voltage	17.37V
Maximum power point current	7.49A
Rated maximum power	130W
Current temperature coefficient	0.05% / K
Voltage temperature coefficient	-0.36% / K

To see how the extracted parameters compare with the actual PV module, various measurement points were taken from one of the PV modules. The measurements were taken after connecting a resistive load across the terminals of the PV module, and varying the resistance of the load from open circuit condition to short circuit condition. The

currents and voltages for the different load values were documented. The setup for measuring voltage and current across the resistive load is shown on Figure 4.14.
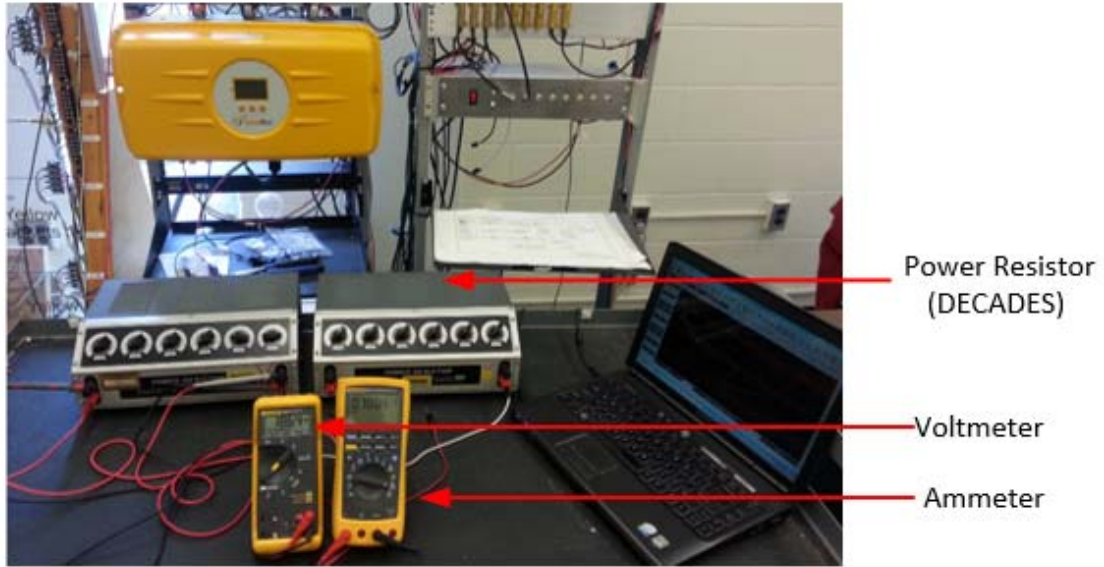
Figure 4.14: **PV voltage-current measurement setup.**

The PV module being measured was located at the roof of the engineering building and is discussed in chapter 5.

From section 4.2, the parameters for the PV module used for this project was extracted and listed on (4.91). These parameters have also been listed on Table 4.10.

Table 4.10: **Extracted PV parameters**

PV Parameters	Value
a	1.8804
n	1.1077
I_{01}	$9.492424 x 10^{-6} A$
I_{o2}	$1.224311 x 10^{-8} A$
R_s	0.001Ω
R_{sh}	10074.2596Ω
I_{pv}	7.92007A

These extracted PV module parameters are used to numerically solve the PV module equation of (4.74), also given on (4.92), for easy reference. The evaluation of (4.74) is done by varying the voltage from zero to the open circuit voltage of 20.76V.

$$
\begin{aligned}
f\left(I_{out}, v_{12}\right) = &-I_{out} + I_{pv} - I_{o1}\left[\exp\left(\frac{v_{12} + I_{out}R_s}{aNV_t}\right) - 1\right] \\
&-I_{o2}\left[\exp\left(\frac{v_{12} + I_{out}R_s}{nNV_t}\right) - 1\right] - \frac{v_{12} + I_{out}R_s}{R_{sh}} \quad .
\end{aligned}
\tag{4.92}
$$

From the numerical evaluation, the current and voltage data are used to plot the I-V and P-V curves of the PV module. The curves from the numerical evaluation are compared with the measured data from Figure 4.14. The comparison of these curves is shown on Figure 4.15 and Figure 4.16.
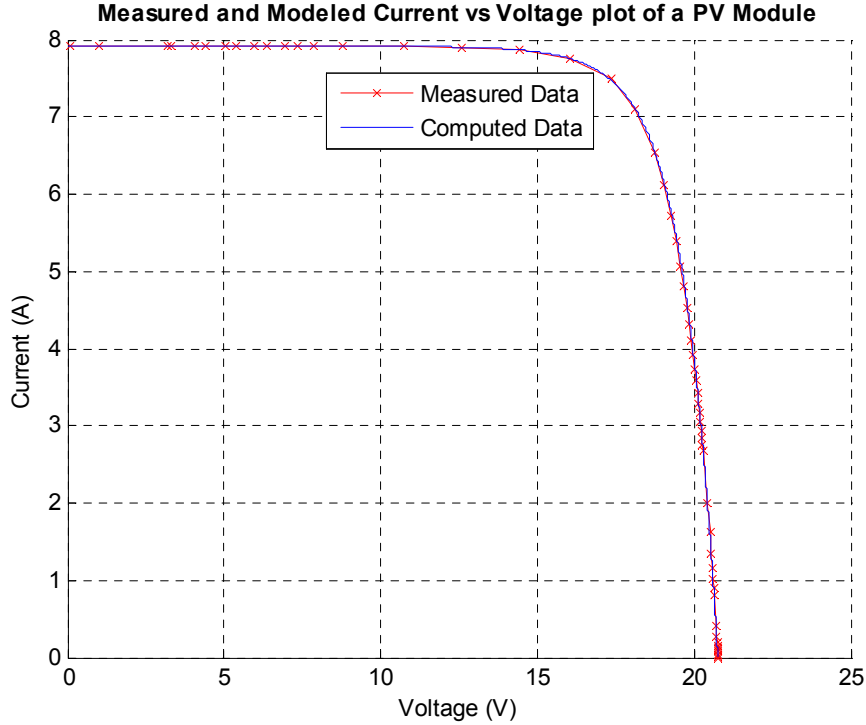
Figure 4.15:   **I-V curve comparison of PV module.**
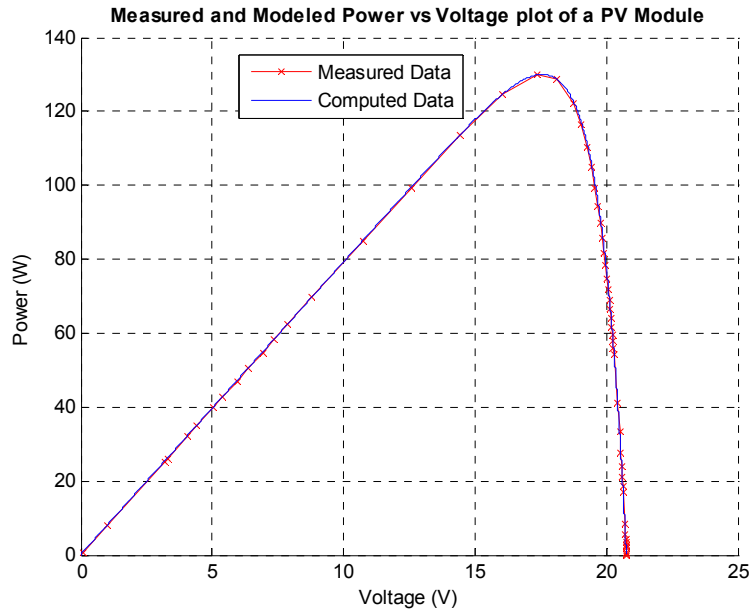
Figure 4.16: **P-V curve comparison of PV module.**

The extracted PV parameters have produced curves that match the experimental curve closely. The deviation of the computed data from the experimental data is given on Figure 4.17, and as can be seen, the highest deviation is only a few milliamps, specifically, 120mA.
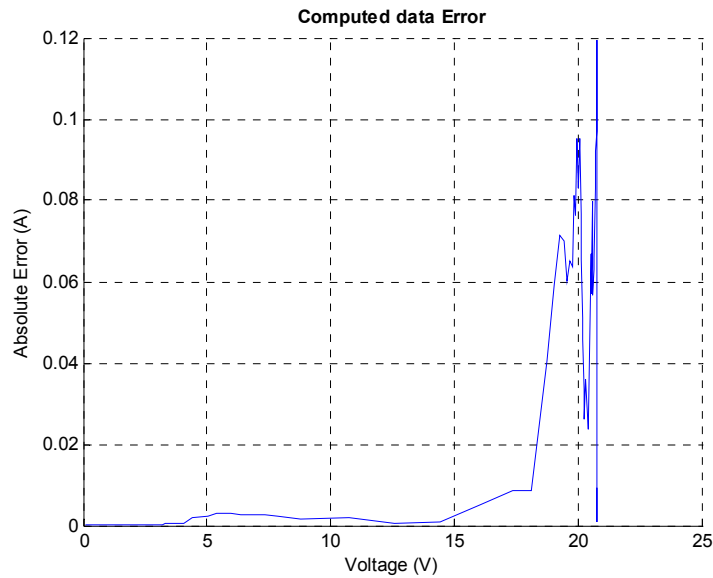
Figure 4.17: **Computed PV data error when compared to the experimental curve.**

4.4   Summary

In this chapter, the Steepest Descent and Fibonacci methods have been used to compute the parameters for the PV module. The Fibonacci search method used is a two dimensional search method. This Fibonacci search method has resulted in an optimized solution set, which are the parameters for the PV module. As confirmed on Figure 4.17, the computed PV module parameters closely match that of the actual PV module used for this research project. Therefore, these parameters are used for the protection scheme of the PV arrays, which is discussed in detail in chapter 6.

5 INTEGRATION OF PV MODEL WITH POWER SYSTEM

In this chapter, the PV array used for this research is integrated with other power system devices. The PV array protection is implemented while the PV system is connected to these other power system devices.

The PV protection algorithm used in the research protect can be applied to both a standalone and grid connected PV system. Most PV systems are interfaced with power electronic devices, storage batteries and loads. Therefore, the PV system used in this research project demonstrates the protection of the PV system in the presence of commonly used PV related power system devices.

PV arrays typically interface with other microgrid components. Therefore, under this research, PV related microgrid components, such as, the lead-acid battery; a MPPT-equipped dc-dc converter; a single-phase inverter; and an ac load have been modelled. The modeling method used, as discussed in section 3.1, is the quadratic integration modeling. The reason these additional power system equipment are modelled is to demonstrate the efficacy of the PV protection system in an actual power system installation. The models for these devices are given in Appendix A through Appendix D, and the simplified integrated system with these power system models, which are used for the numerical simulations for this research, is given on Figure 5.1.

A system similar to Figure 5.1 was designed and built for this research project. The actual installed PV array system used for this research, which is a 1.3kW, 220 volt PV system, is shown on Figure 5.2.
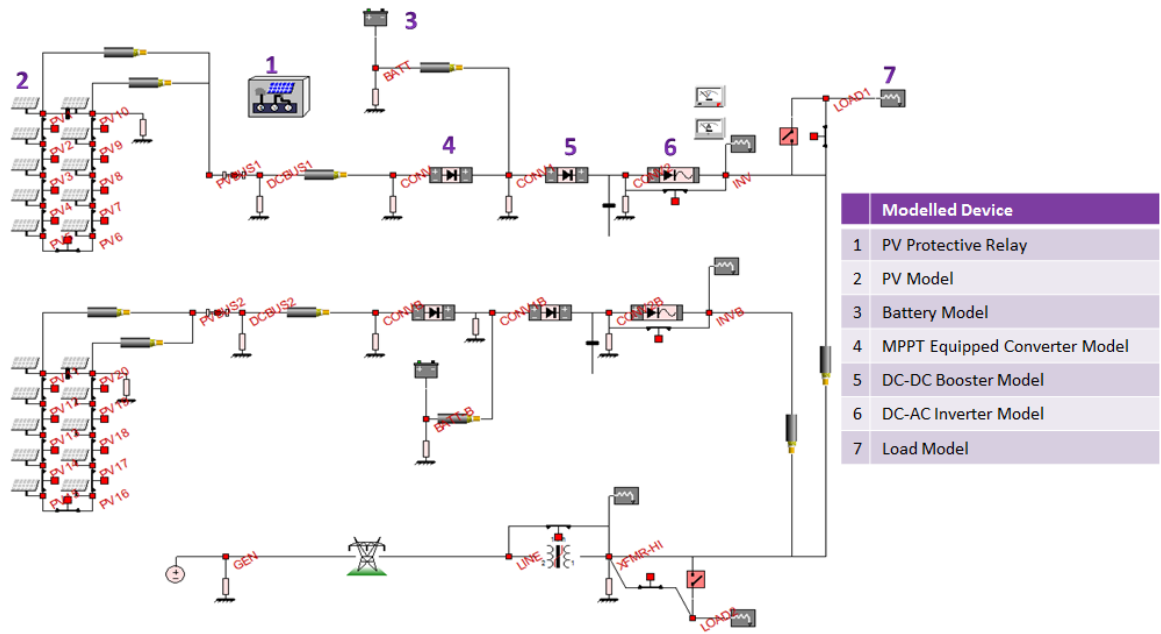
Figure 5.1: Grid-connected PV system.

|	Modelled Device
1	PV Protective Relay
2	PV Model
3	Battery Model
4	MPPT Equipped Converter Model
5	DC-DC Booster Model
6	DC-AC Inverter Model
7	Load Model

Figure 5.2: Photograph of grid-connected PV system.

Also installed are a 2kW inverter with an input voltage range of 150-1000vdc; a 1:1–230vac autotransformer; a 2kW ac load system; and hall-effect current

sensors/voltage dividers for instrumentation. These additional equipment are shown on the instrumentation rack in Figure 5.3.
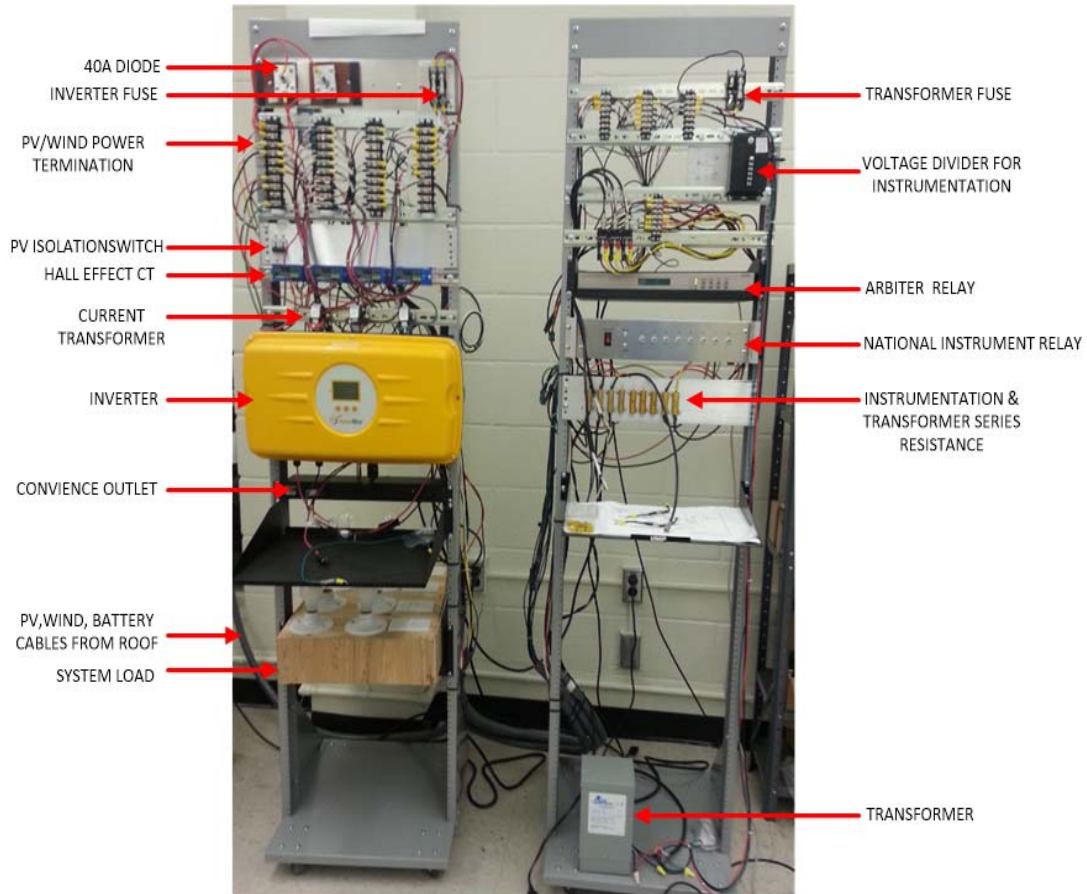
Figure 5.3: **Photograph of instrumentation rack.**

The wiring diagram showing how the hardware system is wired is shown on Figure 5.4. Although a battery system and wind turbine system were installed as shown on Figure 5.4, only the PV system was connected. The battery system was only used in the numerical simulations not on the actual experimental set-up. It is on this integrated system that the PV monitoring and protection is performed and demonstrated.
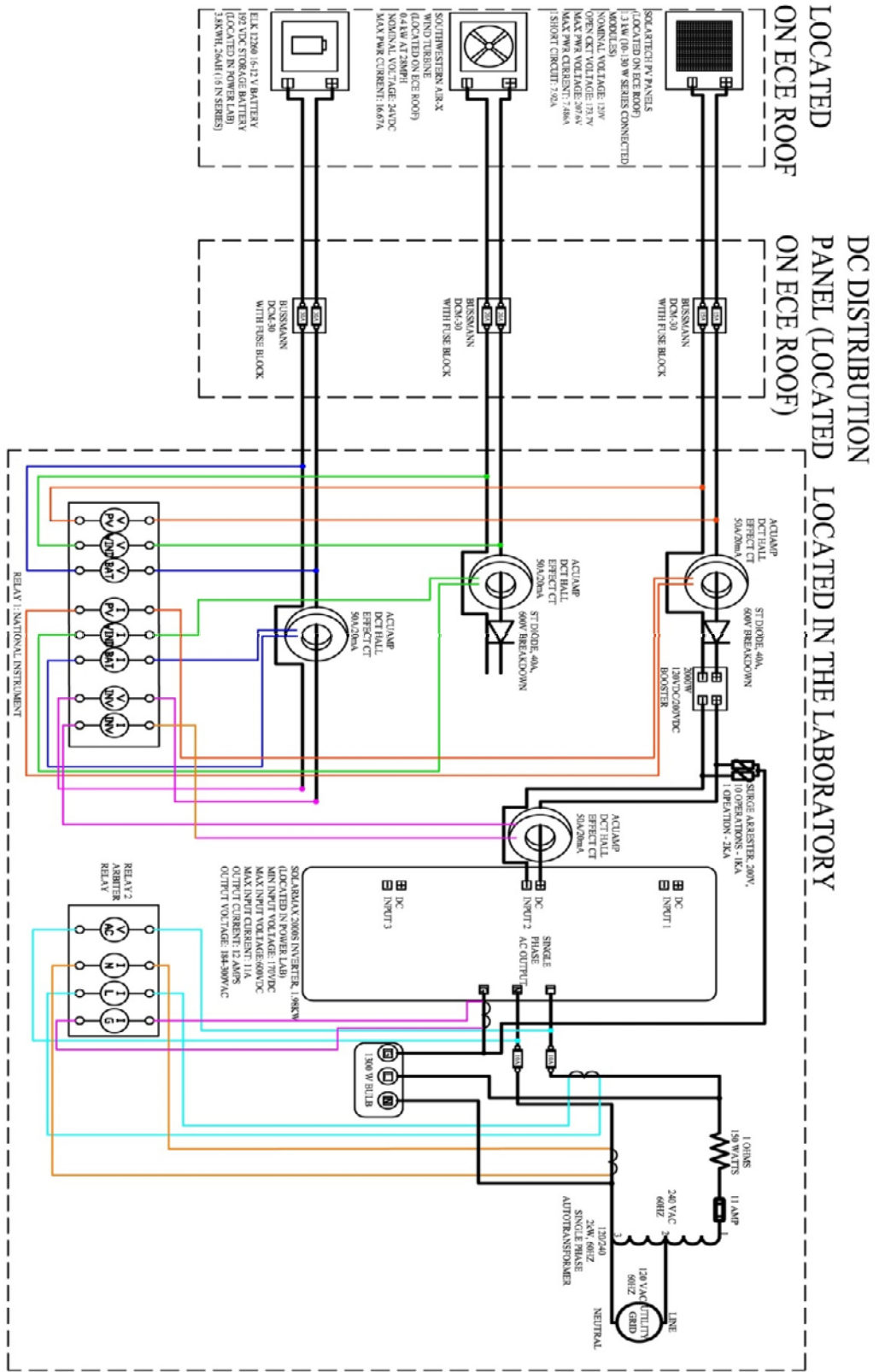
Figure 5.4: PV integration wiring diagram.

6 MODULE-LEVEL PROTECTION OF PV SYSTEMS

The objective of this research is to introduce, and demonstrate a recently developed protection algorithm [4], [33], in the PV industry. The demonstration will mark the first time this scheme is implemented in the protection of the PV array. This protection approach is applicable to any component of the microgrid, and up to the time of this research, the implementation of this scheme has been at a device level [4]. Under this research, this protection has been extended to a system level of protection, the PV array system protection.

Furthermore, in this research this secure protection scheme is implemented on the PV array using numerical simulation, and also using data from an installed PV system. In addition, this research will demonstrate that the difficulty of differentiating fault currents from load current in a PV system can be resolved by the application of this protection approach. The proposed protection approach is a dynamic state estimation-based, module-level, autonomous setting-less protection of the photovoltaic array.

An accurate model of the PV module has been developed both mathematically and in a software environment as demonstrated in chapter 3. From this model, analog data have been electronically generated in the IEEE C37.111 COMTRADE file format. These data, which are synonymous to typical data that would be collected in an electric substation, are comprised of several events. These events include a normal (no-fault) case where no fault exists in the PV array system, a high impedance fault in the PV system, and a line to line/ground fault in the PV array system. The aim of these events is to show that the setting-less protection algorithm is capable of detecting the presence of an anomaly in a PV array system. In this protection scheme, the presence of an anomaly in

the PV array system is detected by indicating a low confidence level in the estimated system state variables. Conversely, for a no-fault condition, the confidence level is maintained at a high confidence level.

The no-fault case and other event conditions were used for the initial debugging of the protection scheme. Upon confirmation of the proper functionality of the protection scheme, raw data from the microgrid system installed on the roof of the electrical engineering building at Van Leer, Georgia Tech, was used to validate the developed protection algorithm. This is the PV array system discussed in chapter 5 and shown on Figure 5.2. The numerical evaluation of this algorithm is covered in chapter 7. The evaluation using raw data from an actual PV installation is covered in chapter 8.

6.1   Module-level Setting-less Protection of PV Array

To perform the setting-less protection of the PV array, some data measurements are required. These measurements fall under two categories namely: across variables and through variables, and will serve as inputs for the protection algorithm as shown on Table 6.1.

Table 6.1:   PV module across and through variables.

Across Variables	Through Variables
$v_1 = PV\ positive\ terminal\ voltage$	$i_1 = PV\ positive\ terminal\ current$
$v_2 = PV\ negative\ terminal\ voltage$	$i_2 = PV\ negative\ terminal\ current$

The PV array used for this research project has current and voltage sensors for the overall PV installation, that is, at the terminals where the PV array connects to the other power system devices. However, for the module-level protection, current and voltage sensors for

each PV module could be used if available, which has been addressed in the numerical

simulations of chapter 7. In the absence of the additional voltage measurements for the

individual PV modules, the voltage at each PV system node can be determined by state

estimation. Using the data measurements from the sensors connected to the PV array, a

DSE is performed. A list of the parameters to be estimated from state estimation is listed

on Table 6.2, and some of these state variables are identified on Figure 6.1.
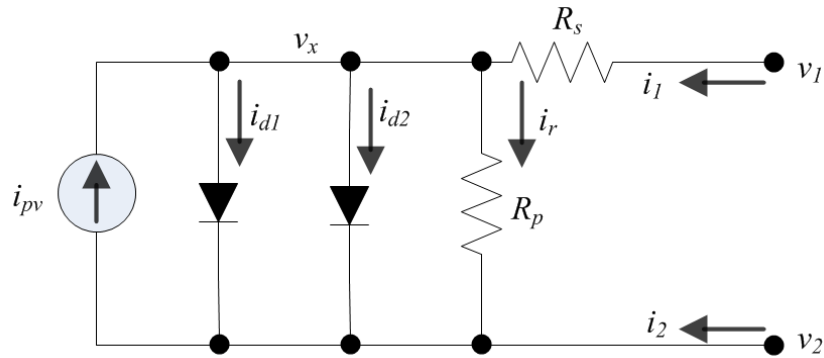
Figure 6.1:   **Schematic for photovoltaic module.**

Table 6.2:   **Estimated state variables from state estimation.**

State Variable	Definition of State Variable
v_1	*PV positive terminal voltage*
v_2	*PV negative terminal voltage*
v_x,	*PV internal voltage (internal state variable)*
$c_1, \lambda_1, \gamma_1, \alpha_1, \alpha_2, \alpha_3, \alpha_4, y_1, y_2, y_3, y_4, y_5,$ $d_1, \lambda_2, \gamma_2, \beta_1, \beta_2, \beta_3, \beta_4, z_1, z_2, z_3, z_4, z_5$	*Internal state variable*

The added benefit of this state estimation-based approach is that internal quantities such as the PV internal voltage, which is usually not provided on the manufacturer's datasheet, can be estimated. Therefore, the estimation of these parameters offers more data that can be used either for protection purposes or for PV array system alarms.

6.1.1 Setting-less Protection of PV Array

This setting-less protection algorithm, a recently developed protection scheme, is new in the protection of PV array. The protection scheme uses DSE as a core part of its functionality. DSE, which is discussed in section 6.1.2, uses the dynamic (time-domain) model of the PV modules. Therefore, the setting-less protection requires an accurate PV model for the DSE to be accurately performed. After DSE of the PV module, a decision is made to trip the PV system for conditions that are not consistent with the device model of the PV.

An overview of the setting-less protection scheme is described on Figure 6.2. From the instrumentation devices, the terminal voltage of the PV system is obtained. This terminal voltage is filtered using DSE on a real-time basis, which yields the real-time operating condition of the PV system.
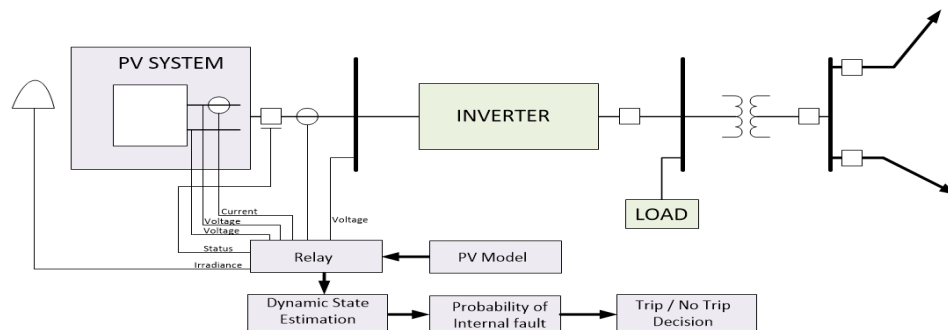
Figure 6.2: **Setting-less component protection scheme.**

After estimating the system state variables, a chi-square test is performed to determine how close the measured data matches the model of the PV system. The result from the chi-squared test is the confidence level or the goodness-of-fit of the PV model to the measured data. The chi-squared test essentially determines the health of the PV system. If the PV system is operating within the confines of its model, then a high confidence level is obtained from the chi-squared test. On the contrary, if the estimated state variable is not consistent with the PV model, the chi-squared test will result in a low confidence level. This low confidence level indicates there is an anomaly in the PV array system. Therefore, a trip signal is issued to isolate the PV system, and an alarm is issued to inform the PV system operator of an event in the PV array system.

The setting-less protection method only trips during anomalies, therefore, the security of the PV system is not compromised. Besides, there is no current magnitude operating setting for this algorithm, contrary to the practice with traditional protection devices. Therefore, human error during the setting procedure is eliminated. The elimination of human error further improves the reliability of this protection algorithm.

The DSE implemented in this research has a standard quadratized algebraic companion form (Q-ACF) which was derived in chapter 3, and also given in (6.1) and (6.2) as

$$\begin{bmatrix} i(t) \\ 0 \\ i(t_m) \\ 0 \end{bmatrix} = Y_{eq} \begin{bmatrix} v(t) \\ y(t) \\ v(t_m) \\ y(t_m) \end{bmatrix} + \begin{bmatrix} v(t) \\ y(t) \\ v(t_m) \\ y(t_m) \end{bmatrix}^T F_{eq} \begin{bmatrix} v(t) \\ y(t) \\ v(t_m) \\ y(t_m) \end{bmatrix} - B_{eq}, \tag{6.1}$$

where

$$B_{eq} = N_{eq} \begin{bmatrix} v(t-h) \\ y(t-h) \end{bmatrix} + M_{eq} \begin{bmatrix} i(t-h) \\ i(t-h) \end{bmatrix} + k_{eq}. \tag{6.2}$$

In (6.1), $i(t)$ and $i(t_m)$ are the computed current at time steps t and t_m respectively, where one integration time step is h. This means the previous integration time step is given by $(t - h)$ as shown in (6.2). The quantity, $i(t_m)$, is the current at the midpoint of an integration time step t_m, given as $(t - h/2)$. The state variables, $v(t)$ and $y(t)$, are the across and internal state variables respectively, at time t. The terms: Y_{eq}, N_{eq} and M_{eq} are coefficient matrices, while the F_{eq} accounts for the non-linear, quadratic portion of the PV array model. In this model, there are no N_{eq} and the M_{eq} terms. The only term that is applicable is the K_{eq} term. Therefore, in this research, $B_{eq} = K_{eq}$ accounts for the constant terms of the PV array model. As was discussed in chapter 3, this numerical integration method assumes that the integrated function varies quadratically within an integration time step.

6.1.2   PV Module Setting-less Protection Methodology

The setting-less protection of the PV method uses data measurements such as PV voltage and current from the PV instrumentation devices. As was listed on Table 6.1, the data measurements are categorized under across and through variables. For each data measurement z_i, there is a mathematical equation $h(x)_i$ that defines that data measurement as a function of the state variables, where i is the ith measured data. These mathematical equations, $h(x)_i$, are the same equations that formed the model of the PV module. Hence, this protection method is a model-based protection method. The

measurements, *z*, can be grouped into three measurements, namely, actual measurements; pseudo measurements; and virtual measurements. These measurement groups are described next, and a partial listing of the measurements for the model used in this research, that of section 3.2.2.4 are listed by group in Table 6.3. A complete listing of the data measurement can be found in Appendix E.

Actual Measurement:

These are measurements that are measured directly from the PV module, namely, the terminal voltage of the PV and the current entering/leaving the PV module terminals. For this research, the measurement standard deviation error for this measurement is assumed to have a small value of 0.01 per unit (p.u), but this value could be larger if the instrumentation device for the data measurement has a low accuracy class.

Pseudo measurements:

These are measurements that can be derived after obtaining other measurements. For example, upon measuring the current that is flowing out of the positive terminal of a PV module, it can be assumed that the same current magnitude is flowing into the negative terminal. Therefore, the negative terminal current is considered a pseudo measurement. The pseudo measurement standard deviation error is assumed to have a larger value of 0.1 p.u compared to the actual measurements.

Table 6.3: **Classification of PV data measurements for a PV module[1].**

			Actual Measurements; standard deviation = 0.01 per unit (p.u.)
$z_1(t) =$	$h_1(x) =$		$v_1(t) - v_2(t) + \eta_1(t)$
$z_2(t) =$	$h_2(x) =$		$v_1(t_m) - v_2(t_m) + \eta_2(t_m)$
$z_3(t) =$	$h_3(x) =$	$i_1(t)$	$= G_s v_1(t) - G_s v_x(t) + \eta_3(t)$
$z_4(t) =$	$h_4(x) =$	$i_1(t_m)$	$= G_s v_1(t_m) - G_s v_x(t_m) + \eta_4(t_m)$
			Pseudo Measurements; standard deviation = 0.1p.u.
$z_5(t) =$	$h_5(x) =$	$i_2(t)$	$= -G_s v_1(t) + G_s v_x(t) + \eta_5(t)$
$z_6(t) =$	$h_6(x) =$	$i_2(t_m)$	$= -G_s v_1(t_m) + G_s v_x(t_m) + \eta_6(t_m)$
			Virtual Measurements; standard deviation = 0.001p.u.
$z_7(t) =$	$h_7(x) =$	0	$= -G_s v_1(t) - G_{sh} v_2(t) + (G_{sh} + G_s) v_x(t) + I_{o1}\left[c_1^2(t) - 1\right]$ $+ I_{o2}\left[d_1^2(t) - 1\right] - i_{pv} + \eta_7(t)$
$z_8(t) =$	$h_8(x) =$	0	$= -c_1(t) + \alpha_4^2(t) + \eta_8(t)$
$z_9(t) =$	$h_9(x) =$	0	$= -\alpha_4(t) + \alpha_1(t)\alpha_3(t) + \eta_9(t)$
$\vdots$	$\vdots$	$\vdots$	$\vdots$
$z_{37}(t) =$	$h_{37}(x) =$	0	$= -\alpha_1(t_m) + \gamma_1^2(t_m) + \eta_{37}(t_m)$
$z_{38}(t) =$	$h_{38}(x) =$	0	$= -\gamma_1(t_m) + 1 + \lambda_1(t_m) + \dfrac{y_1(t_m)}{2!} + \dfrac{y_2(t_m)}{3!} + \dfrac{y_3(t_m)}{4!} + \dfrac{y_4(t_m)}{5!} + \dfrac{y_5(t_m)}{6!}$ $+ \dfrac{y_2(t_m)y_3(t_m)}{7!} + \dfrac{y_2(t_m)y_4(t_m)}{8!} + \dfrac{y_2(t_m)y_5(t_m)}{9!} + \dfrac{y_3(t_m)y_5(t_m)}{10!}$ $+ \dfrac{y_4(t_m)y_5(t_m)}{11!} + \eta_{38}(t_m)$
$\vdots$	$\vdots$	$\vdots$	$\vdots$
$z_{56}(t) =$	$h_{56}(x) =$	0	$= z_1(t_m)z_3(t_m) - z_5(t_m) + \eta_{56}(t_m)$

[1] The complete list of data measurements is shown in Appendix E.

<u>Virtual measurements:</u>

The virtual measurements are the measurements that are not measured but are expected to be zero. For example, from the developed PV model, the virtual measurements correspond to the zeros on the left hand side of (6.1). These virtual measurements are listed in Appendix E. The measurements in this category have the least standard deviation as compared to the previously discussed actual and pseudo measurements. The assumed standard deviation error for the virtual measurements is 0.001pu.

As previous discussed, the approach for this protection is state estimation-based, and uses the weighted least squares method, which has a cost function as shown in (6.3),

$$Minimize\ J(x) = \sum_{i=1}^{m} \left(\frac{h_i(x) - z_i}{\sigma_i} \right)^2, \tag{6.3}$$

where z_i, $h_i(x)$, and σ_i are the data measurements; mathematical equations that defines the data measurements; and the standard deviation of the data measurements; respectively. These measurements are also shown in Appendix E. Equation (6.3) can be rewritten in a more compact form as given in (6.4).

$$J(x) = \left[h(x) - z \right]^T W \left[h(x) - z \right], \tag{6.4}$$

where

$$W = diag \left\{ \frac{1}{\sigma_1^2}, \frac{1}{\sigma_2^2} \cdots \frac{1}{\sigma_{m-1}^2}, \frac{1}{\sigma_m^2} \right\}.$$

The $h_i(x)$ equations which are made up of the PV mathematical model, as shown in Appendix E, are for one PV module. However, in this research, the PV array that is used is comprised of 10 series connected PV modules. In a larger PV array a lot more

interconnections of various PV modules are typical. Therefore, in the protection of the entire PV array, the $h(x)$ equations of Appendix E become system equations and have the form given in (6.5)

$$h_0(x(t)) = x_{1,0}(t) - x_{1,10}(t),$$

$$h_1(x(t)) = x_{2,1}(t) - x_{2,10}(t),$$

$$\vdots$$

$$h_{24}(x(t)) = i_1(t) = G_s x_{1,0}(t) - G_s x_{1,12}(t),$$

$$h_{25}(x(t)) = -G_s x_{1,0}(t) + G_s x_{1,12}(t) + G_s x_{2,1}(t) - G_s x_{2,38}(t),$$

$$\vdots$$

$$h_n(x(t)) = -G_s x_{i,a}(t) - G_{sh} x_{i,b}(t) + (G_{sh} + G_s) x_{i,c}(t) + I_{o1}\left[x_{i,d}(t)^2 - 1\right] + I_{o2}\left[x_{i,e}(t)^2 - 1\right] - i_{pv},$$

(6.5)

where given $x_{i,j}$, x is the state variable, i is the PV module number, and j is the global index of the state variable as was formulated in section 3.4 and [28]. Equation (6.5) can be written in a matrix form as follows:

$$\begin{bmatrix} h(x)_1 \\ \vdots \\ h(x)_n \end{bmatrix} = \begin{bmatrix} & H & \end{bmatrix} x.$$

(6.6)

Expanding (6.4) gives

$$J(x) = x^T H^T W H x - x^T H^T W z - z^T W H x + z^T W z.$$

(6.7)

The gradient of (6.7) is given as

$$\nabla J(x) = 2H^T W H x - H^T W z - z^T W H$$

$$= 2H^T W H x - 2H^T W z,$$

(6.8)

and by minimizing the objective function of (6.3), (6.8) becomes zero. Let $g(x)$ be a function that that represents the minimized cost function given in (6.9).

$$g(x) = H^T W H x - H^T W z. \tag{6.9}$$

Differentiating (6.9) gives

$$g'(x) = H^T W H, \tag{6.10}$$

therefore, given a previous state variable x, the current state variables can be computed by using Newton Raphson approach as given in (6.11).

$$x = x_{previous} - \frac{g(x)}{g'(x)}. \tag{6.11}$$

Substituting the values of $g(x)$ and $g'(x)$ in (6.11) gives the iterative algorithm of determining the state variables of the PV system as given in (6.12).

$$x = x_{previous} - [H^T W H]^{-1}[H^T W (h(x) - z)]. \tag{6.12}$$

Equation (6.12) can also be written as

$$x^{c+1} = x^c - \left(H^T W H\right)^{-1} H^T W \left(h(x^c) - z\right), \tag{6.13}$$

where x^c is the state variable that is currently estimated and x^{c+1} is the next state variable set to be estimated. The H matrix in equation (6.6) is the Jacobian matrix and is computed as shown in equation (6.14).

$$H = \frac{dh(x)}{dx}, \quad computed \ at \ x = x^c. \tag{6.14}$$

Therefore, for the PV model, the H matrix is derived by taking the derivative of the $h(x)_i$ function listed on Appendix E, w.r.t the corresponding state variable. The PV module has a non-linear model, therefore, the H matrix is a function of some state variables. This

means, the H matrix will need to be updated for each analyzed data. Consequently, the contribution of each data measurements to the information matrix $H^T W H$, and vector matrix $H^T W(h(x^c) - z)$ are computed at every time step of the state estimation algorithm.

To form the weight matrix W, the corresponding standard deviations for each group of data measurement, as shown in Appendix E, is converted to the real values and used to form an $m x n$ diagonal matrix. For this diagonal matrix, m is the number of data measured from the PV array system, such as the PV terminal voltage and current, and n is the number of state variables. An m value of 544 is used for this research for the entire PV array system, while the number of state variables (n) for the PV array is 522. The number of state variables is comprised of the state variables at time t, (261 states), and time t_m (261 states), forming 522 state variables. The value for m and n for the individual PV modules are a lot less, with an m value of 28, and n value of 27. In the formulation of the system model, system nodes that are common to two PV modules are counted as one node as illustrated with the two PV modules example of section 3.4 and [28].

Next, a chi-square (goodness of fit) test is performed on the estimated variables. This chi-square test shows the probability that the distribution of the errors from data measurements are within the expected bounds. The degree of freedom for the chi-squared distributed variables is given as

$$v = m - n,$$ (6.15)

where

m = number of data measurements for the PV model = 544, and

n = number of state variables for the PV model = 522.

Furthermore, assuming a normalized residual s_i, the postulation used for this research project is that s_i is Gaussian distributed with a zero mean and standard deviation of 1. Also, the least squares solution minimizes the sum of the squares of s_i, meaning, any other set of state variable vector will be larger in value than the accurate state variable vector. That is, given a state variable χ^2

$$\sum_{i=1}^{m} s_i^2 = \chi^2 \geq \varsigma, \tag{6.16}$$

where s_i is the normalized residue, and

$$\varsigma = \sum_{i=1}^{m} s_i^2(\hat{x}). \tag{6.17}$$

The probability that the event $\chi^2 \geq \varsigma$, is given in equation (6.18).

$$\Pr\left[\chi^2 > \varsigma\right] = 1.0 - \Pr\left[\chi^2 \leq \varsigma\right] = 1.0 - \Pr(\varsigma, \nu). \tag{6.18}$$

This probability in equation (6.18) is used to determine if the residuals s_i are distributed within the expected boundary. A high probability implies that the residuals are within the expected boundary, and therefore, has a high confidence level. On the contrary, if equation (6.18) yields a low probability, then the residuals are higher than the expected statistical value, meaning the result has a low confidence level.

From the foregoing, the data-flow procedure in Figure 6.3 is used to compute the confidence level.
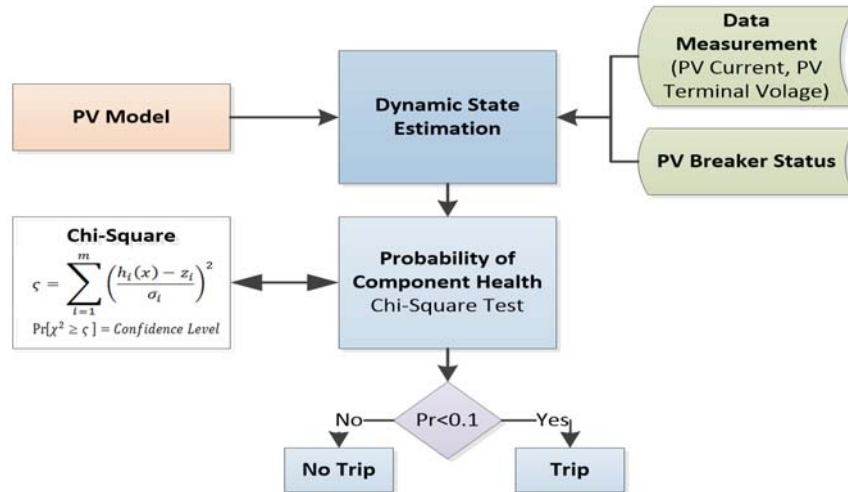
Figure 6.3:   **Logic for confidence level computation.**

Given the PV model and measured data, and assuming the PV breaker status is a one, indicating that the PV is energized and supplying power to the system; a dynamic state estimation is performed using the procedure previously outlined. After the state estimation is performed, a set of state variable for the entire PV system is obtained. Using the Chi-squared test, the probability that the estimated data are valid is determined. This process is repeated for each sampled data measurement.

From the computed confidence level, the setting-less relay makes tripping decision. For this research, a confidence level below 0.1 is considered low at which time a PV trip command, or alert to the PV operator, would be issued. If there are bad data measurements, a low confidence level for two integration time steps could be obtained which then returns to the normal case of high confidence level. The setting-less relay is designed to trip only after a low confidence level has been attained for more than a predetermined duration. Therefore, the relay does not trip the PV system for bad or transient data. This procedure is performed in sets of two data measurements at a time,

times t and t_m, as shown in (6.1). A summary of the procedure for performing the model-

based, module-level protection of the PV array is shown on Figure 6.4.
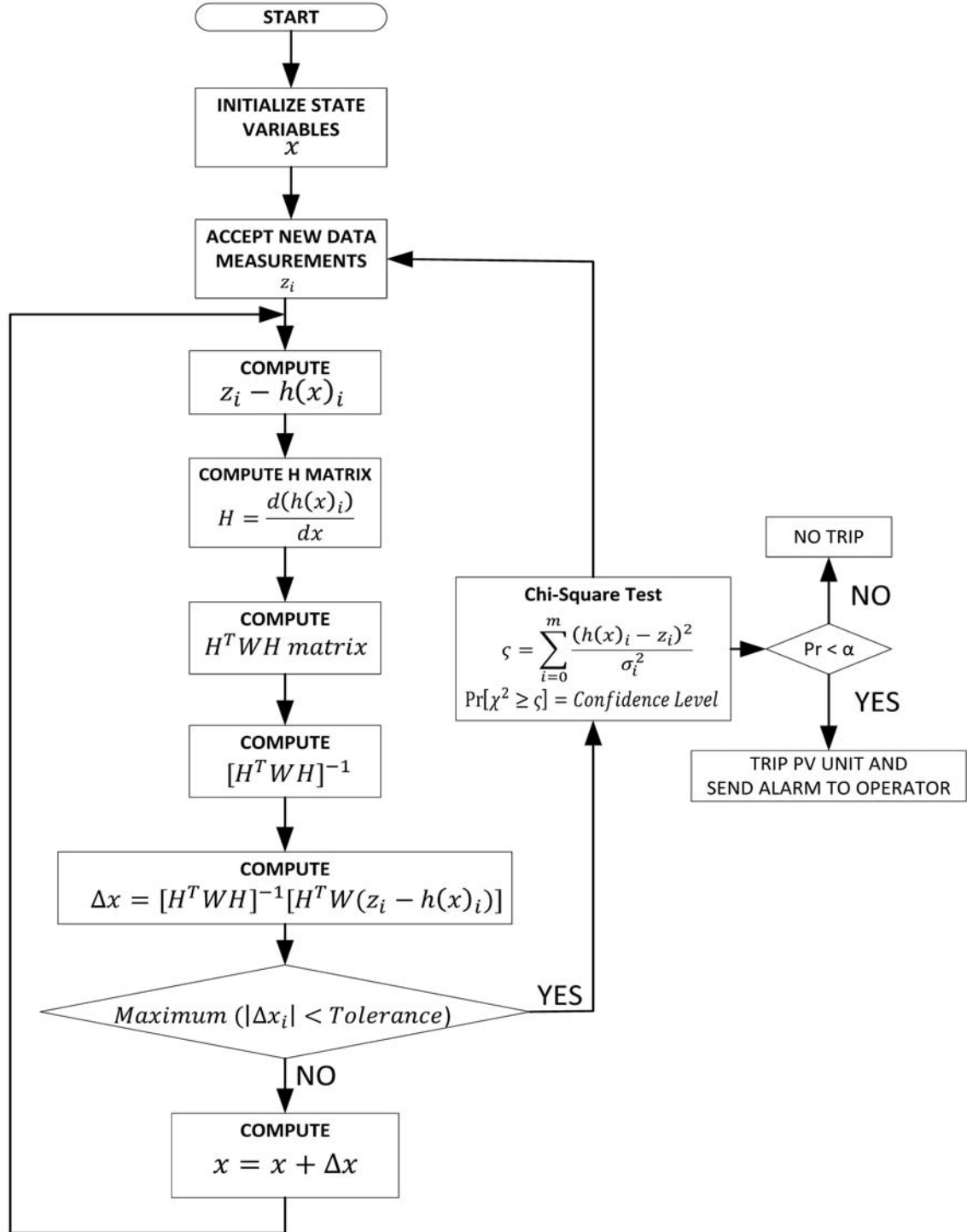
Figure 6.4: **Logic flow for PV array protection.**

6.2　Summary

In this chapter the steps for performing the module-level state estimation-based protection of the PV array has been formulated and discussed. These steps serve as the guideline for the implementations/demonstrations in the subsequent chapters. By using the protection scheme outlined in this chapter, various PV faults are identified. The PV fault conditions are covered in chapters 7-9. The ability to identify these anomalies in the PV array system is instrumental in the PV industry, because of the similarity between the load and fault current magnitudes of the PV array system.

7 DEMONSTRATING EXAMPLE: PV ARRAY PROTECTION

USING NUMERICAL SIMULATIONS

From the algorithm described in chapter 6, the setting-less relay for protecting the PV array system has been developed. The power system network modeled in this chapter is a system of four substations, each comprised of 1.3kW PV array, a storage battery unit, a dc-dc converter, a dc-ac inverter, and system loads switching off and on at different times. The four substations are tied together via a transmission network, to a synchronous generator. The interconnections between these systems are shown on Figure 7.1, which is an extension of the system shown on Figure 5.1.

As shown on Figure 7.1, each substation has a set of PV array, which is comprised of several PV modules. The method described in section 3.4 was used to form the integrated model for the entire PV system on a substation basis. In this chapter, one substation is used to demonstrate the protection algorithm discussed in chapter 6.
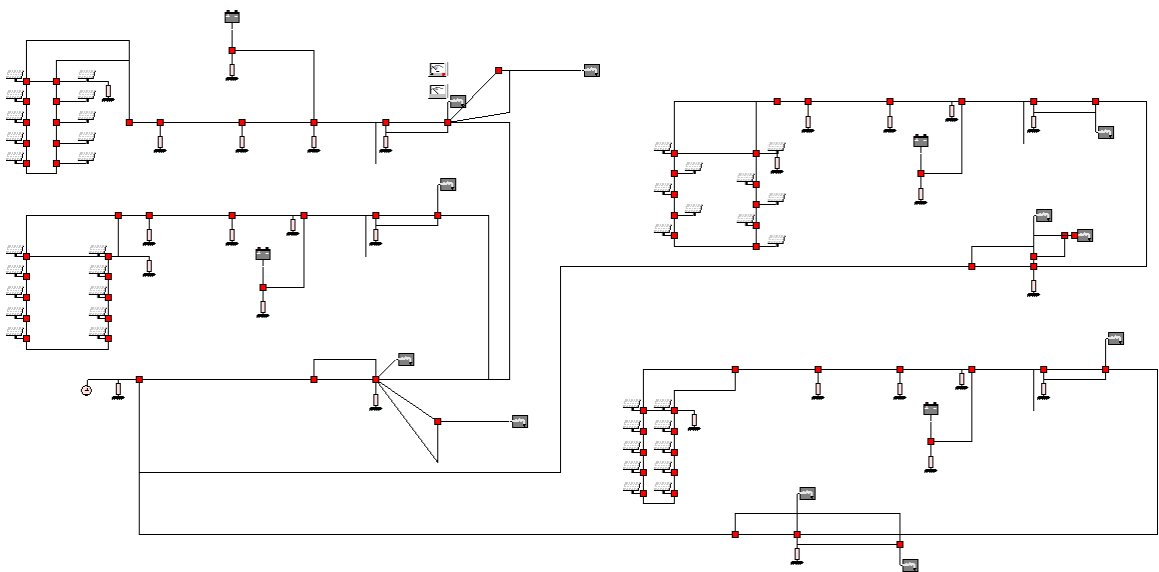
Figure 7.1: **Grid-connected PV array system.**

The objective of this chapter is to show that the proposed protection method is an effective method for protecting PV array systems in the presence of varying temperature, changing solar irradiation, and other transients that PV systems are typically subjected to. The algorithm in chapter 6 has been used to develop a software-based relay which is used to demonstrate the protection of the PV system. The basic interface for the PV setting-less relay is given in Figure 7.2, and does not have any plots as the protection of the PV has not been initiated.
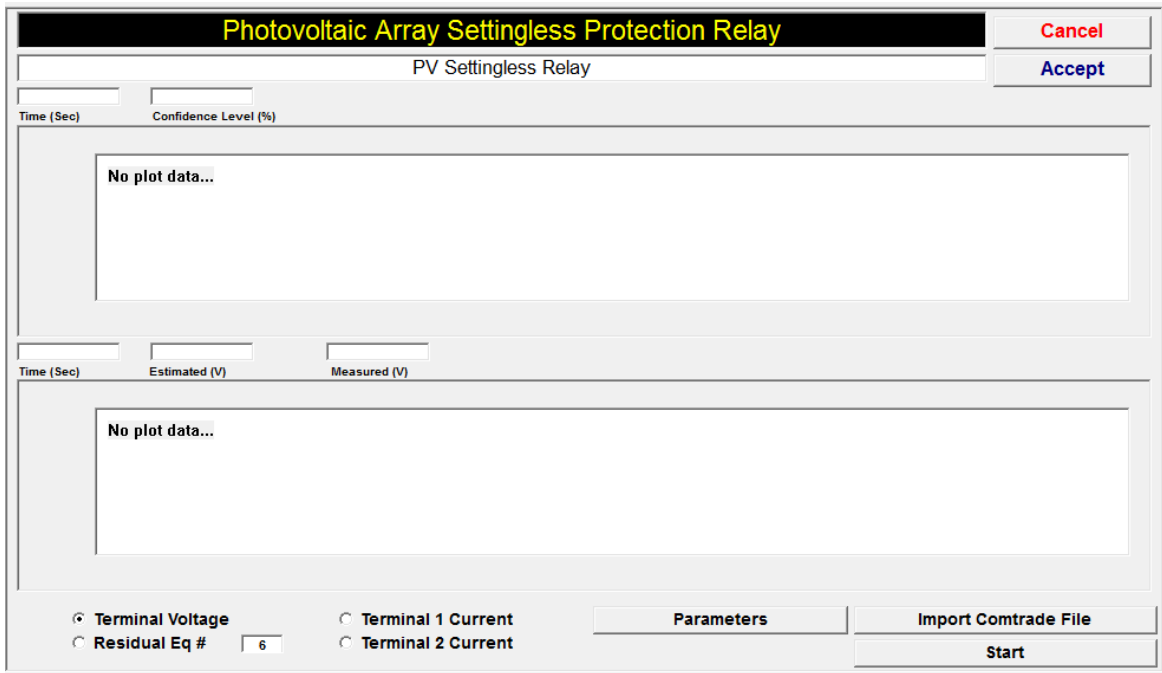
Figure 7.2:   Interface for the setting-less relay for the PV array system.

Before operating the setting-less relay, the information about the protected PV system is required. This information is entered by selecting the "Parameters" button on bottom right of Figure 7.2. The interface that comes up from selecting the "Parameters" button is shown on Figure 7.3,

Figure 7.3: Parameter interface for PV array setting-less relay.

where the parameters such as the base PV voltage, current and power are entered by the user. The base quantities as shown on Figure 7.3 are set at the open circuit voltage, short circuit current and PV module power ratings respectively. Furthermore, the resistances and the other PV module parameters are entered based on the extracted PV module parameters discussed in chapter 4.

7.1 Normal PV Array Operating Conditions with Constant Temperature and Irradiance

The normal operating condition of the PV system in Figure 7.1 was simulated, and the currents and voltages at each node of the PV array were measured and stored in COMTRADE format. The voltmeters and ammeters used for these measurements are shown on Figure 7.4, and these meters are representative of actual potential measuring devices and Hall Effect current sensors used on physical PV array systems. The data measurements for these numerical simulations are comprised of actual measurements, such as the PV array terminal and node voltages and the terminal currents.

111
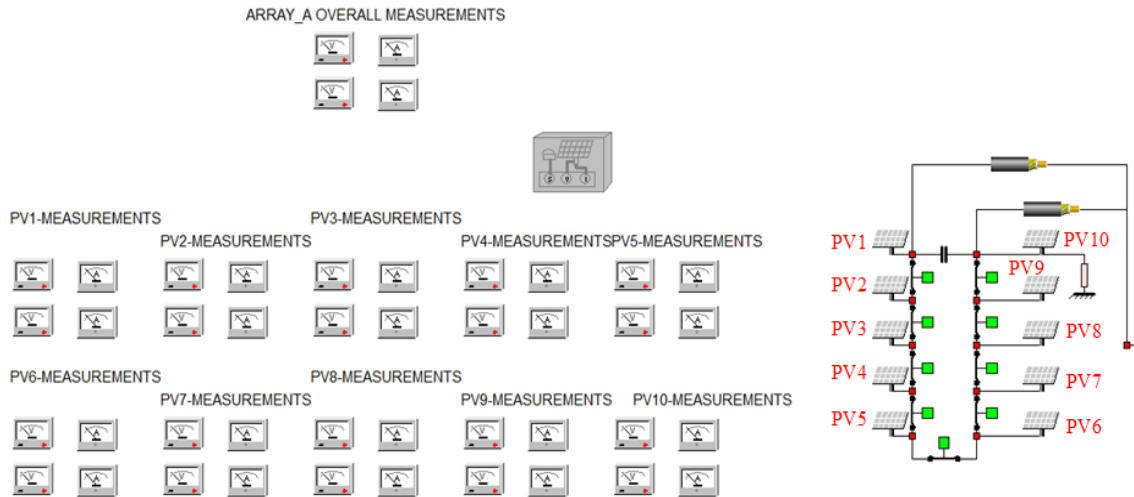
Figure 7.4: Measuring devices for each PV module in the PV system of one substation.

The data measurements are also comprised of the virtual measurements, such as the internal PV module equations, (3.89) – (3.112), and the algebraic sum of currents at the PV array nodes. In the absence of dedicated current sensors for the PV negative terminal, which is not the case for the simulations in this chapter, pseudo measurements are used as shown on Table 6.3. For the measurements in these numerical simulations, the assigned standard deviations for the weight of (6.4) are given on Table 7.1.

Table 7.1: Assigned standard deviation for data measurements.

Data Measurement	Assigned standard deviation
PV Terminal and node voltages	0.1
PV terminal currents - (3.86),(3.87)	0.1
Algebraic sum of node currents	0.01
Current virtual measurement - (3.88)	0.01
All other virtual measurements (3.89)-(3.112)	0.05

These data measurements, which were stored in COMTRADE format, are then imported to the PV setting-less protection relay. The measurement import is performed by selecting the 'Import Comtrade File' button at the bottom right of Figure 7.2. Next, the protection is initiated by selecting the 'Start' button. For this normal-operating-condition case, the numerical simulation result on Figure 7.5 was obtained.
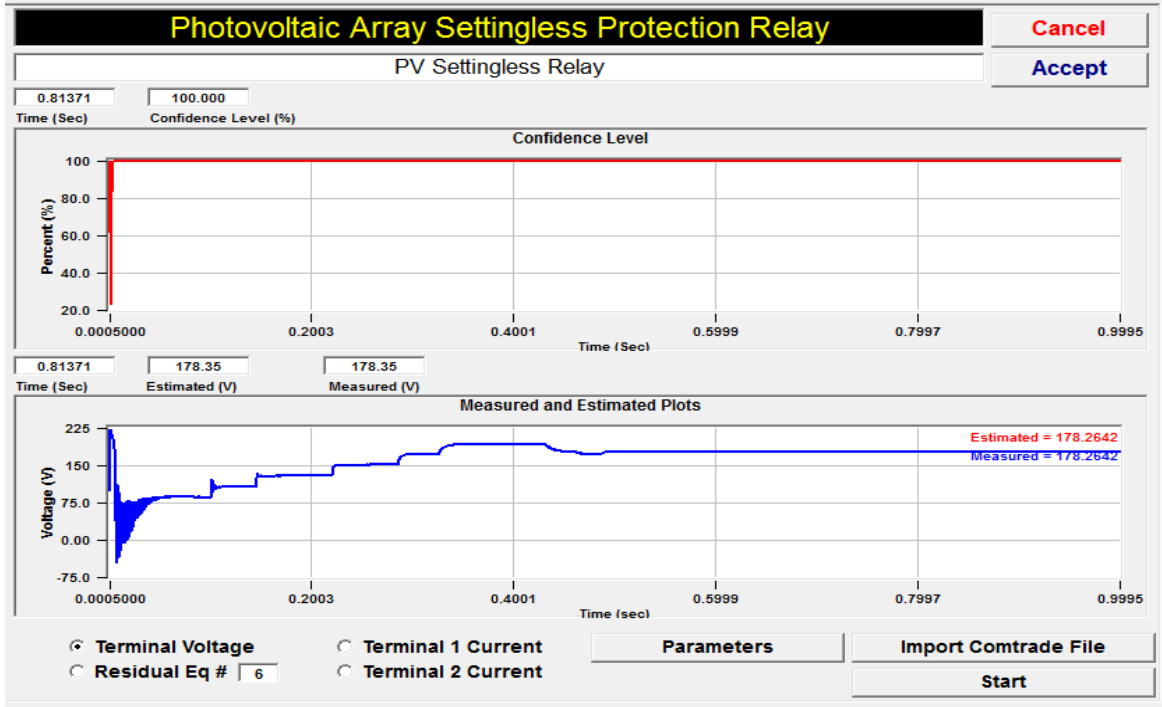
Figure 7.5: **Simulation result for normal operating condition of the PV array system.**

The PV system undergoes a temporary transient once connected to the power system as shown on Figure 7.5. This transient is due to the parasitic capacitance of the PV array system. This capacitance is accounted for by the addition of a capacitor at the terminals of each PV array system on Figure 7.1. Moreover, once the PV system is energized, the MPPT algorithm in the dc-dc booster begins seeking the optimum operating point for the PV array. The operation of the MPPT algorithm accounts for the change in voltage levels in Figure 7.5. As the voltage level changes, the PV system

113

gradually approaches its optimum operating point. The operation of the MPPT algorithm used for this protect is discussed in Appendix B.4.2.

7.2 Normal PV Array Operating Conditions with Changing System Conditions

In Figure 7.5, the temperature and irradiance on the PV system were held constant, however, in a PV array system, it is normal for the temperature and irradiance to vary over time. To simulate this condition, the temperature and insolation on the PV system were varied at four different intervals. The PV system was initiated with an irradiation and temperature of 0.7p.u each. At time 0.12, the irradiation and temperature were changed to 1.0p.u each. The next two irradiation and temperature values were 1.3p.u, 1.0p.u and 1.0p.u, 1.2p.u respectively, as shown on Figure 7.6.

As described in chapter 6, as data measurements are obtained from the PV system, DSE and a goodness-of-fit test are performed to determine if the estimated variables are in agreement with the model of the PV system. From this goodness-of-fit test, the upper plot of Figure 7.6 is obtained, which is expected to have a high value of close to 100% under normal operating conditions. The 100% confidence level is expected because the PV system operation is consistent with the model of the integrated PV system. It should be noted that even in the presence of changes in atmospheric conditions such as temperature and irradiance, and the operation of the MPPT-equipped dc-dc converter, the confidence level of the PV system remained at a high value of 100%.
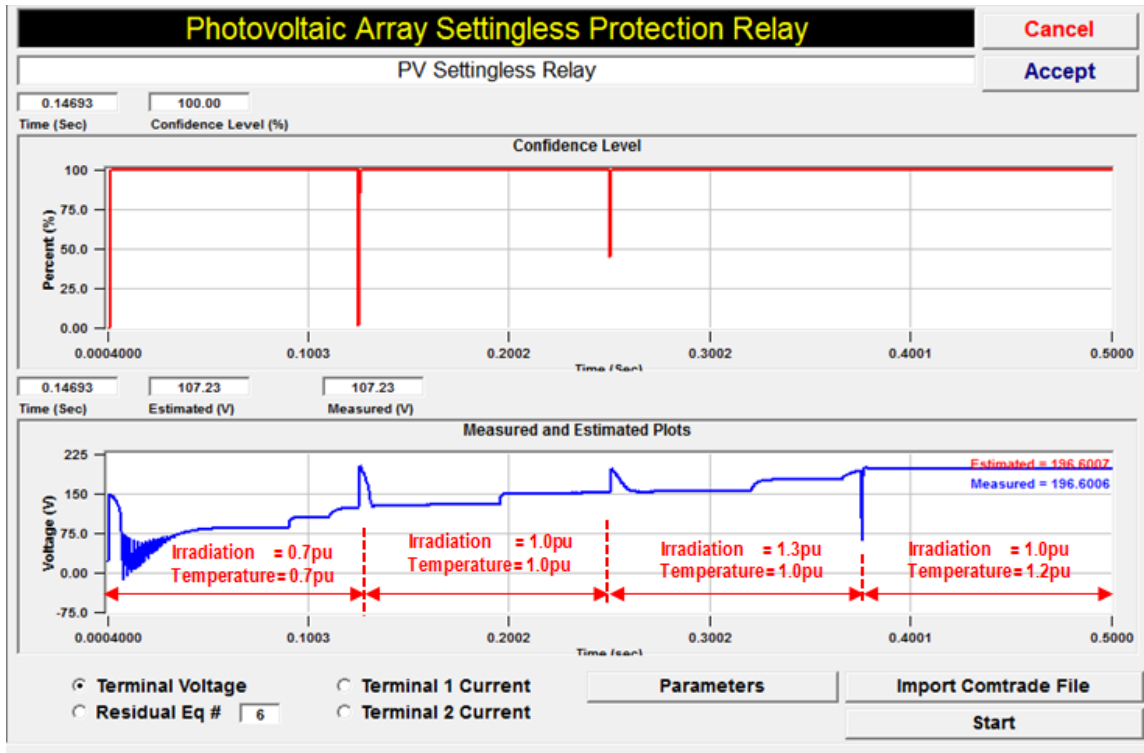
Figure 7.6: Variation of irradiation and temperature in a PV array system.

The value of the cost function given by (6.4) is an indication of how much the estimated state variables, which formed the $h(x)$ mathematical equations in Appendix E, agree with the measured data. Therefore, during normal operating conditions, the cost function is expected to have a low value compared to an abnormal event, on a per unit basis. On Figure 7.7, the plots of the confidence level, (also shown on the upper plot of Figure 7.6), and the cost function are shown. As expected, the cost function, besides the spikes at the points of system operating condition changes, is minimized to below 0.2 per unit. The cost function would typically be in the upwards of the order of 10^2 for abnormal PV system operating conditions. These spikes on Figure 7.7 are due to the significant and abrupt changes in irradiance and temperature during the simulation. These

spikes, however, do not trigger the PV array relay as the duration of the spikes are quite small.
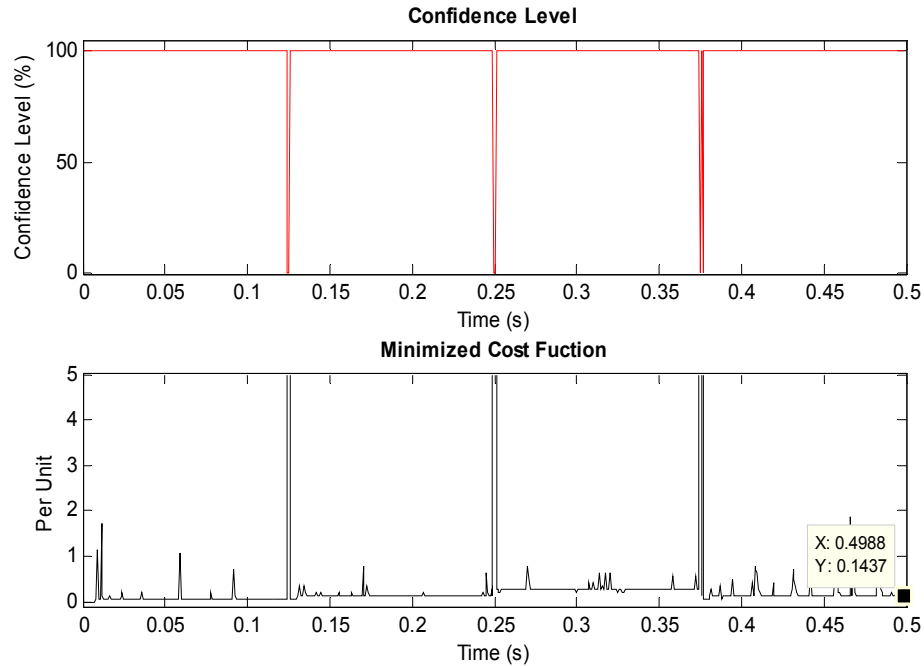
Figure 7.7:   **Confidence level and cost function plots during normal PV array operation.**

Furthermore, the residuals of the current and voltage, which is the difference between the computed and measure data, represented as $h(x) - z$ in (6.4), also provides a good indication of the health of the PV system. For this normal operating condition, the normalized residuals for the terminal and node voltages and currents are shown on Figure 7.8 and Figure 7.9 respectively. The voltage residual is in the order of 10^{-5} p.u as expected for a normal PV operating condition. The current residual, with the exception of the spikes already discussed, is under 0.3p.u, which should be the case when the PV system is operating normally.
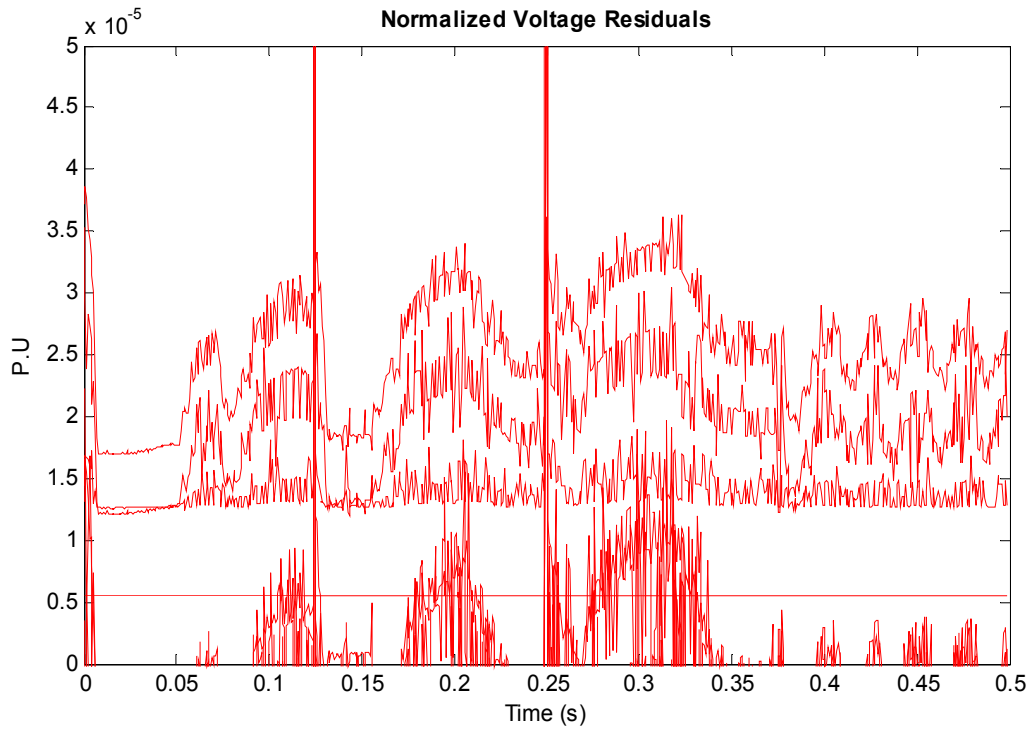
Figure 7.8: Normalized voltage residuals during normal operation.
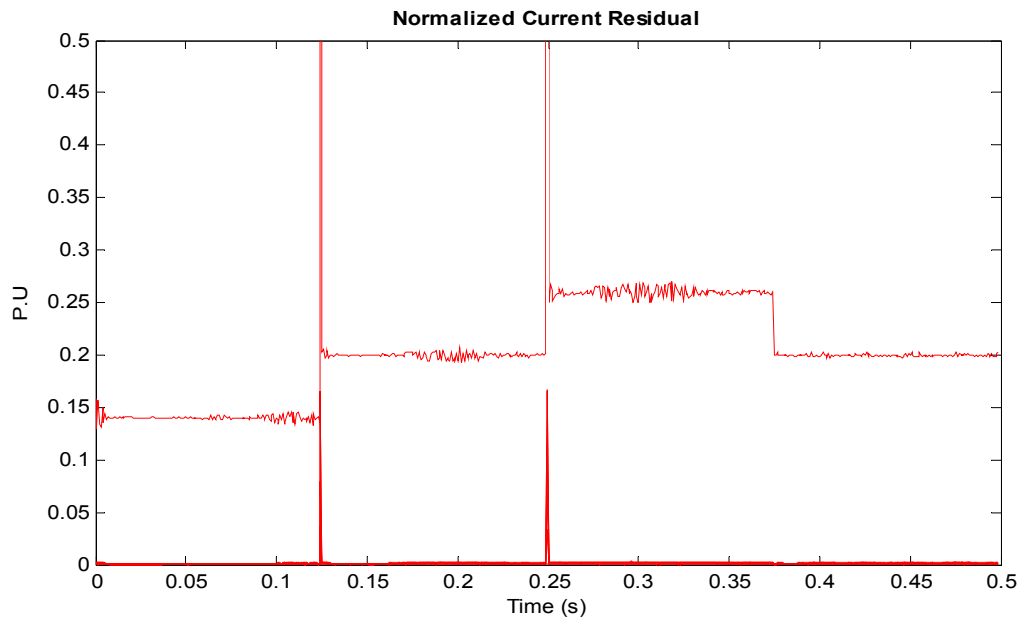
Figure 7.9: Normalized current residuals during normal operation.

Additionally, comparisons between the measured and computed terminal/node currents and voltages of the PV array, are shown on Figure 7.10 through Figure 7.13. From the comparisons, it is clear that these quantities agree with each other. The measured and computed data for both the voltage and current quantities track each other very closely. The changes in current magnitude in Figure 7.12 is due to the MPPT operation of the dc-dc converter, and changes in temperature and solar irradiance on the PV array. The changes in solar irradiance and temperature are as shown on Figure 7.6.
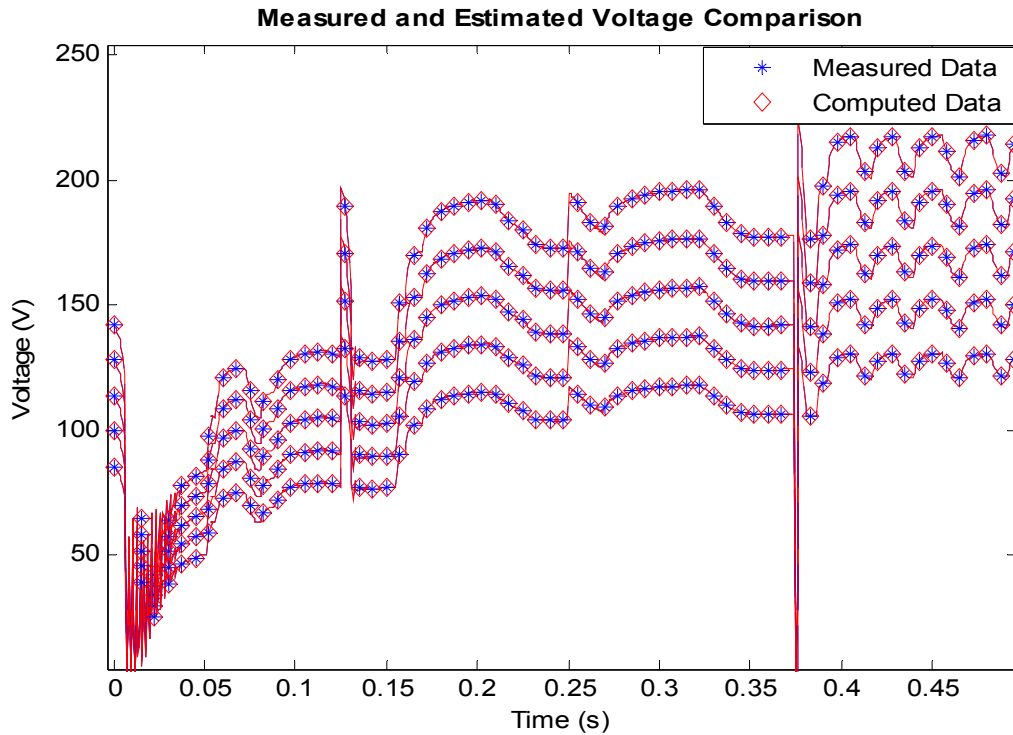
Figure 7.10: **Voltage plot for the top-five nodes during normal operation.**
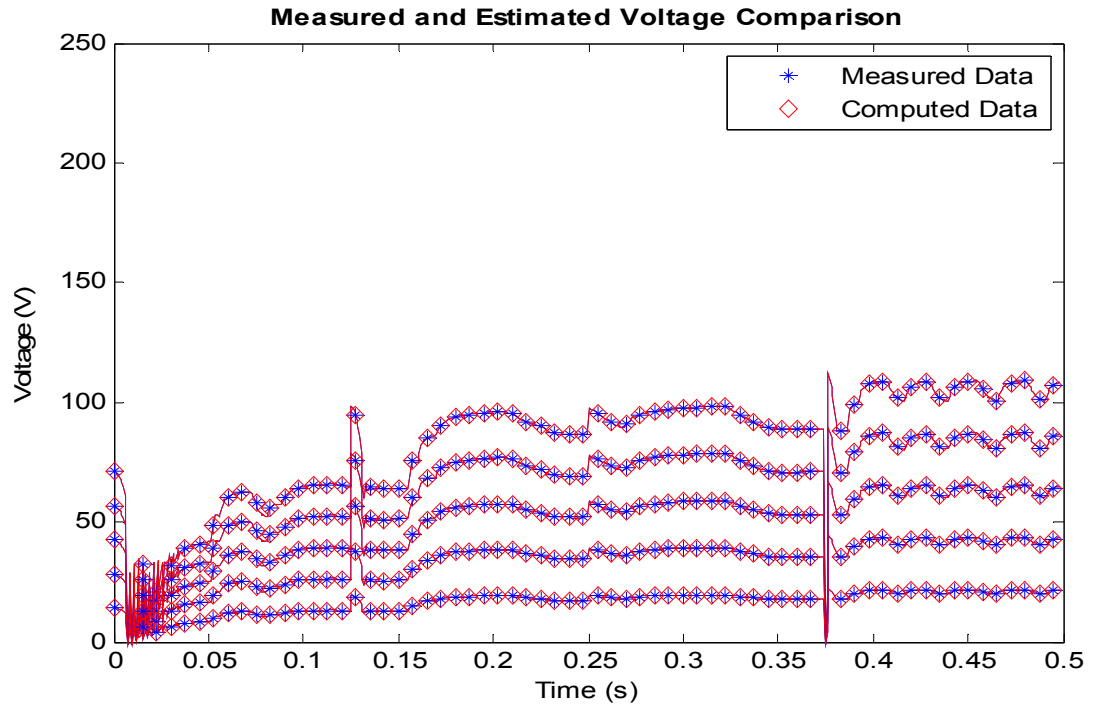
Figure 7.11: **Voltage plot for the bottom-five nodes during normal operation.**
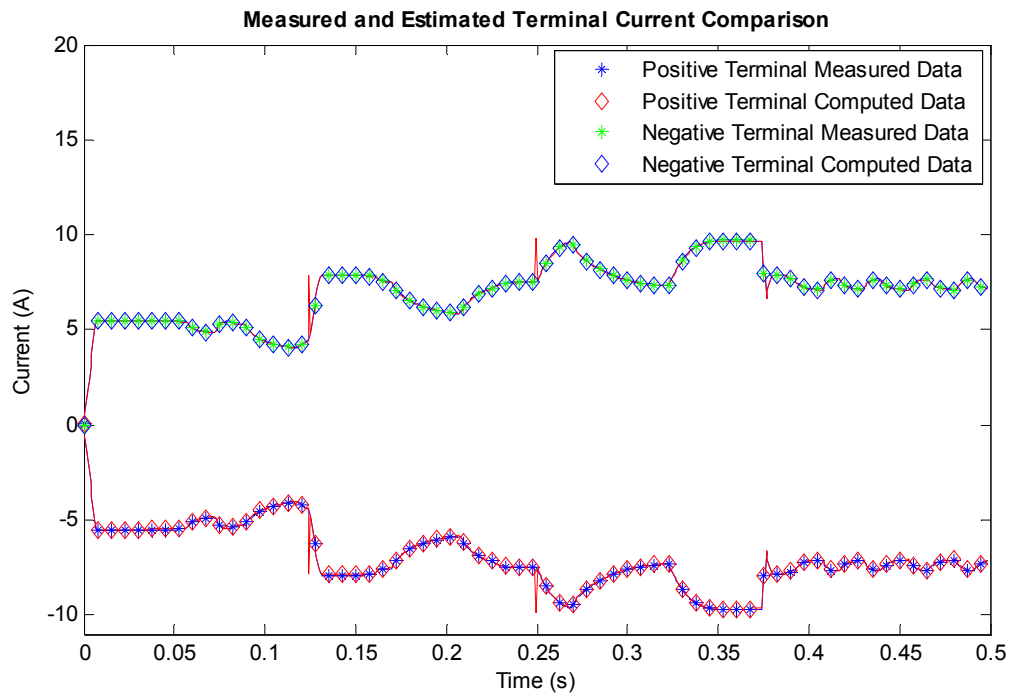
Figure 7.12: **Current plots for the positive and negative array terminals**

during normal operation.

119
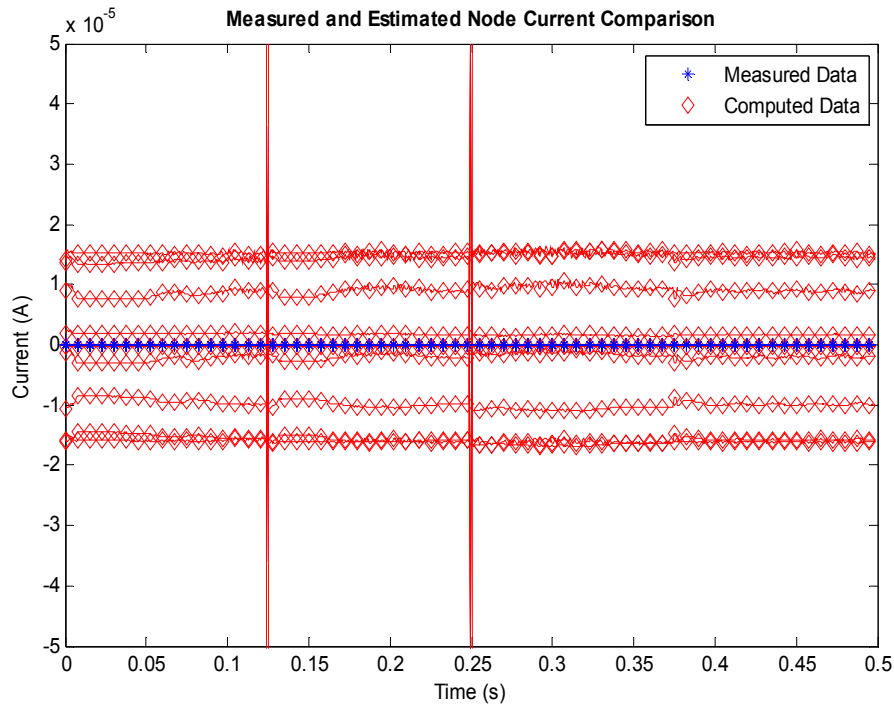
Figure 7.13: **Algebraic sum of current plots at the array nodes during normal operation.**

As demonstrated in this section, the computed PV voltages agree with the measured data even in the presence of varying temperature and irradiance. Also, the protection scheme is not affected by the operation of the MPPT algorithm of the dc-dc converter. Also, the confidence level obtained from this normal-case scenario is consistent with the expectation of a high confidence level value – 100%. Therefore, the protection algorithm has functioned as expected, and in the subsequent sections, its functionality is demonstrated by applying this protection algorithm to abnormal conditions in the PV array system.

7.3 Line to Ground Fault on the PV Array System

In this section, the effect of a line to ground (L-G) fault on the PV array system is discussed. This type of fault can occur if the conductor insulation of PV module is damaged, causing the wiring of the PV module to be exposed. Should this exposed wire touch the PV module mounting structure, which is usually bonded to ground, a line to ground fault is initiated. This ground fault event will cause an abnormal operating condition in the PV array system.

Using the system on Figure 7.1, and after 100ms of simulation, a line to ground fault is initiated on the PV system. This fault is initiated by closing a switch to short the positive terminal of PV module 6 (PV6 of Figure 7.4) to ground. The shorting circuit path was through a low resistance of 0.1Ω. The output of the PV array relay from the simulation is given on Figure 7.14, and is comprised of the confidence level and terminal voltage plots.
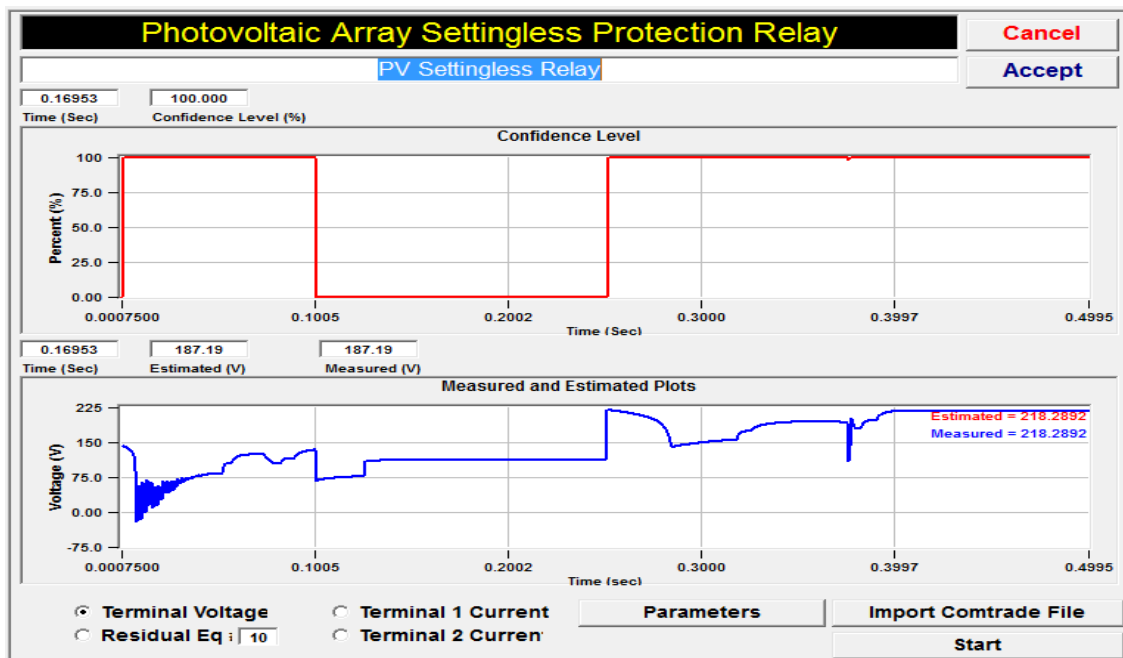
Figure 7.14: Relay output for confidence level and terminal voltage plots during a line to ground fault.

The resulting confidence level with the cost function plot is also shown on Figure 7.15. The rest of the results from this anomaly have also been shown on Figure 7.17 through Figure 7.21.
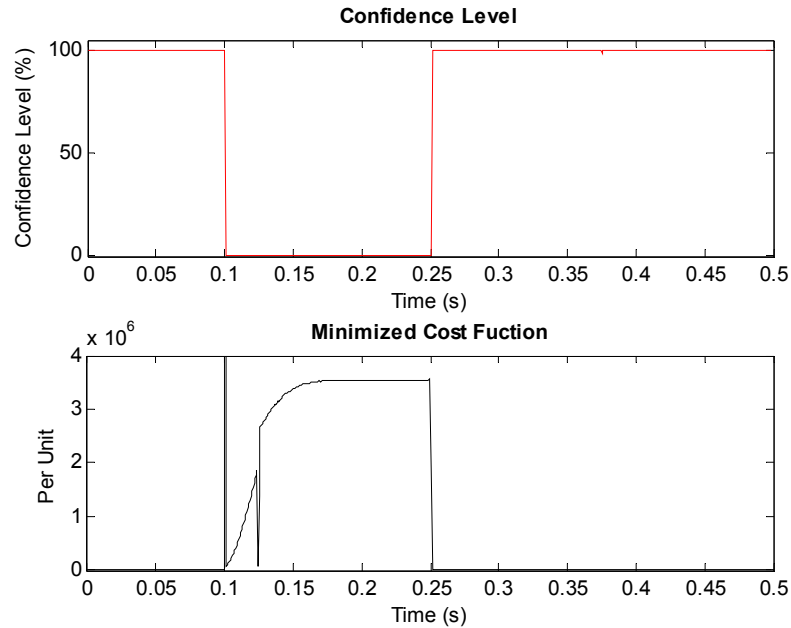
Figure 7.15: Confidence level and cost function plots during a line to ground fault.

As shown on Figure 7.15 prior to the fault initiation, the confidence level of the estimated state variables is at a value of 100%, and the cost function remained at a low value. For the duration of the single line to ground fault, which is between time 0.1 and 0.25 seconds, the confidence level of the estimated state variables drops to zero. Conversely, the cost function jumps to a much higher value as compared to the pre-fault value. The cost function value, on a per unit basis, is quite high when compared to the normal case of section 7.1. The high cost function, as was discussed in section 6.1.2, indicates that (6.3) has not been minimized, which means there is a high probability of

the existence of another set of state variable vector that will yield a lower value than the state variables obtained.

The cost function shown in Figure 7.15 is not minimized when the abnormal condition starts because the best set of state variables used to form the $h(x)$ matrix, resulted in a residual matrix $h(x) - z$, which is much higher than zero. Therefore, a cost function that is not minimized implies the presence of a high residual, which is due to the deviation of the computed measurements from the measured quantities. This high residual will generally lead to a drop in confidence level. The drop in confidence level and increase in cost function show that an abnormal condition has occurred in the PV array system. Therefore, the PV array system needs to be disconnected to isolated the fault, and for the cause of the fault to be investigated. The residual due to the L-G fault on the PV system is plotted on Figure 7.16 and Figure 7.17.
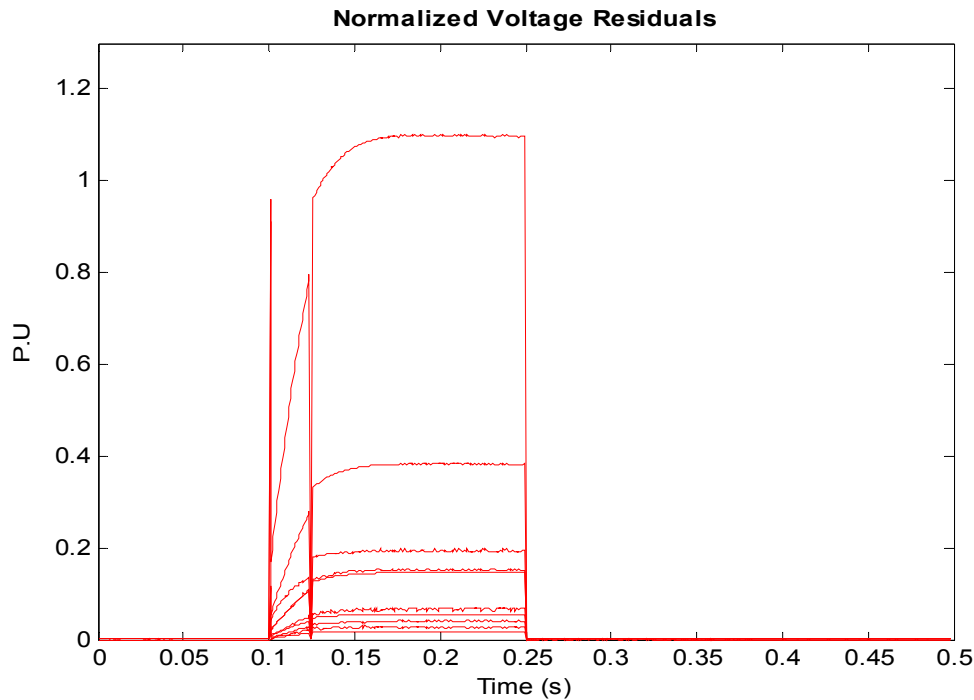
Figure 7.16:   **Normalized voltage residuals during a line to ground fault.**

123
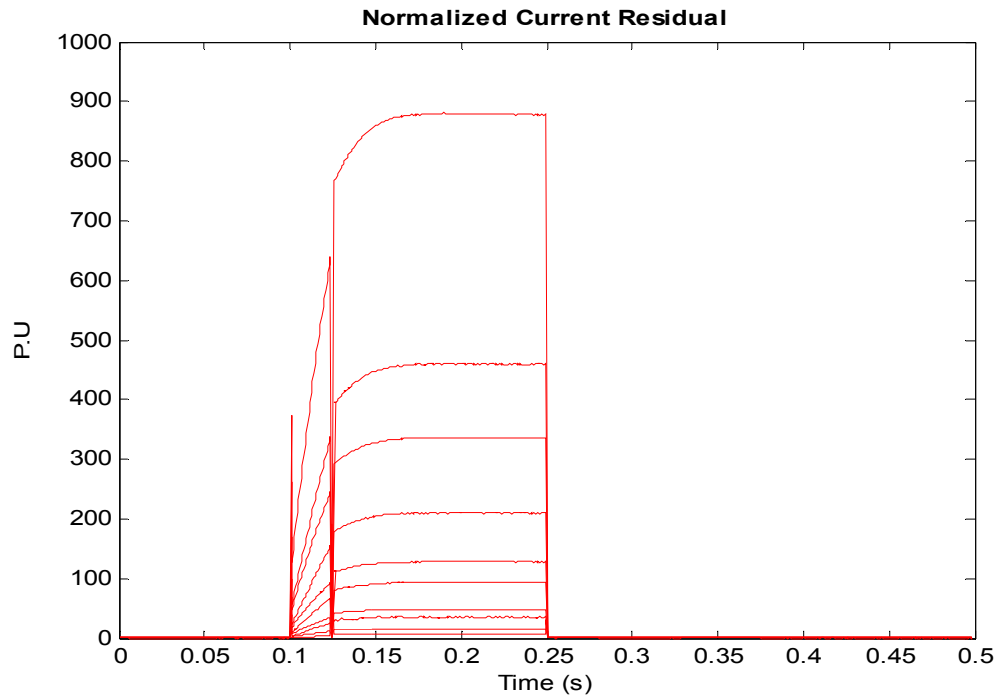
Figure 7.17:   **Normalized current residuals during a line to ground fault.**

The voltage and current residuals of Figure 7.16 and Figure 7.17 respectively, are for the PV module terminal and node quantities. The residuals for the voltage and current, have a high value for the fault duration, and are the major contributors to the non-minimized cost function.

The estimated voltage values track the measured data closely as shown on Figure 7.18 and Figure 7.19. The PV voltage collapses during the line to ground fault condition, and is restored after the fault is cleared. The voltage at some of the PV module terminals did not collapse completely to zero, and this is a function of the location of the fault. The location of this fault is covered in section 7.5.
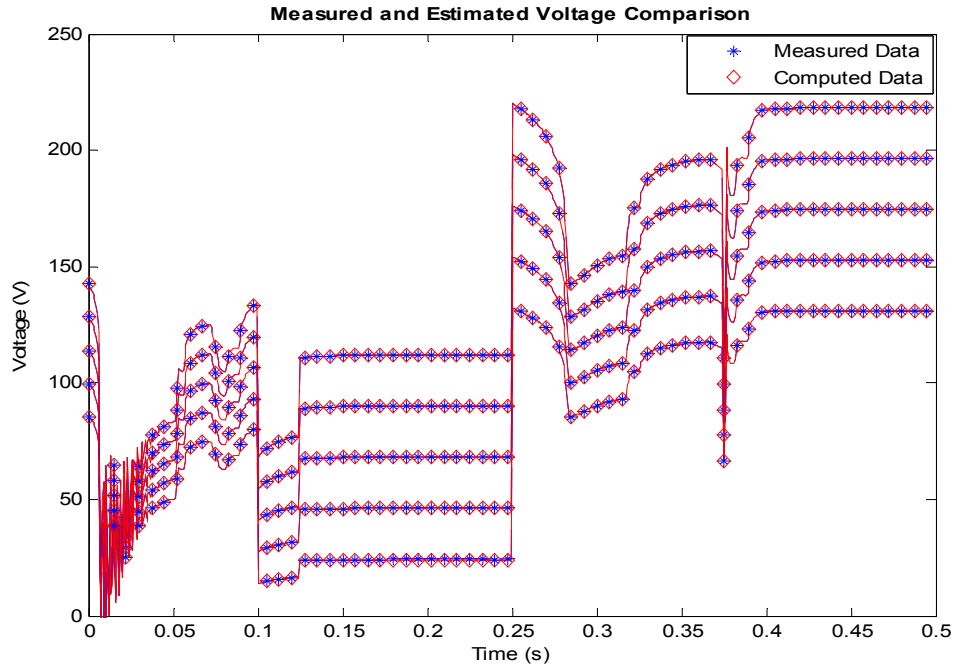
Figure 7.18: **Voltage plot for the top-five nodes during a line to ground fault.**
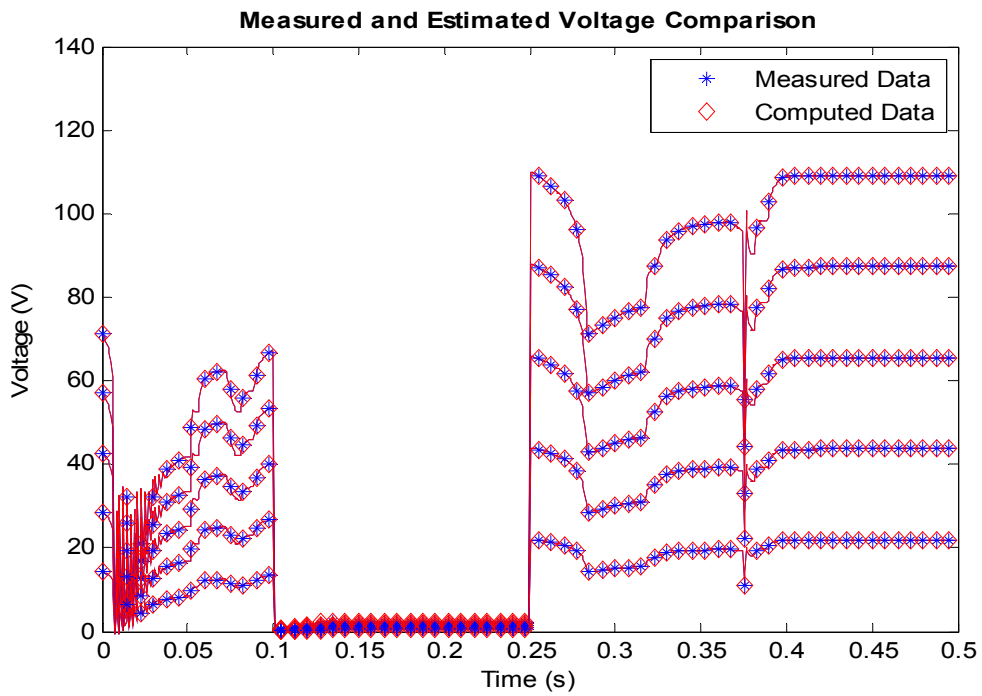
Figure 7.19: **Voltage plot for the bottom-five nodes during a line to ground fault.**

125

The measured and computed terminal and node current data for this simulation are shown on Figure 7.20 and Figure 7.21. By comparing the computed and measured data, it can be seen that the data are in agreement, except for the duration of the fault. During the fault, the measured and computed positive terminal currents differ, and the algebraic sum of the currents at the PV array nodes become non-zero, indicating an anomaly in the PV array system.
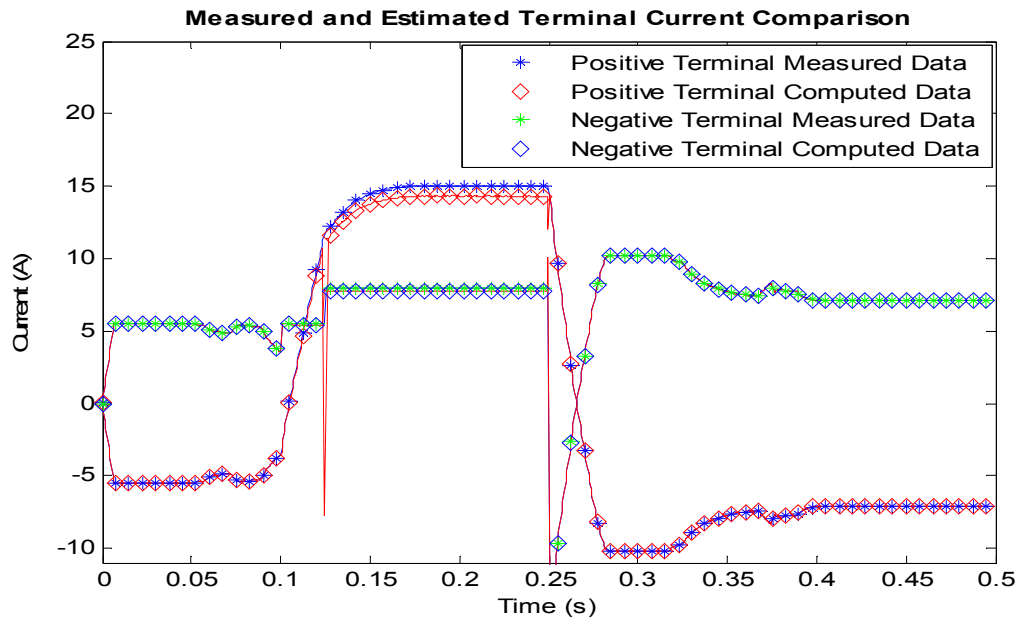
Figure 7.20:   Current plots for the positive and negative array terminals

during a line to ground fault.
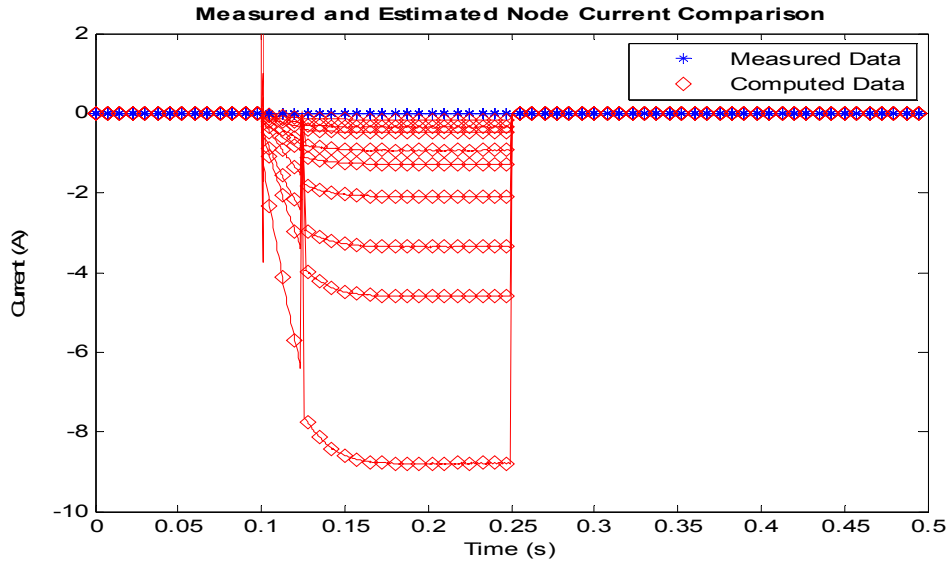
Figure 7.21:   **Algebraic sum of current plots at the array nodes during a line to ground fault.**

These differences between the measure and computed data, also known as the residuals, are the contributors to the increase in cost function on Figure 7.15. Some information can be extracted from the residual data, namely, the location of the anomaly in the PV array system. This fault location determination is covered in section 7.5.

7.4   High impedance Fault on the PV Array System

In the protection of PV array systems, detecting low impedance faults is usually not as challenging as the detection of high impedance faults. This challenge in detecting high impedance faults is due to the fact that certain high impedance faults can yield current magnitudes in the order of hundreds of milliamps, and can easily go undetected. For this research, a high impedance fault of 1000Ω was initialed at the positive terminal of PV6, similar to section 7.3. The result obtained from the PV array relay for this high impedance fault is shown on Figure 7.22.
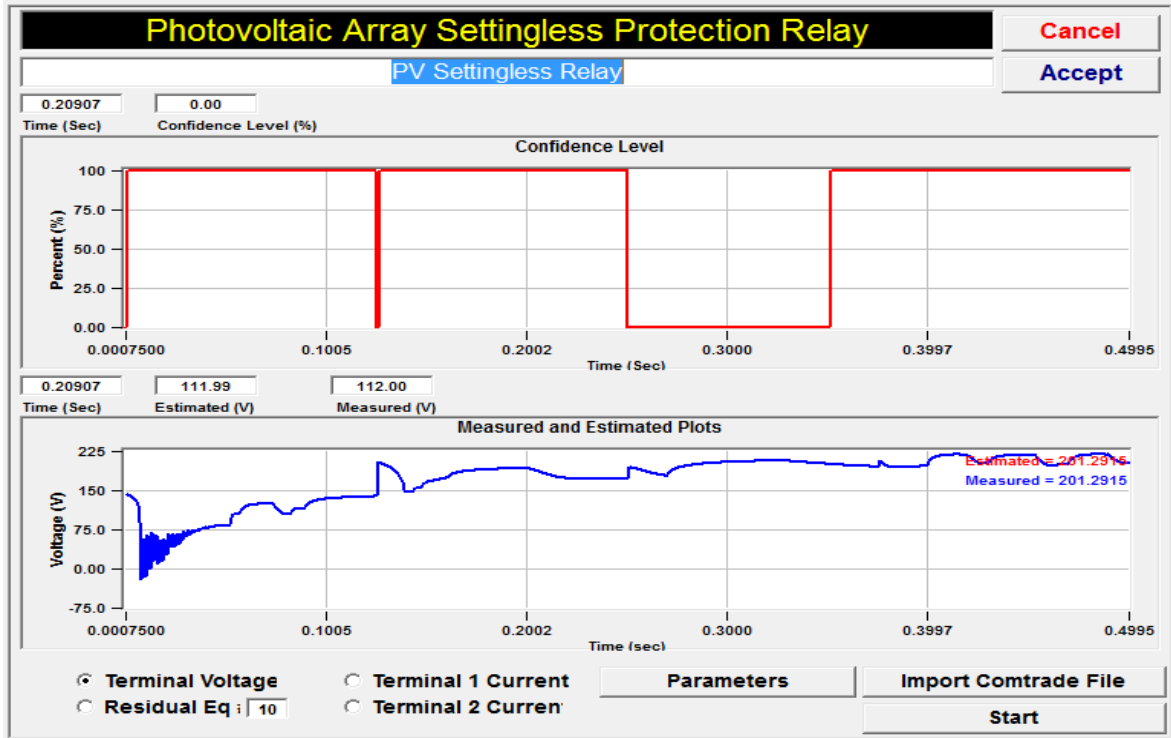
Figure 7.22: Relay output for confidence level and terminal voltage plots during a high impedance fault.

After the high impedance fault is initiated at time 250ms, the confidence level drops for the duration of the fault. This confidence level is also shown on Figure 7.23. The cost function, also shown on Figure 7.23, yields a high value from the fault initiation time of time 250ms till the fault is cleared at time 350ms.
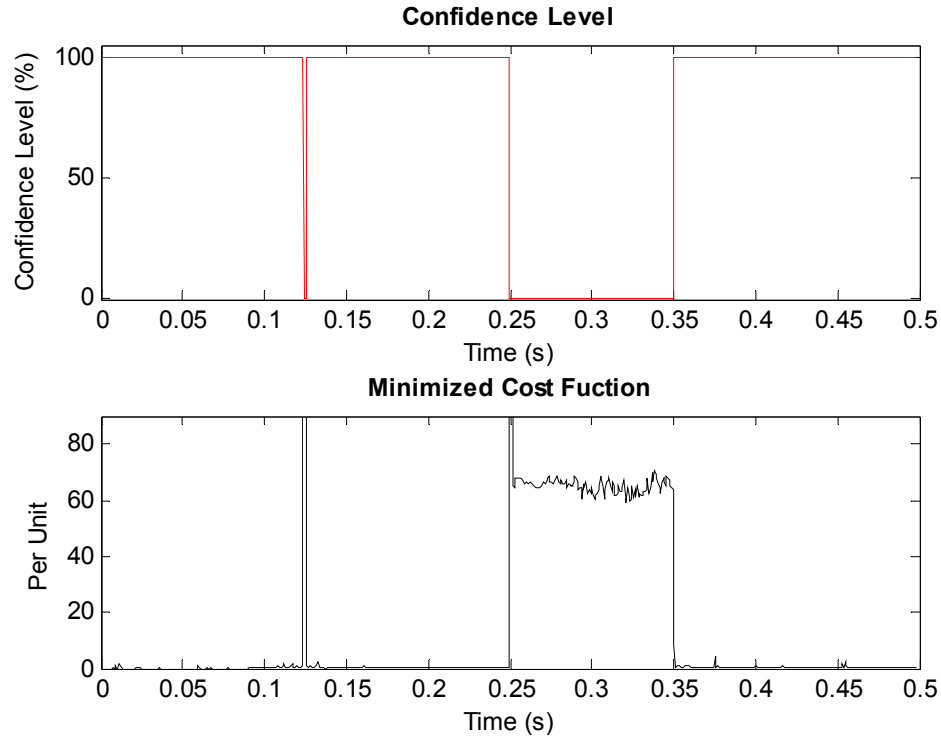
Figure 7.23: Confidence level and cost function plots during a high impedance fault.

Similar to the result in section 7.3, the residual of the voltage and current quantities has a higher value for the duration of the fault as shown on Figure 7.24 and Figure 7.25. It should be observed that the magnitude of the voltage and current residuals for the high impedance fault is a lot less than that of section 7.3. This lesser residual value is what makes the detection of high impedance faults a lot challenging. However, the proposed protection scheme has identified this abnormal condition in the PV array system.

129
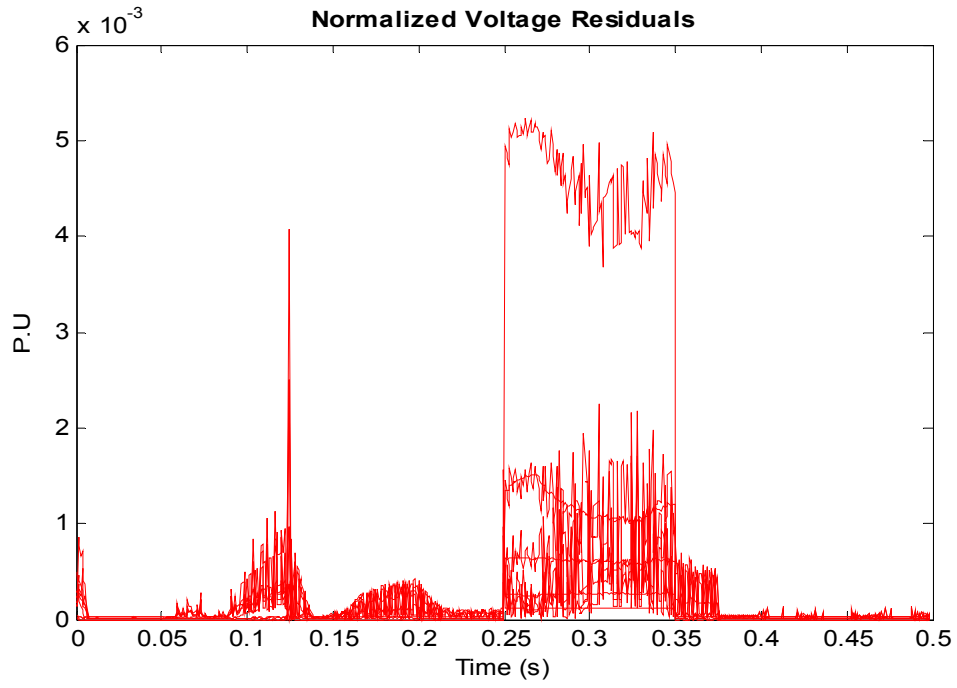
Figure 7.24: Normalized voltage residuals during a high impedance fault.
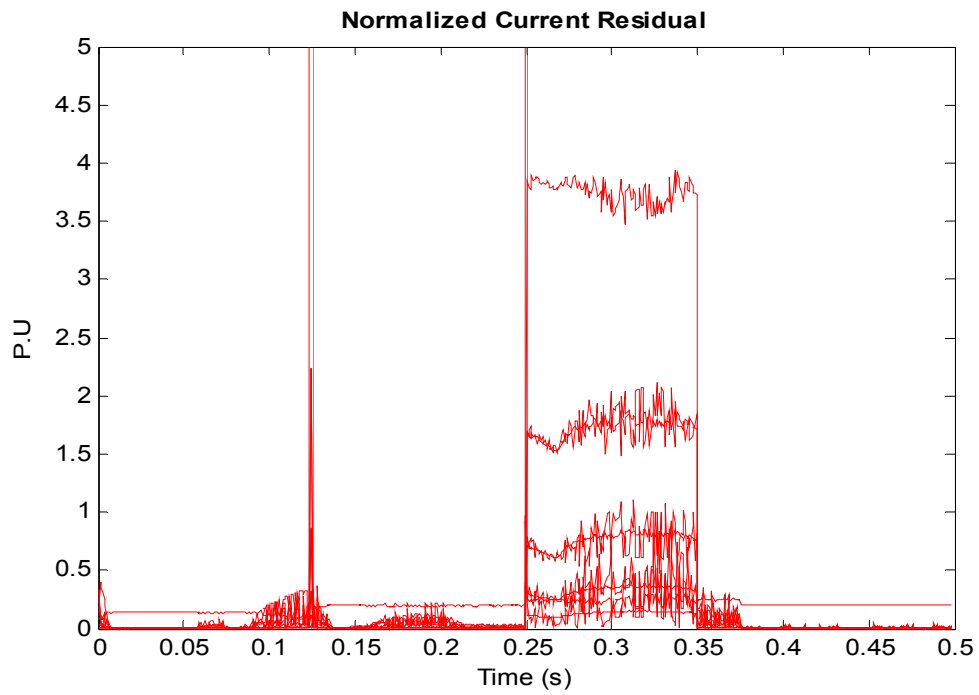
Figure 7.25: Normalized current residuals during a high impedance fault.

The voltage and current comparisons between the measured data and computed data are shown on Figure 7.26 through Figure 7.29. The current and voltage plots appear to be in agreement because the current through the fault path is quite small. In fact, besides Figure 7.29, by visually inspecting the other data measurements, the measured and computed data seem to agree with each other. Therefore, it is no surprise that traditional protection schemes find it challenging to detect these high impedance faults.

The standard deviation of Table 7.1, which forms the weight, W of (6.4), was selected sensitive enough that small deviations between the measure and calculated quantities are detected in the cost function computation as demonstrated on Figure 7.23.
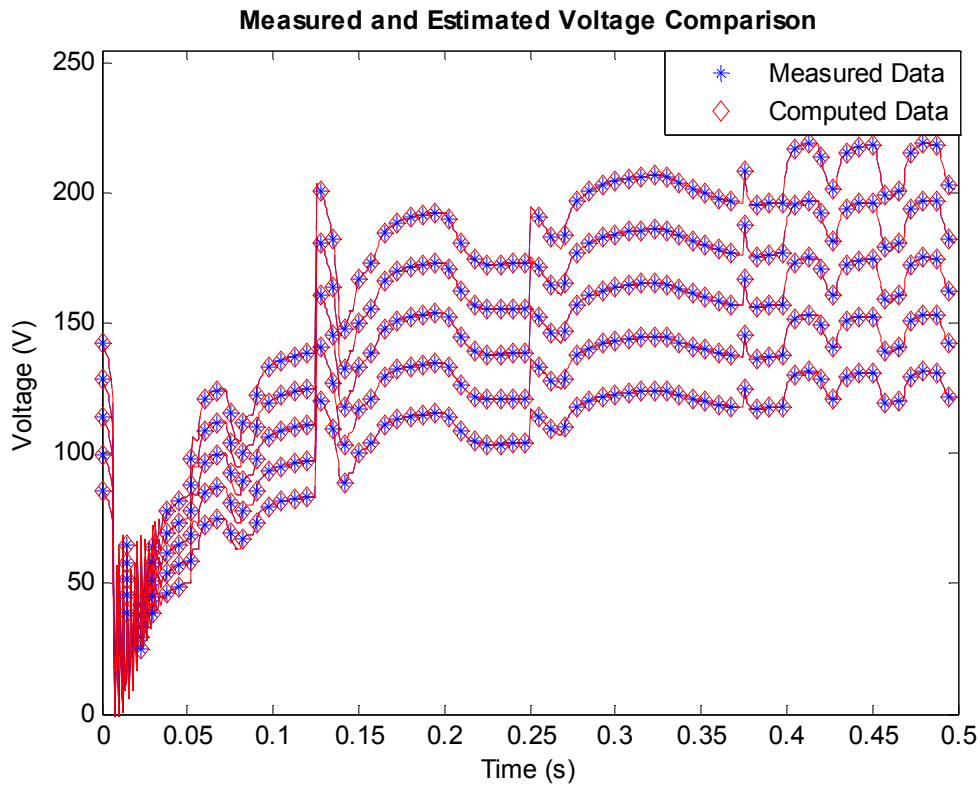
Figure 7.26: **Voltage plot for the top-five nodes during a high impedance fault.**

131
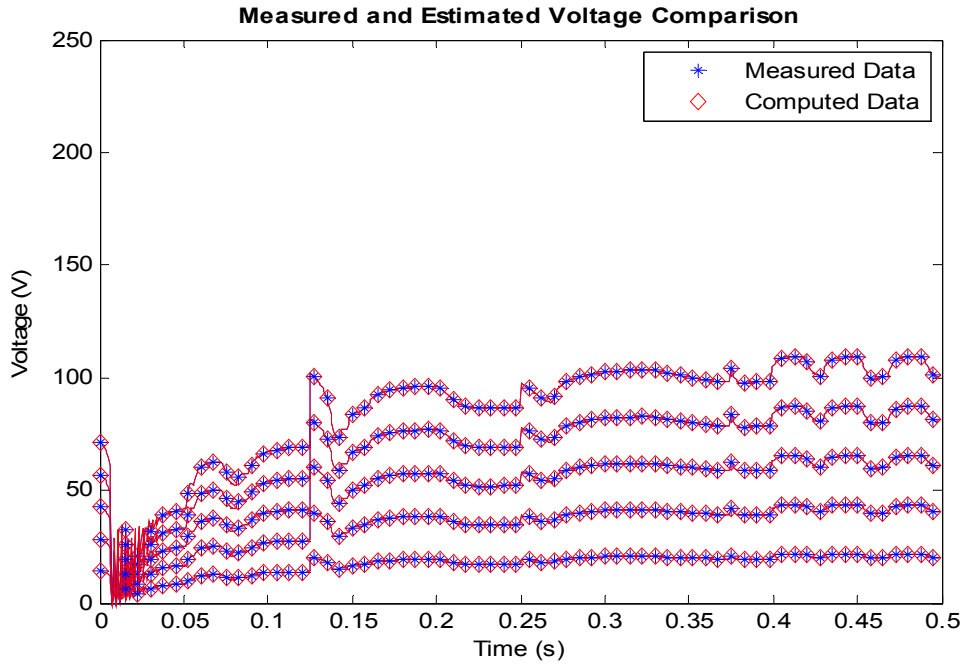
Figure 7.27: Voltage plot for the bottom-five nodes during a high impedance fault.
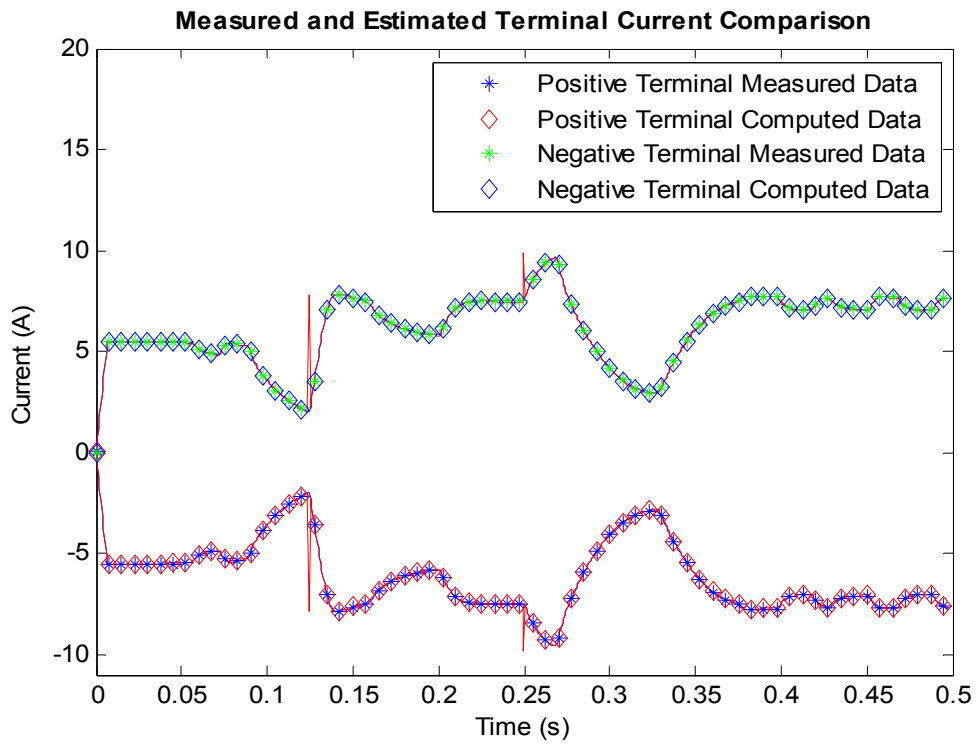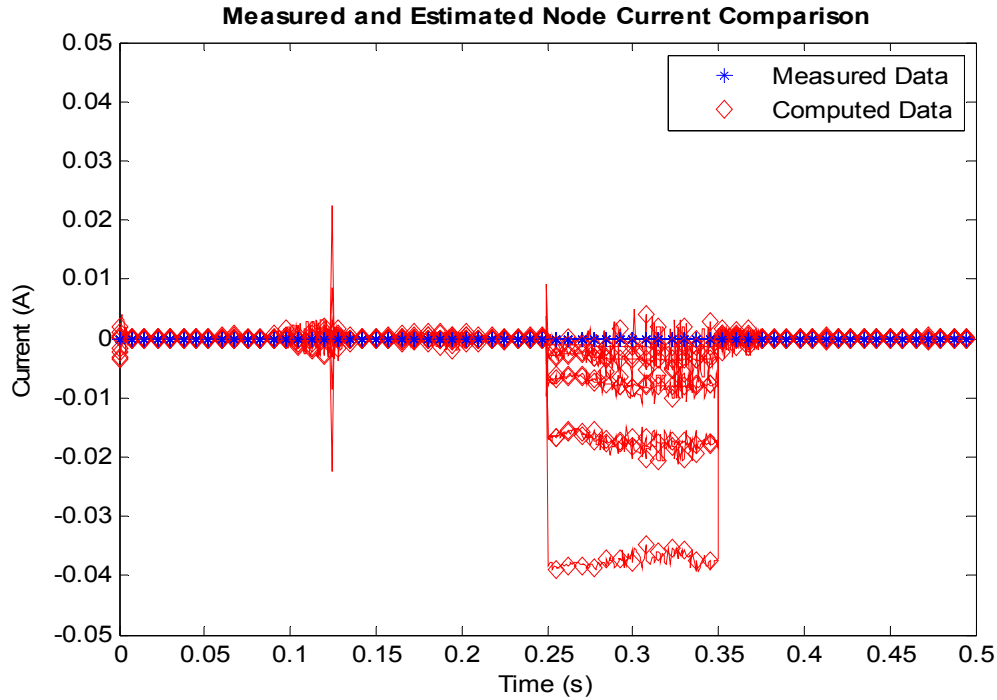

Figure 7.28: Current plots for the positive and negative array terminals

during a high impedance fault.

**Figure 7.29:** Algebraic sum of current plots at the array nodes during a high impedance fault.

From the foregoing, it has been demonstrated that the proposed protection scheme offers an elegant method for protecting the PV array system against both low and high impedance faults. In addition, this protection scheme provides information on the location of the faulted PV module within the PV array system. This fault location determination is covered next.

7.5   Determination of Fault Location from Residual Data

In sections 7.3 and 7.4 the residual for the combined terminal and node voltage/current quantities were discussed. The emphasis in these sections was to identify the presence of a fault in the PV array system. In this section, however, the location of the fault within the PV system is the topic of interest. Therefore, the residual of the faulted module is identified relative to the other residuals to demonstrate the fault location

133

identification. First the system of section 7.3 is discussed, followed by the system in section 7.4.

The voltage and current residuals of section 7.3 were comprised of contributions from the different PV modules. To show the contribution from the faulted PV module relative to the other PV modules, Figure 7.16 and Figure 7.17 are been plotted again as shown on Figure 7.31 and Figure 7.30. And from Figure 7.31 and Figure 7.30, the most contribution to the normalized residual is from the faulted PV module. In section 7.3 the faulted PV module was PV6, therefore from the residual data, the location of the fault can be determined.
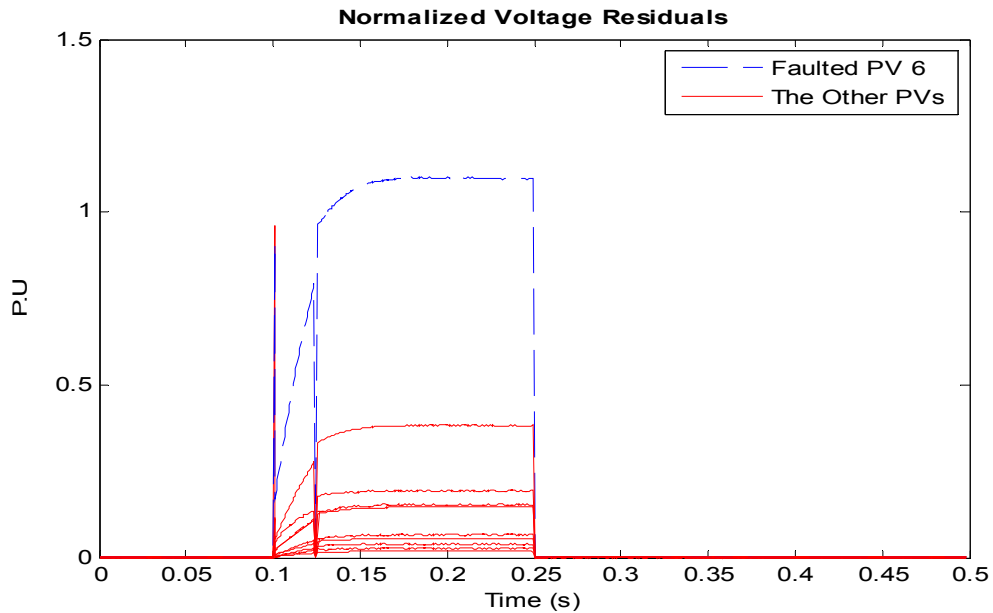
Figure 7.30:   **Voltage residual for the line to ground fault the positive terminal of PV6.**
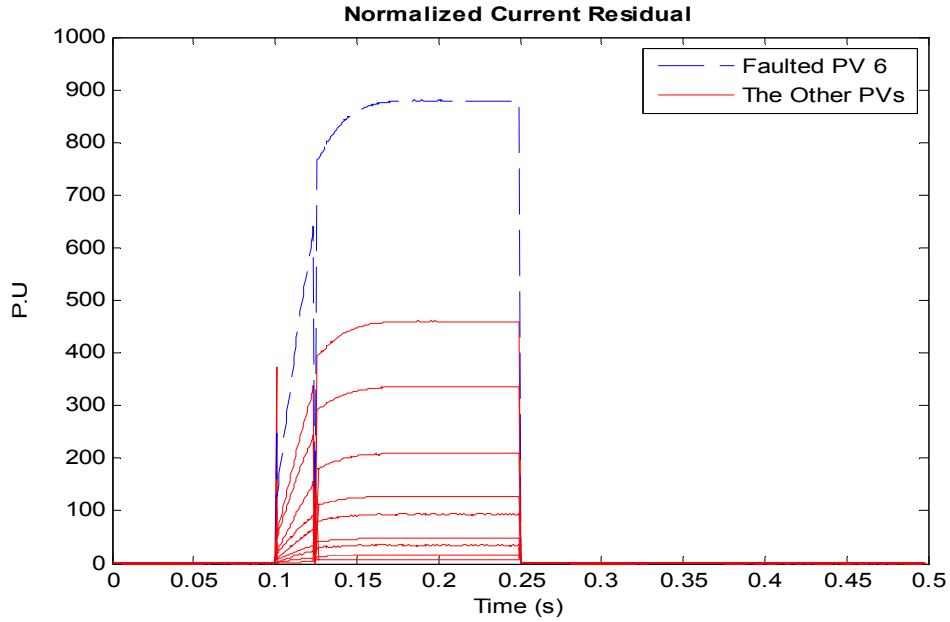
Figure 7.31: **Current residual for the line to ground fault the positive terminal of PV6.**

A similar fault determination analysis is performed on the data from section 7.4. Therefore, the normalized voltage and current residuals have been plotted to indicate the level of contribution from the faulted PV module. These normalized voltage and current plots are shown on Figure 7.33 and Figure 7.32. As expected, PV6, which was the faulted PV module, had the largest normalized residual in comparison to the other PV modules. This increased residual dropped to its pre-fault low value after the fault is cleared at time 350ms.
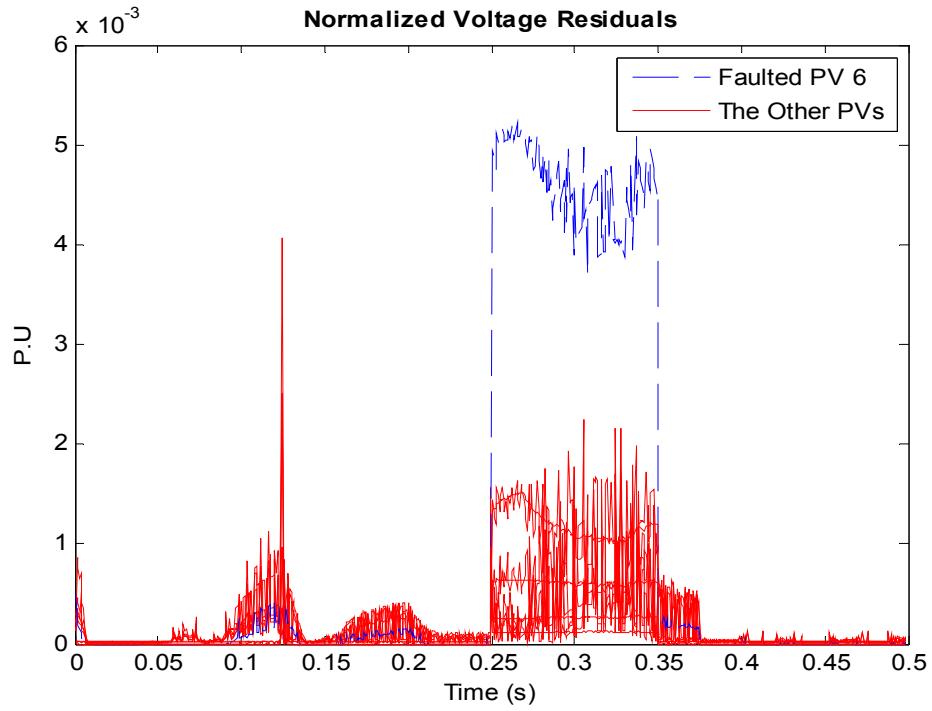
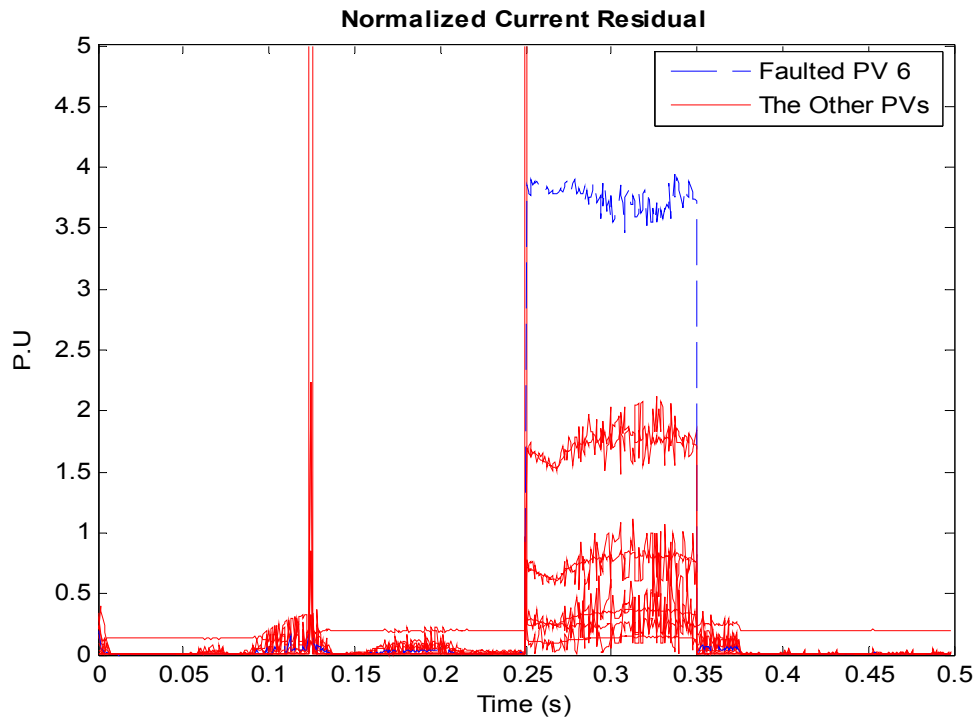**Figure 7.32:**   **Voltage residual for high impedance fault on the positive terminal of PV6.**

Figure 7.33:   **Current residual for high impedance fault on the positive terminal of PV6.**

136

It should be noted that in some cases, a non-faulted PV module could end up with a slightly higher residual than the faulted PV module. However, these PV modules with a higher residual than the faulted PV module are usually adjacent to the faulted PV module. Having non-faulted PV with a higher residual typically occurs when the non-faulted PV module becomes reversed biased due to the faulted adjacent PV module. However, narrowing down the fault location to the faulted PV module and in some cases, the adjacent PV module to the faulted module is quite beneficial in a large PV array installation. This fault location determination has also been demonstrated for various fault conditions in Appendix F.

Therefore the system-level PV array model development together with this protection algorithm offers a tool for determining the location of the fault. The benefit of this enhancement to this recently developed protection approach may not be obvious in a relatively small PV system consisting of less than 20 PV modules. However, for a larger PV system, the PV operator can determine the location of the fault within the PV array from his office, before going to the PV array installation to address the fault issue. This saves the operator time in determining the fault location, and ultimately reduces the loss of revenue to the PV owner.

7.6 Summary

In this chapter, the protection of the PV array has been demonstrated using the algorithm of chapter 6. The protection and modeling methods have provided a robust method for detecting various types of fault under varying atmospheric conditions. The algorithm embedded in this protection approach is the use of the model of a single PV module to formulate the model of a system of PV array. Therefore, this protection

method protects the entire PV array system down to the module-level. In other words, the operating condition of each PV module and consequently that of the entire PV array are known. Any deviation from the mathematical model that defines the operation of each PV module, and that of the PV array system, is considered an anomaly. Also, the protection approach offers the benefit of detecting the location of the faulted PV array, which reduces the time it takes to determine the location of the faulted PV module or modules.

Furthermore, by protecting the PV array as a system, the computational time in estimating the system states is greatly reduced. For instance, given a PV module, there are two terminal voltages to be estimated, say v_{a1} and v_{a2}. If a second PV module is connected in series with this module, this results in three terminal voltages to be estimated, namely, v_{a1}, $v_{a2} = v_{b1}$, and v_{b2}. Therefore, this approach results in effective parameter estimation by reducing the number of estimated states, because v_{b1}, which is the same value as v_{a2}, is not recomputed. Hence, only the voltage at each node is estimated instead of estimating the voltage for PV modules individually. Estimating the voltage for the PV modules individually would have led to additional, yet redundant state variables.

Moreover by protecting the PV array as a system, two current sensors could be used for a group of series connected PV arrays. One sensor would be located at the top (first) node of the series modules, while the other at the bottom (last) node. The measurements for the current through the in-between-PV-modules can be assumed to be the same as the measured terminal currents. These measurements for the in-between-PV-modules would fall under pseudo measurements as discussed in chapter 6. Therefore, this

protection method provides cost saving benefits by reducing the number of current sensor

installations required in the PV array system.

8 DEMONSTRATING EXAMPLE: PV ARRAY PROTECTION ON AN ACTUAL PV INSTALLATION

In chapter 7, the demonstration of the PV protection was performed using numerical simulations. In this chapter, normal operating conditions, and faulted conditions, for both high and low impedance based faults, have been initiated on the PV array used for this research. The purpose of these demonstrations is to illustrate the efficacy of the system-level model, and the protection approach for the PV array system. The physical setup and one-line for the laboratory-scale demonstration are shown on Figure 8.1 and Figure 8.2. The components in Figure 8.1 have each been labeled in Figure 5.3.

Figure 8.1: Laboratory setup for PV array fault analysis.
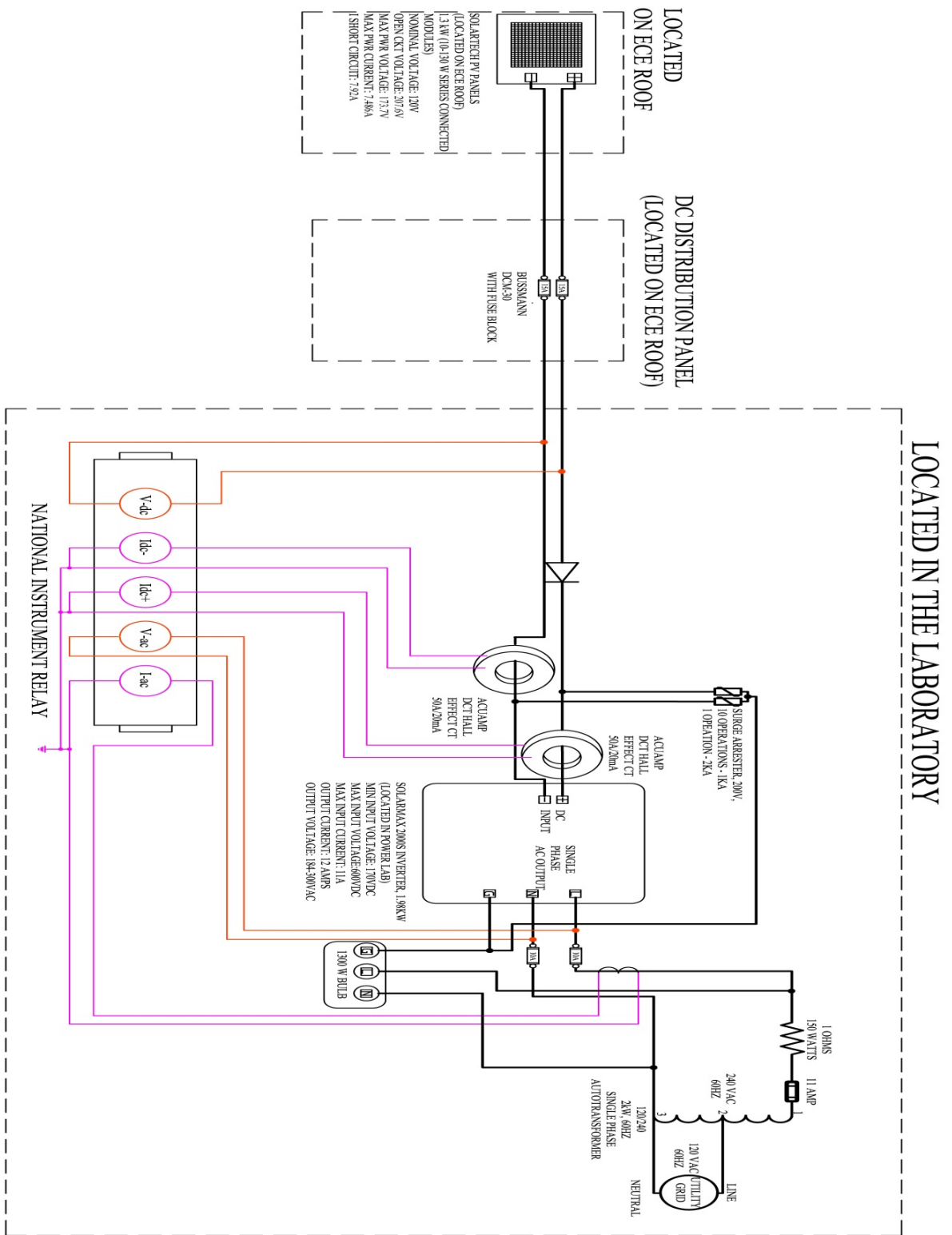
**Figure 8.2:** One-line diagram for laboratory-scale PV array fault analysis.

A snapshot of the raw data measurement from the instrumentation devices connected to the PV array system of Figure 8.2 is shown on Figure 8.3. The top two data measurements are the PV array voltage and current respectively, and the next two are the inverter ac voltage and current respectively.
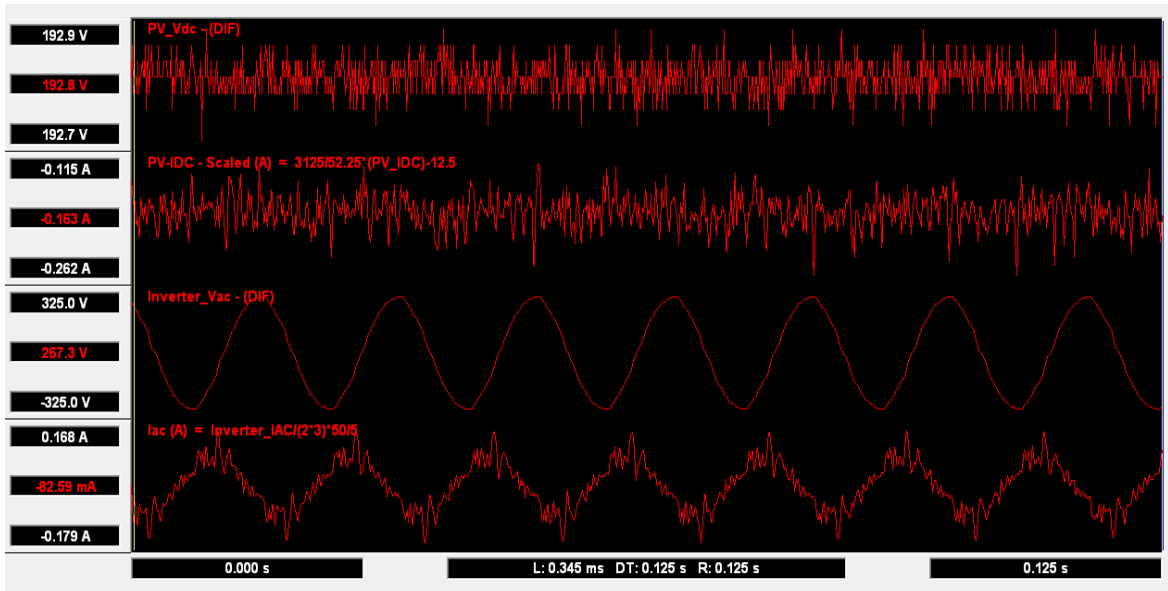
Figure 8.3:   PV and inverter data measurements.

The dc and ac voltages were connected directly to the data acquisition unit – a National Instrument (NI) device. However, the dc and ac currents were scale down before connecting to the NI device. The dc currents were passed through current sensors, while the ac currents were routed through current transformers (CTs). These scaled-down ac and dc currents were passed through a 2 ohm resistor and a 50 ohm resistor respectively. The voltage across the 2 and 50 ohm resistors is what the NI device measured. Measuring the voltage across the 2 and 50 ohm resistors was necessary because the low signal port used on the NI device only accepted up to 10V. Also, the conductor for the ac current was wrapped around the CT three times to ensure a high enough current magnitude was brought to the NI device. Due to these intermediate connections, the necessary

142

conversions were performed to the measured voltage and current quantities to ensure accurate primary quantities were displayed, as shown on Figure 8.3. The setup for the current and voltage instrumentation measurements is shown on Figure 8.4.
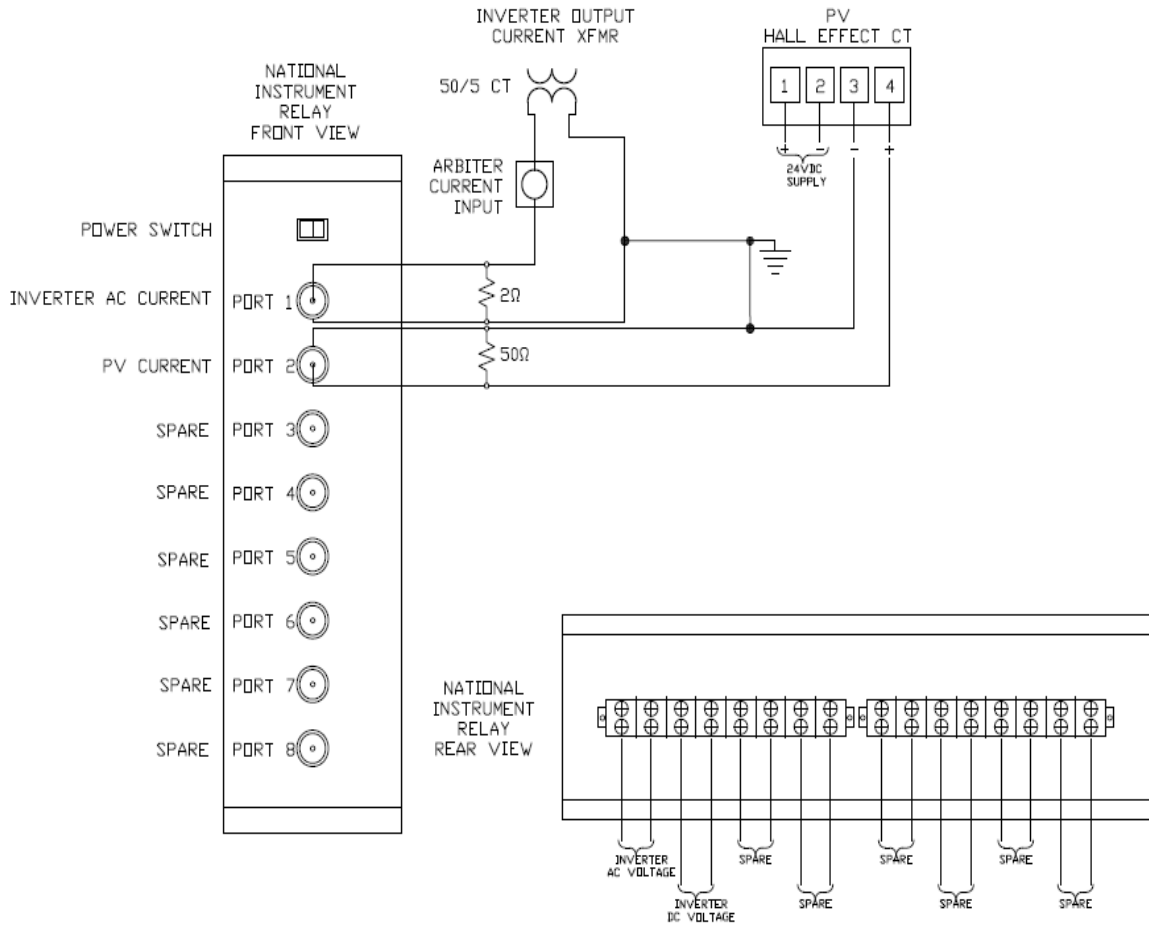

Figure 8.4: **Wiring for NI data acquisition unit.**

The dc and ac voltages were connected to the rear of the NI device as shown on the bottom right of Figure 8.4. The rear of the NI device could handle as high as 600Vdc/Vac, therefore, no voltage scaling was necessary. The PV array dc voltage and the ac voltage from the inverter were connected directly to the NI device.

The current sensors and CTs used for this research are shown on Figure 8.5. The dc current (Hall-Effect) sensors are located on top, in blue, and the CTs located below.

As shown on Figure 8.5, the primary current carrying conductors were wound around the CTs three times due to the small magnitude of the current. This current scaling is accounted for in the ac current parameter conversion of Figure 8.3.
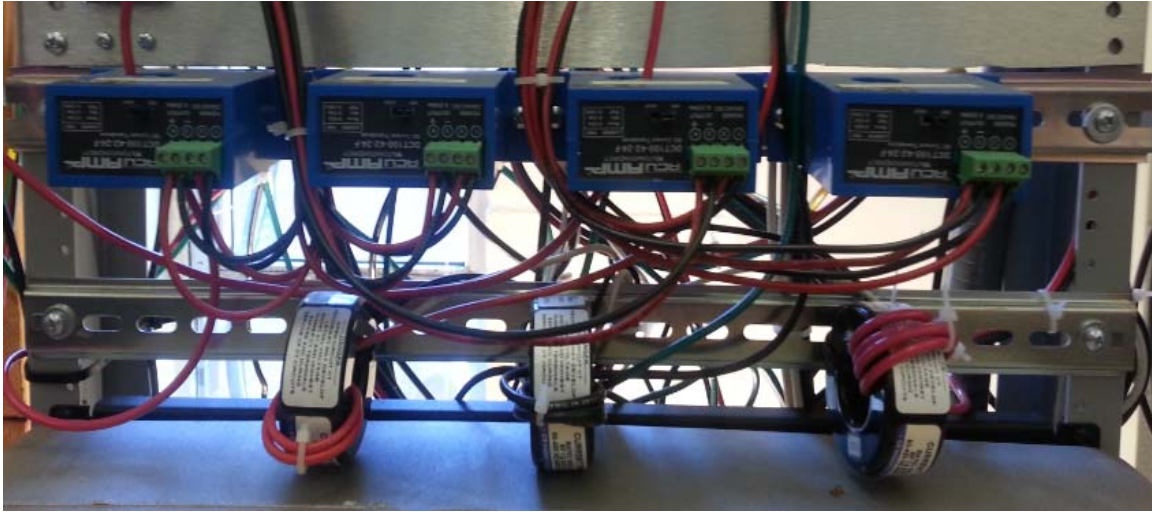
Figure 8.5:   **Current sensors (top) and CTs (bottom) used for research project.**

The National Instrument data acquisition unit (DAU) used for this research project is shown on Figure 8.6. This is the same device that was depicted schematically on Figure 8.4. Above the DAU are the resistors used by the DAU for instrumentation, also shown on Figure 8.4.

Figure 8.6:   **National Instrument data acquisition unit (bottom) with scaling resistors (top).**

There were not nearly as many instrumentation devices for the physical system of this research as there were in the numerical simulations of chapter 7. The reduced instrumentation device count was mainly due to cost limitations. However, even with the reduction in instrumentation devices, the protection scheme for this project remains effective as demonstrated in sections 8.2 and 8.3. In the absence of dedicated Hall Effect sensors for each PV module, and dedicated potential measurements for each node of the PV array, the following assumptions were made:

under normal PV array system operations

i) the current through the series connected PV modules is the same. Any deviation from this assumption is expected to be captured by the protection scheme as an anomaly in the PV system.

ii) the voltage across each of the series connected PV modules in the same vicinity (i.e. subjected to the same solar irradiance,) will generally be the same. The terminal voltage across the set of series PV modules will be distributed evenly between the series connected PV modules. In other words, for any given series connected PV module, a terminal voltage of γ/k is expected on that PV module, for a system with k-series-connected PV modules, and with a combined system terminal voltage of γ.

These assumptions are accounted for in this protection scheme by assigning these assumed measurements as pseudo measurements with a high standard deviation. The assigned standard deviations for the weight of the data measurement for this chapter are shown on Table 8.1.

Table 8.1:   **Assigned standard deviation for physical system data measurements.**

Data Measurement	Assigned standard deviation
PV Terminal and node voltages	0.01
PV terminal currents - (3.86),(3.87)	0.001
Algebraic sum of node currents	0.0001
Current virtual measurement - (3.88)	0.04
virtual measurements - (3.94)-(3.106)	9.0
All other virtual measurements (3.89)-(3.112)	0.01

The methods used in chapter 7 to analyze the various operating conditions of the PV array system, are also used in this chapter to analyze the data from an actual PV installation. The implementation of this protection scheme on the data from the actual PV array installation for this project is discussed next.

8.1 Normal PV Array Operation

Similar to the procedure in chapter 7, the normal PV operating condition was used to verify that the protection algorithm was functioning correctly, and that the values selected for the standard deviations given in Table 8.1 are appropriate for this PV array system. The parameters used for this demonstration is from the extracted parameters of chapter 4, and these parameters are shown on Figure 8.7.
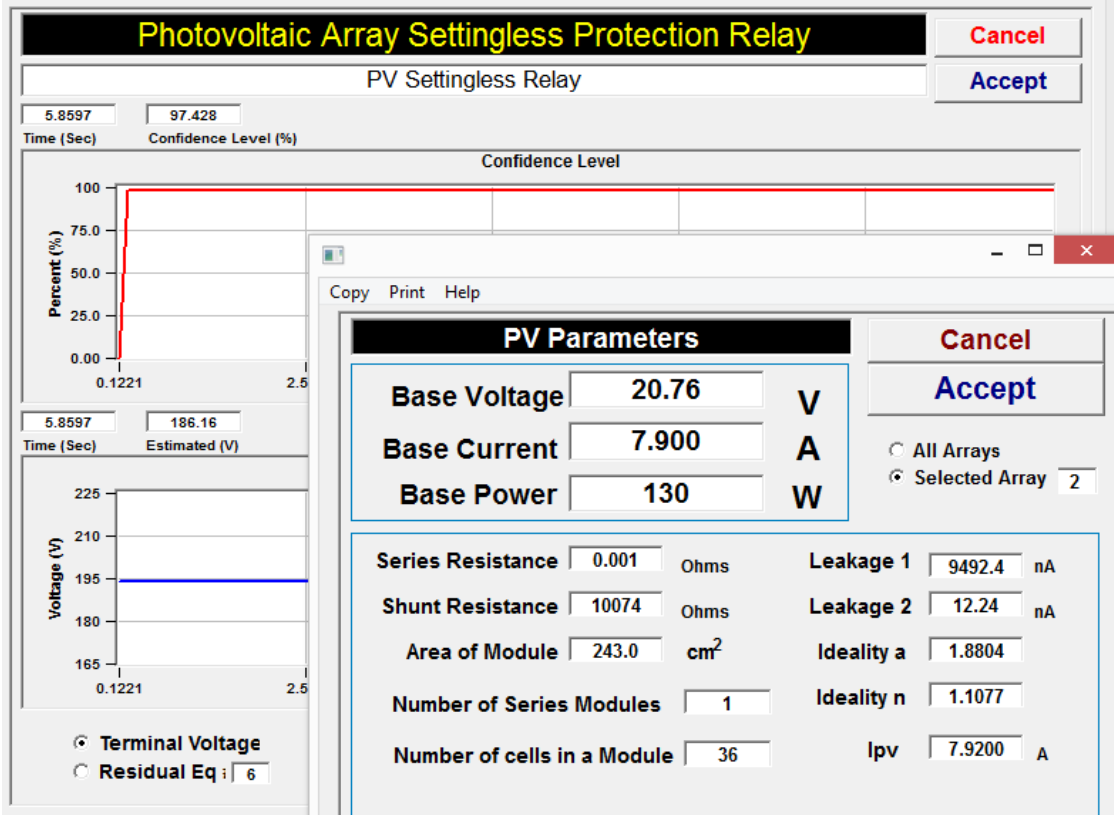
Figure 8.7:   Parameter entry for actual PV array system protection.

Following the procedures performed in chapter 7, as data measurements were taken from the PV array system, DSE was performed on the data. Applying the proposed protection scheme on the actual data from the PV array system resulted in a confidence level and the terminal voltage plots on Figure 8.8. As shown on Figure 8.8, the confidence level of the PV system is at a high value of 100%. A combined plot of the confidence level and cost function is shown on Figure 8.9. This result is in agreement with the results obtained from chapter 7.
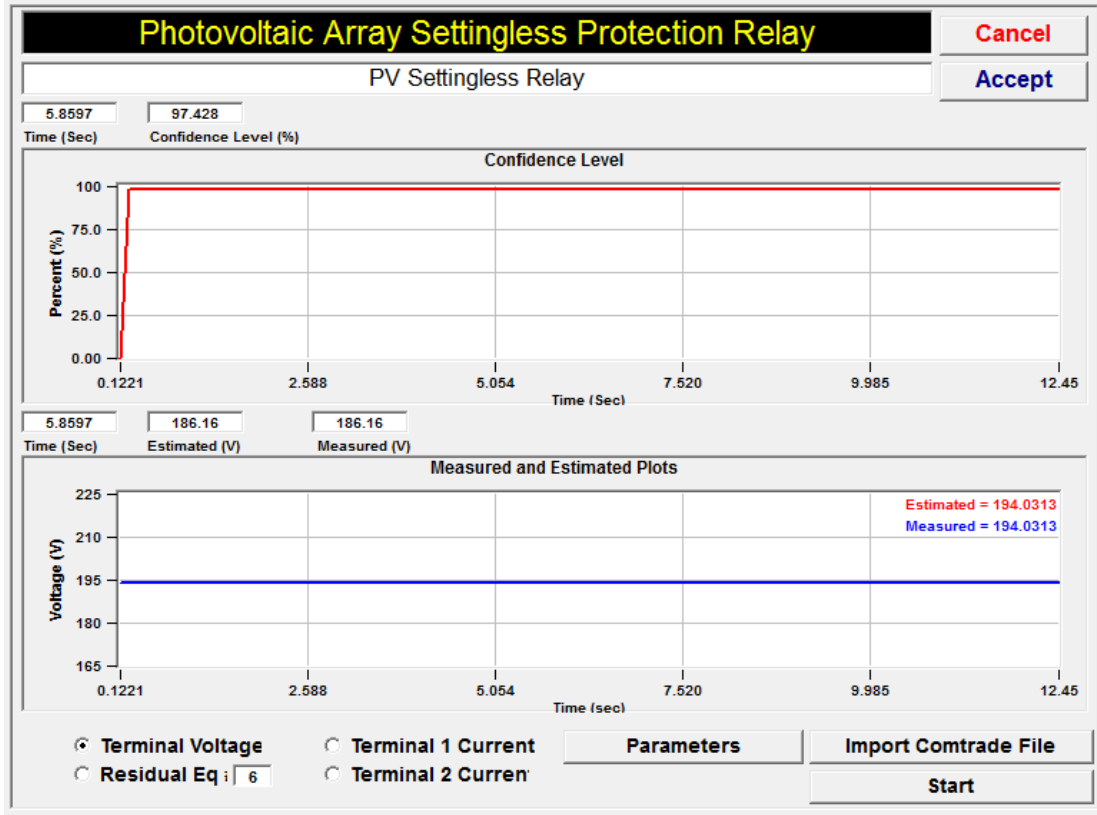
**Figure 8.8:** Actual PV array system protection result.
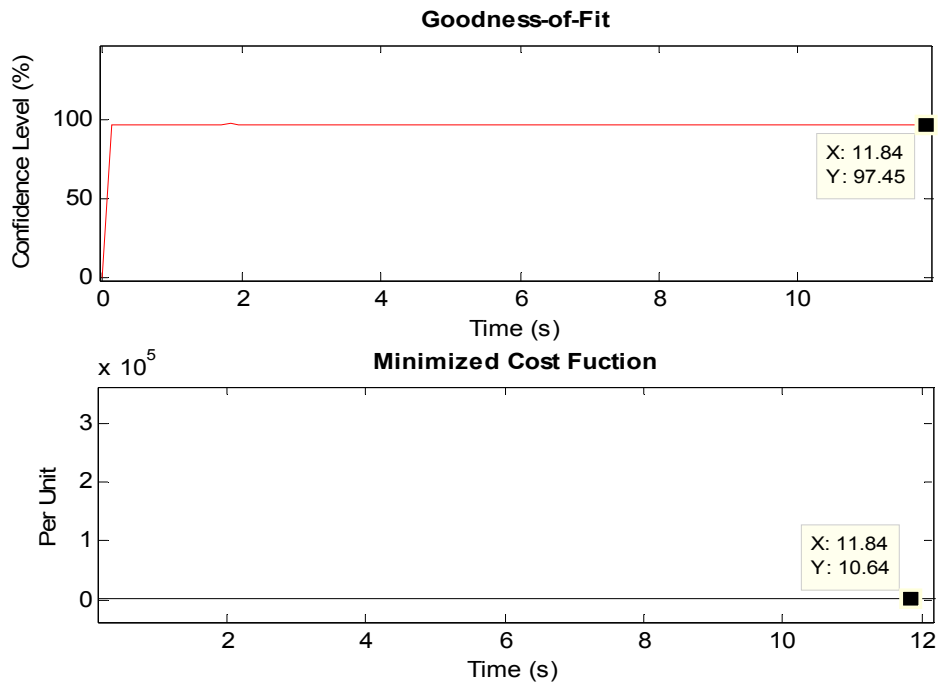

Figure 8.9: Confidence level and minimized cost function plots for a normal PV operation case.

148

Furthermore, there was a close agreement between the measured and estimated data of the PV array voltage as shown on Figure 8.10. The PV array current measurement and the currents derived from the state estimated parameters, were also compared. By comparing between the measured and computed data, it is clear that the data measurements agree as shown on Figure 8.11.
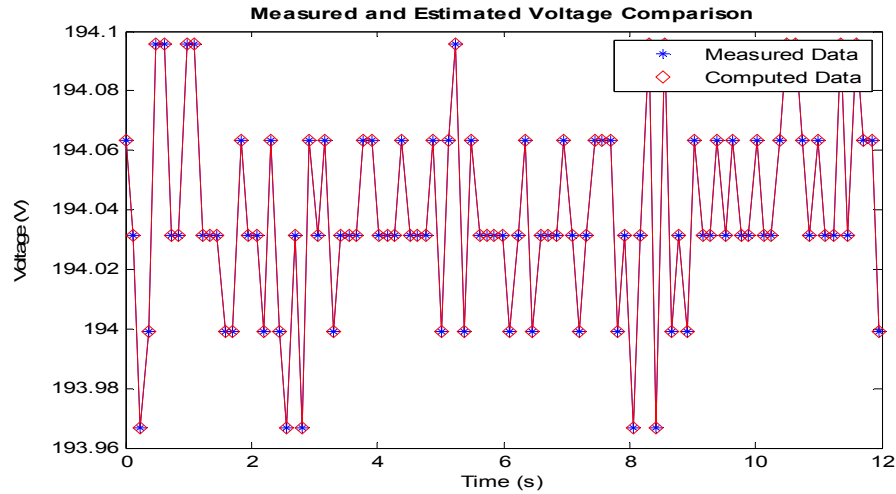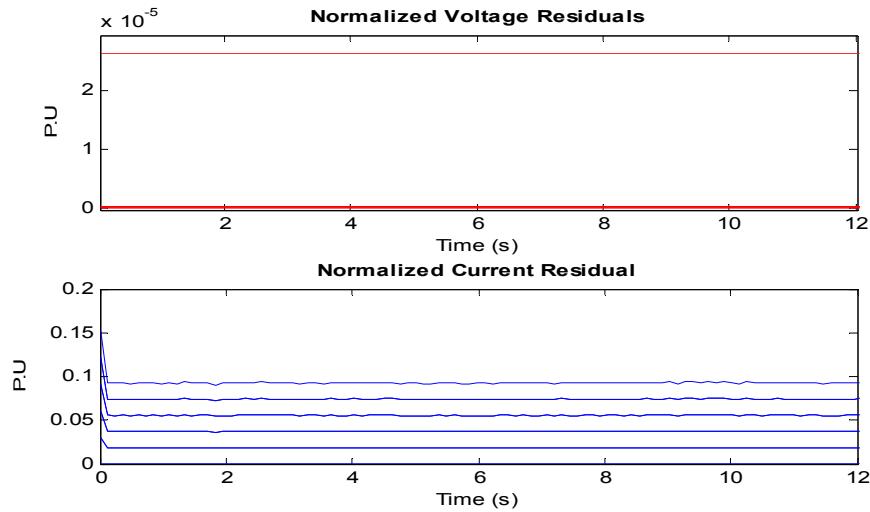

Figure 8.10:   **PV array system terminal voltage comparison - normal case.**
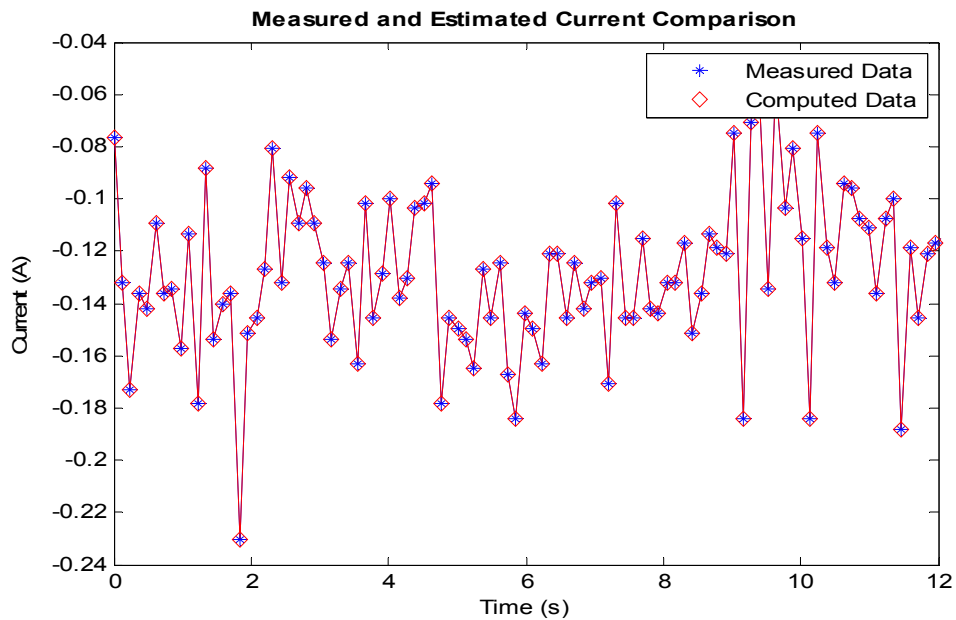
Figure 8.11:   **PV array system terminal current comparison - normal case.**

Also noteworthy is the normalized residual for the voltage and current measurements. As discussed in chapter 7, the normalized residuals give an indication of how much the computed values have deviated from the measured data. These residual plots are shown on Figure 8.12 and both have low values. These low values were expected because there are no anomalies in the PV array system.


Figure 8.12: **PV array system normalized terminal voltage and current residuals - normal case.**

From the foregoing, the results obtained from this normal-case analysis of the actual PV installation have yielded acceptable results. Next, the faulted-PV-array-system case is discussed, by demonstrating the proposed protection scheme on fault data from the actual PV installation.

8.2 Low Impedance Fault on the PV array

To demonstrate the response of the proposed protection scheme to a ground fault on the PV array system, a ground fault was initiated on the positive terminal of the PV array. The ground fault was initiated by connecting one terminal of the PV array to ground, before the current entry points to the Hall-Effect current sensors as shown on

Figure 8.13. A 60A dc breaker was connected in series with the fault-initiating resistor. The purpose of the switch was to facilitate the initiation and interruption of the PV array fault current without exposing personnel to electrical hazard. For the low impedance fault, the resistance value used was a 1 ohm resistor.
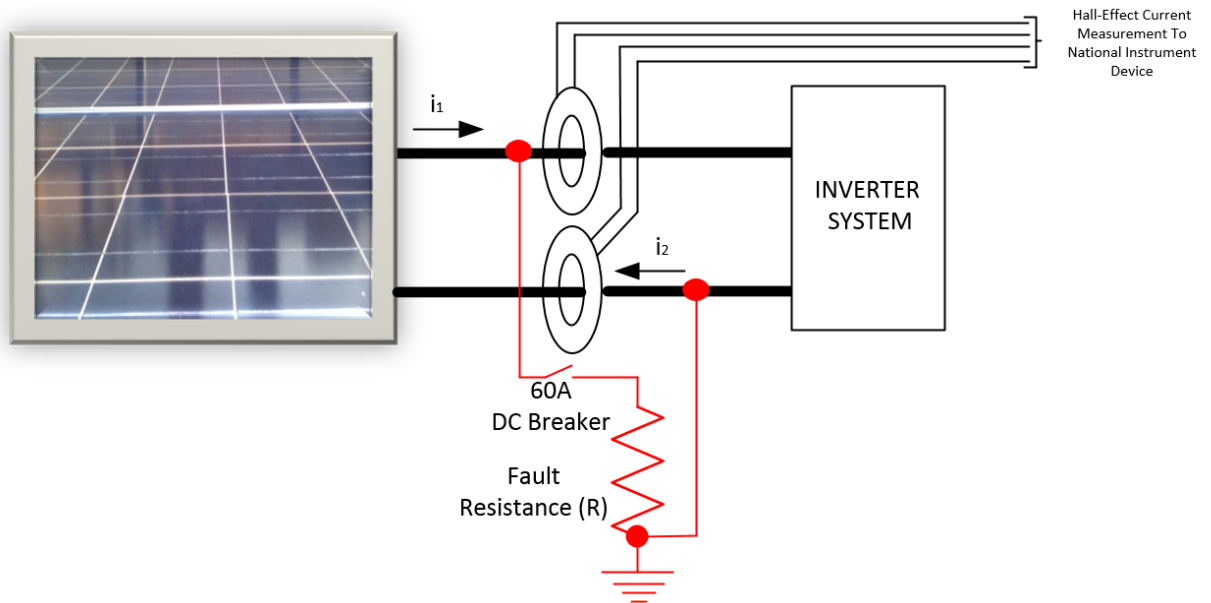

Figure 8.13:   PV array fault initiation - single line to ground case [28].

The PV array was only subjected to this low impedance fault condition for a couple of seconds. The streaming potential and current data measurements were brought to the NI device. This data measurement was stored in the IEEE C37.111 COMTRADE format using the software program WinXFM. This stored data measurements were imported to the software-based, PV array relay of chapter 7. Upon analyzing the collected data, by the application of the protection scheme outlined in chapter 6, the results showing the confidence level and minimized cost function of the PV array data was obtained. These confidence level and cost function data are shown on Figure 8.14. As shown on Figure 8.14, up to the fault initiation time, the confidence level remains high at

100%. This value drops to zero upon the initiation of the line to ground fault through the 1-Ohm resistor shown on Figure 8.13. The confidence level remains at zero until the fault is completely cleared which is just after time $t = 4$ seconds. A comparison between the measured and estimated voltage is shown on Figure 8.15, and the agreement between these data can be seen.
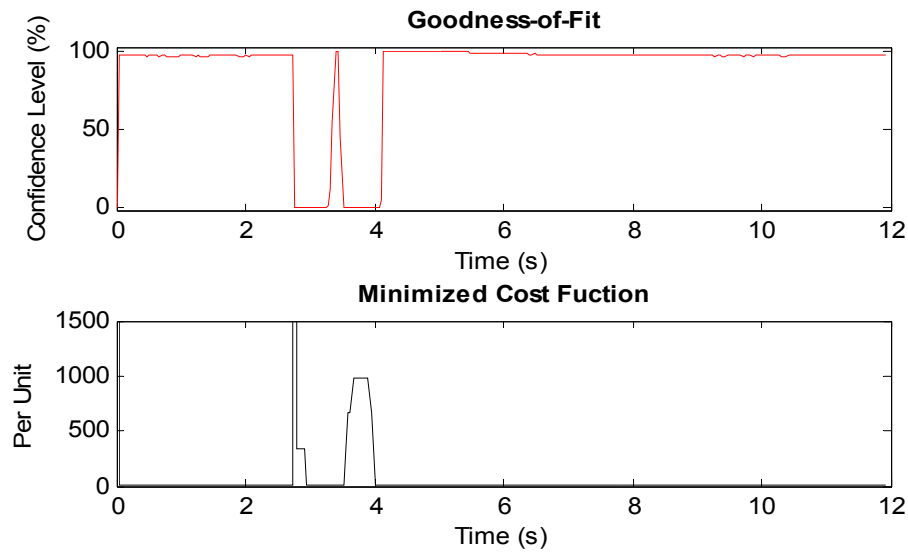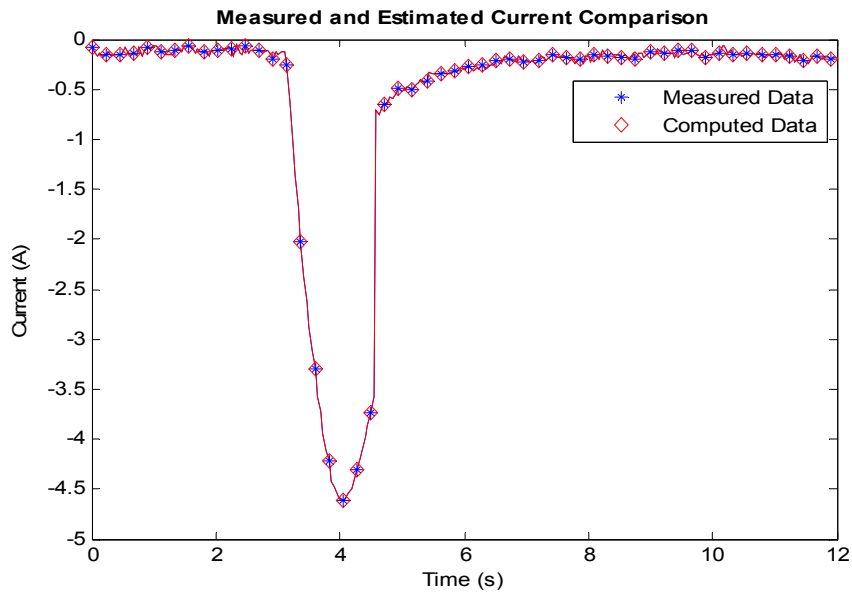

Figure 8.14: PV array data confidence level and minimized cost function - low-impedance fault.
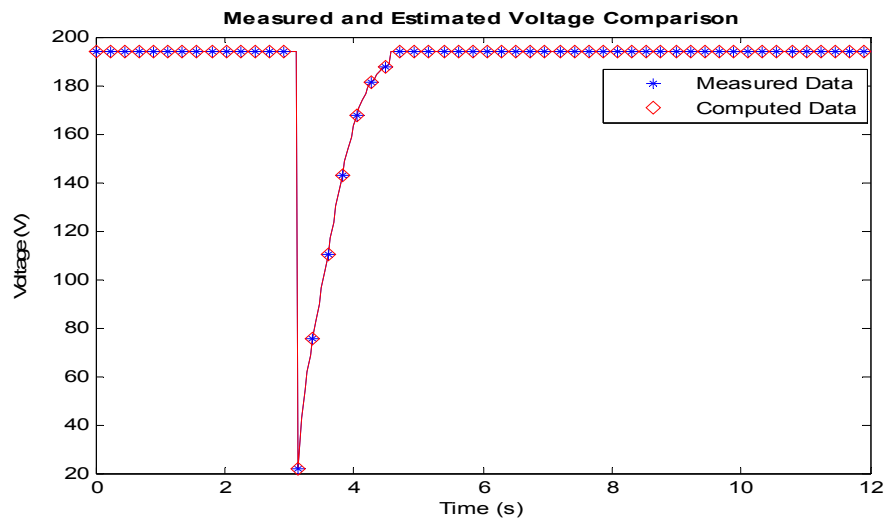

Figure 8.15: PV array measured and estimated fault voltage comparison - low-impedance fault.

The computed terminal current has been compared against the measured current from the PV array system as well. This comparison is shown on Figure 8.16, and these data agree.

Figure 8.16:   **PV array measured and estimated fault current comparison- low-impedance fault.**

The normalized residual for the single-line-to-ground-fault case is shown on Figure 8.17. It can be seen that the residual magnitude is a lot higher as compared to the normal PV array operation plot of Figure 8.12. The increase in the normalized residual values, and the cost function, coupled with the drop in confidence level, indicate an anomaly in the PV array system, for the duration shown on Figure 8.14.
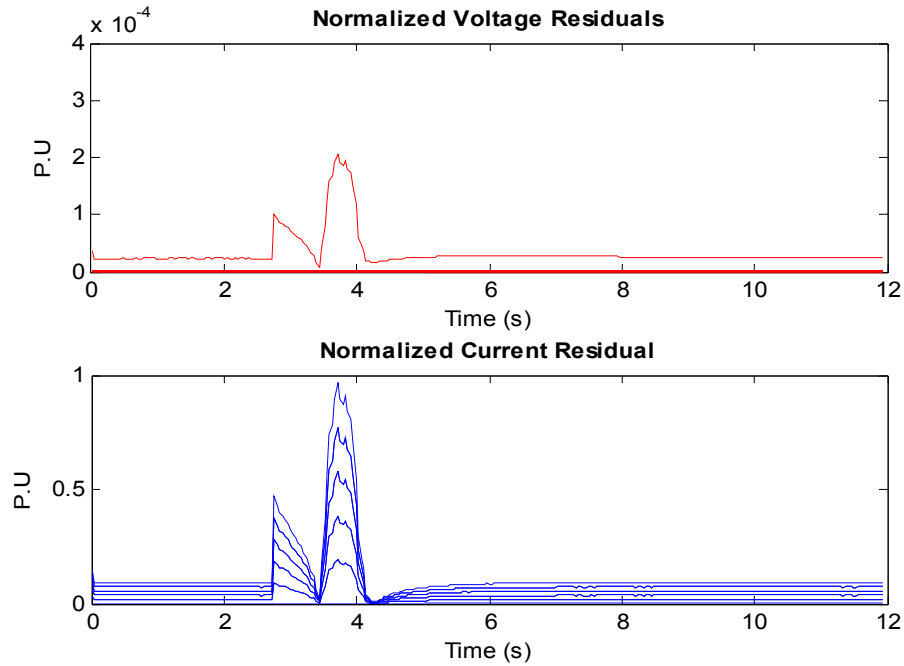
**Figure 8.17:** PV array normalized residual- low-impedance fault.

From the foregoing, the proposed protection scheme has been demonstrated on data from an actual PV array system. The protection scheme detected the abnormal operation of a single line to ground fault within the PV array system. Another type of fault is initiated on this same system, but with a higher fault impedance, to demonstrate the sensitivity of the protection scheme.

8.3   High Impedance Fault on the PV array

In this section, the PV protection algorithm is implemented under a high-impedance fault condition. For this fault, the resistor value of Figure 8.13 was a 100-ohm resistor. The value selected was one that would keep the dissipated power through the resistor within the limits of the resistor to prevent failure.

The same procedures implemented in section 8.2 were followed in this section and the obtained results are shown on Figure 8.18 - Figure 8.21. When the high impedance fault was initiated, the confidence level dropped, and the cost function was no longer minimized as shown on Figure 8.18. These changes in confidence level and cost function indicate the computed state variables are not the best set of solution for the function $h(x)$ that defines the measured data z(t). In other words, there is an anomaly in the PV array system.
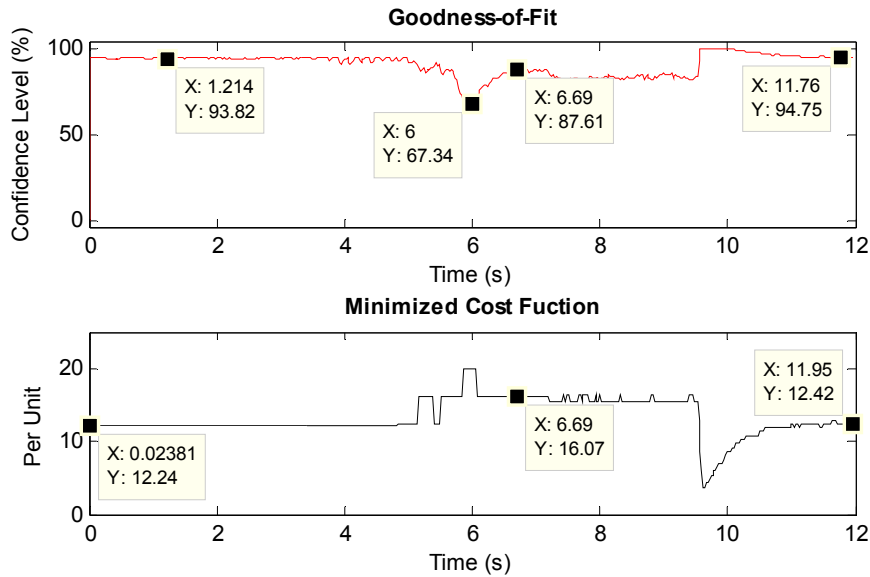

Figure 8.18: **PV array data confidence level and minimized cost function**

- high-impedance fault [28].

A comparison between the measured and computed voltage and current quantities has been performed as shown on Figure 8.19 and Figure 8.20 respectively. Although the computed voltage and current quantities appear to track the measured data, for the duration of the fault, there is a slight increase in normalized current residual plot of Figure 8.21, which should be under 0.1p.u as shown on Figure 8.12. This increase in normalized residual plot indicates an anomaly in the PV system. The normalized residual
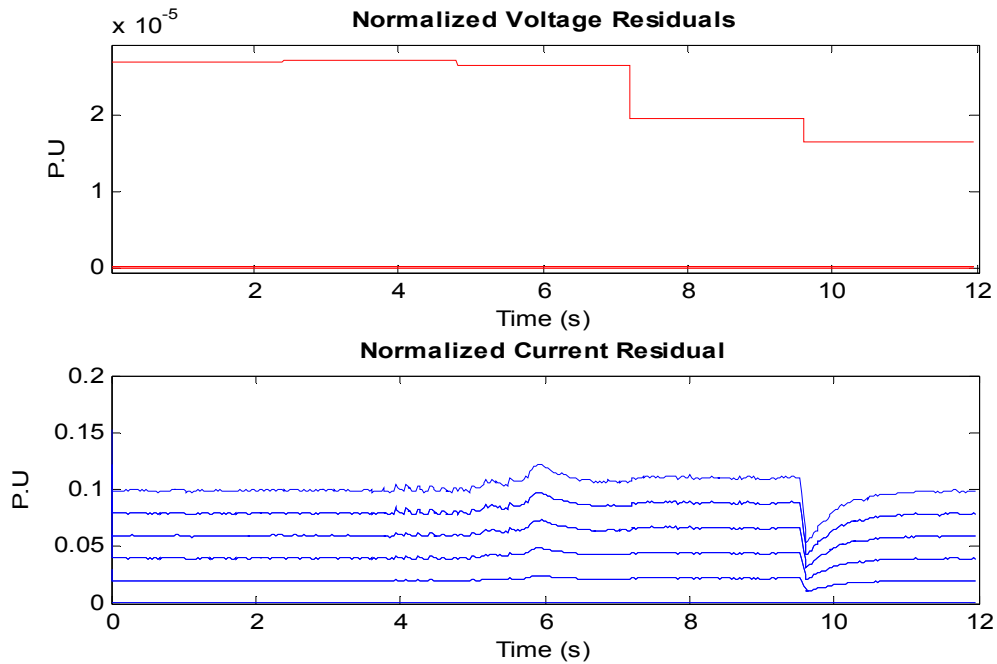
155

for this fault is not as high as the low-impedance fault case discussed in section 8.2, because the high impedance fault impact on the PV array system is a lot lesser.
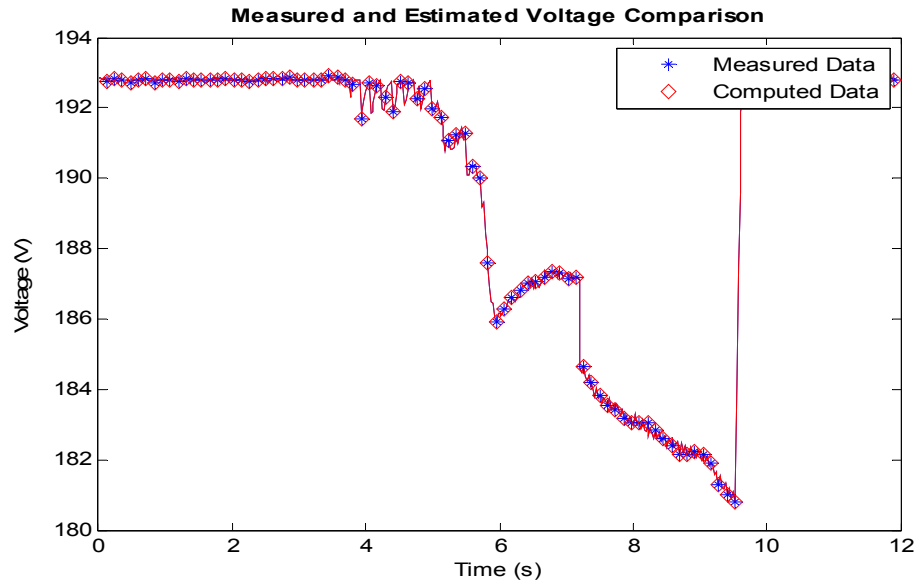
Figure 8.19: PV array measured and estimated fault voltage comparison

- high-impedance fault [28].
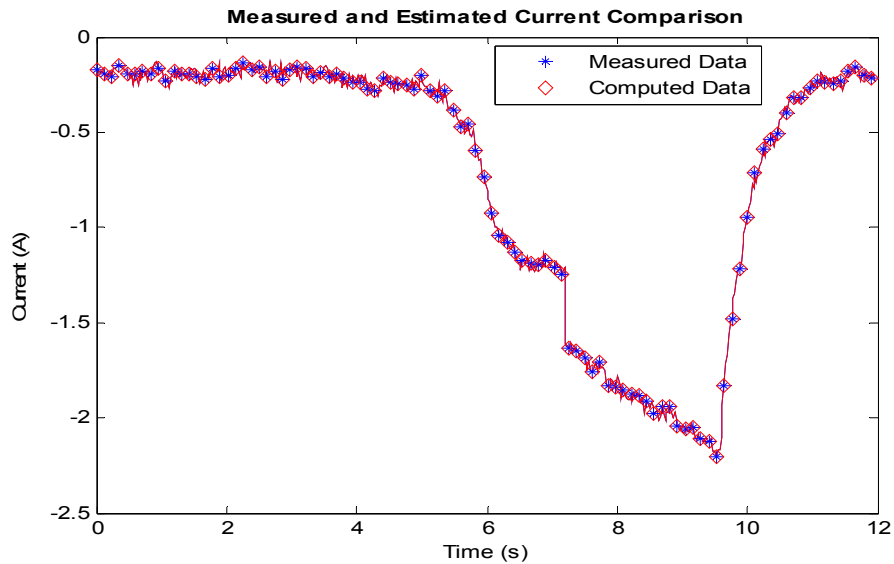
Figure 8.20: PV array measured and estimated fault current comparison

- high-impedance fault [28].

Figure 8.21:   **PV normalized residual - high-impedance fault.**

8.4   Summary

The module–level protection of the PV array system has been extended to data measurements from an actual PV array installation. The PV module parameters used for these analyses are the PV module parameters that were obtained from chapter 4. From the demonstrations in this chapter, it has been confirmed that the protection algorithm is not limited to the computer based PV array model, but also effective on date from a physical system.

Certain assumptions were made in these analyses, such as, the assumption that series connected arrays will have the same current flow, unless an anomaly exists in the system. Therefore, the measured terminal currents were extended to each PV module in

the same series connection. Furthermore, voltage readings from each of the PV nodes were not measured directly, only the terminal voltage was measured. The node voltages were assigned a pseudo measurement equal to the terminal voltage divided by 10, the total number of series connected PV modules.

From the results obtained so far, it has been demonstrated that in a larger PV array system, where extra instrumentation may be cost prohibitive, this protection scheme can still be implemented effectively. This reduction in the required instrumentation provides cost savings to the user. More specifically, as of the time of this research, the Hall-Effect sensors that were purchased for this project were $40 each. Therefore, in a large PV system were hundreds of PV modules are commonly installed, protecting the entire array with just current information at the terminals of series connected set of modules, will result in huge savings.

9 DEMONSTRATING EXAMPLE: MODULE-LEVEL MONITORING AND DIAGNOSTICS OF A PV ARRAY SYSTEM

In the chapters 7 and 8, the focus has been the identification of a fault condition on the PV array system, and also the identification of the fault location. However, in a PV system, the PV operator may be interested in other information about the PV array, such as, the performance and health of the PV modules. This chapter addresses the provision of condition based monitoring of the PV array system.

When a PV cell is shaded, it becomes reversed biased to the good PV cells connected in series with it [32]. Consequently, the shaded PV cell could serve as a load to the other good, properly functioning PV cells. Therefore, this shaded PV cell limits the current of its string of series connected PV cells. To obtain the maximum power available from the PV array, it is important that this shading condition be detected and addressed. As a solution to this issue, by-pass diodes are typically connected in parallel to PV cells. These by-pass diodes ensure that a shaded cell does not limit the rest of the cells within the series string. However, this solution only avoids, rather than solves, the shading issue. Besides, the system operator may never know that an anomaly exists within the PV array system. At a more global level, a PV module or a group of PV modules could be dusty, or shaded, compared to its other series connected PV modules. These shaded/dusty modules result in the limitation of the output of that series group of PV modules. This chapter demonstrates how the presented protection algorithm can be used to identify this shading effect. The identification of the shaded/dusty PV module condition is invaluable information to the PV operator. With the shaded PV module information, the PV array

operator can now ensure the maximum power from the PV array is always been extracted, by addressing any shading conditions on the PV array system.

Over the lifetime of a PV array installation, a given PV module may perform below an expected threshold as compared to other healthy PV modules of the same age and characteristic. This PV module underperformance could be a factor of physical damage or other defects within the module. The PV operator needs this underperformance information to perform condition-based monitoring and/or schedule proactive replacement of the defective modules. Therefore, this information can help ensure a planned outage to a section of the PV system rather than an outage due to a failed module. Besides, a failed module may lead to a longer PV system restoration time, than if the PV module or set of PV modules were repaired proactively.

Therefore, in this chapter, the PV array system is monitored to produce diagnostic data. The diagnostic feature will operate alongside the protection of the PV array system. First, the identification of PV shading is addressed, followed by the method for identifying underperforming PV modules. The combined effects of changes in temperature and irradiation on the PV array have already been demonstrated in chapter 7. It was demonstrated that these atmospheric changes do not affect the presented protection scheme. Therefore, in this chapter, the combined temperature-irradiance variation will not be covered, just the irradiation and temperature changes in relation to the shading effect and underperformance of PV modules within the PV array. Also, the standard deviation for the data measurements of this chapter is the same as Table 7.1.

9.1 PV monitoring: Identification of PV shading

To demonstrate the effect of shading on the PV array system, the irradiance on PV module No.2 (PV2) of Figure 7.4 was reduced to 99% of its nominal value. The irradiance on the rest of the PV modules was kept at the nominal value. The shading on PV2 was initiated between times100ms and 230ms. The 1% reduction in irradiance is selected to demonstrate that if the presented protection scheme works at only a 1% shading, then any worse shading condition, that is, any shading greater than 1%, will be detected with greater ease. It is expected that the shaded PV module 2 will become reverse biased, thereby serving as a load to the other healthy series connected PV modules. The simulation result of this shading is shown on Figure 9.1.
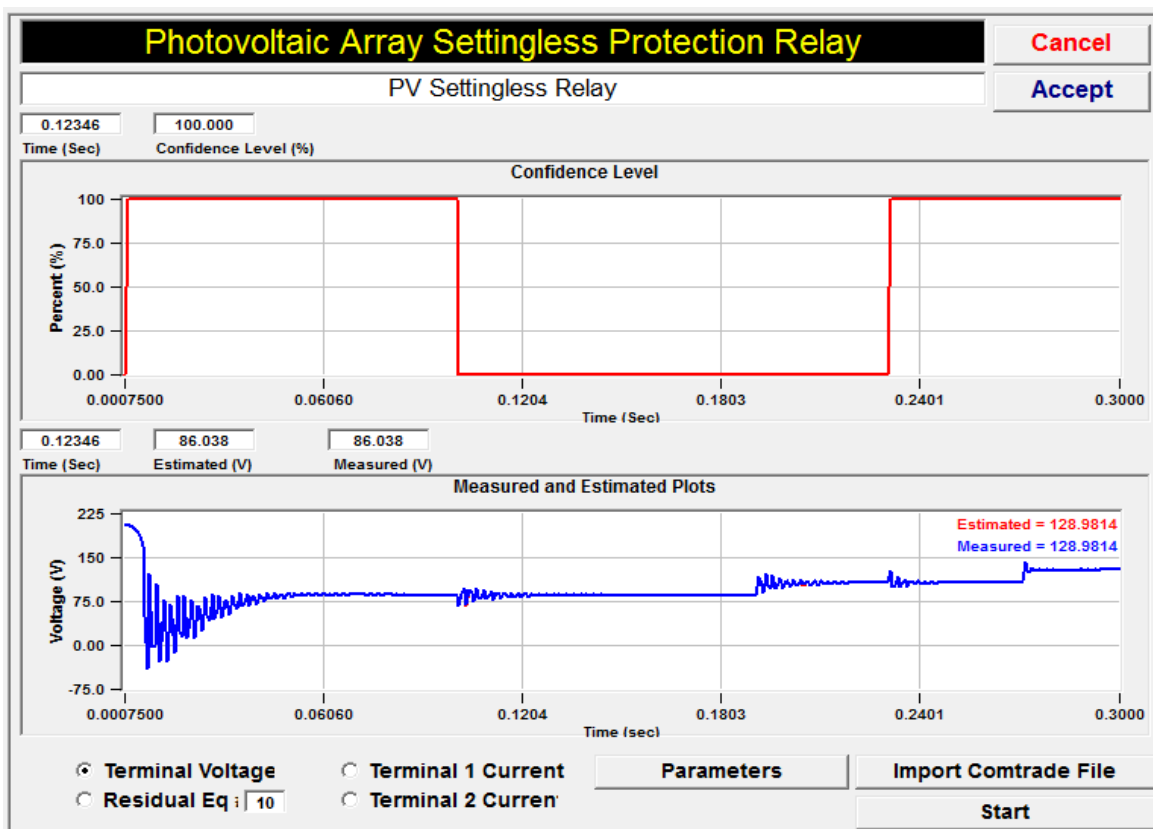

Figure 9.1:   **Confidence level and terminal voltage plots of the PV array**

with 1% shading on PV2.

During the shading of PV2, around time 200ms, the MPPT algorithm operates to find the new, optimum operating condition for the PV array. However, the protection scheme was not affected as illustrated on Figure 9.1. After the shading condition was removed at time 230ms, the MPPT begins seeking the new, optimum operation point at around time 270ms. However, the confidence level of the estimated state variables remains at the pre-anomaly value of 100%. Therefore the operation of the PV array system beyond time 230ms is said to be consistent with the PV array model. The computed and measured voltages on each of the array nodes, and the terminal currents are shown on Figure 9.2 and Figure 9.3. Also, the algebraic sum of the currents at each PV array node is given on Figure 9.4.
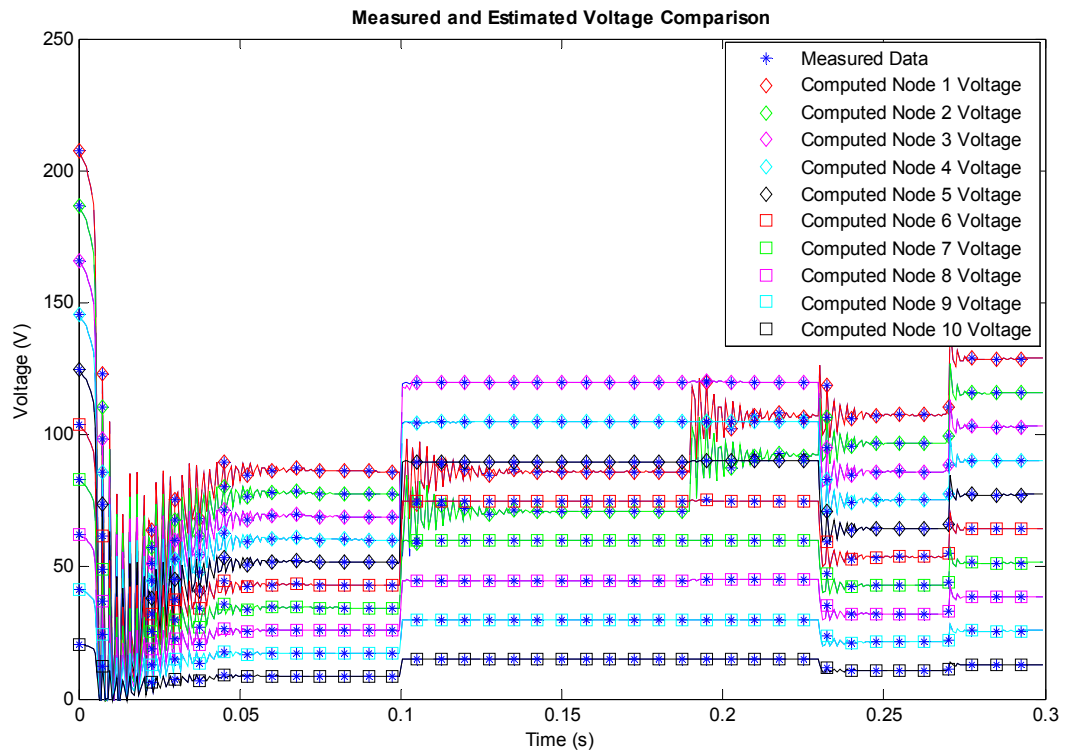
Figure 9.2:   **Terminal voltage plots of the PV array system with 1% shading on PV2.**
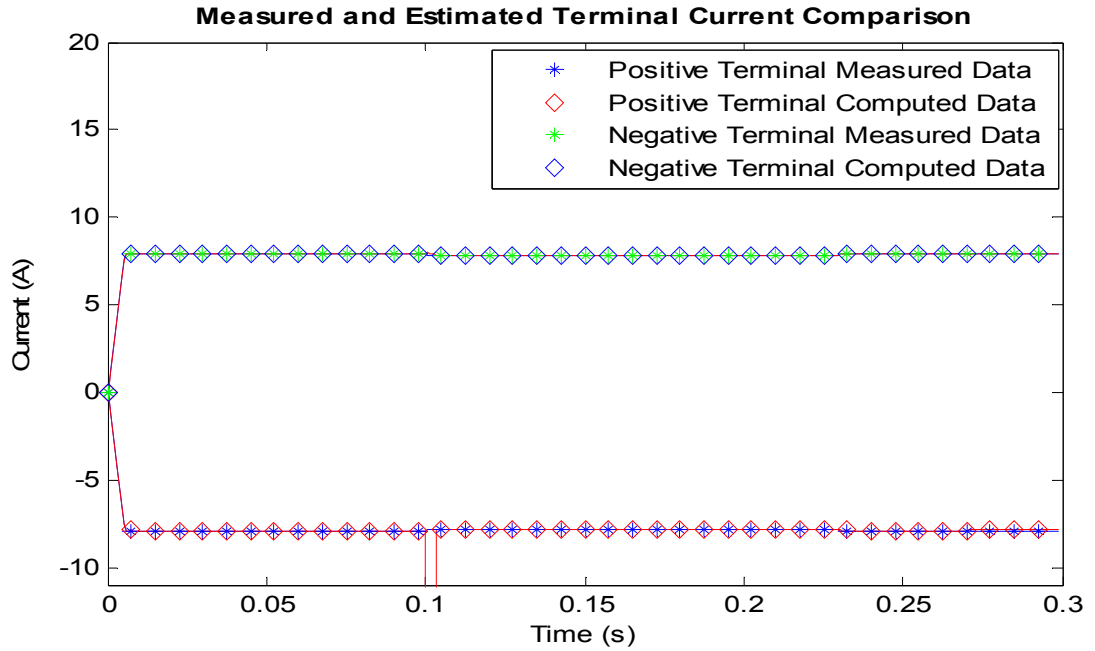
Figure 9.3: **Terminal current plots of the PV array system with 1% shading on PV2.**
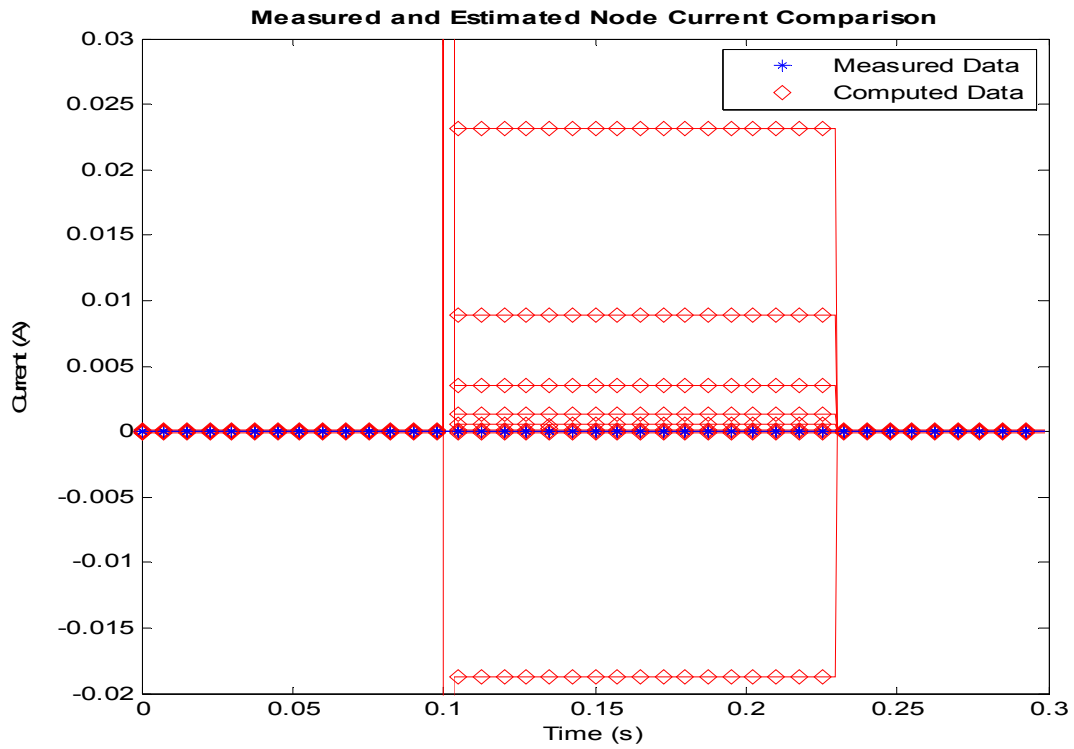

Figure 9.4: **Algebraic sum of current plots at the array nodes with 1% shading on PV2.**

The measured and computed parameters are in agreement as shown on Figure 9.2 and Figure 9.3. However, the computed algebraic current differs from the measured value as presented on Figure 9.4. The differences between the measured and computed node current measurements contribute to the drop in confidence level during the shading. Also, prior to the shading condition, the PV array terminal voltage, was previously the highest voltage in the PV array system. After the shading began, the terminal voltage of the PV became the fourth highest. The node 2 voltage, which was originally the second highest node voltage, is now the sixth highest node voltage. The drop on voltage from the positive terminal of PV module 3 to PV module 2 is due to the shading on PV module 2, which caused PV2 to be reversed biased. Once the shading on PV2 was removed the voltage relationship between the different nodes was restored as shown on Figure 9.2.

A similar result was obtained after a 1% shading on PV module 10 (PV10). The confidence level and terminal voltage plots for the shading on PV10 is given on Figure 9.5. Also, the voltages at the various nodes of the PV array are shown on Figure 9.6.
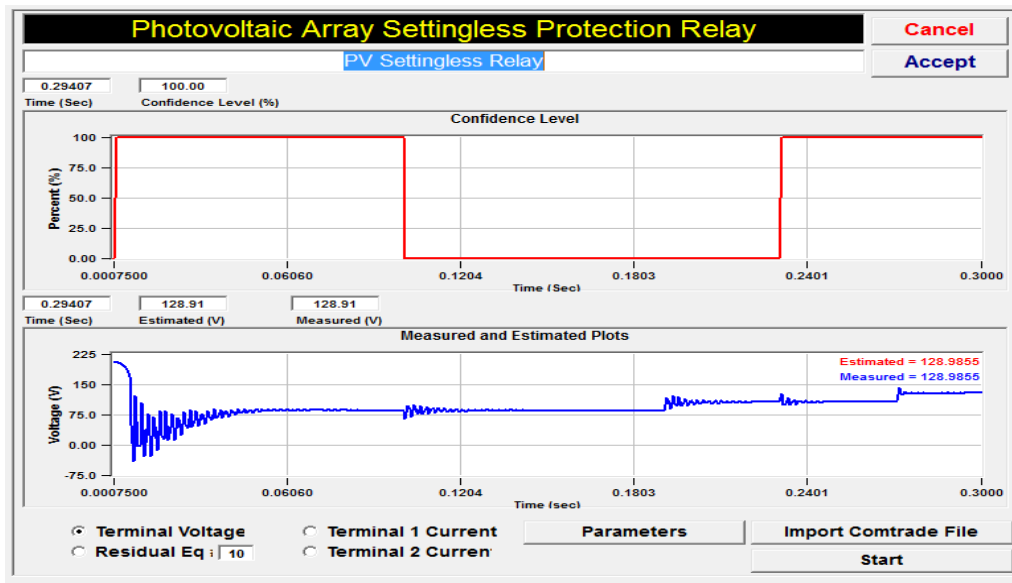

Figure 9.5:   **Confidence level and terminal voltage plots of the PV array**

with 1% shading on PV10.
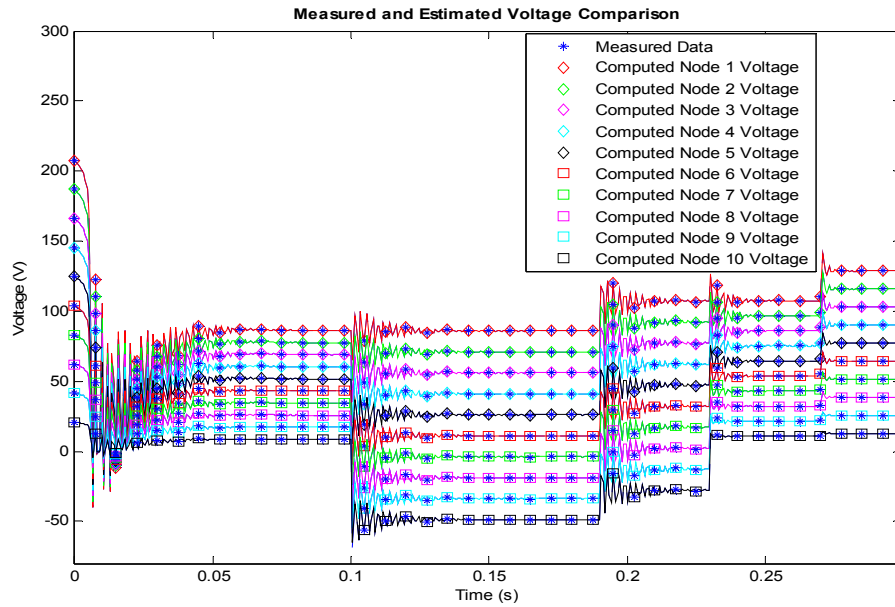
Figure 9.6:   **Terminal voltage plots of the PV array system with 1% shading on PV10.**

For this shading on PV10, the PV10 became reversed biased resulting in the negative values, relative to ground, for its next five adjacent PV modules. Although there is an agreement between the measured and computed voltage data measurements as shown in Figure 9.7, the algebraic sum of the current at the PV array nodes produced non-zero values.
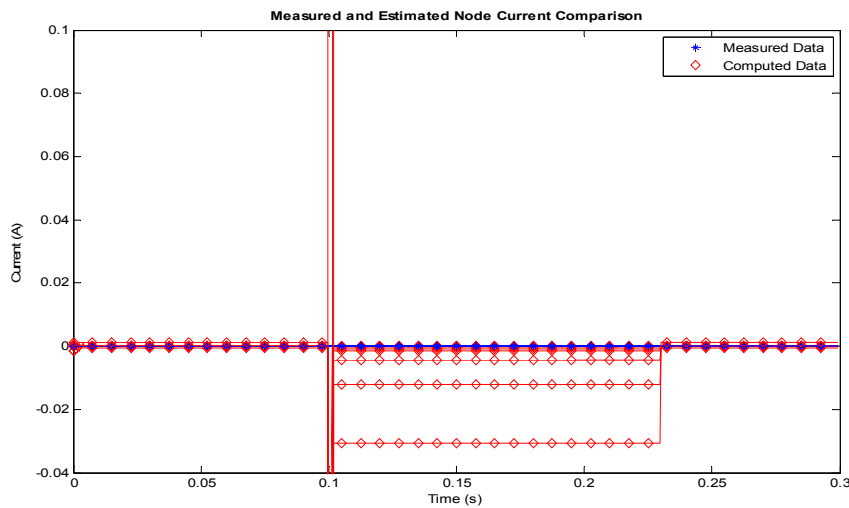
Figure 9.7:   **Algebraic sum of current plots at the array nodes with 1% shading on PV10.**

165

Therefore, the two shading conditions have been successfully identified in the PV array system, using the presented protection algorithm. Consequently, the PV system operator can be notified with an alarm, to inspect and restore the PV module/modules to its normal state.

9.2   PV diagnostics: Identification of underperforming PV module

From the state estimation-based protection scheme performed in chapters 7 and 8, and section 9.1, the voltage at each node of the PV array system is known. This section of the research uses the PV system node voltage data to validate the voltage across each PV module. From the validated voltages, if any one PV module is underperforming with respect to the rest of the PV modules, that PV number is indicated. This underperformance data is useful to the PV array operator or owner who may not just want to know that a PV module is underperforming, but wishes to also know which specific PV module is underperforming. Identifying the specific module that is underperforming eliminates the need of inspecting more PV modules than necessary. Besides, the number of PV modules in some PV array installations could be in the hundreds, therefore, randomly inspecting the PV modules to locate underperforming modules would be a time consuming effort.

In identifying the underperforming PV modules, there is no distinction between the shaded PV module condition, and a situation where the PV module is underperforming due to deterioration. To illustrate the PV module underperformance identification, two examples are given. The first example is the analysis of the shaded PV2 of section 9.1. The second example is one where PV modules 2 and 7 are subjected

to a slightly higher temperature than the other PV modules. A flow diagram showing the steps for identifying underperforming PV modules is given on Figure 9.8.
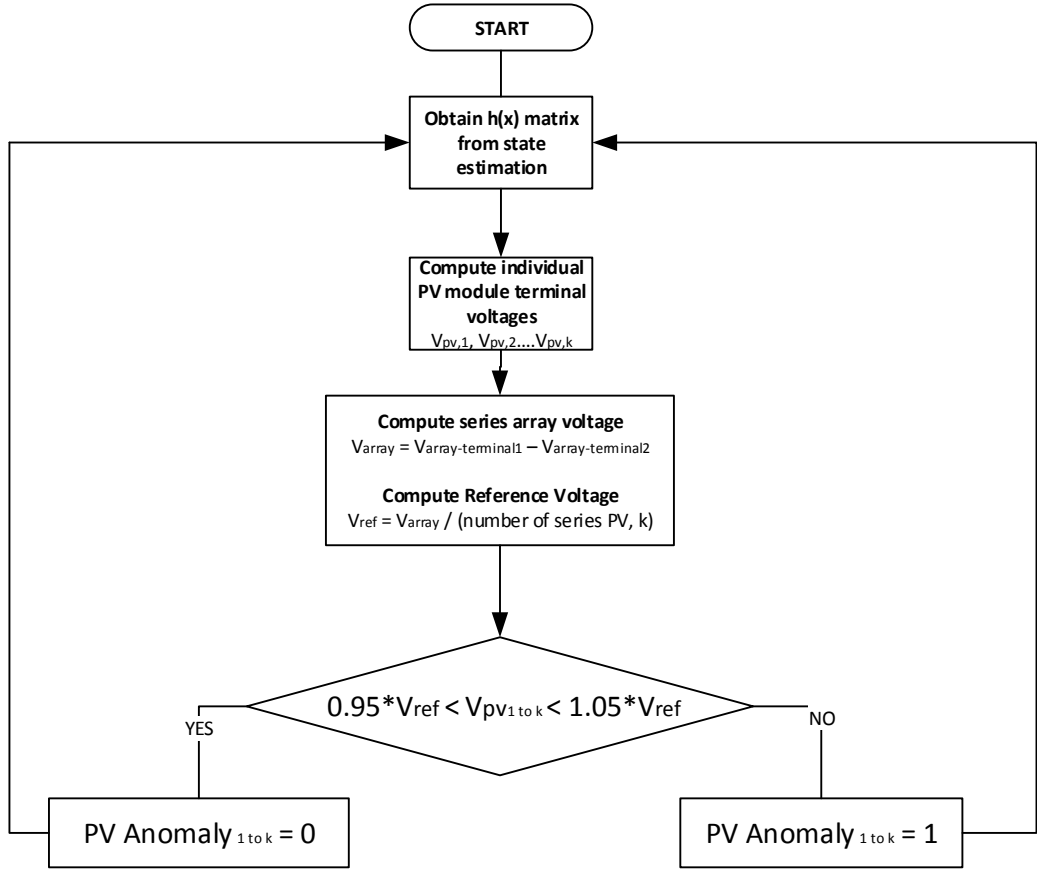

Figure 9.8:   **Flow chart of PV array system diagnostics.**

As shown in the logic diagram of Figure 9.8, the voltage of each series connected PV module is compared against a reverence voltage V_{ref}. This V_{ref} is the average voltage across the set of series connected PV modules. That is, for k series connected PV modules,

$$V_{ref} = \frac{1}{k}\sum_{i=1}^{k} v_i,$$ (9.1)

where i is the series PV module index. If any of the PV modules has a terminal voltage that is less than or greater than V_{ref} by 5% or more, the PV module is identified for the PV system operator to inspect. This voltage validation process is performed for all the PV modules, while the protection scheme is implemented.

By applying this logic flow to the PV2 shading condition of section 9.1, a continuous validation of each of PV module voltage was performed. The simulation result from this monitoring is shown on Figure 9.9. The plot on Figure 9.9 is consistent with the PV2 shading condition of section 9.1, because it was on PV2 that the shading was done.
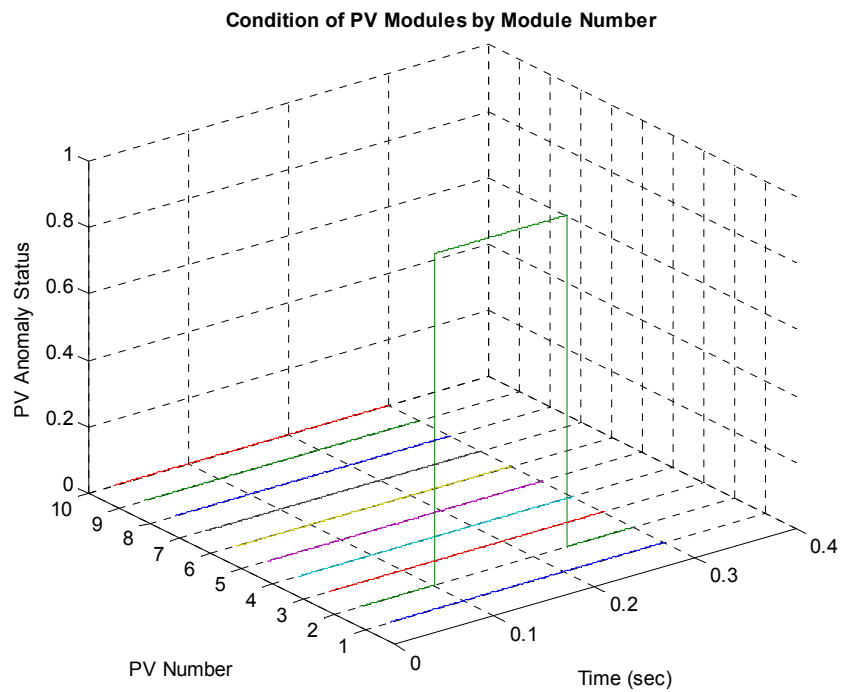
Figure 9.9:   **PV module status plot indicating the underperformance of PV2 module.**

168

In the next illustration, the temperature of a PV module is changed to simulate an underperforming module. The open circuit voltage of the PV module is a temperature dependent quantity with the relationship

$$V_{oc} = V_{oc,n} - k\Delta_T,$$ (9.2)

where k is the PV module voltage temperature coefficient, and Δ_T is the change in temperature from STC. The term $V_{oc,n}$ is the nominal open circuit voltage of the PV module. The PV module current is also temperature dependent as given in (3.6), also repeated in (9.3).

$$i_{pv} = \left(i_{pv,n} + k_1\Delta_T \right) \frac{S}{S_n}.$$ (9.3)

Therefore, from (9.2) and (9.3) a change in temperature of a PV module will affect the voltage and current of that PV module. If the affected PV module is within a set of series connected PV modules, its terminal current has to be the same as the current through the other series modules. In other words, the PV module with the least terminal current will effectively limit the current flow in its other series modules. For this reason, in determining the performance of the PV array, emphasis was given to the validation of the terminal voltage of the individual PV modules. The voltage validation also provided information that identified the least power producing PV module. That is, given the same current through a series connected PV array, the PV module operating at a lower terminal voltage yields less power than the other PV modules.

A 10% PV module temperature increase was initiated on PV module 10 between time 150ms and 200ms. The temperature of the other PV modules in the series set was kept at 300° K. The confidence level and PV array terminal voltage plots obtained from

this temperature change is shown on Figure 9.10. From Figure 9.10, after the temperature change was initiated at time 150ms, the confidence level dropped to 95%. At time 175ms, the MPPT sought for the new, optimum operation point for the PV array system. This MPPT operation made the temperature change anomaly more pronounced because as the PV module voltage increases, the PV module moves to the region of its I-V curve where the current at a given voltage is significantly different from one temperature to another temperature at the same voltage.
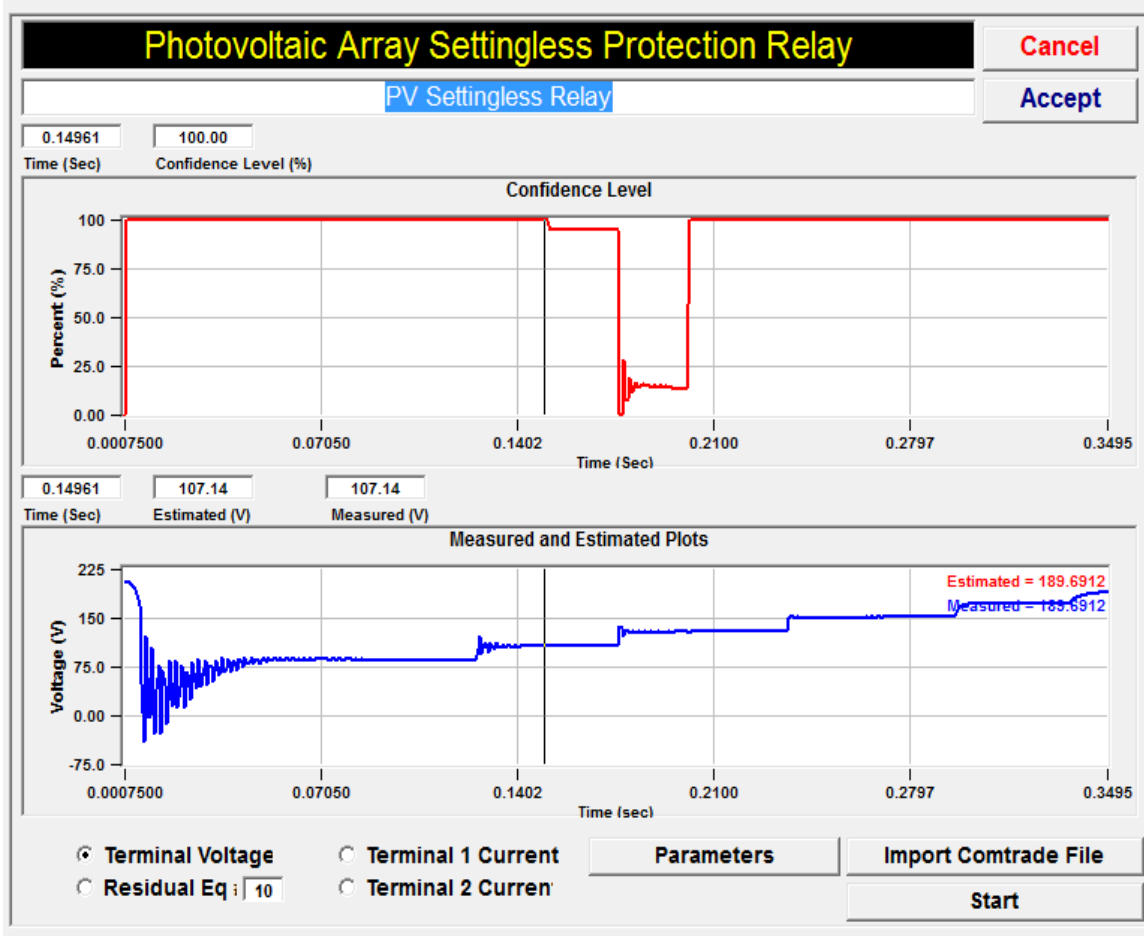

Figure 9.10: Confidence level and minimized cost function plot for underperforming PV.

The MPPT operation resulted in the decrease in confidence level to 20% as shown on Figure 9.10. From the foregoing, it is not sufficient to only monitor the confidence level in the determination of underperforming PV modules. Some underperformance as shown between times 100ms and 175ms may not be significant enough to be identified as an anomaly. However, by applying the voltage validation diagnostics logic of Figure 9.8 to the PV array system, the plot on Figure 9.11 was generated. From Figure 9.11 the anomaly in the PV array system was recognized starting from its inception at time 150ms, till it was cleared at time 200ms. Moreover, the specific PV module that was underperforming has been indicated, which is PV module 10.
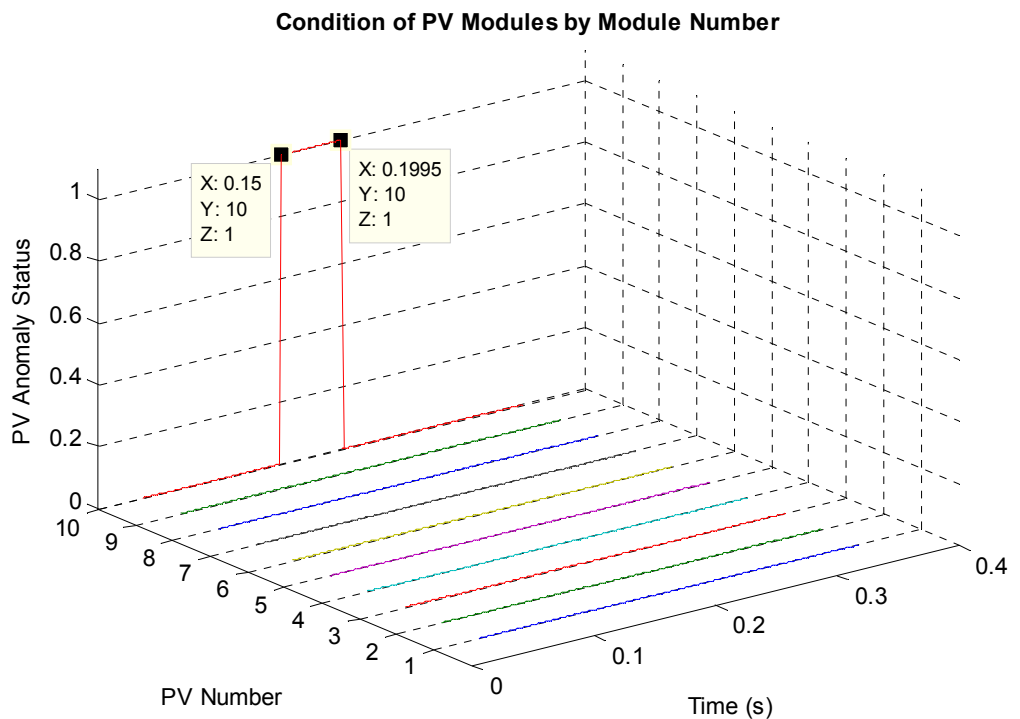
Figure 9.11: **PV status indicating an anomaly on PV module 10.**

Therefore, using the logic on Figure 9.8, no guesses have to be made regarding which PV modules need to be inspected and possibly replaced. The logic on Figure 9.8

171

identifies the specific underperforming PV module/modules as shown on Figure 9.9 and Figure 9.11, thereby, reducing the PV anomaly troubleshooting time.

9.3 Summary

In this chapter, the shading effect on a system of PV array has been simulated numerically. Using the proposed settling-less protection scheme, the shaded PV module was identified. Also, the logic for identifying an underperforming PV module has been demonstrated. Therefore, in addition to protecting the PV array system from various fault conditions as illustrate in chapter 7, chapter 8, and Appendix F, the condition-based monitoring of the PV array system has been implemented using the software-based PV array relay. With the combination of these protection and diagnostic schemes, the PV operator/owner is always aware of the health of the PV array system, and is guaranteed that the entire PV array system is adequately protected.

This PV array health information that is provided to the PV operator aids in reducing the downtime of the PV array system. Using the PV array health information, the PV array operator can schedule a planned PV system outage for maintenance, or proactively replace PV modules that have been persistently underperforming. The alternative to proactive replacement of underperforming modules is to waiting till a PV module fails, after which it is replaced. But this alternative could lead to a longer downtime of the PV system. Ultimately, these protection and diagnostic schemes ascertain the maximum output power potential of the PV array is attained, because any shading effects and/or underperforming PV modules are detected and identified as have been illustrated.

10 CONCLUSIONS AND FUTURE WORK

In this chapter, the conclusion of this research including the contributions and significance of each contribution is discussed. Also, the potential future work of this research is addressed, and a listing of the publications/awards during this research has been provided.

10.1 Conclusion

In this research, a recently developed protection scheme - the setting-less protection, has been applied, for the first time, to the field of PV arrays. Also, to date, this protection algorithm has been implemented on traditional protection zones for individual power system devices, but this research extends this protection to a microgrid, specifically, a system of PV network composed of several PV modules. Several illustrative examples have been included in chapters 7 through 9. These examples demonstrate the effectiveness of this protection scheme even in the presence of changing atmospheric conditions and with the operation of MPPT equipped dc-dc converters.

10.1.1 Contributions of Research

Under this research, the following contributions have been made to the field of PV arrays modeling, protection and control. These contributions are as follows:

- the development of the model of a PV module using QI modeling,

- the steps for extracting parameters of a PV module,

- the application and extension of the setting-less protection scheme to the protection of an integrated system of devices, namely, the PV modules,

- a method to determine the location of a faulted PV module within an array

- a scheme for providing condition-based monitoring of PV array systems.

The significance of each of these contributions is discussed next.

10.1.2 Significance of each Contribution

In this research, five major contributions have been made in to the PV industry. In this section, these contributions along with the significance of the contributions are discussed.

A two-diode PV model has been developed using QI modeling. This modeling applies a scaling factor to the Taylor series expansion of the exponential terms of the model of the PV module. Then the higher order terms of the Taylor series expansion are reduced to at most second order terms using the quadratization technique. By applying the scaling factor, the resulting model of the PV module becomes more accurate than if the scaling factor were not used. The order of accuracy of this scaling factor over the same Taylor series expansion without the scaling factor has been demonstrated to be in the order of 10^{-9} [27]. This developed model of the PV array was simulated to compare its performance with a physical PV module with acceptable results as demonstrated in section 3.3. The significance of this PV model is that its accuracy will aid in performing accurate PV array system state estimation, reliable condition-based monitoring of the PV array, accurate load flow analysis, and other microgrid/power system-based analytical studies.

The accuracy of the model of the PV module is only realized when correct parameters of the PV module have been determined. Therefore, for this research a novel approach to extract the PV parameters, namely, the ideality constants, leakage currents, PV module internal current, shunt resistance and series resistances has been presented.

This approach is based on the use of an extra PV measurement point to solve five of the PV parameters, namely, $I_{01}, I_{02}, R_s, R_p, I_{pv}$, using the Steepest Descent numerical method. In addition, the Fibonacci optimization method was used to determine the other two PV parameters, which are the ideality constants a, and n. A comparison was performed between numerically generated data using the determined PV module parameters and data measurements from a physical PV module. It was shown that the maximum error from this comparison was below 0.12A for the PV modules used for this research. This contribution is important because accurate PV module parameters are required to adequately model the PV module. Besides, the presented PV protection approach for this research requires an accurate model of the protected system. Therefore, these extracted parameters ensure an accurate PV model is used in the PV array protection.

Up to this point, the recently developed setting-less protection has only been implemented on traditional zones of protection for individual power system equipment. This research extends this protection to a system of PV array. Demonstrative examples have been provided to show the protection of the system of PV arrays. On the significance of this contribution, by implementing the PV array protection as a system, one relay can be used to protect the entire PV system without loss of sensitivity for cell-level anomalies within PV modules [34]. If this protection were done at individual PV module protective zone level, this research, for example, would have required 10 individual relays to protect all the individual PV modules. The significance of this contribution is that the PV array is adequately protected against various anomalies that PV array systems are subjected to. Thereby, ensuring the designed lifespan of the PV

array system is realized. Also, the significance of the system level protection is that it results in cost savings to the PV owner for an application where this protection scheme is developed into a physical substation device. The significance of this contribution becomes more apparent in the protection of larger PV installations where a lot more PV modules are interconnected.

The residual data from the PV array protection scheme has been used to develop a method for identifying the location of faulted PV modules. The significance of this contribution is that it saves the PV operator a tremendous amount of time in the inspection of various PV modules to determine the faulted module. The time savings becomes more significant in larger PV installations. By quickly determining the location of the faulted PV module, steps can be taken to isolate and/or replace the faulted module and re-energize the PV array system. This quick PV array system restoration and reconnection to the power network, reduces the downtime of the PV array. Besides, reducing the downtime of the PV array ensures the lost revenue incurred by the PV owner is minimized.

Lastly, in this research, condition-based monitoring of the PV array system has been presented with examples. From the PV array system monitoring, the shading and underperformance of a PV module are identified and brought to the attention of the PV system operator. This information is invaluable to a PV system operator, and is a significant contribution in the PV industry because it maximizes the power yield of the PV array. The maximization of the PV array power output yield is possible because of the PV array condition data. From this data, the PV operator can schedule a planned outage to perform maintenance to, or proactively replace underperforming PV modules. This

maintenance/replacement ultimately extends the life of the PV array and maximizes its output power yield, which consequently maximizes the revenue to the PV owner.

10.2 Future work

This research has covered several topics in the PV modeling and protection fields. However, there are some areas that can be further researched on. Therefore, this section discusses the areas that further research can be performed.

This research was based on an actual system that is comprised of 10 identical series connected PV modules. Therefore, the developed PV array system for this research was developed to match this system. Numerical simulations of the protection of a series, parallel PV array system have been performed in [34]. However, this protection has not been performed on data from a physical series, parallel PV array system. As a follow up to this research, the developed integrated system of PV array will need to be extended to a physically installed series, parallel PV array system.

Furthermore, under this research, one set of PV parameter was used to form the system of PV array. The use of one set of PV parameter was because the PV modules for this research were identical. In general, PV module parameters in a larger PV array installation may be different, and have slightly different characteristics. The system integration method outlined in this research will need to be modified to accept and use different sets of parameters to reconstruct the integrated PV system model. This integrated PV system will now be comprised of dissimilar PV modules. Additionally, the scheme for detecting an underperforming PV module will need to be modified to include PV array systems with dissimilar PV modules. A modification of this underperformance scheme is required because, given the parameter differences among the PV modules, the

PV system voltages may not be evenly distributed across a set of series connected PV modules.

The protection and demonstration discussed in this research uses a personal computer for its computation. Another area of future work is the development of a protective relay hardware, a physical PV array relay. This relay would contain the necessary computer processor and the input terminals for accepting and calibrating the various PV array measurements. These measurements include voltage, current, temperature and irradiance measurements. Also, this relay should have the required communication infrastructure for the PV operator to download PV event reports. This equipment will then become a standalone hardware that can be used within the microgrid for the protection of PV arrays.

10.3 Awards and Publications

Awards

GE-Georgia Tech Year 3 Smart Grid Challenge Runner-up Award for the challenge problem: Reduction of fossil fuel spinning reserve in the power system.

Publications

[1] A. Umana, A. Meliopoulos, "The modeling of a two-diode photovoltaic modue for power system simulations," *47th North American Power Symosium,* 2015.

[2] A. Umana, A. Meliopoulos, "The extraction of photovoltaic module parameters using Fibonacci and Steepest Descent methods," *47th North American Power Symosium,* 2015.

[3] A. Umana, A. Meliopoulos, "Detection of cell-level fault conditions within a photovoltaic array system," *IEEE PES Transmission and Distribution Conference and Exposition*, 2016. In Press.

[4] D. Zhao, A. Melioupous, Z. Tan, A. Umana, R. Fan "A market-based operation method for distribution system with distributed generation and demand response," *North American Power Symosium,* 2013, pp. 1-6.

APPENDIX

Appendix A Model of Lead-Acid Battery

In this appendix, the mathematical model for the lead-acid battery is presented. Furthermore, the algebraic companion model form for the lead-acid battery is derived. The schematic for the lead acid battery is depicted in Figure A.1. This schematic, which was obtained from [35], is used for the lead-acid battery modeling.
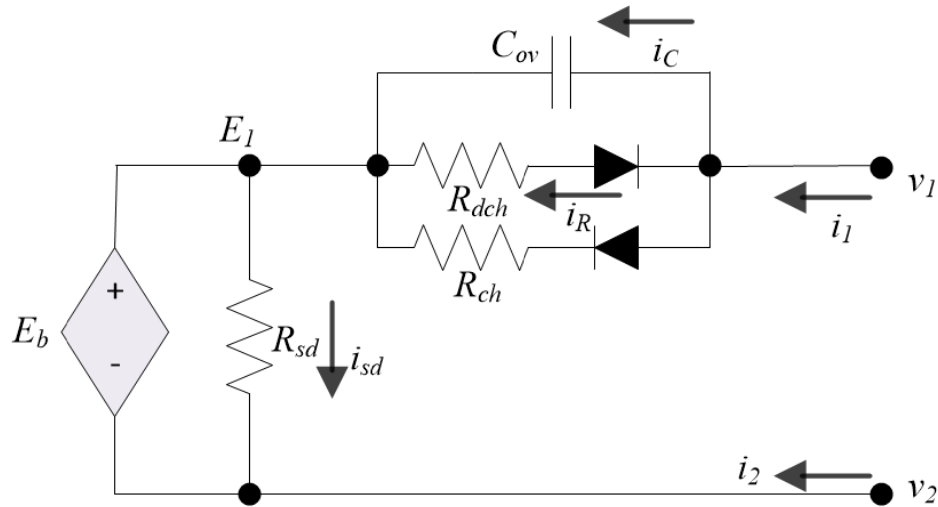
Figure A.1: Schematic for Lead-Acid Battery.

A.1. Time-domain Model of a Lead-Acid Battery – Compact Form

From Figure A.1, the lead-acid battery model can either be in the standby mode, charge mode or the discharge mode. In the standby mode, the capacity of the battery slowly decreases due to the current i_{sd}, however, the battery would have to be in the standby mode for a considerably long time to significantly reduce the battery capacity. In the charge mode, the R_{dch} branch in the capacitor-resistors parallel circuit of Figure A.1

is seen as an open circuit while the R_{ch} branch is seen as an open circuit during the discharge mode.

The series charging resistor R_{ch} is divided into two resistances to account for the initial transience of the battery in [35]. The two resistances are shown in (A.1). Also, the series discharging resistor R_{dch} is composed of two resistances as shown in (A.2), where the resistance with the subscript i accounts for the change of terminal voltage from the open circuit voltage during the transient interval.

$$R_{ch} = R_{bci} + R_{bc}. \qquad (A.1)$$

$$R_{dch} = R_{bdi} + R_{bd}. \qquad (A.2)$$

The transience in the lead-acid battery dies off within 5 minutes, therefore, for this lead-acid battery model, the resistance due to the transience will be ignored. From [35] R_{bc}, R_{bd} and R_{sd} for a Yuasa NP4-12 battery are expressed as a function of the state of charge (SoC), and are shown in (A.3) and (A.4), which are given in ohms, and (A.5) which is given in kΩ.

$$R_{bc} = 9.32x10^{-5}(SoC)^2 + 0.01(SoC) + 0.028, \qquad (A.3)$$

$$R_{bd} = 2.926\exp(-0.042 * SoC), \qquad (A.4)$$

$$R_{sd} = -0.039(SoC)^2 + 4.27(SoC) - 19.23, \qquad (A.5)$$

The capacitor in the capacitor-resistance parallel circuit of Figure A.1 is expressed in (A.6),

$$C_{ov} = \frac{t_{ov}}{5R_{bdi}}. \qquad (A.6)$$

where t_{ov} is the setting time of the transience, and R_{bdi} (or R_{chi} in the case of charging) is the resistance during transient interval.

However, since the transient interval is ignored in this model, a steady state capacitive value of 40F (obtained from [35]) is used for the simulation of this lead-acid battery.

The relationship between SoC and the operating current is given in (A.7) .

$$0 = i_1 - \left(\frac{C_n}{100}\right)\frac{d}{dt} y,$$

(A.7)

where C_n is the nominal capacity of the battery in amp-hours and y is given as follows:

$$y = SoC - SoC_o.$$

(A.8)

The SoC_o term in (A.8) is a constant. The lead acid battery can operate either in the discharge or charge mode, therefore, similar models have been developed for these modes. Also, when the SoC goes to zero – charge-depleted mode, the battery current goes to zero and remains at zero till the battery is charged. These three models – charge; discharge; charge-depleted models are derived in the subsequent subsections.

A.1.1. Lead-Acid Battery Charge Mode – Compact Form

In this subsection, the model for the lead-acid battery charge mode is derived. Assuming $v_c = v_1 - E_1$; $1/R_{sh} = G_{ch}$; i_R, the current through the series resistance; and i_c, the current through the series capacitor, the mathematical model for the lead-acid battery can be given as follows:

$$i_1(t) = i_C(t) + i_R(t),$$

(A.9)

$$i_2(t) = -i_C(t) - i_R(t),$$

(A.10)

$$i_R(t) = G_{ch} v_c(t), \tag{A.11}$$

$$i_C(t) = \frac{C_{ov} dv_c(t)}{dt}, \tag{A.12}$$

$$E_b(t) = E_1(t) - v_2(t), \tag{A.13}$$

$$i_{sd}(t) = E_b(t) G_{sd}. \tag{A.14}$$

By using linear approximation technique, the relationship between E_b and SoC is obtainable from the battery manufacturer's datasheet and is given as:

$$0 = E_b(t) - m * SoC(t) - Z, \tag{A.15}$$

where:

m = gradient of the open circuit voltage and remaining capacity in the battery, and

Z = the intercept on the E_b axis.

The compact lead-acid battery model for the charge mode is summarized in the following equations:

$$i_1(t) = i_R(t) + i_C(t), \tag{A.16}$$

$$i_2(t) = -i_R(t) - i_C(t), \tag{A.17}$$

$$0 = -\frac{C_{ov} dv_c(t)}{dt} + i_c(t), \tag{A.18}$$

$$0 = -\left(\frac{C_n}{100}\right)\frac{d}{dt} y(t) + i_R(t) + i_C(t), \tag{A.19}$$

$$0 = -v_2(t) + E_1(t) - E_b(t), \tag{A.20}$$

$$0 = v_1(t) - v_2(t) - E_b(t) - v_c(t), \tag{A.21}$$

$$0 = (v_1(t) - E_1(t))G_{ch} - i_R(t), \tag{A.22}$$

$$0 = E_b(t) - m * SoC(t) - Z, \tag{A.23}$$

$$0 = E_b(t)G_{sd} - i_{sd}(t), \tag{A.24}$$

$$0 = i_{sd}(t) - i_R(t) - i_c(t) + i_b(t), \tag{A.25}$$

$$0 = SoC(t) - y(t) - SoC_o. \tag{A.26}$$

Equations (A.16) - (A.26) can be written in a compact form as follows:

$$\begin{bmatrix} I \\ 0 \end{bmatrix} = A \begin{bmatrix} V \\ Y \end{bmatrix} + B \frac{d}{dt} \begin{bmatrix} V \\ Y \end{bmatrix}, \tag{A.27}$$

where $I = [i_1(t)\ i_2(t)]^T$,

$V = [v_1(t)\ v_2(t)\ ]^T$,

$Y = [\ E_1(t)\ E_b(t)\ v_c(t)\ SoC(t)\ i_{sd}(t)\ i_R(t)\ i_c(t)\ i_b(t)\ y(t)]^T$,

$$A = \begin{bmatrix} 0 & 0 & 0 & 0 & 0 & 0 & 0 & 0 & 0 & 0 & 0 \\ 0 & 0 & 0 & 0 & 0 & 0 & 0 & 0 & 0 & 0 & 0 \\ 0 & 0 & 0 & 0 & 0 & 0 & 0 & 0 & 1 & 0 & 0 \\ 0 & 0 & 0 & 0 & 0 & 0 & 0 & 1 & 1 & 0 & 0 \\ 0 & 0 & 0 & 0 & 0 & 0 & 0 & 0 & 0 & 0 & 0 \\ 0 & 0 & 0 & 0 & 0 & 0 & 0 & 0 & 0 & 0 & 0 \\ 0 & 0 & 0 & 0 & 0 & 0 & 0 & 0 & 0 & 0 & 0 \\ 0 & 0 & 0 & 0 & 0 & 0 & 0 & 0 & 0 & 0 & 0 \\ 0 & 0 & 0 & 0 & 0 & 0 & 0 & 0 & 0 & 0 & 0 \\ 0 & 0 & 0 & 0 & 0 & 0 & 0 & 0 & 0 & 0 & 0 \\ 0 & 0 & 0 & 0 & 0 & 0 & 0 & 0 & 0 & 0 & 0 \end{bmatrix}, \tag{A.28}$$

$$B = \begin{bmatrix} 0 & 0 & 0 & 0 & 0 & 0 & 0 & 0 & 0 & 0 & 0 \\ 0 & 0 & 0 & 0 & 0 & 0 & 0 & 0 & 0 & 0 & 0 \\ 0 & 0 & 0 & 0 & -C_{ov} & 0 & 0 & 0 & 0 & 0 & 0 \\ 0 & 0 & 0 & 0 & 0 & 0 & 0 & 0 & 0 & 0 & -\dfrac{C_n}{100} \\ 0 & 0 & 0 & 0 & 0 & 0 & 0 & 0 & 0 & 0 & 0 \\ 0 & 0 & 0 & 0 & 0 & 0 & 0 & 0 & 0 & 0 & 0 \\ 0 & 0 & 0 & 0 & 0 & 0 & 0 & 0 & 0 & 0 & 0 \\ 0 & 0 & 0 & 0 & 0 & 0 & 0 & 0 & 0 & 0 & 0 \\ 0 & 0 & 0 & 0 & 0 & 0 & 0 & 0 & 0 & 0 & 0 \\ 0 & 0 & 0 & 0 & 0 & 0 & 0 & 0 & 0 & 0 & 0 \\ 0 & 0 & 0 & 0 & 0 & 0 & 0 & 0 & 0 & 0 & 0 \end{bmatrix}. \tag{A.29}$$

A.1.2. *Lead-Acid Battery Discharge Mode – Compact Form*

The discharge mode is similar to the charge mode given in appendix A.1.1, except that the expression $1/R_{dch} = G_{dch}$ is used. Therefore, for the discharge mode model, equation (A.30) supersedes equations (A.22).

$$0 = (v_1(t) - E_1(t))G_{dch} - i_R(t) . \tag{A.30}$$

A.1.3. *Lead-Acid Battery Charge-Depleted Mode – Compact Form*

The charge-depleted mode is similar to the discharge mode given in appendix A.1.2, except that the value of Z in (A.23) is zero resulting in equation (A.31), which replaces the (A.23) equation of appendix A.1.2.

$$0 = E_b(t) - m * SoC(t). \tag{A.31}$$

Although a model is derived for the charge-depleted mode, during simulation, it is assumed that the battery will be disconnected before its SoC goes to zero to prevent the damage of the battery.

A.2. Time-domain Model of a Lead-Acid Battery – Quadratized Form

The compact model derived in appendix A.1 is comprised of linear terms only. Therefore, the quadratized model is the same at the compact model. It is only necessary to write the compact model of appendix A.1 in the algebraic companion form (ACF). The ACF of the lead-acid battery model is discussed next.

A.3. Time-domain Model of a Lead-Acid Battery - ACF

The ACF of the lead-acid battery is obtained by performing quadratic integration to the compact model of appendix A.1 with an integration time step of h. By performing QI to the set of equations in appendix A.1.1 the ACF is obtained as follows:

$$
\begin{bmatrix} i(t) \\ 0 \\ i(t_m) \\ 0 \end{bmatrix} = \begin{bmatrix} \dfrac{h}{6}A+B & \dfrac{2h}{3}A \\ -\dfrac{h}{24}A & \dfrac{h}{3}A+B \end{bmatrix} \begin{bmatrix} v(t) \\ y(t) \\ v(t_m) \\ y(t_m) \end{bmatrix} - \begin{bmatrix} B-\dfrac{h}{6}A \\ B-\dfrac{5h}{24}A \end{bmatrix} \begin{bmatrix} v(t-h) \\ y(t-h) \end{bmatrix},
\tag{A.32}
$$

where $i(t) = \begin{bmatrix} i_1(t) i_2(t) \end{bmatrix}^T$,

$$ v(t) = \begin{bmatrix} v_1(t) v_2(t) \end{bmatrix}^T, $$

$$ y(t) = \begin{bmatrix} E_1(t) E_b(t) v_c(t) SoC(t) i_{sd}(t) i_R(t) i_c(t) i_b(t) y(t) \end{bmatrix}^T, $$

and t_m is due to the $t - h/2$ integration time-step contribution.

Equation (A.32) can be written in the form:

$$
\begin{bmatrix} i(t) \\ 0 \\ i(t_m) \\ 0 \end{bmatrix} = Y_{eq1} \begin{bmatrix} v(t) \\ y(t) \\ v(t_m) \\ y(t_m) \end{bmatrix} - B_{eq1},
\tag{A.33}
$$

where

$$Y_{eq1} = \begin{bmatrix} \dfrac{h}{6}A+B & \dfrac{2h}{3}A \\ -\dfrac{h}{24}A & \dfrac{h}{3}A+B \end{bmatrix}, \tag{A.34}$$

$$B_{eq1} = N_{eq} \begin{bmatrix} v(t-h) \\ y(t-h) \end{bmatrix}, \tag{A.35}$$

$$N_{eq} = \begin{bmatrix} B-\dfrac{h}{6}A \\ B-\dfrac{5h}{24}A \end{bmatrix}. \tag{A.36}$$

The remaining equations: (A.16)-(A.17), (A.20)-(A.26) which did not have differential terms are then added to Y_{eq1} and B_{eq1}. The following additions are made to the Y_{eq1} matrix:

$$Y_{eq2} = \begin{bmatrix} 0 & 0 & 0 & 0 & 0 & 0 & 0 & 1 & 1 & 0 & 0 \\ 0 & 0 & 0 & 0 & 0 & 0 & 0 & -1 & -1 & 0 & 0 \\ 0 & 0 & 0 & 0 & 0 & 0 & 0 & 0 & 0 & 0 & 0 \\ 0 & 0 & 0 & 0 & 0 & 0 & 0 & 0 & 0 & 0 & 0 \\ 0 & -1 & 1 & -1 & 0 & 0 & 0 & 0 & 0 & 0 & 0 \\ 1 & -1 & 0 & -1 & -1 & 0 & 0 & 0 & 0 & 0 & 0 \\ G_{ch} & 0 & -G_{ch} & 0 & 0 & 0 & 0 & 1 & 0 & 0 & 0 \\ 0 & 0 & 0 & 1 & 0 & -m & 0 & 0 & 0 & 0 & 0 \\ 0 & 0 & 0 & G_{sd} & 0 & 0 & -1 & 0 & 0 & 0 & 0 \\ 0 & 0 & 0 & 0 & 0 & 0 & 1 & -1 & -1 & 1 & 0 \\ 0 & 0 & 0 & 0 & 0 & 1 & 0 & 0 & 0 & 0 & 1 \end{bmatrix}, \tag{A.37}$$

where $G_{ch} = G_{dch}$ for the discharge case, and the following is added to the B_{eq1} matrix:

$$B_{eq2} = \begin{bmatrix} 0 \\ 0 \\ 0 \\ 0 \\ 0 \\ 0 \\ 0 \\ Z \\ 0 \\ 0 \\ SoC_0 \end{bmatrix}.$$
(A.38)

The complete Quadratized algebraic companion form is now written as:

$$\begin{bmatrix} i(t) \\ 0 \\ i(t_m) \\ 0 \end{bmatrix} = Y_{eq} \begin{bmatrix} v(t) \\ y(t) \\ v(t_m) \\ y(t_m) \end{bmatrix} - B_{eq},$$
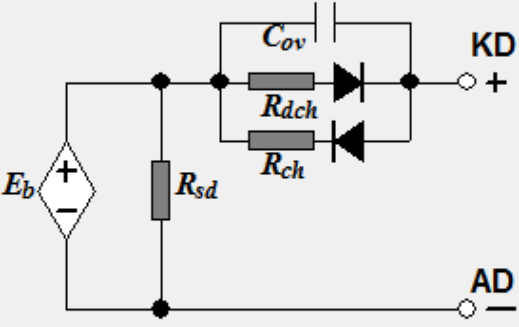(A.39)

where

$$Y_{eq} = Y_{eq1} + Y_{eq2},$$

$$B_{eq} = B_{eq1} + B_{eq2}.$$

This battery model has been implemented in the software program WinIGS using C++. The developed user interface for this model is shown on Figure A.2. From the interface, the user can enter the amp-hour capacity rating of the battery, voltage rating and other parameters typically given from the manufacture's datasheet.

Figure A.2: User interface for battery model.

Appendix B DC-DC Converter Model

In this appendix, the DC-DC converter model used for this research is discussed. The schematic for the DC-DC converter for this modeling is depicted in Figure B.1. This converter schematic was obtained from [36]. The compact model is developed first, and then the quadratized ACF model is developed.
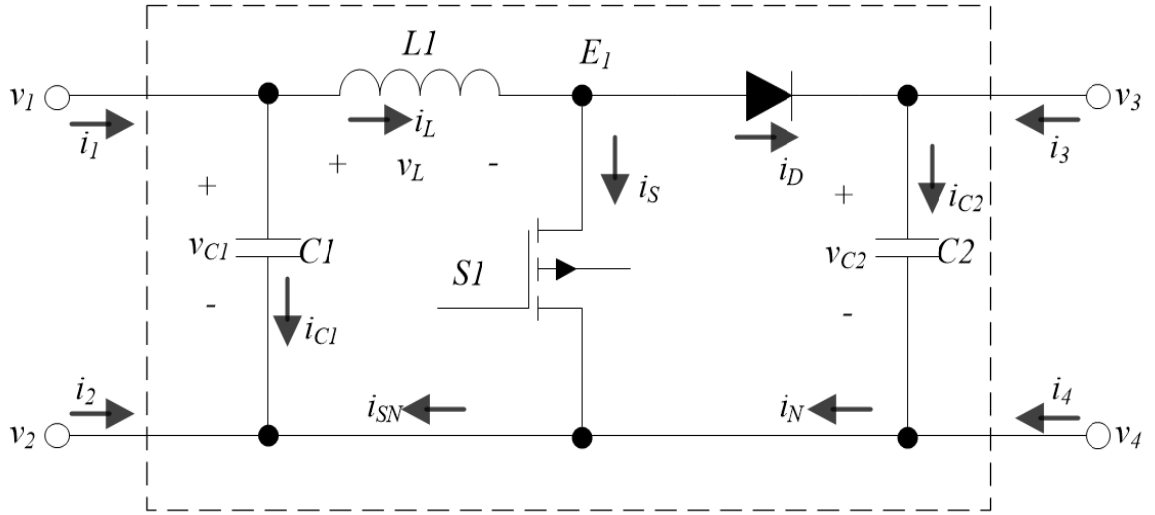
Figure B.1: Schematic for dc-dc boost converter.

B.1. Time-domain Model of a DC-DC Boost Converter – Compact Form.

From Figure B.1, the following system equations are derived:

$$i_1(t) = i_L(t) + i_{c1}(t), \tag{B.1}$$

$$i_2(t) = -i_{c1}(t) - i_{sN}(t), \tag{B.2}$$

$$i_3(t) = -i_D(t) + i_{c2}(t), \tag{B.3}$$

$$i_4(t) = -i_{c2}(t) + i_N(t), \tag{B.4}$$

$$v_L(t) = L_1 f(t), \tag{B.5}$$

$$i_{c1}(t) = C_1 g(t), \tag{B.6}$$

$$i_{c2}(t) = C_2 h(t), \tag{B.7}$$

$$v_2(t) = v_4(t), \tag{B.8}$$

$$i_S(t) = G_S(E_1(t) - v_2(t)), \tag{B.9}$$

$$i_D(t) = G_D(E_1(t) - v_3(t) - v_D), \tag{B.10}$$

$$i_S(t) = i_L(t) - i_D(t), \tag{B.11}$$

$$i_{SN}(t) = i_S(t) + i_N(t), \tag{B.12}$$

$$v_L(t) = v_1(t) - E_1(t), \tag{B.13}$$

$$v_{c1}(t) = v_1(t) - v_2(t), \tag{B.14}$$

$$v_{c2}(t) = v_3(t) - v_4(t), \tag{B.15}$$

$$f(t) = \frac{d}{dt} i_L(t), \tag{B.16}$$

$$g(t) = \frac{d}{dt} v_{c1}(t), \tag{B.17}$$

$$h(t) = \frac{d}{dt} v_{c2}(t), \tag{B.18}$$

The above equations are rewritten and summarized as follows:

$$i_1(t) = i_L(t) + i_{c1}(t), \tag{B.19}$$

$$i_2(t) = -i_{c1}(t) - i_{SN}(t) \tag{B.20}$$

$$i_3(t) = -i_D(t) + i_{c2}(t), \tag{B.21}$$

$$i_4(t) = i_N(t) - i_{c2}(t), \tag{B.22}$$

$$0 = \frac{v_L(t)}{L_1} - f(t), \tag{B.23}$$

$$0 = i_{c1}(t) - C_1 g(t), \tag{B.24}$$

$$0 = i_{c2}(t) - C_2 h(t), \tag{B.25}$$

$$0 = v_2(t) - v_4(t), \tag{B.26}$$

$$0 = G_S v_2(t) - G_S E_1(t) + i_S(t), \tag{B.27}$$

$$0 = G_D v_3(t) - G_D E_1(t) + i_D(t) + G_D v_D, \tag{B.28}$$

$$0 = -i_L(t) + i_S(t) + i_D(t), \tag{B.29}$$

$$0 = i_N(t) + i_S(t) - i_{SN}(t), \tag{B.30}$$

$$0 = -v_1(t) + E_1(t) + v_L(t), \tag{B.31}$$

$$0 = -v_1(t) + v_2(t) + v_{c1}(t), \tag{B.32}$$

$$0 = -v_3(t) + v_4(t) + v_{c2}(t), \tag{B.33}$$

$$0 = \frac{d}{dt} i_L(t) - f(t), \tag{B.34}$$

$$0 = \frac{d}{dt} v_{c1}(t) - g(t), \tag{B.35}$$

$$0 = \frac{d}{dt} v_{c2}(t) - h(t). \tag{B.36}$$

Equations (B.34) - (B.36) can be written as follows:

$$\begin{bmatrix} I \\ 0 \end{bmatrix} = A \begin{bmatrix} V \\ Y \end{bmatrix} + B \frac{d}{dt} \begin{bmatrix} V \\ Y \end{bmatrix}, \tag{B.37}$$

where $I = \left[i_1(t) i_2(t) i_3(t) i_4(t) \right]^T$,

$V = \left[v_1(t) v_2(t) v_3(t) v_4(t) \right]^T$,

$Y = \left[E_1(t) v_{c1}(t) v_{c2}(t) v_L(t) i_L(t) i_N(t) i_S(t) i_D(t) i_{C1}(t) i_{c2}(t) i_{SN}(t) f(t) g(t) h(t) \right]^T$,

$$A = \begin{bmatrix}
0 & 0 & 0 & 0 & 0 & 0 & 0 & 0 & 0 & 0 & 0 & 0 & 0 & 0 & 0 & 0 & 0 & 0 \\
0 & 0 & 0 & 0 & 0 & 0 & 0 & 0 & 0 & 0 & 0 & 0 & 0 & 0 & 0 & 0 & 0 & 0 \\
0 & 0 & 0 & 0 & 0 & 0 & 0 & 0 & 0 & 0 & 0 & 0 & 0 & 0 & 0 & 0 & 0 & 0 \\
0 & 0 & 0 & 0 & 0 & 0 & 0 & 0 & 0 & 0 & 0 & 0 & 0 & 0 & 0 & 0 & 0 & 0 \\
0 & 0 & 0 & 0 & 0 & 0 & 0 & 0 & 0 & 0 & 0 & 0 & 0 & 0 & 0 & 0 & 0 & 0 \\
0 & 0 & 0 & 0 & 0 & 0 & 0 & 0 & 0 & 0 & 0 & 0 & 0 & 0 & 0 & 0 & 0 & 0 \\
0 & 0 & 0 & 0 & 0 & 0 & 0 & 0 & 0 & 0 & 0 & 0 & 0 & 0 & 0 & 0 & 0 & 0 \\
0 & 0 & 0 & 0 & 0 & 0 & 0 & 0 & 0 & 0 & 0 & 0 & 0 & 0 & 0 & 0 & 0 & 0 \\
0 & 0 & 0 & 0 & 0 & 0 & 0 & 0 & 0 & 0 & 0 & 0 & 0 & 0 & 0 & 0 & 0 & 0 \\
0 & 0 & 0 & 0 & 0 & 0 & 0 & 0 & 0 & 0 & 0 & 0 & 0 & 0 & 0 & 0 & 0 & 0 \\
0 & 0 & 0 & 0 & 0 & 0 & 0 & 0 & 0 & 0 & 0 & 0 & 0 & 0 & 0 & 0 & 0 & 0 \\
0 & 0 & 0 & 0 & 0 & 0 & 0 & 0 & 0 & 0 & 0 & 0 & 0 & 0 & 0 & 0 & 0 & 0 \\
0 & 0 & 0 & 0 & 0 & 0 & 0 & 0 & 0 & 0 & 0 & 0 & 0 & 0 & 0 & 0 & 0 & 0 \\
0 & 0 & 0 & 0 & 0 & 0 & 0 & 0 & 0 & 0 & 0 & 0 & 0 & 0 & 0 & 0 & 0 & 0 \\
0 & 0 & 0 & 0 & 0 & 0 & 0 & 0 & 0 & 0 & 0 & 0 & 0 & 0 & 0 & 0 & 0 & 0 \\
0 & 0 & 0 & 0 & 0 & 0 & 0 & 0 & 0 & 0 & 0 & 0 & 0 & 0 & 0 & -1 & 0 & 0 \\
0 & 0 & 0 & 0 & 0 & 0 & 0 & 0 & 0 & 0 & 0 & 0 & 0 & 0 & 0 & 0 & -1 & 0 \\
0 & 0 & 0 & 0 & 0 & 0 & 0 & 0 & 0 & 0 & 0 & 0 & 0 & 0 & 0 & 0 & 0 & -1
\end{bmatrix}, \qquad \text{(B.38)}$$

$$B = \begin{bmatrix}
0 & 0 & 0 & 0 & 0 & 0 & 0 & 0 & 0 & 0 & 0 & 0 & 0 & 0 & 0 & 0 & 0 & 0 \\
0 & 0 & 0 & 0 & 0 & 0 & 0 & 0 & 0 & 0 & 0 & 0 & 0 & 0 & 0 & 0 & 0 & 0 \\
0 & 0 & 0 & 0 & 0 & 0 & 0 & 0 & 0 & 0 & 0 & 0 & 0 & 0 & 0 & 0 & 0 & 0 \\
0 & 0 & 0 & 0 & 0 & 0 & 0 & 0 & 0 & 0 & 0 & 0 & 0 & 0 & 0 & 0 & 0 & 0 \\
0 & 0 & 0 & 0 & 0 & 0 & 0 & 0 & 0 & 0 & 0 & 0 & 0 & 0 & 0 & 0 & 0 & 0 \\
0 & 0 & 0 & 0 & 0 & 0 & 0 & 0 & 0 & 0 & 0 & 0 & 0 & 0 & 0 & 0 & 0 & 0 \\
0 & 0 & 0 & 0 & 0 & 0 & 0 & 0 & 0 & 0 & 0 & 0 & 0 & 0 & 0 & 0 & 0 & 0 \\
0 & 0 & 0 & 0 & 0 & 0 & 0 & 0 & 0 & 0 & 0 & 0 & 0 & 0 & 0 & 0 & 0 & 0 \\
0 & 0 & 0 & 0 & 0 & 0 & 0 & 0 & 0 & 0 & 0 & 0 & 0 & 0 & 0 & 0 & 0 & 0 \\
0 & 0 & 0 & 0 & 0 & 0 & 0 & 0 & 0 & 0 & 0 & 0 & 0 & 0 & 0 & 0 & 0 & 0 \\
0 & 0 & 0 & 0 & 0 & 0 & 0 & 0 & 0 & 0 & 0 & 0 & 0 & 0 & 0 & 0 & 0 & 0 \\
0 & 0 & 0 & 0 & 0 & 0 & 0 & 0 & 0 & 0 & 0 & 0 & 0 & 0 & 0 & 0 & 0 & 0 \\
0 & 0 & 0 & 0 & 0 & 0 & 0 & 0 & 0 & 0 & 0 & 0 & 0 & 0 & 0 & 0 & 0 & 0 \\
0 & 0 & 0 & 0 & 0 & 0 & 0 & 0 & 0 & 0 & 0 & 0 & 0 & 0 & 0 & 0 & 0 & 0 \\
0 & 0 & 0 & 0 & 0 & 0 & 0 & 0 & 0 & 0 & 0 & 0 & 0 & 0 & 0 & 0 & 0 & 0 \\
0 & 0 & 0 & 0 & 0 & 0 & 0 & 0 & 1 & 0 & 0 & 0 & 0 & 0 & 0 & 0 & 0 & 0 \\
0 & 0 & 0 & 0 & 0 & 1 & 0 & 0 & 0 & 0 & 0 & 0 & 0 & 0 & 0 & 0 & 0 & 0 \\
0 & 0 & 0 & 0 & 0 & 0 & 1 & 0 & 0 & 0 & 0 & 0 & 0 & 0 & 0 & 0 & 0 & 0
\end{bmatrix}. \qquad \text{(B.39)}$$

B.2. Time-domain Model of a DC-DC Boost Converter – Quadratized Form

The compact model derived in appendix B.1 is comprised of linear terms only. Therefore, the quadratized model is the same at the compact model. It is only necessary to write the compact model in ACF, which is discussed next.

B.3. Time-domain Model of a DC-DC Boost Converter – ACF

The ACF of the DC-DC converter model is obtained by performing quadratic integration of the compact model of equations (B.19) - (B.36) with an integration time step of h. By performing QI on the compact model, the ACF is obtained as follows:

$$
\begin{bmatrix} i(t) \\ 0 \\ i(t_m) \\ 0 \end{bmatrix} = \begin{bmatrix} \dfrac{h}{6}A+B & \dfrac{2h}{3}A \\ -\dfrac{h}{24}A & \dfrac{h}{3}A+B \end{bmatrix} \begin{bmatrix} v(t) \\ y(t) \\ v(t_m) \\ y(t_m) \end{bmatrix} - \begin{bmatrix} B-\dfrac{h}{6}A \\ B-\dfrac{5h}{24}A \end{bmatrix} \begin{bmatrix} v(t-h) \\ y(t-h) \end{bmatrix},
$$

$$(B.40)$$

where $i(t) = \begin{bmatrix} i_1(t) & i_2(t) & i_3(t) & i_4(t) \end{bmatrix}^T$,

$$v(t) = \begin{bmatrix} v_1(t) v_2(t) v_3(t) v_4(t) \end{bmatrix}^T,$$

$$y(t) = \begin{bmatrix} E_1(t) v_{c1}(t) v_{c2}(t) v_L(t) i_L(t) & i_N(t) i_S(t) i_D(t) i_{C1}(t) i_{C2}(t) i_{SN}(t) f(t) g(t) h(t) \end{bmatrix}^T,$$

and t_m is due to the $t - h/2$ integration time-step contribution.

Equation (B.40) is written in the form

$$
\begin{bmatrix} i(t) \\ 0 \\ i(t_m) \\ 0 \end{bmatrix} = Y_{eq1} \begin{bmatrix} v(t) \\ y(t) \\ v(t_m) \\ y(t_m) \end{bmatrix} - B_{eq},
$$

$$(B.41)$$

194

where

$$Y_{eq1} = \begin{bmatrix} \dfrac{h}{6}A + B & \dfrac{2h}{3}A \\[3mm] -\dfrac{h}{24}A & \dfrac{h}{3}A + B \end{bmatrix},$$

(B.42)

$$B_{eq1} = N_{eq} \begin{bmatrix} v(t-h) \\ y(t-h) \end{bmatrix},$$

(B.43)

and

$$N_{eq} = \begin{bmatrix} B - \dfrac{h}{6}A \\[3mm] B - \dfrac{5h}{24}A \end{bmatrix}.$$

(B.44)

The equations, (B.19) - (B.33), which did not have differential terms, are then added to the Y_{eq1} and B_{eq1} matrices. The following is added to the Y_{eq1} matrix:

$Y_{eq2} =$

$$\begin{bmatrix}
0 & 0 & 0 & 0 & 0 & 0 & 0 & 0 & 1 & 0 & 0 & 0 & 1 & 0 & 0 & 0 & 0 & 0 \\
0 & 0 & 0 & 0 & 0 & 0 & 0 & 0 & 0 & 0 & 0 & 0 & -1 & 0 & -1 & 0 & 0 & 0 \\
0 & 0 & 0 & 0 & 0 & 0 & 0 & 0 & 0 & 0 & 0 & -1 & 0 & 1 & 0 & 0 & 0 & 0 \\
0 & 0 & 0 & 0 & 0 & 0 & 0 & 0 & 0 & 1 & 0 & 0 & 0 & -1 & 0 & 0 & 0 & 0 \\
0 & 0 & 0 & 0 & 0 & 0 & 0 & \dfrac{v_L}{L_1} & 0 & 0 & 0 & 0 & 0 & 0 & 0 & -1 & 0 & 0 \\
0 & 0 & 0 & 0 & 0 & 0 & 0 & 0 & 0 & 0 & 0 & 0 & 1 & 0 & 0 & 0 & -C_1 & 0 \\
0 & 0 & 0 & 0 & 0 & 0 & 0 & 0 & 0 & 0 & 0 & 0 & 0 & 1 & 0 & 0 & 0 & -C_2 \\
0 & 1 & 0 & -1 & 0 & 0 & 0 & 0 & 0 & 0 & 0 & 0 & 0 & 0 & 0 & 0 & 0 & 0 \\
0 & G_s & 0 & 0 & -G_s & 0 & 0 & 0 & 0 & 0 & 1 & 0 & 0 & 0 & 0 & 0 & 0 & 0 \\
0 & 0 & G_D & 0 & -G_D & 0 & 0 & 0 & 0 & 0 & 0 & 1 & 0 & 0 & 0 & 0 & 0 & 0 \\
0 & 0 & 0 & 0 & 0 & 0 & 0 & 0 & -1 & 0 & 1 & 1 & 0 & 0 & 0 & 0 & 0 & 0 \\
0 & 0 & 0 & 0 & 0 & 0 & 0 & 0 & 0 & 1 & 1 & 0 & 0 & 0 & -1 & 0 & 0 & 0 \\
-1 & 0 & 0 & 0 & 1 & 0 & 0 & 1 & 0 & 0 & 0 & 0 & 0 & 0 & 0 & 0 & 0 & 0 \\
-1 & 1 & 0 & 0 & 0 & 1 & 0 & 0 & 0 & 0 & 0 & 0 & 0 & 0 & 0 & 0 & 0 & 0 \\
0 & 0 & -1 & 1 & 0 & 0 & 1 & 0 & 0 & 0 & 0 & 0 & 0 & 0 & 0 & 0 & 0 & 0 \\
0 & 0 & 0 & 0 & 0 & 0 & 0 & 0 & 0 & 0 & 0 & 0 & 0 & 0 & 0 & 0 & 0 & 0 \\
0 & 0 & 0 & 0 & 0 & 0 & 0 & 0 & 0 & 0 & 0 & 0 & 0 & 0 & 0 & 0 & 0 & 0 \\
0 & 0 & 0 & 0 & 0 & 0 & 0 & 0 & 0 & 0 & 0 & 0 & 0 & 0 & 0 & 0 & 0 & 0
\end{bmatrix},$$

(B.45)

where G_S and G_D are the conductance used for the switch and diode models respectively.

The following is added to the B_{eq1} matix:

$$B_{eq2} = \begin{bmatrix} 0 \\ 0 \\ 0 \\ 0 \\ 0 \\ 0 \\ 0 \\ 0 \\ 0 \\ -G_D v_D \\ 0 \\ 0 \\ 0 \\ 0 \\ 0 \\ 0 \\ 0 \\ 0 \end{bmatrix}.$$ (B.46)

The quadratized algebraic companion form is written as

$$\begin{bmatrix} i(t) \\ 0 \\ i(t_m) \\ 0 \end{bmatrix} = Y_{eq} \begin{bmatrix} v(t) \\ y(t) \\ v(t_m) \\ y(t_m) \end{bmatrix} - B_{eq},$$ (B.47)

where $Y_{eq} = Y_{eq1} + Y_{eq2}$ and $B_{eq} = B_{eq1} + B_{eq2}$.

Therefore, a complete summary of the ACF system model is as follows:

$$i_1(t) = i_L(t) + i_{c1}(t),$$ (B.48)

$$i_2(t) = -i_{c1}(t) - i_{sN}(t),$$ (B.49)

$$i_3(t) = -i_D(t) + i_{c2}(t),$$ (B.50)

$$i_4 = i_N(t) - i_{c2}(t),$$ (B.51)

$$0 = \frac{v_L(t)}{L_1} - f(t), \tag{B.52}$$

$$0 = i_{c1}(t) - C_1 g(t), \tag{B.53}$$

$$0 = i_{c2}(t) - C_2 h(t), \tag{B.54}$$

$$0 = v_2(t) - v_4(t), \tag{B.55}$$

$$0 = G_S v_2(t) - G_S E_1(t) + i_S(t), \tag{B.56}$$

$$0 = G_D v_3(t) - G_D E_1(t) + i_D(t) + G_D v_D, \tag{B.57}$$

$$0 = -i_L(t) + i_S(t) + i_D(t), \tag{B.58}$$

$$0 = i_N(t) + i_S(t) - i_{SN}(t), \tag{B.59}$$

$$0 = -v_1(t) + E_1(t) + v_L(t), \tag{B.60}$$

$$0 = -v_1(t) + v_2(t) + v_{c1}(t), \tag{B.61}$$

$$0 = -v_3(t) + v_4(t) + v_{c2}(t) \tag{B.62}$$

$$0 = i_L(t) - \frac{h}{6} f(t) - \frac{2h}{3} f(t_m) + i_L(t-h) + \frac{h}{6} f(t-h), \tag{B.63}$$

$$0 = v_{C1}(t) - \frac{h}{6} g(t) - \frac{2h}{3} g(t_m) + v_{C1}(t-h) + \frac{h}{6} g(t-h), \tag{B.64}$$

$$0 = v_{C2}(t) - \frac{h}{6} h(t) - \frac{2h}{3} h(t_m) + v_{C2}(t-h) + \frac{h}{6} h(t-h). \tag{B.65}$$

The t_m portion is very similar to the above summarized equations except the last three equations. The t_m equations are given as follows:

$$i_1(t_m) = i_L(t_m) + i_{c1}(t_m), \tag{B.66}$$

$$i_2(t_m) = -i_{c1}(t_m) - i_{sN}(t_m), \tag{B.67}$$

$$i_3\left(t_m\right) = -i_D\left(t_m\right) + i_{c2}\left(t_m\right), \tag{B.68}$$

$$i_4 t_m = i_N\left(t_m\right) - i_{c2}\left(t_m\right), \tag{B.69}$$

$$0 = \frac{v_L\left(t_m\right)}{L_1} - f\left(t_m\right), \tag{B.70}$$

$$0 = i_{c1}\left(t_m\right) - C_1 g\left(t_m\right), \tag{B.71}$$

$$0 = i_{c2}\left(t_m\right) - C_2 h\left(t_m\right), \tag{B.72}$$

$$0 = v_2\left(t_m\right) - v_4\left(t_m\right), \tag{B.73}$$

$$0 = G_S v_2\left(t_m\right) - G_S E_1\left(t_m\right) + i_S\left(t_m\right), \tag{B.74}$$

$$0 = G_D v_3\left(t_m\right) - G_D E_1\left(t_m\right) + i_D\left(t_m\right) + G_D v_D, \tag{B.75}$$

$$0 = -i_L\left(t_m\right) + i_S\left(t_m\right) + i_D\left(t_m\right), \tag{B.76}$$

$$0 = i_N\left(t_m\right) + i_S\left(t_m\right) - i_{SN}\left(t_m\right), \tag{B.77}$$

$$0 = -v_1\left(t_m\right) + E_1\left(t_m\right) + v_L\left(t_m\right), \tag{B.78}$$

$$0 = -v_1\left(t_m\right) + v_2\left(t_m\right) + v_{c1}\left(t_m\right), \tag{B.79}$$

$$0 = -v_3\left(t_m\right) + v_4\left(t_m\right) + v_{c2}\left(t_m\right), \tag{B.80}$$

$$0 = \frac{h}{24} f\left(t\right) + i_L\left(t_m\right) - \frac{h}{3} f\left(t_m\right) + i_L\left(t-h\right) + \frac{5h}{24} f\left(t-h\right), \tag{B.81}$$

$$0 = \frac{h}{24} g\left(t\right) + v_{C1}\left(t_m\right) - \frac{h}{3} g\left(t_m\right) + v_{C1}\left(t-h\right) + \frac{5h}{24} g\left(t-h\right), \tag{B.82}$$

$$0 = \frac{h}{24} h\left(t\right) + v_{C2}\left(t_m\right) - \frac{h}{3} h\left(t_m\right) + v_{C2}\left(t-h\right) + \frac{5h}{24} h\left(t-h\right). \tag{B.83}$$

This model has been implemented in the WinIGS software. The developed GUI for the converter is shown on Figure B.2.
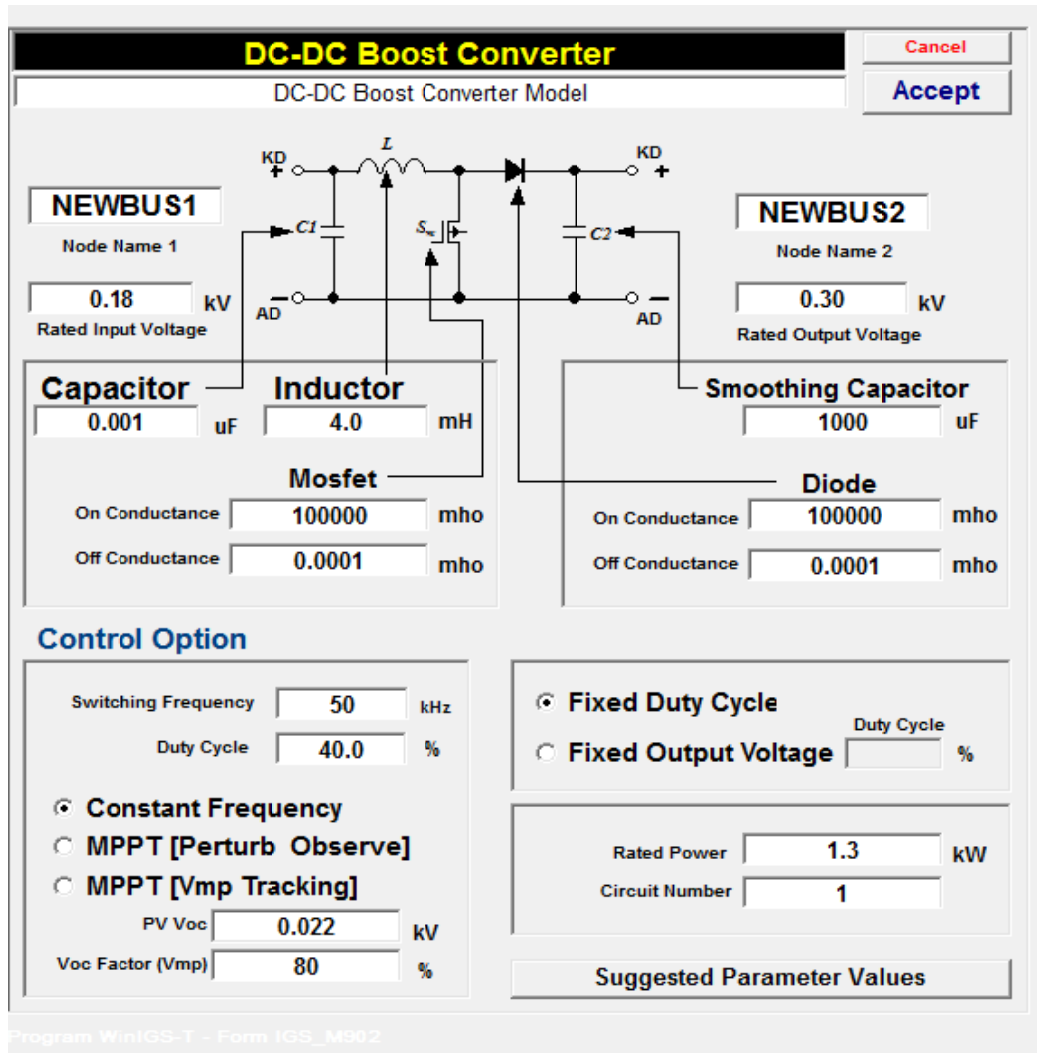
Figure B.2: Schematic for dc-dc boost converter.

B.4. Control Algorithm for DC-DC boost converter

Three control algorithms are implemented with this dc-dc boost converter. These control algorithms are as follows:

- Constant frequency & duty cycle

- Perturb and observe

- Fractional open circuit voltage

These algorithms are discussed next.

B.4.1. Constant Frequency/duty cycle

This control method is a passive control method which simulates the dc-dc boost converter with no intelligence. The user selects the parameters for the converter and simulates at a fixed frequency and duty cycle. This control option is useful if a user wants to quickly determine the response of the dc-dc converter to a given set of parameters. The constant frequency and duty cycle option is shown on Figure B.2.

B.4.2. Perturb and Observe

The Perturb and Observe (P&O) method of locating the MPP of a PV module is the method used in the research. Before explaining the operation of the P&O method, the behavior of the PV module to the operation of the DC-DC converter is explained. If the switch s_1 of Figure B.1 is closed, and kept closed, with a PV module connected to the v_1, v_2 terminal, this will appear as a short circuit to the PV module, hence, the PV will operate at its short circuit characteristics. Conversely, if switch s_1 is open, and kept open, this will appear as an open circuit to the PV module, therefore, it will operate in its open circuit condition. This mean, the voltage will gravitate toward the open circuit voltage, while its current will approach zero. Therefore, by varying the turn on and off time (duty cycle) of switch s_1, at a set frequency, the PV module can be caused to operate at either one of its two extreme operation conditions, namely, the short circuit and open circuit conditions, or at an operational point that is in-between these extreme.

For this research project, PWM switching method is used, therefore, the switching frequency of the converter remains the same, while the duty cycle is varied (perturbed) till the optimum operational point of the PV module is achieved. As the operation point of the PV changes, the change in power with respect to the corresponding change in

voltage is monitored to determine the direction that the duty cycle needs to change. As indicated in Figure B.3, the change in power with respect to the change in voltage will remain either positive or negative as the duty cycle moves in a given direction, till it crosses the maximum power point, where the polarity of change in power with respect to voltage will change. When this happens, the duty cycle direction need to be reversed to get back to the already found maximum power point.
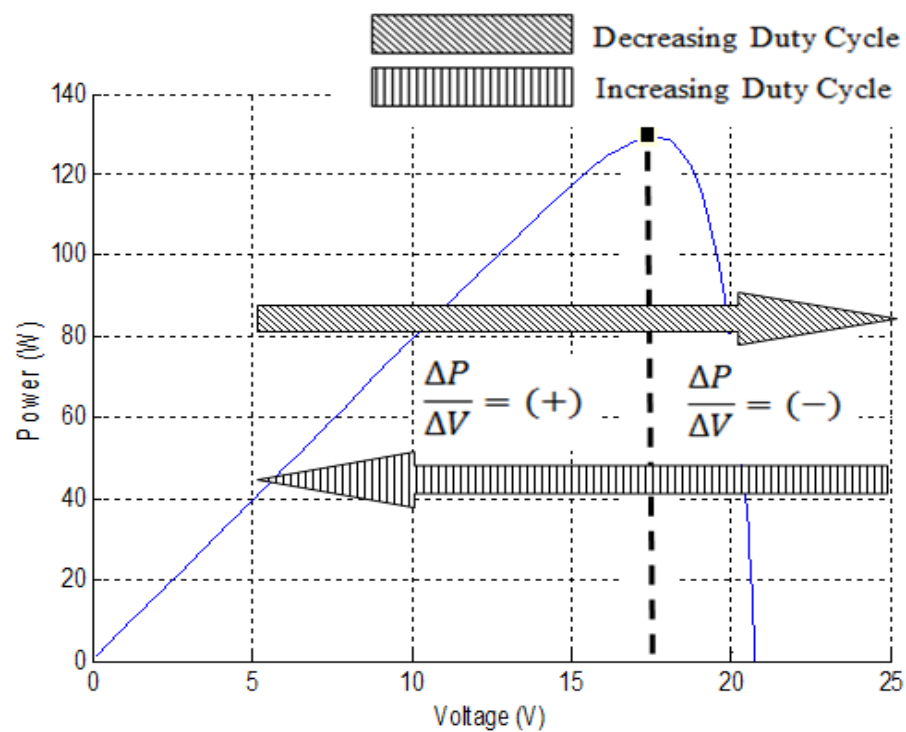
Figure B.3: Determining direction of change in duty cycle.

For this research project, the procedure for determining the maximum power point of the PV module is as follows:

i) An array of size 100 is created to hold the duty cycles from 1 to 100. Then a pointer is created to point at an initial array address to obtain the initial duty cycle for the dc-dc converter. For this research, an initial duty cycle of 60% was selected. The objective was to select an operating point that was to the left of the maximum power

point of Figure B.3. Two other arrays for voltage and current measurements are created with size 10 each. These voltage and current arrays are used for storing instantaneous current and voltage readings which are averaged to determine PV power output as shown on (B.84).

$$P_{average} = \frac{1}{10} \sum_{m=0}^{9} v[m]i[m],$$
(B.84)

where v and i are the voltage and current across and through the converter respectively.

This method performs better in the presence of ripples in the current and voltage data measurements. Therefore the P&O method will operate effectively even during occasional transience that may cause one of the data measurements to spike.

ii) Next, voltage and current data measurements are taken at every integration time step, and the average power ($P_{average}$) is computed from the last 10 data measurements. As new current-voltage data are available, the data measurement 10 integration time steps ago is replaced with new data measure before $P_{average}$ is computed. After the initial transience from the PV energization has settled, a snapshot of the measure data are stored, as $P_{avg-previous}$ and $V_{avg-previous}$. The duty cycle is then perturbed, by decreasing the duty cycle. By following the convention shown on Figure B.3, the duty cycle is decreased with the expectation that the change in power with respect to the corresponding change in voltage ($\Delta P/\Delta V$) will remain positive till we get to the maximum power point. If the initial duty cycle were selected such that the operating point is on the right of Figure B.3, then the duty cycle pointer would need to increase. Instead of moving the array pointer one index at a time, which would result in a longer MPP arrival time, this research starts with an initial pointer move of 10.

iii) After the determined settling time of the system due to the perturbation, which for this research is 100 times the switching period, at a switching frequency of 20kHz was empirically selected, a new $P_{average}$ is computed and compared with $P_{avg-previous}$ to determine if the change in duty cycle resulted positive $\Delta P/\Delta V$. If $\Delta P/\Delta V$ remains positive, $P_{avg-previous}$ is updated with $P_{average}$, the duty cycle pointer is decreased by five indices, and the system allowed to settle after the oscillations that followed due to the perturbation. This decrease by five indices is continued till $\Delta P/\Delta V$ becomes negative indicating that the MPP has been attained.

iv) Since $\Delta P/\Delta V$ is now negative, the duty cycle index is increased by one, essentially moving left on Figure B.3 to get back to MPP. The duty cycle continues to increase by one after it is determined that $\Delta P/\Delta V$ is negative. Once $\Delta P/\Delta V$ becomes positive, the duty cycle index is decreased by a point and the perturbation concluded.

This P&O algorithm has been used for this research with good results, and its implementation is used to corroborate the efficacy of the protection and diagnostic scheme presented under this research work.

B.4.3. Fractional Open Circuit Voltage

This control option is used for computing the maximum power point of a PV module. This method of operation assumes the maximum power point of the connected PV lies between 75% and 80% of the open circuit voltage of the PV module. The maximum power voltage of the PV module is usually given on the datasheet of the PV. However, for this method, several maximum power point voltages will need to be collected for different irradiance levels.

In this method of operation, the converter switch closes when the input voltage of the converter is above the maximum power voltage, and opens when the voltage is below the maximum power voltage. By operating around the set maximum power voltage, the maximum power is extracted from the PV module. This method does not give the real maximum power point as the system needs to be tuned from time to time. A possible improvement to this method is to actively sweep the maximum power voltage around a predetermined voltage range, to ensure the maximum power is extracted for the given insolation level.

B.5. Parameter Computation

The parameters for the dc-dc converter can be determined computationally [38]. Given ΔI and ΔV, the inductance and capacitive values is computed as follows:

$$K = 1 - \frac{V_{in}}{V_{out}}, \tag{B.85}$$

$$L = \frac{v_{in} K}{\Delta I * f}, \tag{B.86}$$

$$C = \frac{I_0 K}{f * \Delta V}, \tag{B.87}$$

$$L_{critical} = \frac{K * V_{in}}{2 * I_o * f}, \tag{B.88}$$

$$C_{critical} = \frac{I_o K}{2 * V_o * f}, \tag{B.89}$$

where
$$I_0 = \frac{V_0}{R} = \frac{P_0}{V_0}.$$
(B.90)

For easy reference to the user, these parameter computations are performed within the GUI of Figure B.4. This GUI for the suggested parameters is given on Figure B.4.

Figure B.4: GUI for suggested dc-dc boost converter parameters.

Appendix C Single phase inverter

In this appendix, the time-domain model of the single-phase inverter used for this research is presented. This appendix will also address the operation of the inverter. Furthermore, the method for determining the switching time of the inverter switches is discussed as well.

C.1. Time-Domain Model of a single-phase inverter – Compact Form

The schematic for the DC-AC inverter which was used for this time domain modeling was obtained from [37] with some modifications as depicted on Figure C.1.
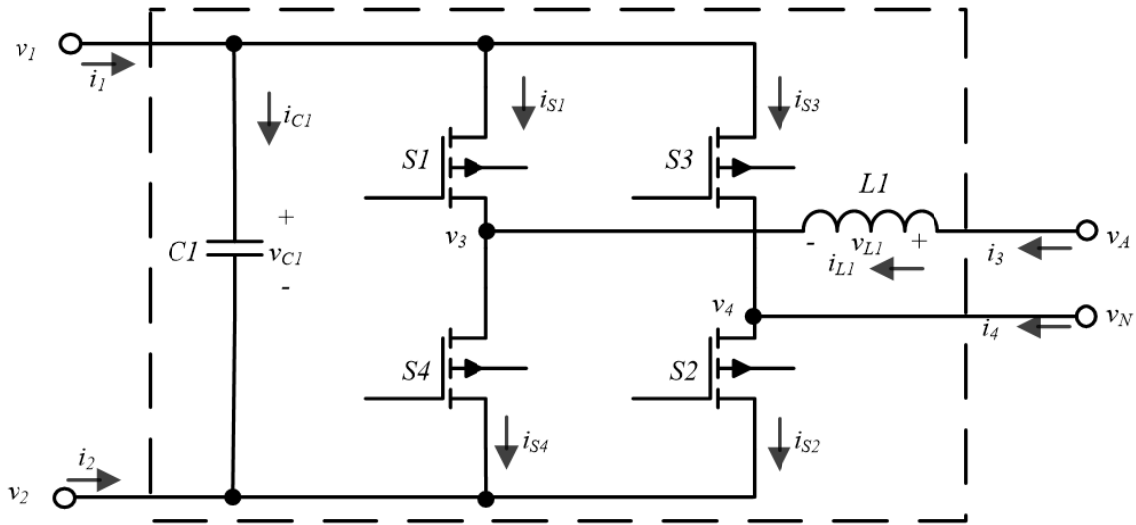
Figure C.1: Schematic for single-phase inverter model.

From Figure C.1, the mathematical equations that govern the operation of this inverter are generated as follows:

$$i_1(t) = i_{c1}(t) + i_{s1}(t) + i_{s3}(t), \tag{C.1}$$

$$i_2(t) = -i_{c1}(t) - i_{s4}(t) - i_{s2}(t), \tag{C.2}$$

$$i_3(t) = i_{L1}(t), \tag{C.3}$$

$$i_4(t) = i_{s2}(t) - i_{s3}(t), \tag{C.4}$$

$$v_{L1}(t) / L_1 = f(t), \tag{C.5}$$

$$v_{L1}(t) = v_A(t) - v_3(t), \tag{C.6}$$

$$v_N(t) = v_4(t), \tag{C.7}$$

$$v_{c1}(t) = v_1(t) - v_2(t), \tag{C.8}$$

$$i_{c1}(t) = C_1 g(t), \tag{C.9}$$

$$i_{L1}(t) = i_{s4}(t) - i_{s1}(t), \tag{C.10}$$

$$i_{s1}(t) = G_{s1}\left(v_1(t) - v_3(t)\right), \tag{C.11}$$

$$i_{s2}(t) = G_{s2}\left(v_4(t) - v_2(t)\right), \tag{C.12}$$

$$i_{s3}(t) = G_{s3}\left(v_1(t) - v_4(t)\right), \tag{C.13}$$

$$i_{s4}(t) = G_{s4}\left(v_3(t) - v_2(t)\right), \tag{C.14}$$

$$f(t) = \frac{d}{dt} i_{L1}(t), \tag{C.15}$$

$$g(t) = \frac{d}{dt} v_{c1}(t), \tag{C.16}$$

Equations (C.1) - (C.16), do not have higher order terms and do not need to be quadratized. These equations can be rewritten and summarized as follows:

$$i_1(t) = i_{c1}(t) + i_{s1}(t) + i_{s3}(t), \tag{C.17}$$

$$i_2(t) = -i_{c1}(t) - i_{s2}(t) - i_{s4}(t), \tag{C.18}$$

$$i_3(t) = i_{L1}(t), \tag{C.19}$$

$$i_4(t) = i_{s2}(t) - i_{s3}(t), \tag{C.20}$$

$$0 = -v_{L1}(t)/L_1 + f(t), \tag{C.21}$$

$$0 = -v_A(t) + v_3(t) + v_{L1}(t), \tag{C.22}$$

$$0 = -v_N(t) + v_4(t), \tag{C.23}$$

$$0 = v_{c1}(t) - v_1(t) + v_2(t), \tag{C.24}$$

$$0 = -i_{c1}(t) + C_1 g(t), \tag{C.25}$$

$$0 = -i_{L1}(t) - i_{s1}(t) + i_{s4}(t), \tag{C.26}$$

$$0 = -i_{s1}(t) + G_{s1} v_1(t) - G_{s1} v_3(t), \tag{C.27}$$

$$0 = -i_{s2}(t) - G_{s2} v_2(t) + G_{s2} v_4(t), \tag{C.28}$$

$$0 = -i_{s3}(t) + G_{s3} v_1(t) - G_{s3} v_4(t), \tag{C.29}$$

$$0 = -i_{s4}(t) - G_{s4} v_2(t) + G_{s4} v_3(t), \tag{C.30}$$

$$0 = \frac{d}{dt} i_{L1}(t) - f(t), \tag{C.31}$$

$$0 = \frac{d}{dt} v_{c1}(t) - g(t), \tag{C.32}$$

The compact form of these equations is given below:

$$\begin{bmatrix} I \\ 0 \end{bmatrix} = M \begin{bmatrix} V \\ Y \end{bmatrix} + N, \tag{C.33}$$

where $I = \begin{bmatrix} i_1(t) & i_2(t) & i_3(t) & i_4(t) \end{bmatrix}^T$,

$V = \begin{bmatrix} v_1(t) & v_2(t) & v_A(t) & v_N(t) \end{bmatrix}^T$,

$Y = \begin{bmatrix} v_3(t) & v_4(t) & v_{c1}(t) & v_{L1}(t) & i_{c1}(t) & i_{L1}(t) & i_{s1}(t) & i_{s2}(t) & i_{s3}(t) & i_{s4}(t) & f(t) & g(t) \end{bmatrix}^T$.

$$
M = \begin{bmatrix}
0 & 0 & 0 & 0 & 0 & 0 & 0 & 0 & 1 & 0 & 1 & 0 & 1 & 0 & 0 & 0 \\
0 & 0 & 0 & 0 & 0 & 0 & 0 & 0 & -1 & 0 & 0 & -1 & 0 & -1 & 0 & 0 \\
0 & 0 & 0 & 0 & 0 & 0 & 0 & 0 & 0 & 1 & 0 & 0 & 0 & 0 & 0 & 0 \\
0 & 0 & 0 & 0 & 0 & 0 & 0 & 0 & 0 & 0 & 0 & 1 & -1 & 0 & 0 & 0 \\
0 & 0 & 0 & 0 & 0 & 0 & 0 & -\dfrac{1}{L_1} & 0 & 0 & 0 & 0 & 0 & 0 & 1 & 0 \\
0 & 0 & -1 & 0 & 1 & 0 & 0 & 1 & 0 & 0 & 0 & 0 & 0 & 0 & 0 & 0 \\
0 & 0 & 0 & -1 & 0 & 1 & 0 & 0 & 0 & 0 & 0 & 0 & 0 & 0 & 0 & 0 \\
-1 & 1 & 0 & 0 & 0 & 0 & 1 & 0 & 0 & 0 & 0 & 0 & 0 & 0 & 0 & 0 \\
0 & 0 & 0 & 0 & 0 & 0 & 0 & 0 & -1 & 0 & 0 & 0 & 0 & 0 & 0 & C_1 \\
0 & 0 & 0 & 0 & 0 & 0 & 0 & 0 & 0 & -1 & -1 & 0 & 0 & 1 & 0 & 0 \\
G_{s1} & 0 & 0 & 0 & -G_{s1} & 0 & 0 & 0 & 0 & 0 & -1 & 0 & 0 & 0 & 0 & 0 \\
0 & -G_{s2} & 0 & 0 & 0 & -G_{s2} & 0 & 0 & 0 & 0 & 0 & -1 & 0 & 0 & 0 & 0 \\
G_{S3} & 0 & 0 & 0 & 0 & -G_{s3} & 0 & 0 & 0 & 0 & 0 & 0 & -1 & 0 & 0 & 0 \\
0 & -G_{s4} & 0 & 0 & G_{s3} & 0 & 0 & 0 & 0 & 0 & 0 & 0 & 0 & -1 & 0 & 0 \\
0 & 0 & 0 & 0 & 0 & 0 & 0 & 0 & 0 & 0 & 0 & 0 & 0 & 0 & -1 & 0 \\
0 & 0 & 0 & 0 & 0 & 0 & 0 & 0 & 0 & 0 & 0 & 0 & 0 & 0 & 0 & -1
\end{bmatrix}, \qquad (C.34)
$$

$$
N = \begin{bmatrix}
0 \\
0 \\
0 \\
0 \\
0 \\
0 \\
0 \\
0 \\
0 \\
0 \\
0 \\
0 \\
0 \\
0 \\
\dfrac{d}{dt} i_{L1}(t) \\
\dfrac{d}{dt} v_{c1}(t)
\end{bmatrix}, \qquad (C.35)
$$

C.2. Time Domain Model of a Single-phase Inverter – Quadratized Form

The compact form of the single phase DC-AC inverter model only has linear terms as shown on (C.17) - (C.32), therefore, the quadratized form is the same as the compact form. Next, the algebraic companion form is discussed.

C.3. Time Domain Model of a Single-phase Inverter – ACF

The ACF of the single phase DC-AC inverter model is obtained by performing quadratic integration of the compact model of (C.17) - (C.32), which are already quadratized. After quadratic integration, a complete summary of the ACF system model is written as follows:

$$i_1 = i_{c1}(t) + i_{s1}(t) + i_{s3}(t),$$ (C.36)

$$i_2 = -i_{c1}(t) - i_{s2}(t) - i_{s4}(t),$$ (C.37)

$$i_3 = i_{L1}(t),$$ (C.38)

$$i_4 = i_{s2}(t) - i_{s3}(t),$$ (C.39)

$$0 = -v_{L1}(t)/L_1 + f(t),$$ (C.40)

$$0 = -v_A(t) + v_3(t) + v_{L1}(t),$$ (C.41)

$$0 = -v_N(t) + v_4(t),$$ (C.42)

$$0 = v_{c1}(t) - v_1(t) + v_2(t),$$ (C.43)

$$0 = -i_{c1}(t) + C_1 g(t),$$ (C.44)

$$0 = -i_{L1}(t) - i_{s1}(t) + i_{s4}(t),$$ (C.45)

$$0 = -i_{s1}(t) + G_{s1}v_1(t) - G_{s1}v_3(t), \tag{C.46}$$

$$0 = -i_{s2}(t) - G_{s2}v_2(t) + G_{s2}v_4(t), \tag{C.47}$$

$$0 = -i_{s3}(t) + G_{s3}v_1(t) - G_{s3}v_4(t), \tag{C.48}$$

$$0 = -i_{s4}(t) - G_{s4}v_2(t) + G_{s4}v_3(t), \tag{C.49}$$

$$0 = i_L(t) - \frac{h}{6}f(t) - \frac{2h}{3}f(t_m) - i_L(t-h) - \frac{h}{6}f(t-h), \tag{C.50}$$

$$0 = v_{C1}(t) - \frac{h}{6}g(t) - \frac{2h}{3}g(t_m) - v_{C1}(t-h) - \frac{h}{6}g(t-h). \tag{C.51}$$

The t_m portion is very similar to the above equation except the bottom two equations. The t_m equations are given as follows:

$$i_1 = i_{c1}(t_m) + i_{s1}(t_m) + i_{s3}(t_m), \tag{C.52}$$

$$i_2 = -i_{c1}(t_m) - i_{s2}(t_m) - i_{s4}(t_m), \tag{C.53}$$

$$i_3 = i_{L1}(t_m), \tag{C.54}$$

$$i_4 = i_{s2}(t_m) - i_{s3}(t_m), \tag{C.55}$$

$$0 = -v_{L1}(t_m)/L_1 + f(t_m), \tag{C.56}$$

$$0 = -v_A(t_m) + v_3(t_m) + v_{L1}(t_m), \tag{C.57}$$

$$0 = -v_N(t_m) + v_4(t_m), \tag{C.58}$$

$$0 = v_{c1}(t_m) - v_1(t_m) + v_2(t_m), \tag{C.59}$$

$$0 = -i_{c1}(t_m) + C_1 g(t_m), \tag{C.60}$$

$$0 = -i_{L1}(t_m) - i_{s1}(t_m) + i_{s4}(t_m), \tag{C.61}$$

$$0 = -i_{s1}(t_m) + G_{s1}v_1(t_m) - G_{s1}v_3(t_m), \tag{C.62}$$

$$0 = -i_{s2}(t_m) - G_{s2}v_2(t_m) + G_{s2}v_4(t_m),$$

(C.63)

$$0 = -i_{s3}(t_m) + G_{s3}v_1(t_m) - G_{s3}v_4(t_m),$$

(C.64)

$$0 = -i_{s4}(t_m) - G_{s4}v_2(t_m) + G_{s4}v_3(t_m),$$

(C.65)

$$0 = \frac{h}{24}f(t) + i_L(t_m) - \frac{h}{3}f(t_m) - i_L(t-h) - \frac{5h}{24}f(t-h),$$

(C.66)

$$0 = \frac{h}{24}g(t) + v_{C1}(t_m) - \frac{h}{3}g(t_m) - v_{C1}(t-h) - \frac{5h}{24}g(t-h),$$

(C.67)

$$\begin{bmatrix} i(t) \\ 0 \\ i(t_m) \\ 0 \end{bmatrix} = Y_{eq} \begin{bmatrix} v(t) \\ y(t) \\ v(t_m) \\ y(t_m) \end{bmatrix} - B_{eq},$$

(C.68)

where $i(t) = \left[i_1(t)i_2(t)i_3(t)i_4(t)\right]^T$,

$$v(t) = \left[v_1(t)v_2(t)v_A(t)v_N(t)\right]^T,$$

$$y(t) = \left[v_3(t)v_4(t)v_{c1}(t)v_{L1}(t)i_{c1}(t)i_{L1}(t)i_{s1}(t)i_{s2}(t)i_{s3}(t)i_{s4}(t)f(t)g(t)\right]^T.$$

C.4. Operation of the Single-phase Inverter

This single phase inverter uses sinusoidal PWM for its operation as shown on the GUI on Figure C.2. The pulse width modulation is formulated by constructing the triangular waveform of Figure C.3 using the following equations:

$$f_{2n-1}(t) = 4(n-1) - 4fM_f t,$$

(C.69)

$$f_{2n}(t) = -(4n-2) + 4fM_f t,$$

(C.70)

where $1 \le n \le \infty$.
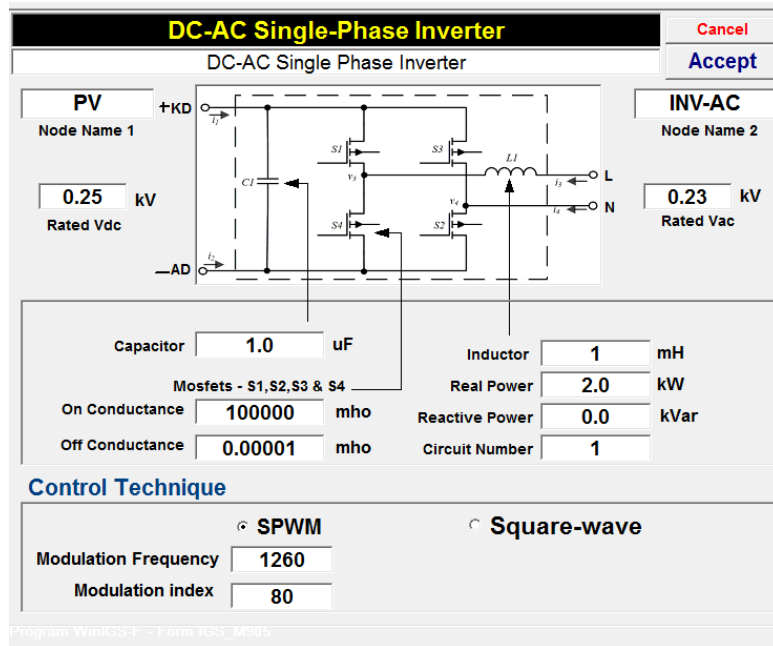
Figure C.2: GUI for single-phase inverter.
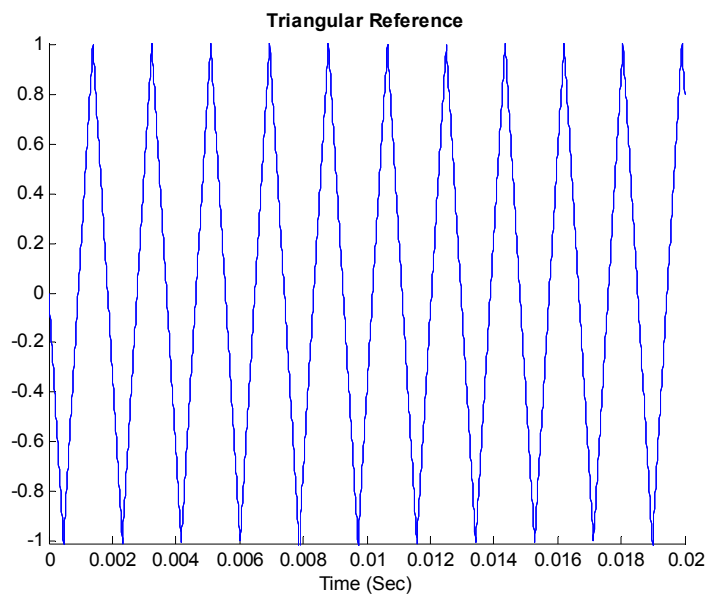
Figure C.3: Triangular reference for PWM.

A sinusoidal waveform, which is the carrier, is superimposed on Figure C.3. This sinusoidal waveform is given as

213

$$g(t) = Ma * Sin(\omega t),\qquad\qquad\text{(C.71)}$$

where Ma is the modulation index.

This superimposed sinusoid is shown on Figure C.4. The modulation index for this sinusoidal PWM is 80%, which can be confirmed by the peak value of the sinusoid in Figure C.4.
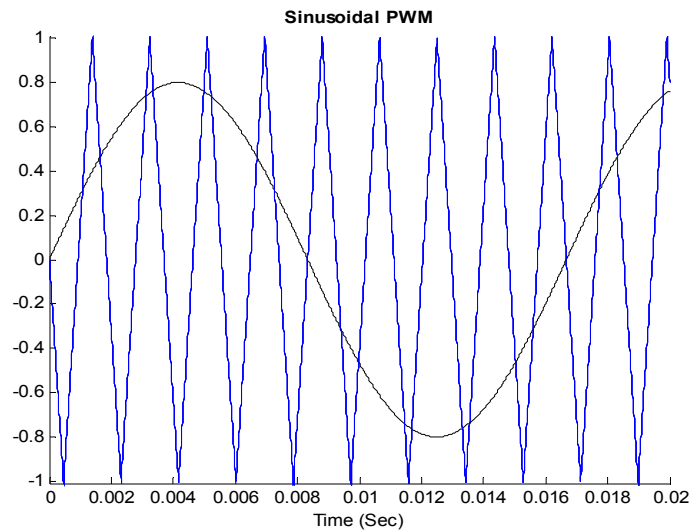
Figure C.4: Sinusoidal for PWM.

When the sinusoidal waveform is greater that the triangular reference, switches S1 and S2 of Figure C.1 are turn on while S3 and S4 are kept off. And when the sinusoidal waveform is less than the triangular reference the S1 and S2 are turn off while S3 and S4 are turned on.

Determining switching time

To determine the accurate time to turn the switches of Figure C.1 on and off, the intersection between the carrier and triangular reference waveforms of Figure C.4 needs

to be determined. The Newton-Raphson iterative approach is used to determine these intersections, which is given as follows:

Let the function describing the intersection of the two functions f(t) and g(t) be written as shown in

$$h(t) = f(t) - g(t), \tag{C.72}$$

with the derivative given as:

$$h'(t) = f'(t) - g'(t), \tag{C.73}$$

therefore, the intersection time t_1 is computed iteratively by using (C.74).

$$t_1 = t_{1, previous\ iteration} - \frac{h(t)}{h'(t)}, \tag{C.74}$$

In this modeling, after three iterations (C.74) converges to the intersection time. Using this approach, the intersections of the two functions have been determined as shown on Figure C.5.
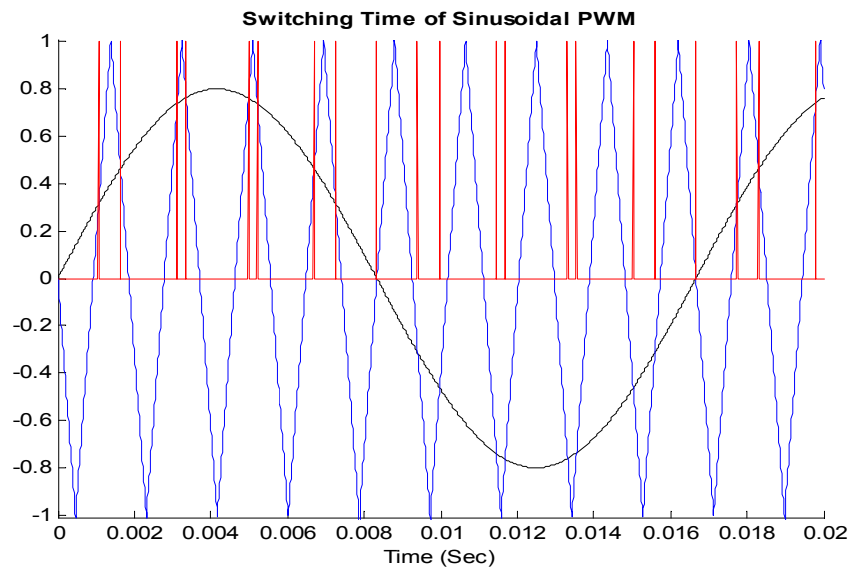
Figure C.5: Switching time of sinusoidal PWM.

A simple PV-inverter system was designed as shown on Figure C.6.
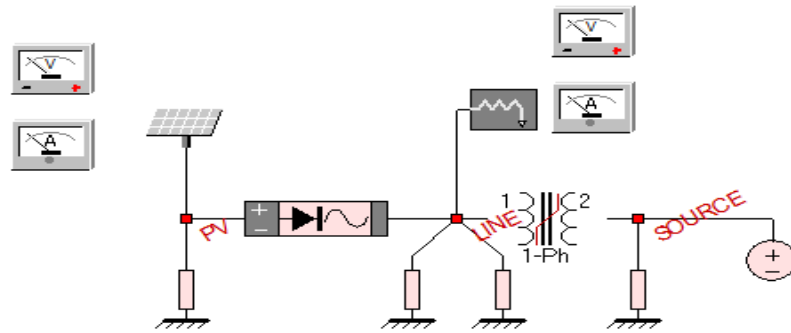
Figure C.6: Circuit for inverter simulation.

This system was simulated showing both the output voltage and current, and the switching pulses of switches S1/S2 and S3/S4 as shown on Figure C.7. The switching pulses of switches S1/S2 and S3/S4 are identified as v_{s1} and v_{s3} on Figure C.7.
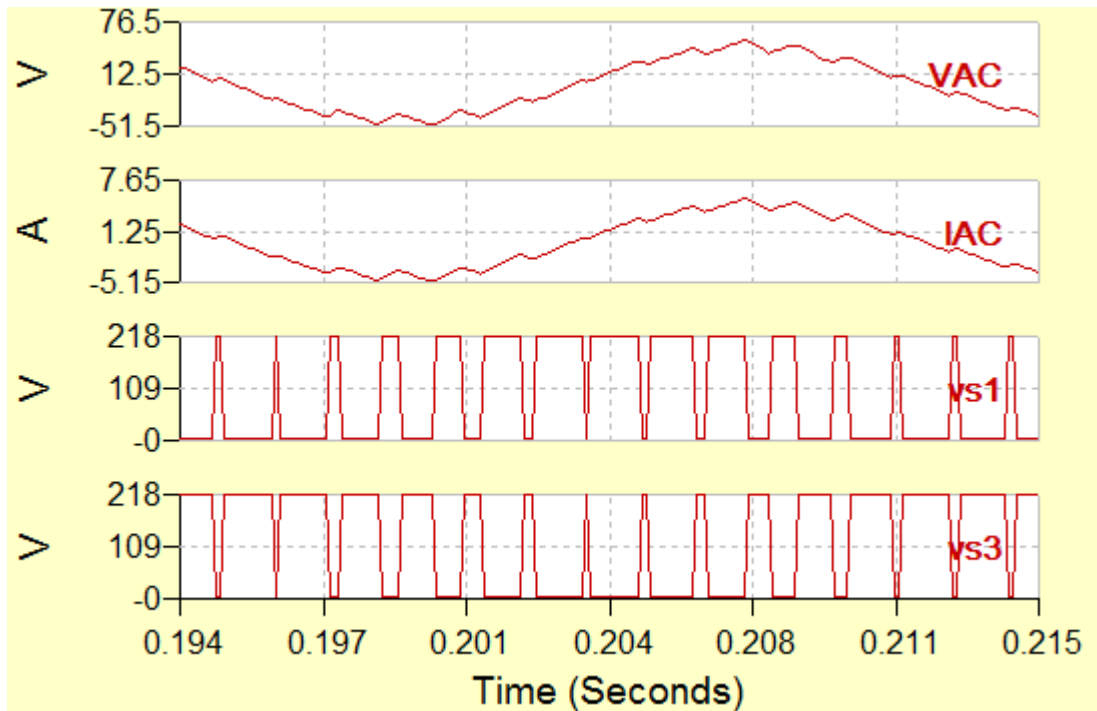
Figure C.7: Output waveform of sinusoidal PWM.

Appendix D   Single-phase Load Model

In this appendix, the load model used for the research is developed. The schematic for the load system is shown on Figure D.1.
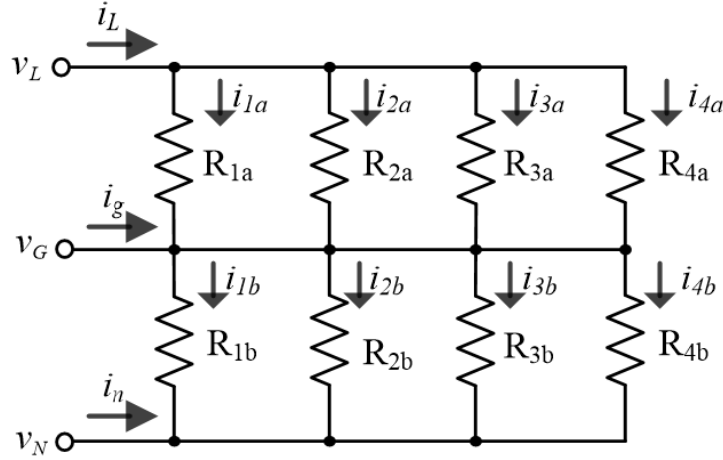
Figure D.1: Schematic for single-phase load.

From Figure D.1 the following set of system equations are derived:

$$i_L = i_{line},$$
(D.1)

$$i_g = i_{neutral} - i_{line},$$
(D.2)

$$i_n = -i_{neutral},$$
(D.3)

$$i_{line} = i_{1a} + i_{2a} + i_{3a} + i_{4a},$$
(D.4)

$$i_{neutral} = i_{1b} + i_{2b} + i_{3b} + i_{4b},$$
(D.5)

$$0 = -i_{1a} + G_{1a}\left(v_L - v_G\right),$$
(D.6)

$$0 = -i_{2a} + G_{2a}\left(v_L - v_G\right),$$
(D.7)

$$0 = -i_{3a} + G_{3a}\left(v_L - v_G\right),$$
(D.8)

$$0 = -i_{4a} + G_{4a}\left(v_L - v_G\right),$$
(D.9)

$$0 = -i_{1b} + G_{1b}\left(v_G - v_N\right), \tag{D.10}$$

$$0 = -i_{2b} + G_{2b}\left(v_G - v_N\right), \tag{D.11}$$

$$0 = -i_{3b} + G_{3b}\left(v_G - v_N\right), \tag{D.12}$$

$$0 = -i_{4b} + G_{4b}\left(v_G - v_N\right), \tag{D.13}$$

D.1. Time-Domain Model of a single-phase load – Compact Form.

In formulating the compact model for the single-phase load model, equations (D.1) - (D.13) are rewritten as follows:

$$i_L\left(t\right) = i_{line}\left(t\right), \tag{D.14}$$

$$i_g\left(t\right) = -i_{line}\left(t\right) + i_{neutral}\left(t\right), \tag{D.15}$$

$$i_n\left(t\right) = -i_{neutral}\left(t\right), \tag{D.16}$$

$$0 = -i_{line}\left(t\right) + i_{1a}\left(t\right) + i_{2a}\left(t\right) + i_{3a}\left(t\right) + i_{4a}\left(t\right), \tag{D.17}$$

$$0 = -i_{neutral}\left(t\right) + i_{1b}\left(t\right) + i_{2b}\left(t\right) + i_{3b}\left(t\right) + i_{4b}\left(t\right), \tag{D.18}$$

$$0 = G_{1a}v_L\left(t\right) - G_{1a}v_G\left(t\right) - i_{1a}\left(t\right), \tag{D.19}$$

$$0 = G_{2a}v_L\left(t\right) - G_{2a}v_G\left(t\right) - i_{2a}\left(t\right), \tag{D.20}$$

$$0 = G_{3a}v_L\left(t\right) - G_{3a}v_G\left(t\right) - i_{3a}\left(t\right), \tag{D.21}$$

$$0 = G_{4a}v_L\left(t\right) - G_{4a}v_G\left(t\right) - i_{4a}\left(t\right), \tag{D.22}$$

$$0 = G_{1b}v_G\left(t\right) - G_{1b}v_N\left(t\right) - i_{1b}\left(t\right), \tag{D.23}$$

$$0 = G_{2b}v_G\left(t\right) - G_{2b}v_N\left(t\right) - i_{2b}\left(t\right), \tag{D.24}$$

$$0 = G_{3b}v_G\left(t\right) - G_{3b}v_N\left(t\right) - i_{3b}\left(t\right), \tag{D.25}$$

$$0 = G_{4b}v_G(t) - G_{4b}v_N(t) - i_{4b}(t),$$ (D.26)

Equations (D.1) - (D.13) are then written in a compact matrix form as follows:

$$\begin{bmatrix} I \\ 0 \end{bmatrix} = Y_{eq} \begin{bmatrix} V \\ Y \end{bmatrix},$$ (D.27)

where $I = \begin{bmatrix} i_L(t) i_g(t) i_n(t) \end{bmatrix}^T$

$$V = \begin{bmatrix} v_L(t) v_G(t) v_N(t) \end{bmatrix}^T$$

$$Y = \begin{bmatrix} i_{line}(t) i_{neutral}(t) i_{1a}(t) i_{2a}(t) i_{3a}(t) i_{4a}(t) i_{1b}(t) i_{2b}(t) i_{3b}(t) i_{4b}(t) \end{bmatrix}^T$$

$$Y_{eq} = \begin{bmatrix}
0 & 0 & 0 & 1 & 0 & 0 & 0 & 0 & 0 & 0 & 0 & 0 & 0 \\
0 & 0 & 0 & -1 & 1 & 0 & 0 & 0 & 0 & 0 & 0 & 0 & 0 \\
0 & 0 & 0 & 0 & -1 & 0 & 0 & 0 & 0 & 0 & 0 & 0 & 0 \\
0 & 0 & 0 & -1 & 0 & 1 & 1 & 1 & 1 & 0 & 0 & 0 & 0 \\
0 & 0 & 0 & 0 & -1 & 0 & 0 & 0 & 0 & 1 & 1 & 1 & 1 \\
G_{1a} & -G_{1a} & 0 & 0 & 0 & -1 & 0 & 0 & 0 & 0 & 0 & 0 & 0 \\
G_{2a} & -G_{2a} & 0 & 0 & 0 & 0 & -1 & 0 & 0 & 0 & 0 & 0 & 0 \\
G_{3a} & -G_{3a} & 0 & 0 & 0 & 0 & 0 & -1 & 0 & 0 & 0 & 0 & 0 \\
G_{4a} & -G_{4a} & 0 & 0 & 0 & 0 & 0 & 0 & -1 & 0 & 0 & 0 & 0 \\
G_{1b} & -G_{1b} & 0 & 0 & 0 & 0 & 0 & 0 & 0 & -1 & 0 & 0 & 0 \\
G_{2b} & -G_{2b} & 0 & 0 & 0 & 0 & 0 & 0 & 0 & 0 & -1 & 0 & 0 \\
G_{3b} & -G_{3b} & 0 & 0 & 0 & 0 & 0 & 0 & 0 & 0 & 0 & -1 & 0 \\
G_{4b} & -G_{4b} & 0 & 0 & 0 & 0 & 0 & 0 & 0 & 0 & 0 & 0 & -1
\end{bmatrix}.$$ (D.28)

D.2. Time-Domain Model of a single-phase load – Quadratized Form

The compact model form of the single phase load is comprised of linear terms only. Therefore, the quadratized model is the same at the compact model. The operation of the single phase load is discussed next.

D.3. Operation of the Single-phase Load Model

The GUI of the single phase load is shown on Figure D.2., and based on the voltage level of the source and the desired total power of the load, the GUI is modified accordingly. This load model was designed to match the single-phase load used for the research. The schematic and photograph of the actual load used for the research are shown on Figure D.3 and Figure D.4 respectively.
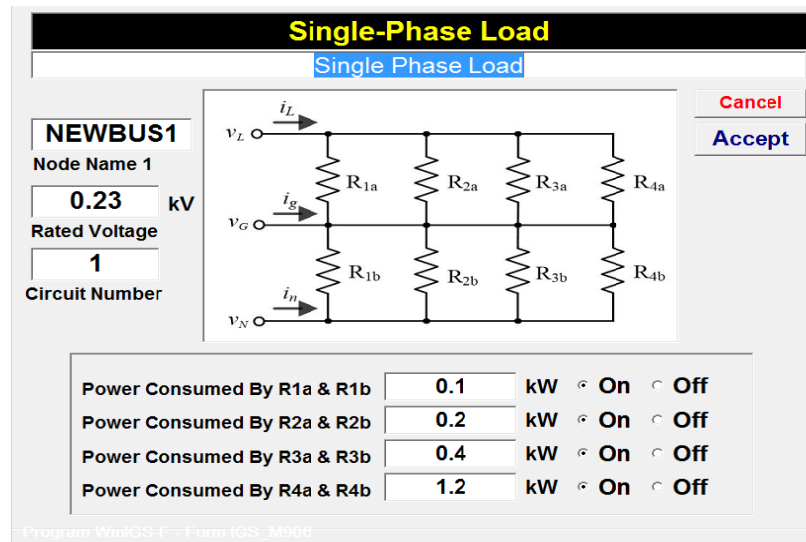
Figure D.2: GUI for load model.
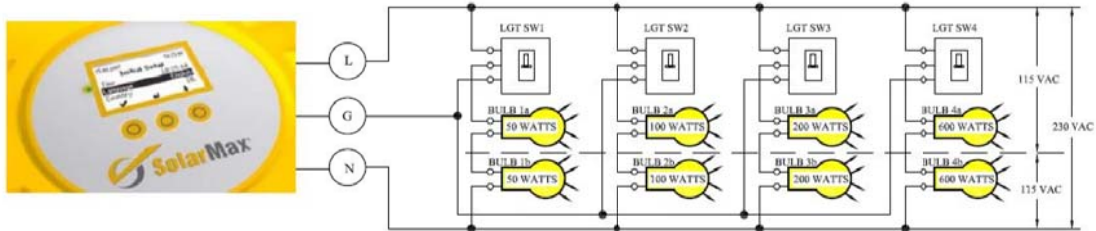
Figure D.3: Schematic for the actual single-phase load used for this research.

Figure D.4: Photograph of single-phase load.

Appendix E Classification of photovoltaic data measurements

for a Photovoltaic Module

Table E.1: **Classification of PV data measurements for a PV module.**

Actual Measurements; standard deviation = 0.01 per unit (p.u.)			
$z_1(t) =$	$h_1(x) =$		$v_1(t) - v_2(t) + \eta_1(t)$
$z_2(t) =$	$h_2(x) =$		$v_1(t_m) - v_2(t_m) + \eta_2(t_m)$
$z_3(t) =$	$h_3(x) =$	$i_1(t)$	$= G_s v_1(t) - G_s v_x(t) + \eta_3(t)$
$z_4(t_m) =$	$h_4(x) =$	$i_1(t_m)$	$= G_s v_1(t_m) - G_s v_x(t_m) + \eta_4(t_m)$
Pseudo Measurements; standard deviation = 0.1p.u.			
$z_5(t) =$	$h_5(x) =$	$i_2(t)$	$= -G_s v_1(t) + G_s v_x(t) + \eta_5(t)$
$z_6(t_m) =$	$h_6(x) =$	$i_2(t_m)$	$= -G_s v_1(t_m) + G_s v_x(t_m) + \eta_6(t_m)$
Virtual Measurements; standard deviation = 0.001p.u.			
$z_7(t) =$	$h_7(x) =$	0	$= -G_s v_1(t) - G_{sh} v_2(t) + (G_{sh} + G_s) v_x(t) + I_{o1}\left[c_1^2(t) - 1\right]$ $+ I_{o2}\left[d_1^2(t) - 1\right] - i_{pv} + \eta_7(t)$
$z_8(t) =$	$h_8(x) =$	0	$= -c_1(t) + \alpha_4^2(t) + \eta_8(t)$
$z_9(t) =$	$h_9(x) =$	0	$= -\alpha_4(t) + \alpha_1(t)\alpha_3(t) + \eta_9(t)$
$z_{10}(t) =$	$h_{10}(x) =$	0	$= -\alpha_3(t) + \alpha_2^2(t) + \eta_{10}(t)$
$z_{11}(t) =$	$h_{11}(x) =$	0	$= -\alpha_2(t) + \alpha_1^2(t) + \eta_{11}(t)$
$z_{12}(t) =$	$h_{12}(x) =$	0	$= -\alpha_1(t) + \gamma_1^2(t) + \eta_{12}(t)$
$z_{13}(t) =$	$h_{13}(x) =$	0	$= -\gamma_1(t) + 1 + \lambda_1(t) + \dfrac{y_1(t)}{2!} + \dfrac{y_2(t)}{3!} + \dfrac{y_3(t)}{4!} + \dfrac{y_4(t)}{5!} + \dfrac{y_5(t)}{6!} + \dfrac{y_2(t)y_3(t)}{7!}$ $+ \dfrac{y_2(t)y_4(t)}{8!} + \dfrac{y_2(t)y_5(t)}{9!} + \dfrac{y_3(t)y_5(t)}{10!} + \dfrac{y_4(t)y_5(t)}{11!} + \eta_{13}(t)$
$z_{14}(t) =$	$h_{14}(x) =$	0	$= -40\lambda_1(t)aN_s V_T + v_x(t) - v_2(t) + \eta_{14}(t)$

$z_{15}(t) =$	$h_{15}(x) =$	0	$= \lambda_1(t)^2 - y_1(t) + \eta_{15}(t)$
$z_{16}(t) =$	$h_{16}(x) =$	0	$= \lambda_1(t) y_1(t) - y_2(t) + \eta_{16}(t)$
$z_{17}(t) =$	$h_{17}(x) =$	0	$= y_1^2(t) - y_3(t) + \eta_{17}(t)$
$z_{18}(t) =$	$h_{18}(x) =$	0	$= y_1(t) y_2(t) - y_4(t) + \eta_{18}(t)$
$z_{19}(t) =$	$h_{19}(x) =$	0	$= y_1(t) y_3(t) - y_5(t) + \eta_{19}(t)$
$z_{20}(t) =$	$h_{20}(x) =$	0	$= -d_1(t) + \beta_4^2(t) + \eta_{20}(t)$
$z_{21}(t) =$	$h_{21}(x) =$	0	$= -\beta_4(t) + \beta_1(t) \beta_3(t) + \eta_{21}(t)$
$z_{22}(t) =$	$h_{22}(x) =$	0	$= -\beta_3(t) + \beta_2^2(t) + \eta_{22}(t)$
$z_{23}(t) =$	$h_{23}(x) =$	0	$= -\beta_2(t) + \beta_1^2(t) + \eta_{23}(t)$
$z_{24}(t) =$	$h_{24}(x) =$	0	$= -\beta_1(t) + \gamma_2^2(t) + \eta_{24}(t)$
$z_{25}(t) =$	$h_{25}(x) =$	0	$= -\gamma_2(t) + 1 + \lambda_2(t) + \dfrac{z_1(t)}{2!} + \dfrac{z_2(t)}{3!} + \dfrac{z_3(t)}{4!} + \dfrac{z_4(t)}{5!} + \dfrac{z_5(t)}{6!} + \dfrac{z_2(t) z_3(t)}{7!}$ $+ \dfrac{z_2(t) z_4(t)}{8!} + \dfrac{z_2(t) z_5(t)}{9!} + \dfrac{z_3(t) z_5(t)}{10!} + \dfrac{z_4(t) z_5(t)}{11!} + \eta_{25}(t)$
$z_{26}(t) =$	$h_{26}(x) =$	0	$= -40 \lambda_2(t) n N_s V_T + v_x(t) - v_2(t) + \eta_{26}(t)$
$z_{27}(t) =$	$h_{27}(x) =$	0	$= \lambda_2(t)^2 - z_1(t) + \eta_{27}(t)$
$z_{28}(t) =$	$h_{28}(x) =$	0	$= \lambda_2(t) z_1(t) - z_2(t) + \eta_{28}(t)$
$z_{29}(t) =$	$h_{29}(x) =$	0	$= z_1^2(t) - z_3(t) + \eta_{29}(t)$
$z_{30}(t) =$	$h_{30}(x) =$	0	$= z_1(t) z_2(t) - z_4(t) + \eta_{30}(t)$
$z_{31}(t) =$	$h_{31}(x) =$	0	$= z_1(t) z_3(t) - z_5(t) + \eta_{31}(t)$
$z_{32}(t_m) =$	$h_{32}(x) =$	0	$= -G_s v_1(t_m) - G_{sh} v_2(t_m) + (G_{sh} + G_s) v_x(t_m) + I_{o1} \left[c_1^2(t_m) - 1 \right]$ $+ I_{o2} \left[d_1^2(t_m) - 1 \right] - i_{pv} + \eta_{32}(t_m)$
$z_{33}(t_m) =$	$h_{33}(x) =$	0	$= -c_1(t_m) + \alpha_4^2(t_m) + \eta_{33}(t_m)$

Table E.1 (continued)

$z_{34}(t_m) =$	$h_{34}(x) =$	0	$= -\alpha_4(t_m) + \alpha_1(t_m)\alpha_3(t_m) + \eta_{34}(t_m)$
$z_{35}(t_m) =$	$h_{35}(x) =$	0	$= -\alpha_3(t_m) + \alpha_2^2(t_m) + \eta_{35}(t_m)$
$z_{36}(t_m) =$	$h_{36}(x) =$	0	$= -\alpha_2(t_m) + \alpha_1^2(t_m) + \eta_{36}(t_m)$
$z_{37}(t_m) =$	$h_{37}(x) =$	0	$= -\alpha_1(t_m) + \gamma_1^2(t_m) + \eta_{37}(t_m)$
$z_{38}(t_m) =$	$h_{38}(x) =$	0	$= -\gamma_1(t_m) + 1 + \lambda_1(t_m) + \dfrac{y_1(t_m)}{2!} + \dfrac{y_2(t_m)}{3!} + \dfrac{y_3(t_m)}{4!} + \dfrac{y_4(t_m)}{5!} + \dfrac{y_5(t_m)}{6!}$ $+ \dfrac{y_2(t_m)y_3(t_m)}{7!} + \dfrac{y_2(t_m)y_4(t_m)}{8!} + \dfrac{y_2(t_m)y_5(t_m)}{9!}$ $+ \dfrac{y_3(t_m)y_5(t_m)}{10!} + \dfrac{y_4(t_m)y_5(t_m)}{11!} + \eta_{38}(t_m)$
$z_{39}(t_m) =$	$h_{39}(x) =$	0	$= -40\lambda_1(t_m)aN_sV_T + v_x(t_m) - v_2(t_m) + \eta_{39}(t_m)$
$z_{40}(t_m) =$	$h_{40}(x) =$	0	$= \lambda_1(t_m)^2 - y_1(t_m) + \eta_{40}(t_m)$
$z_{41}(t_m) =$	$h_{41}(x) =$	0	$= \lambda_1(t_m)y_1(t_m) - y_2(t_m) + \eta_{41}(t_m)$
$z_{42}(t_m) =$	$h_{42}(x) =$	0	$= y_1^2(t_m) - y_3(t_m) + \eta_{42}(t_m)$
$z_{43}(t_m) =$	$h_{43}(x) =$	0	$= y_1(t_m)y_2(t_m) - y_4(t_m) + \eta_{43}(t_m)$
$z_{44}(t_m) =$	$h_{44}(x) =$	0	$= y_1(t_m)y_3(t_m) - y_5(t_m) + \eta_{44}(t_m)$
$z_{45}(t_m) =$	$h_{45}(x) =$	0	$= -d_1(t_m) + \beta_4^2(t_m) + \eta_{45}(t_m)$
$z_{46}(t_m) =$	$h_{46}(x) =$	0	$= -\beta_4(t_m) + \beta_1(t_m)\beta_3(t_m) + \eta_{46}(t_m)$
$z_{47}(t_m) =$	$h_{47}(x) =$	0	$= -\beta_3(t_m) + \beta_2^2(t_m) + \eta_{47}(t_m)$
$z_{48}(t_m) =$	$h_{48}(x) =$	0	$= -\beta_2(t_m) + \beta_1^2(t_m) + \eta_{48}(t_m)$
$z_{49}(t_m) =$	$h_{49}(x) =$	0	$= -\beta_1(t_m) + \gamma_2^2(t_m) + \eta_{49}(t_m)$
$z_{50}(t_m) =$	$h_{50}(x) =$	0	$= -\gamma_2(t_m) + 1 + \lambda_2(t_m) + \dfrac{z_1(t_m)}{2!} + \dfrac{z_2(t_m)}{3!} + \dfrac{z_3(t_m)}{4!} + \dfrac{z_4(t_m)}{5!} + \dfrac{z_5(t_m)}{6!} + \dfrac{z_2(t_m)z_3(t_m)}{7!}$ $+ \dfrac{z_2(t_m)z_4(t_m)}{8!} + \dfrac{z_2(t_m)z_5(t_m)}{9!} + \dfrac{z_3(t_m)z_5(t_m)}{10!} + \dfrac{z_4(t_m)z_5(t_m)}{11!} + \eta_{50}(t_m)$

Table E.1 (continued)

$z_{51}(t_m)=$	$h_{51}(x)=$	0	$=-40\lambda_2(t_m)nN_sV_T+v_x(t_m)-v_2(t_m)+\eta_{51}(t_m)$
$z_{52}(t_m)=$	$h_{52}(x)=$	0	$=\lambda_2(t_m)^2-z_1(t_m)+\eta_{52}(t_m)$
$z_{53}(t_m)=$	$h_{53}(x)=$	0	$=\lambda_2(t_m)z_1(t_m)-z_2(t_m)+\eta_{53}(t_m)$
$z_{54}(t_m)=$	$h_{54}(x)=$	0	$=z_1^2(t_m)-z_3(t_m)+\eta_{54}(t_m)$
$z_{55}(t_m)=$	$h_{55}(x)=$	0	$=z_1(t_m)z_2(t_m)-z_4(t_m)+\eta_{55}(t_m)$
$z_{56}(t_m)=$	$h_{56}(x)=$	0	$=z_1(t_m)z_3(t_m)-z_5(t_m)+\eta_{56}(t_m)$

Appendix F   Simulation Result of Various Operating

Conditions in the PV Array System

In this appendix, various fault conditions within the PV array system of chapter 7 is presented. These events cover operating conditions with and without series diodes. The plots include the confidence level and cost function plots as was presented in chapters 7 and 8. Next, the voltages at the various nodes of the PV array in Figure F.1 are shown five at a time. The other plots include the measured and computed terminal current plots, the algebraic sum of the currents at each node, and then the voltage and current residuals for the data measurements. These plots are presented for each considered event in the subsequent subsections.
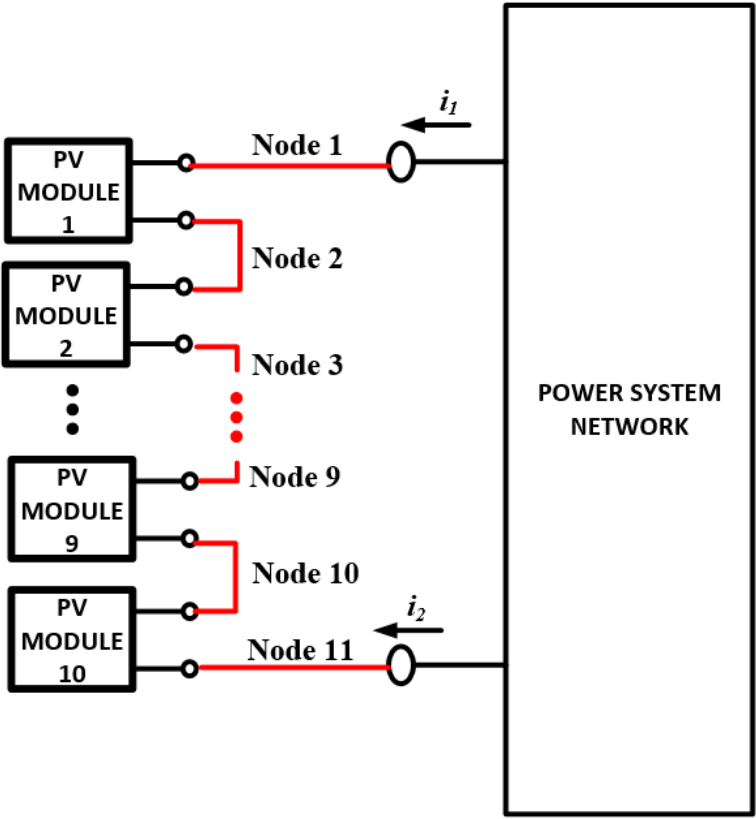
Figure F.1: Node index of the series connected photovoltaic array.

F.1. Simulation Result with Photovoltaic Module Number 6 Terminals Shorted and no Blocking Diode
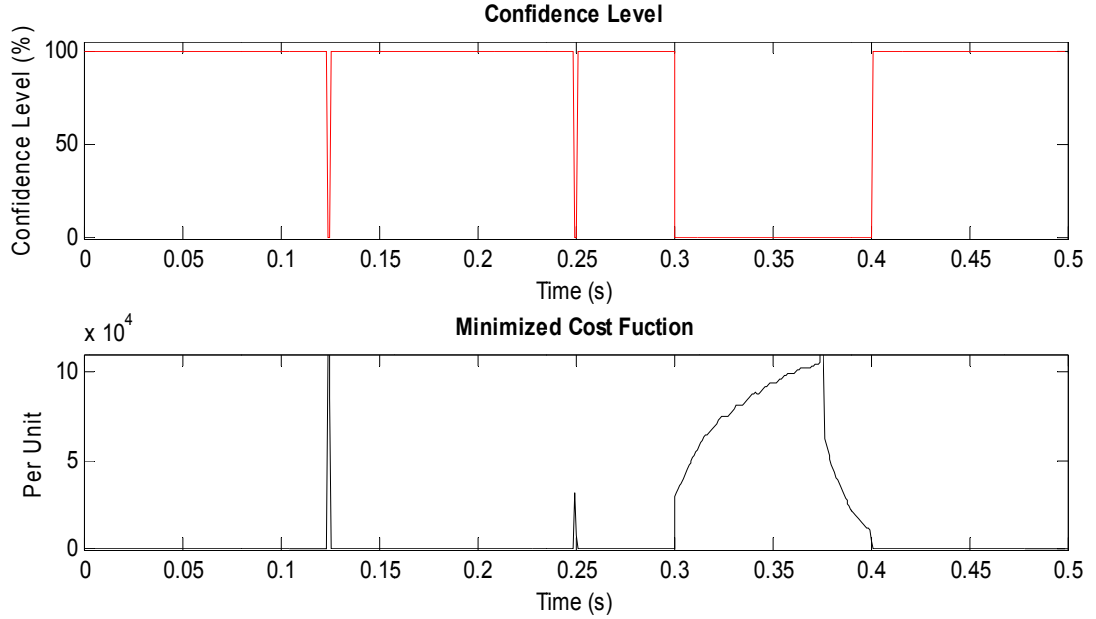
Figure F.2: Confidence level and cost function plots with photovoltaic module 6 shorted.
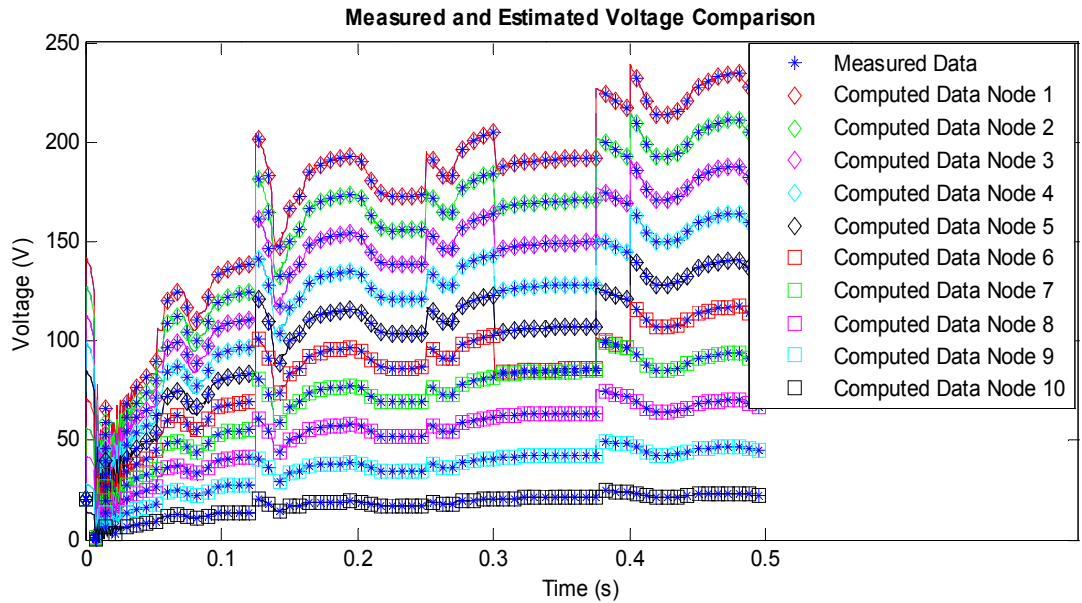
Figure F.3: Computed and measured voltage plots comparison for nodes 1 to 10.
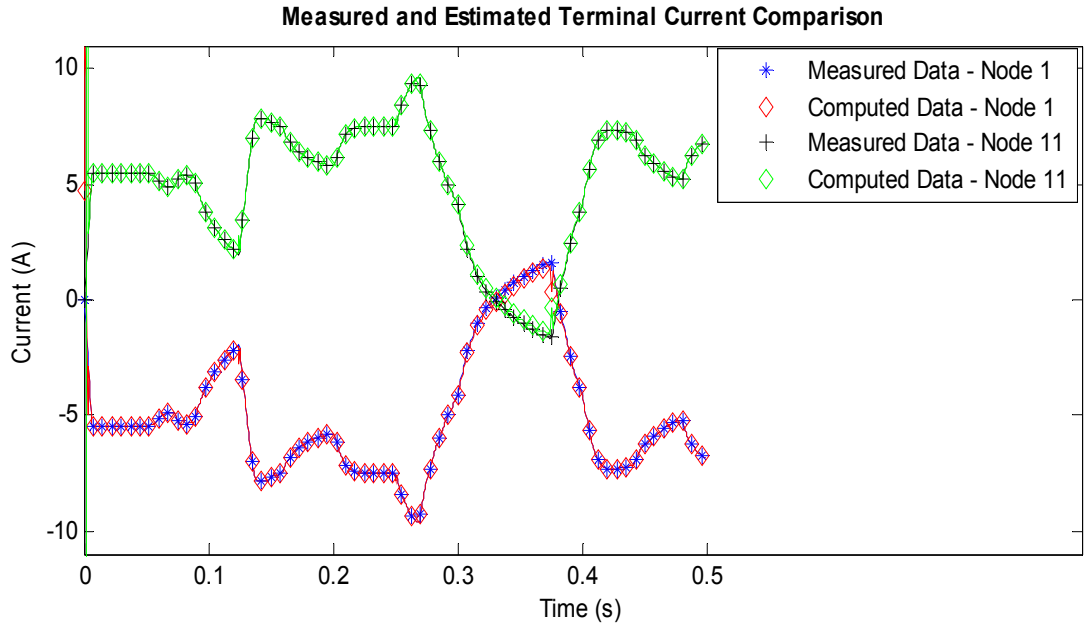
Figure F.4: Computed and measured terminal current plots comparison for nodes 1 and 11.
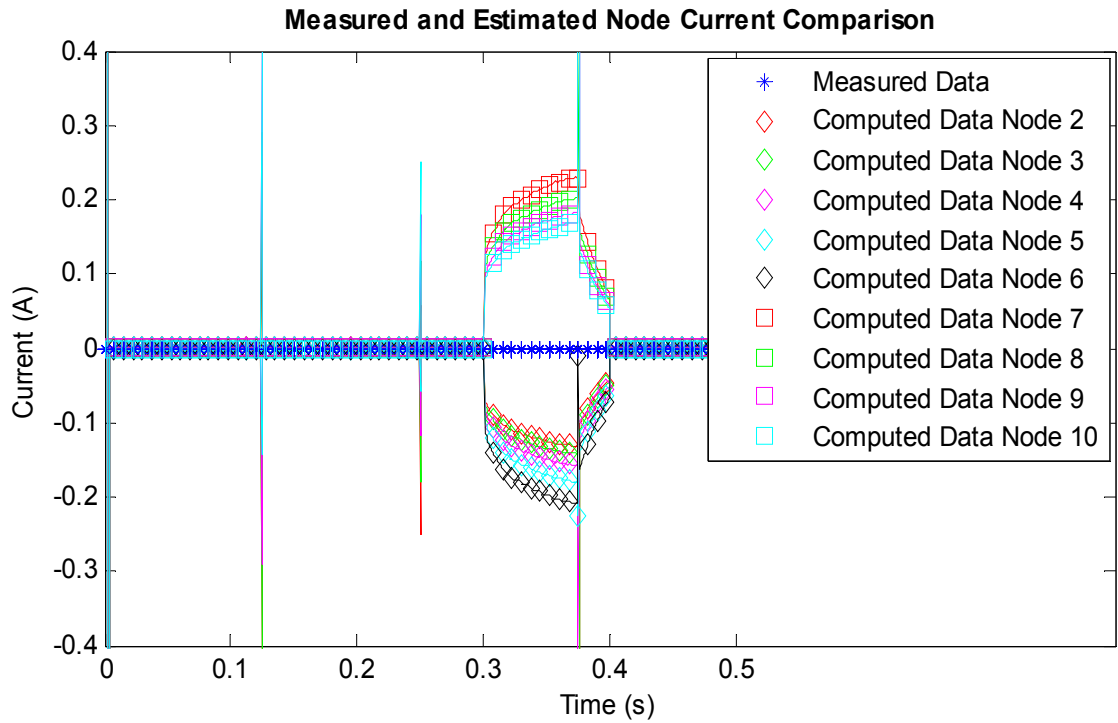
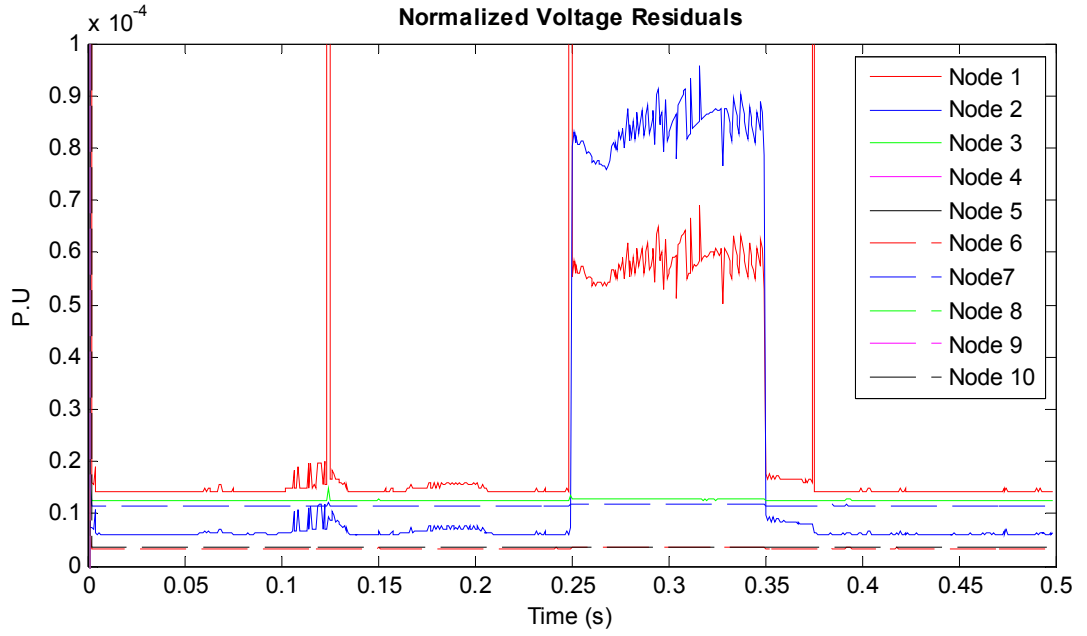**Figure F.5: Computed and measured current plots comparison for nodes 2 through 10.**

228
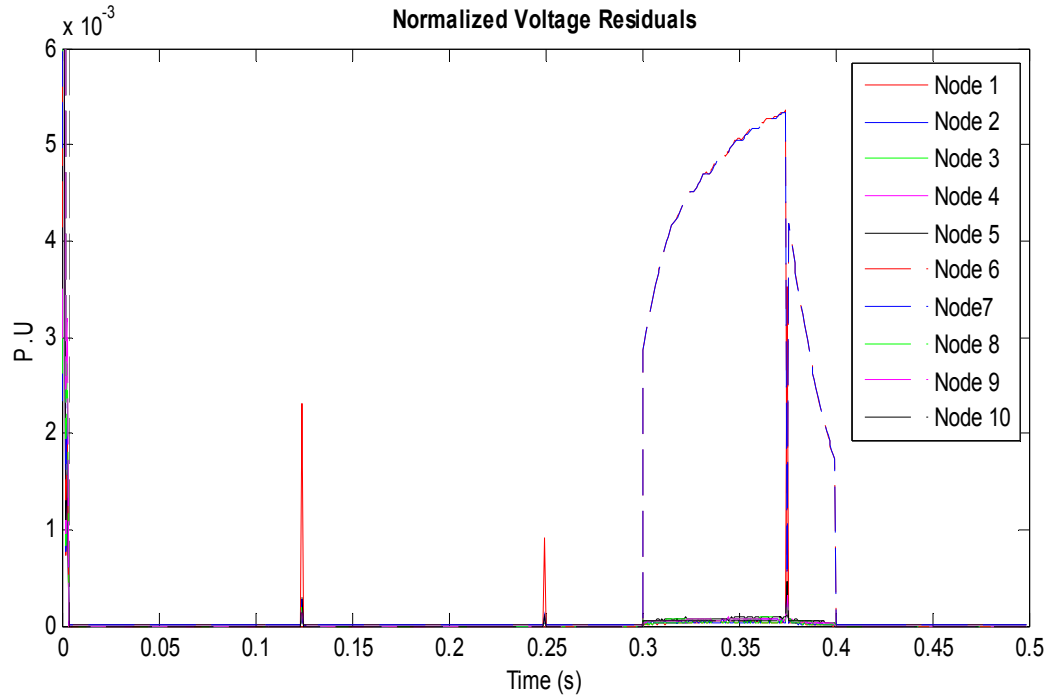
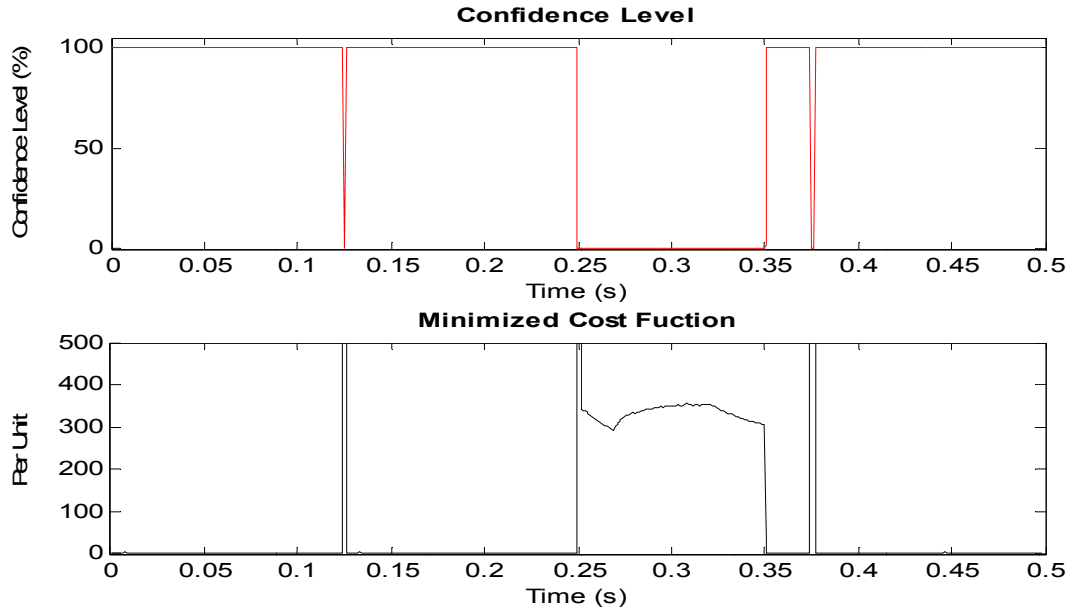**Figure F.6: Voltage residual plots for the case with photovoltaic module 6 shorted.**
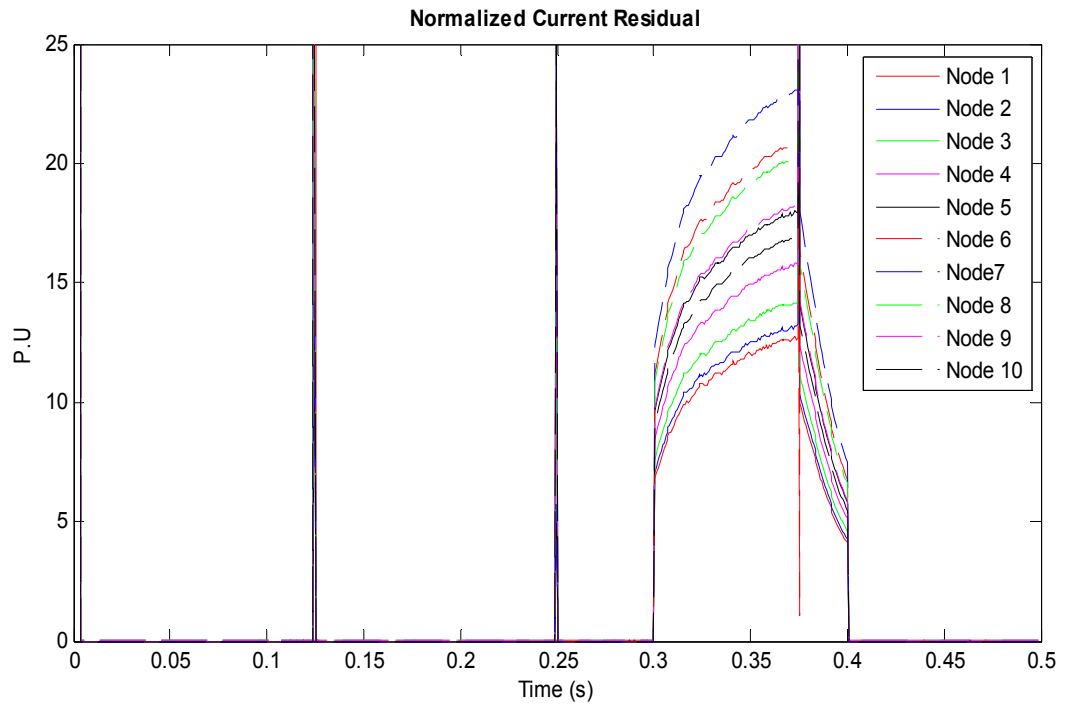
Figure F.7: Current residual plots for the case with photovoltaic module 6 shorted.

F.2. Simulation Result with Photovoltaic Module Number 6 Terminals Shorted in the Presence of Blocking Diode.
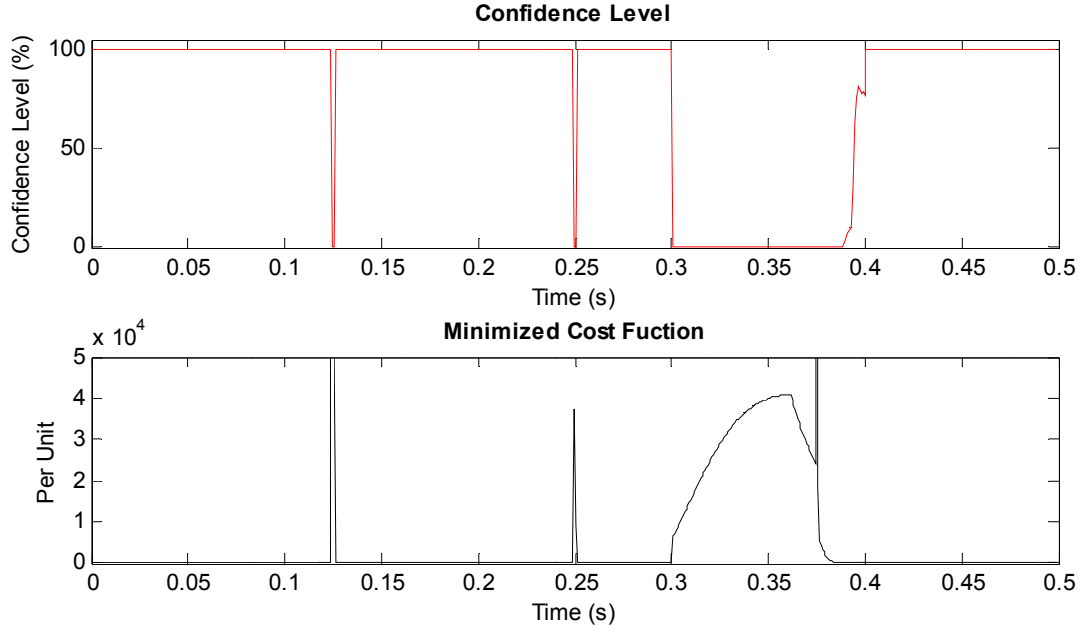
Figure F.8: Confidence level and cost function plots with photovoltaic module 6 shorted.
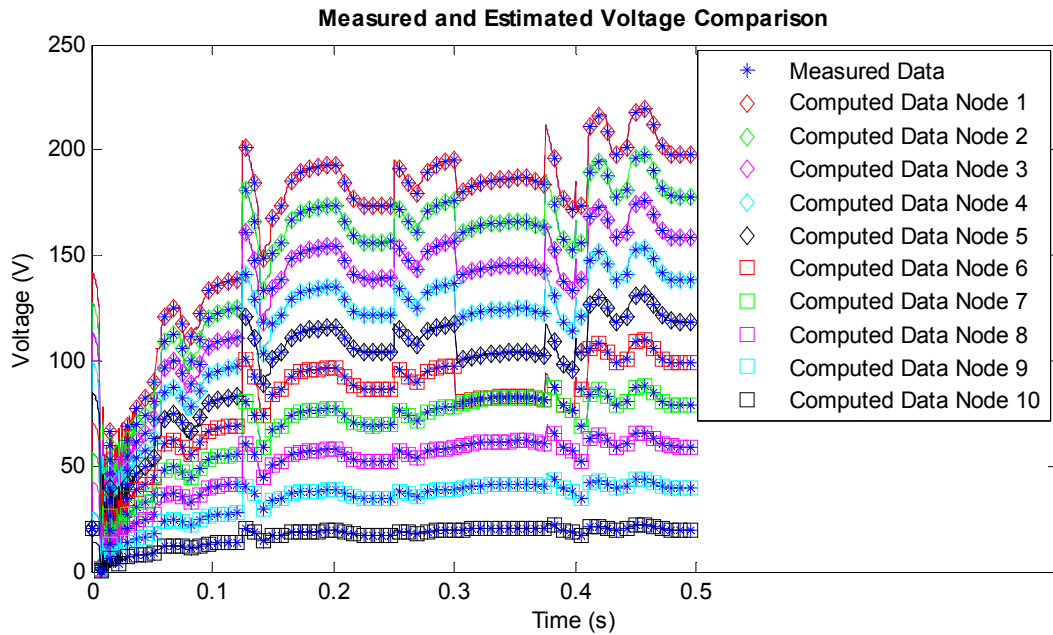
Figure F.9: Computed and measured voltage plots comparison for nodes 1 to 10.
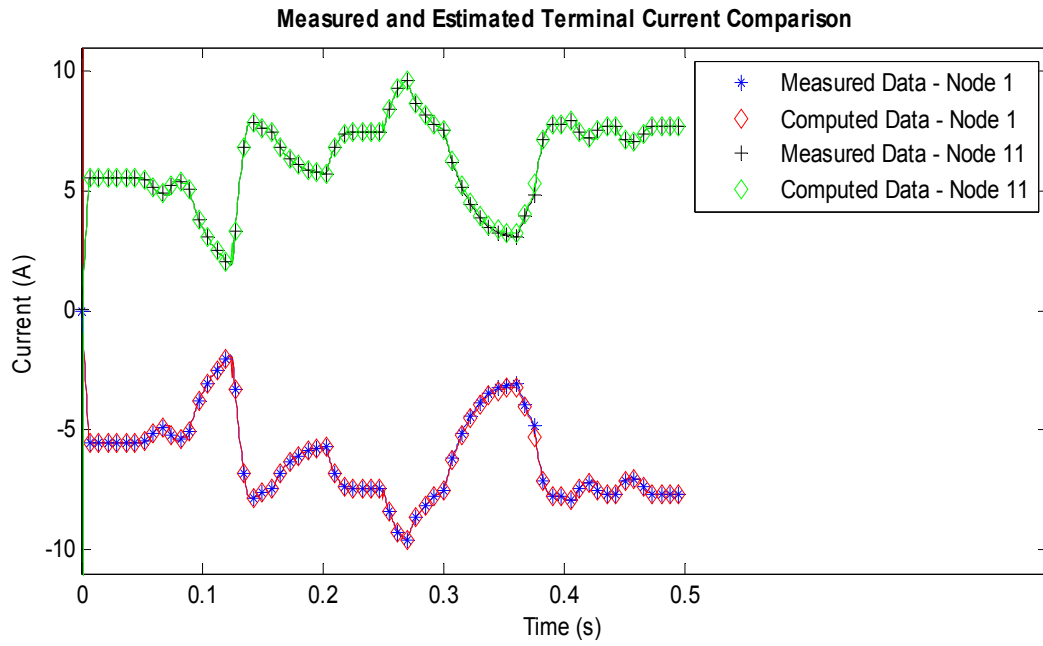
Figure F.10: Computed and measured terminal current plots comparison for nodes 1 and 11.
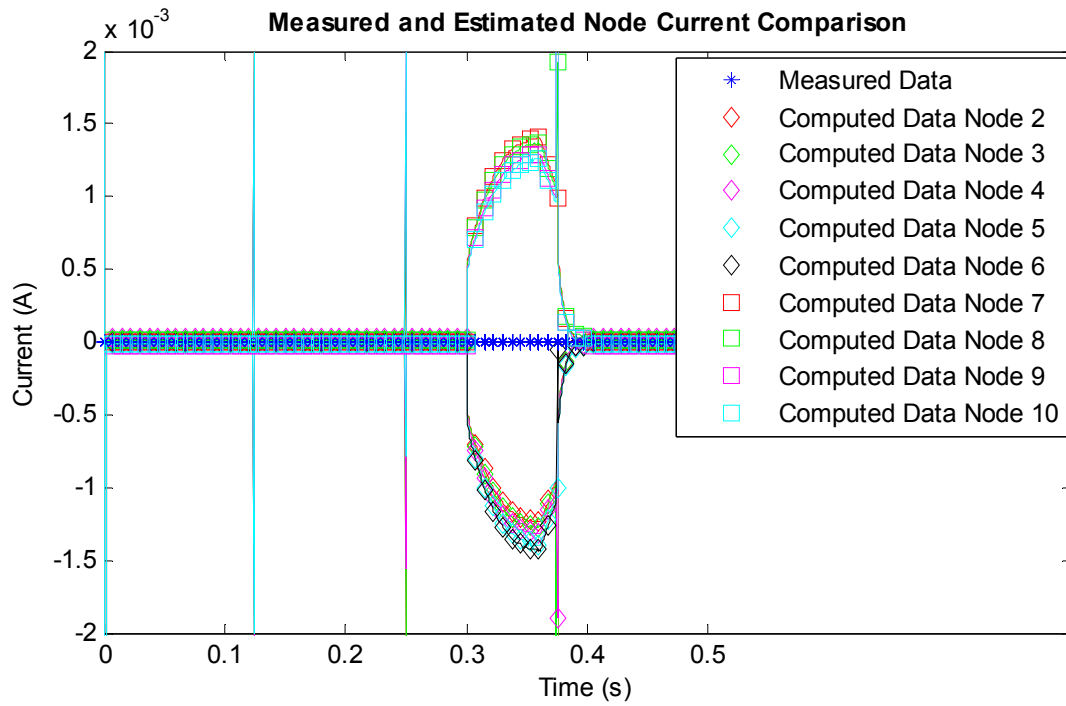
Figure F.11: Computed and measured current plots comparison for nodes 2 through 10.

231
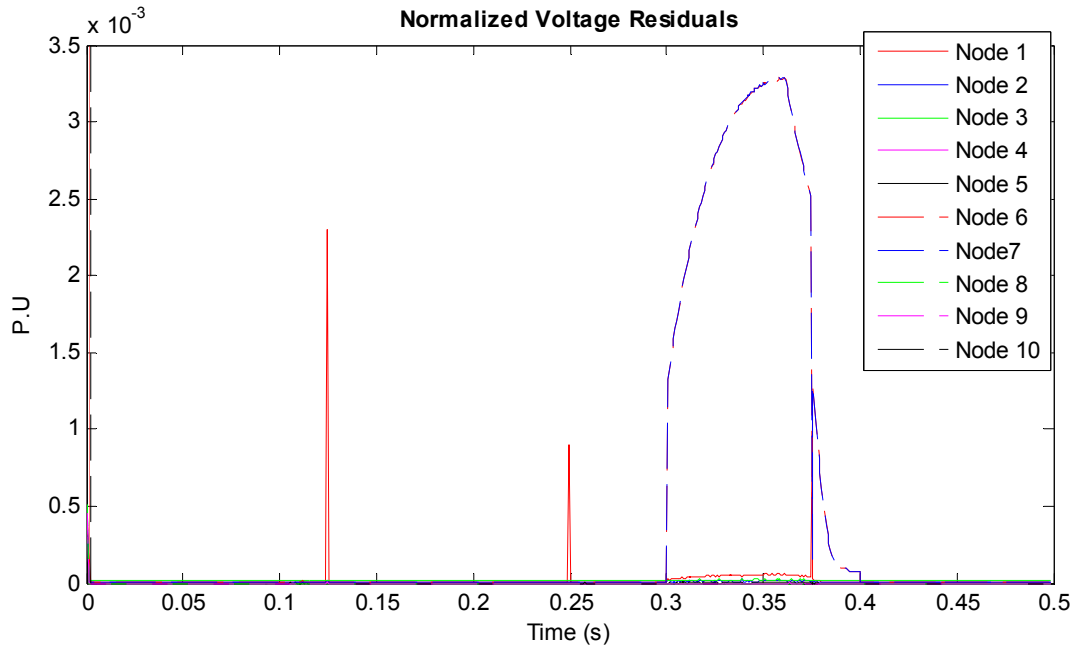
Figure F.12: Voltage residual plots for the case photovoltaic module 6 shorted.
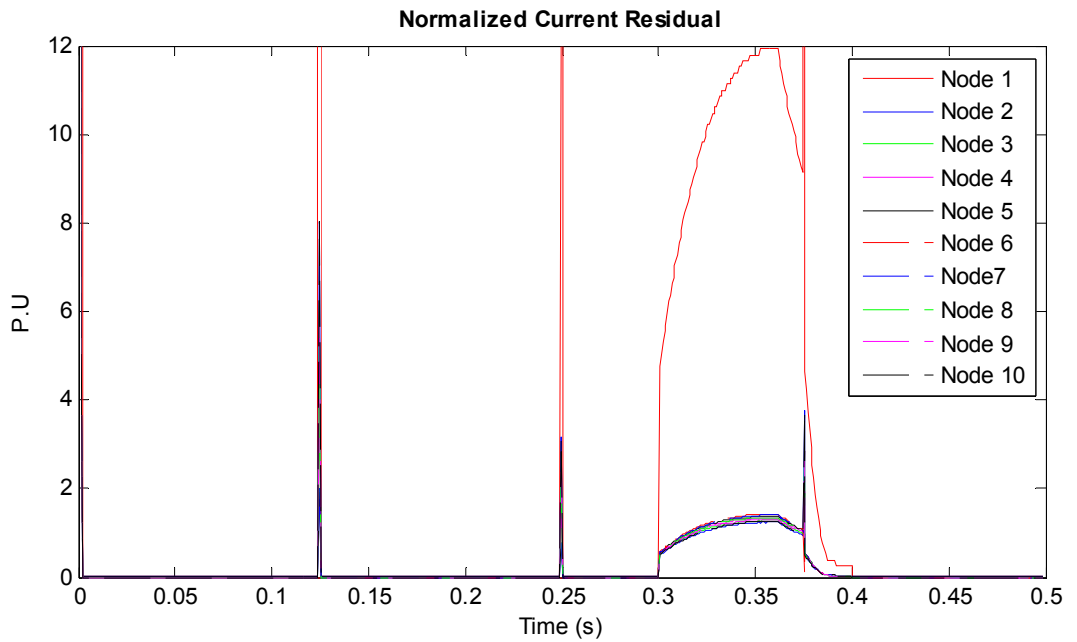
Figure F.13: Current residual plots for the case photovoltaic module 6 shorted.

F.3. Simulation Result with the Cell of Photovoltaic Module Number 2 Shorted to Ground with no Blocking Diode.
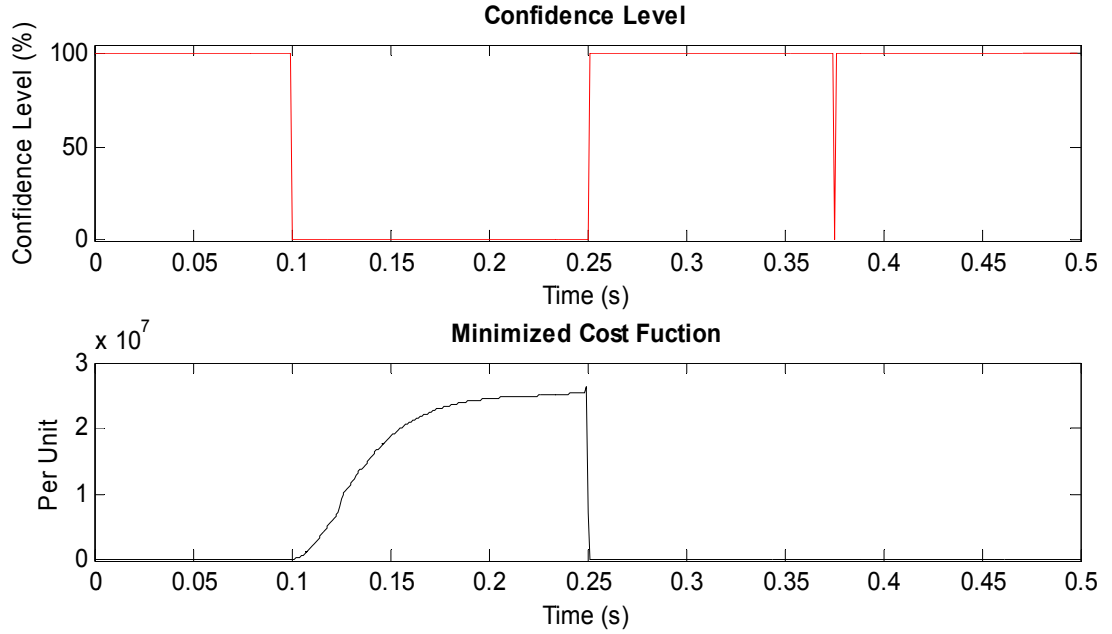
Figure F.14: Confidence level and cost function plots with photovoltaic module 2 shorted to ground.
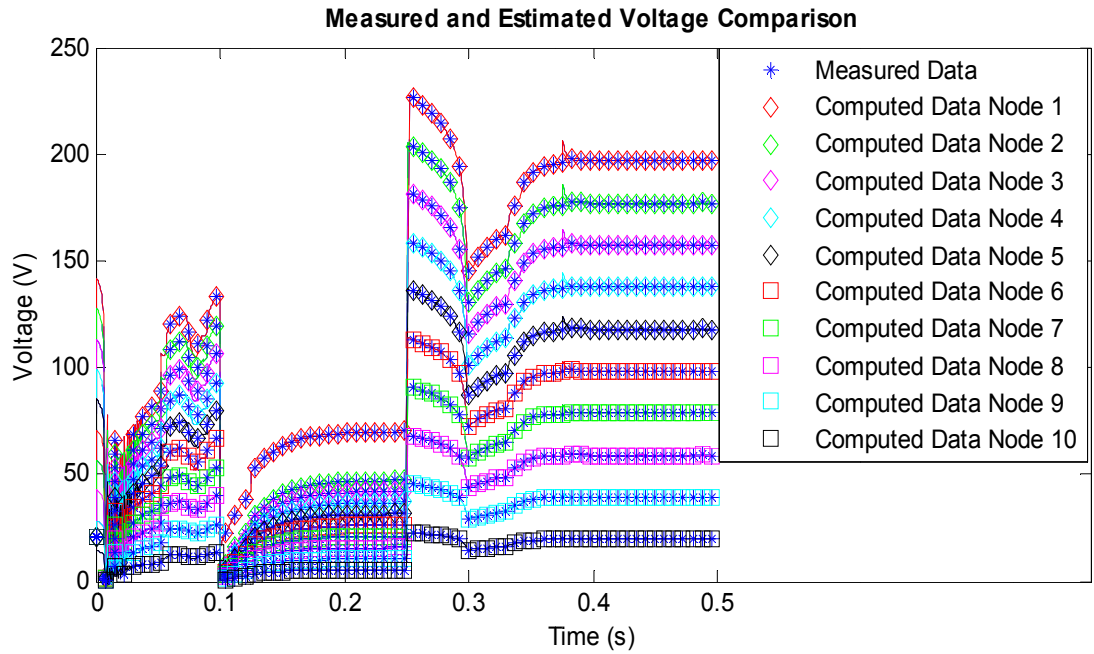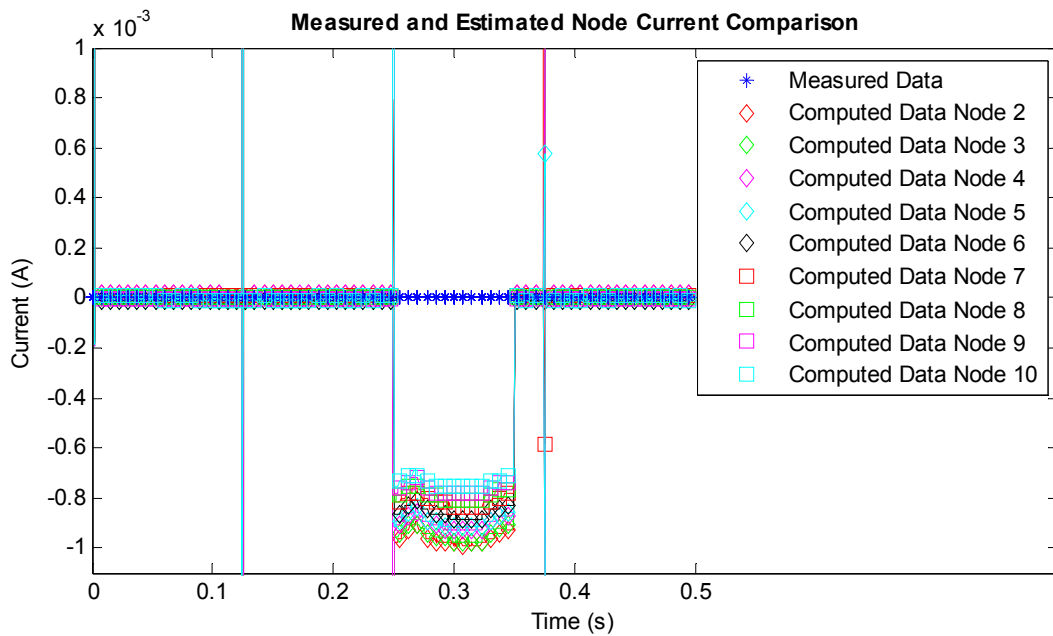

Figure F.15: Computed and measured voltage plots comparison for nodes 1 to 10.
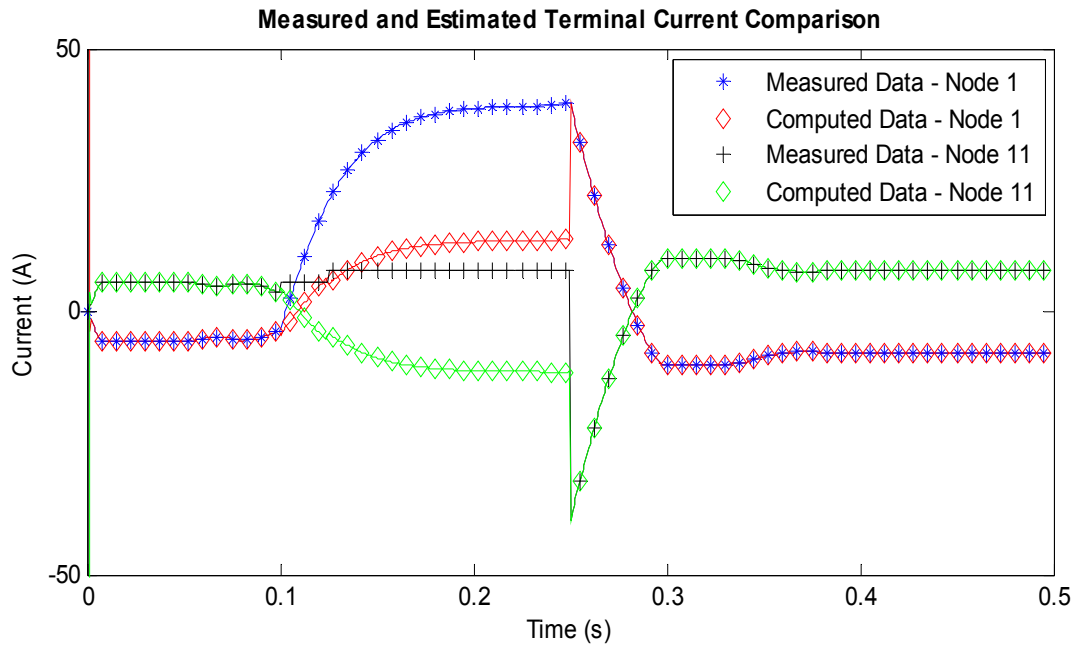
Figure F.16: Computed and measured terminal current plots comparison for nodes 1 and 11.
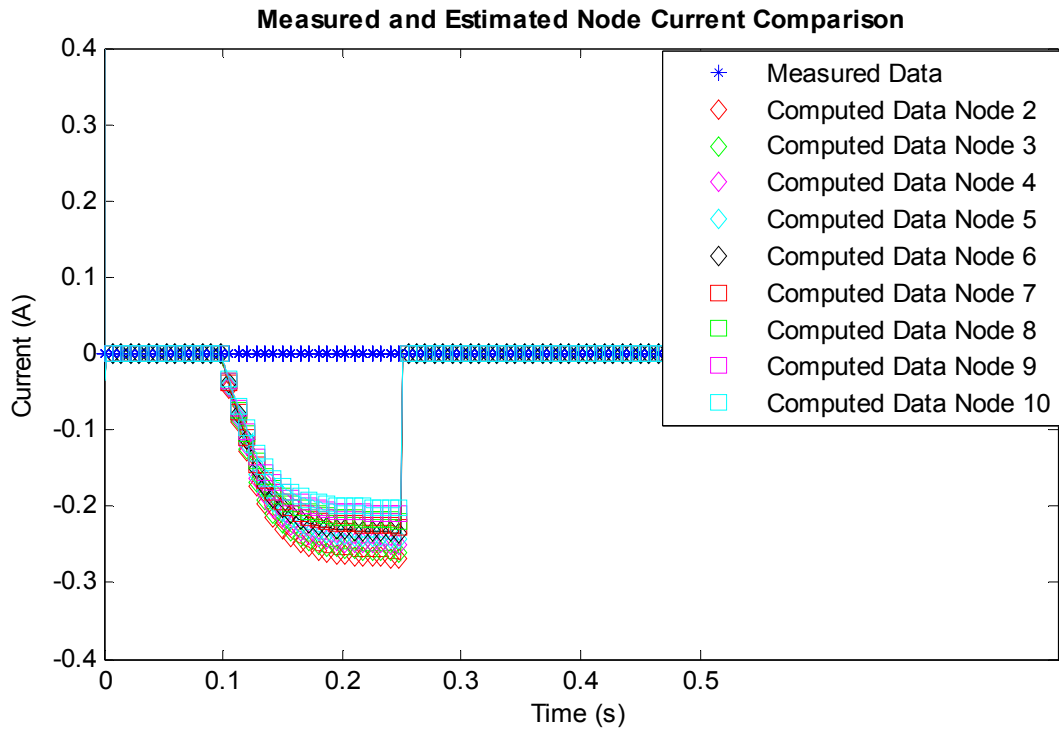
Figure F.17: Computed and measured current plots comparison for nodes 2 through 10.

234
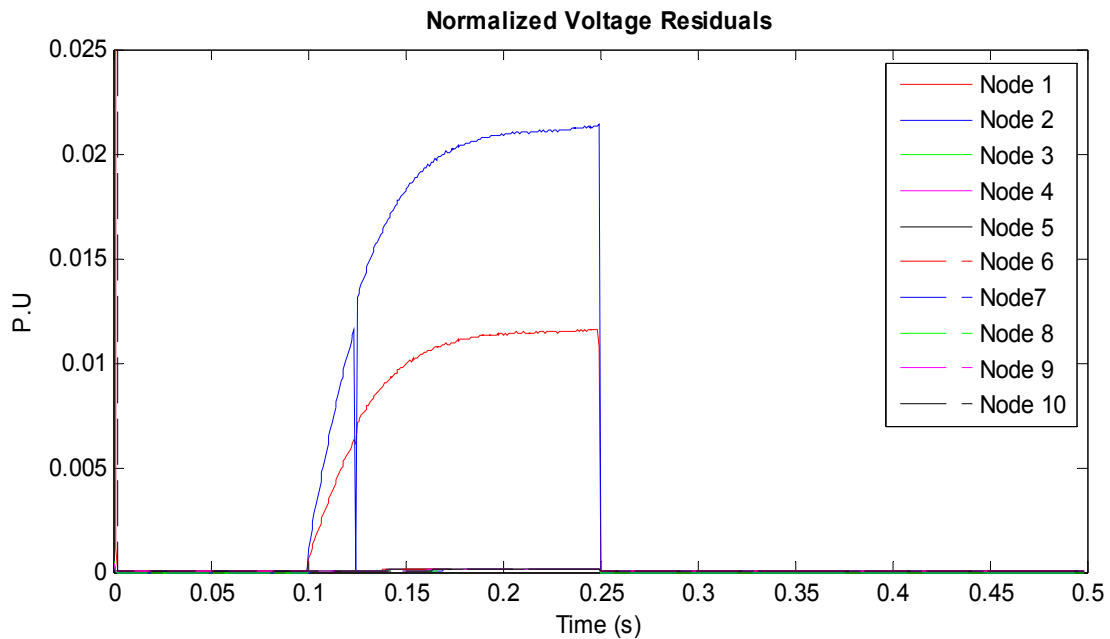
Figure F.18: Voltage residual plots for the case with photovoltaic module 2 cell shorted to ground.
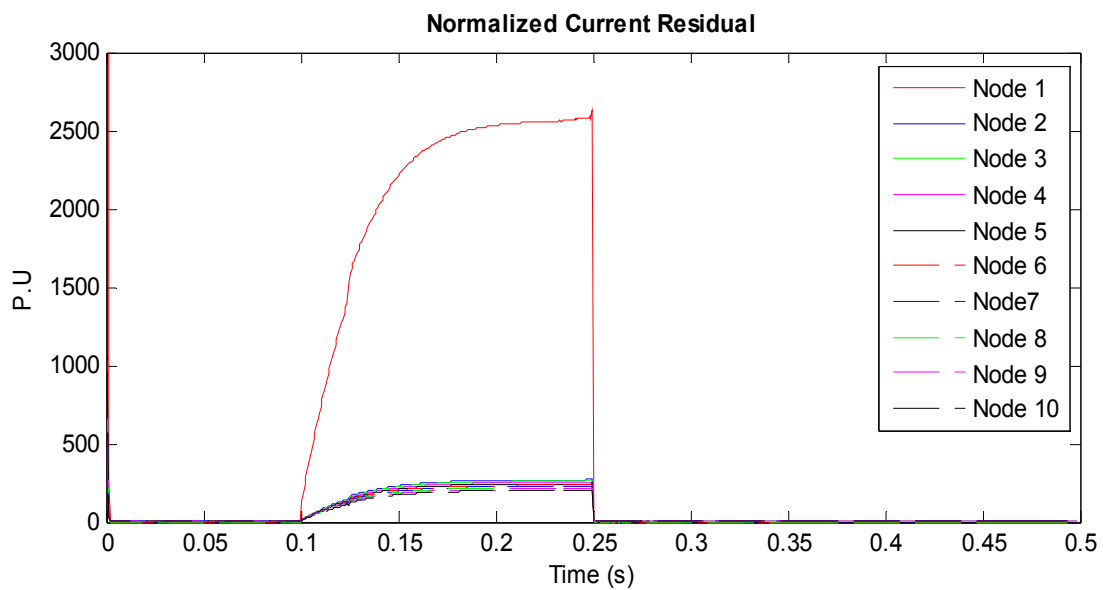
Figure F.19: Current residual plots for the case with photovoltaic module 2 cell shorted to ground.

F.4. Simulation Result with the Cell of Photovoltaic Module Number 2 Shorted to Ground in the Presence of a Blocking Diode.
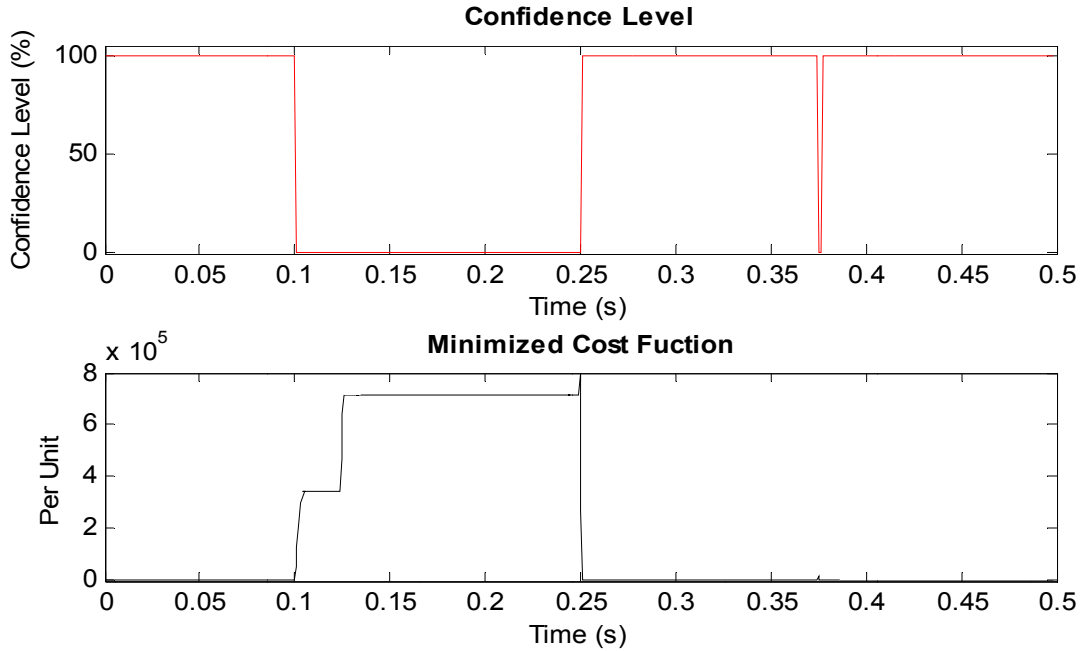
Figure F.20: Confidence level and cost function plots with photovoltaic module 2 shorted to ground.
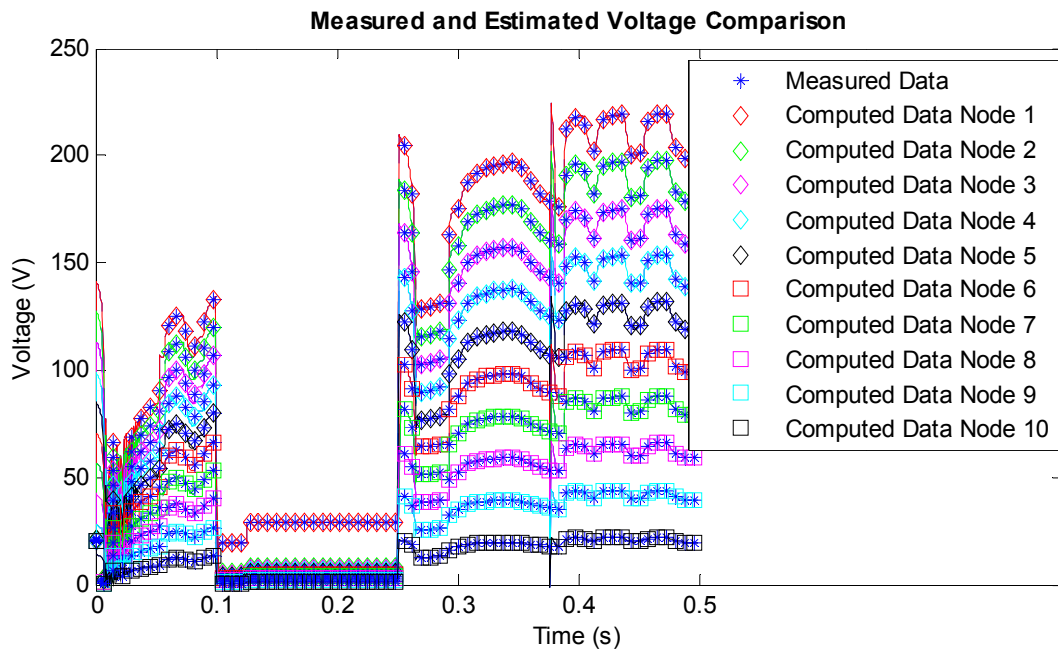
Figure F.21: Computed and measured voltage plots comparison for nodes 1 to 10.
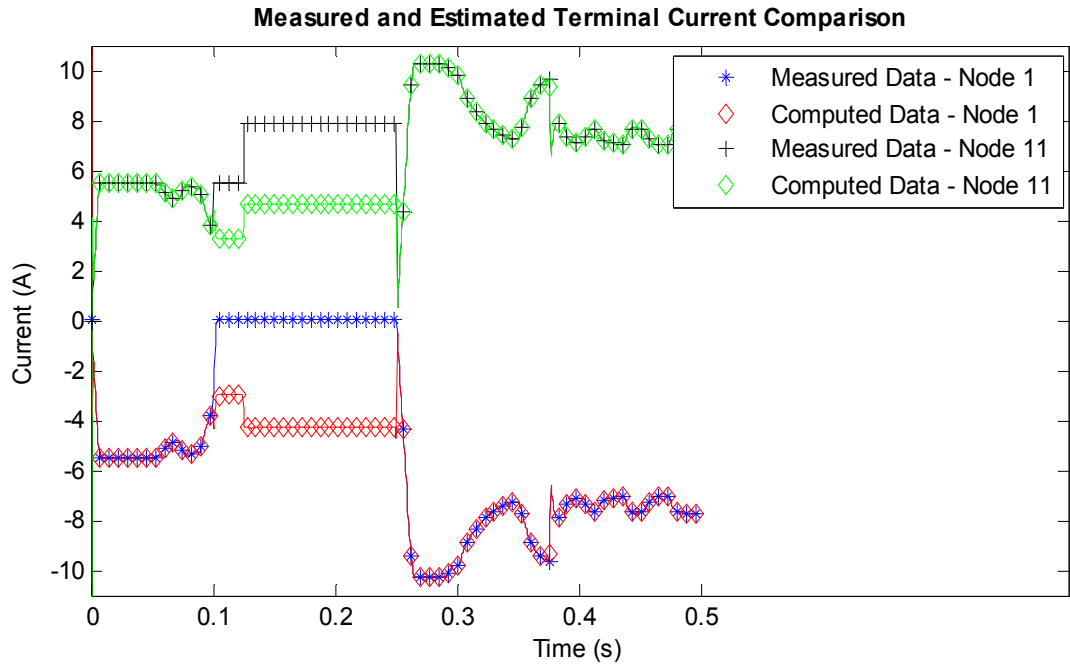
Figure F.22: Computed and measured terminal current plots comparison for nodes 1 and 11.
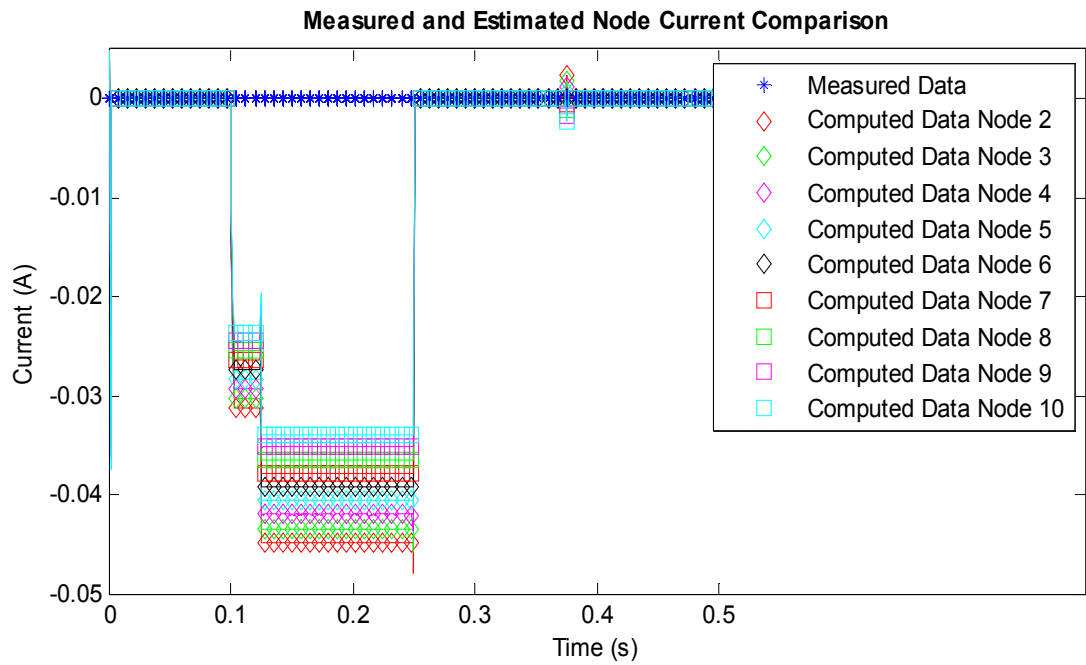
Figure F.23: Computed and measured current plots comparison for nodes 2 through 10.
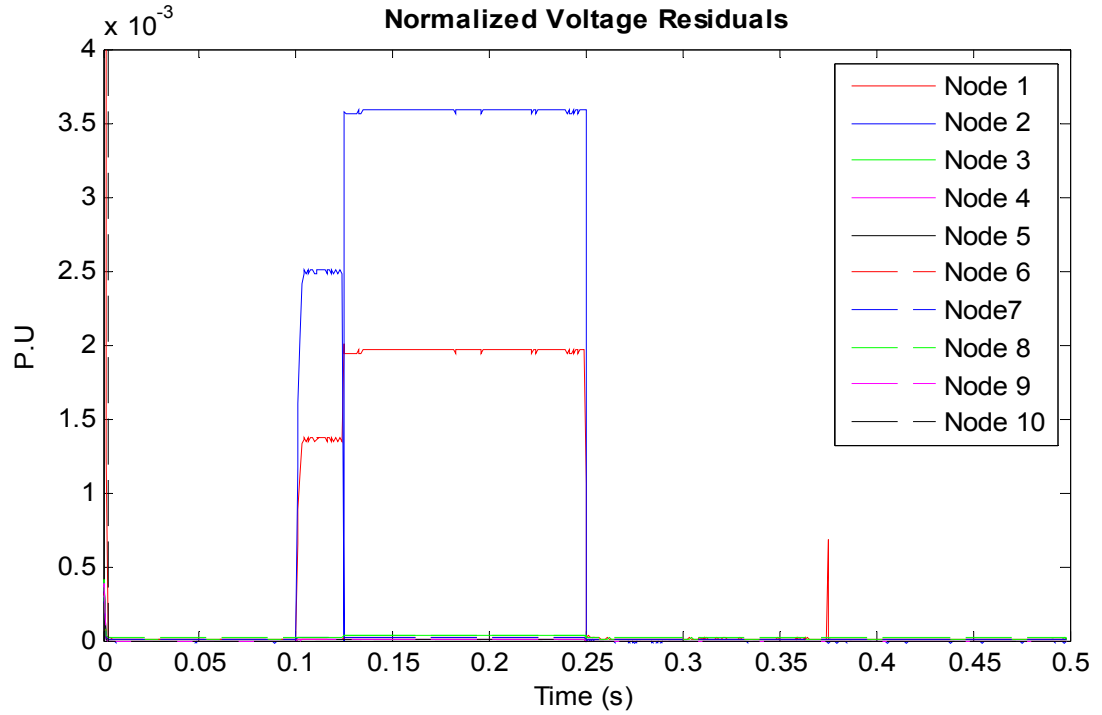
**Figure F.24: Voltage residual plots for the case with photovoltaic module 2 cell shorted to ground.**
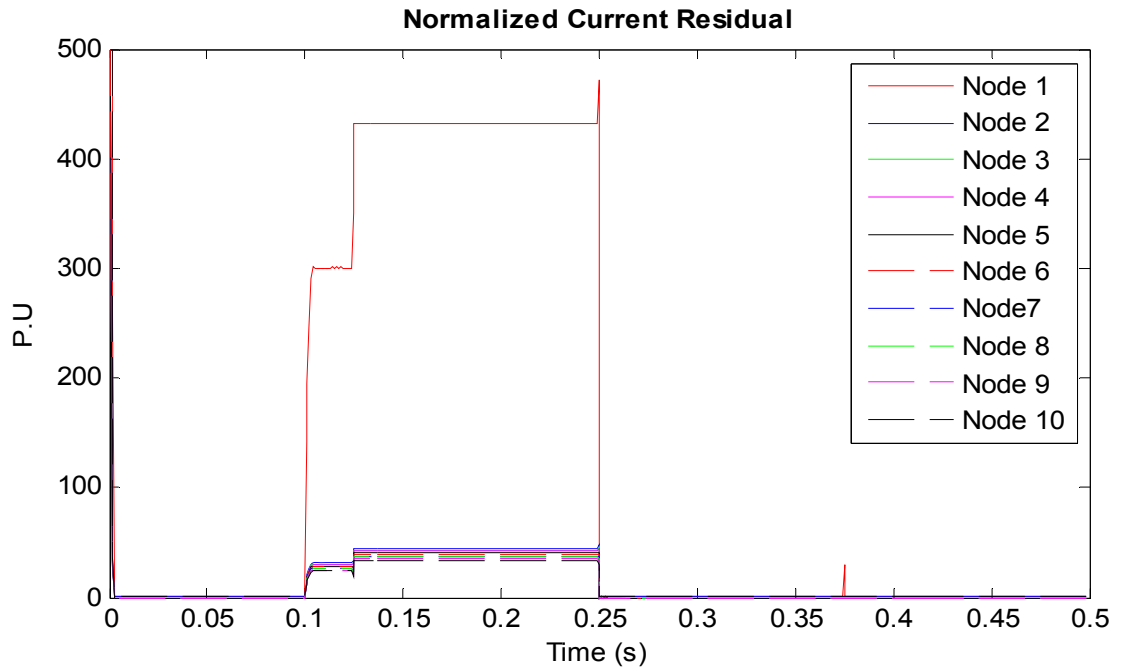
Figure F.25: Current residual plots for the case with photovoltaic module 2 cell shorted to ground.

238

F.5. Simulation Result for a High Impedance Fault from Photovoltaic Module Number 2 cell to Ground with no Blocking Diode
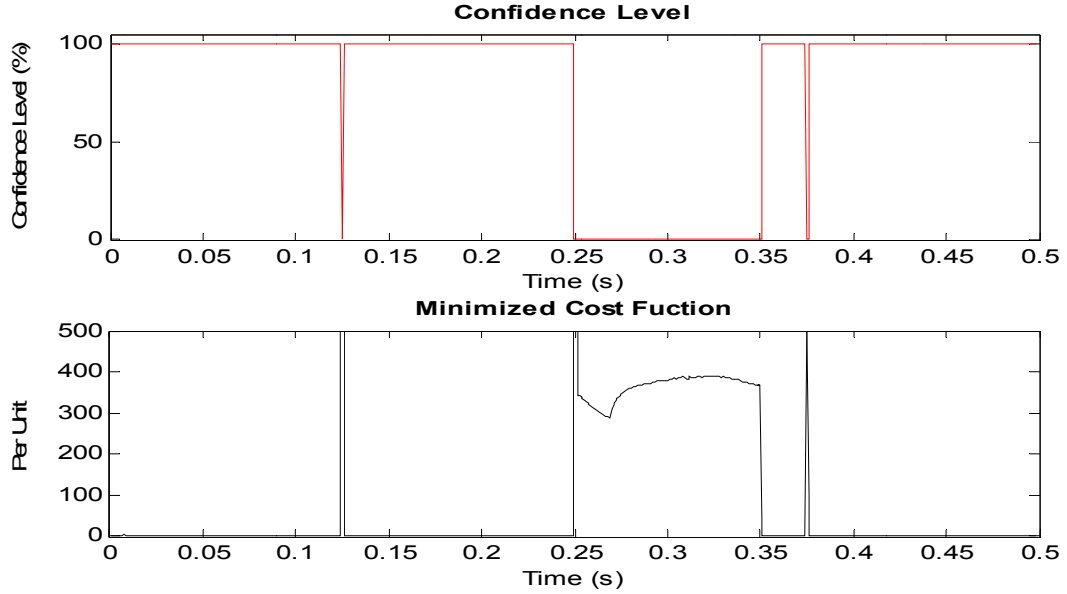
Figure F.26: Confidence level and cost function plots during a high impedance fault on the photovoltaic cell of module 2.
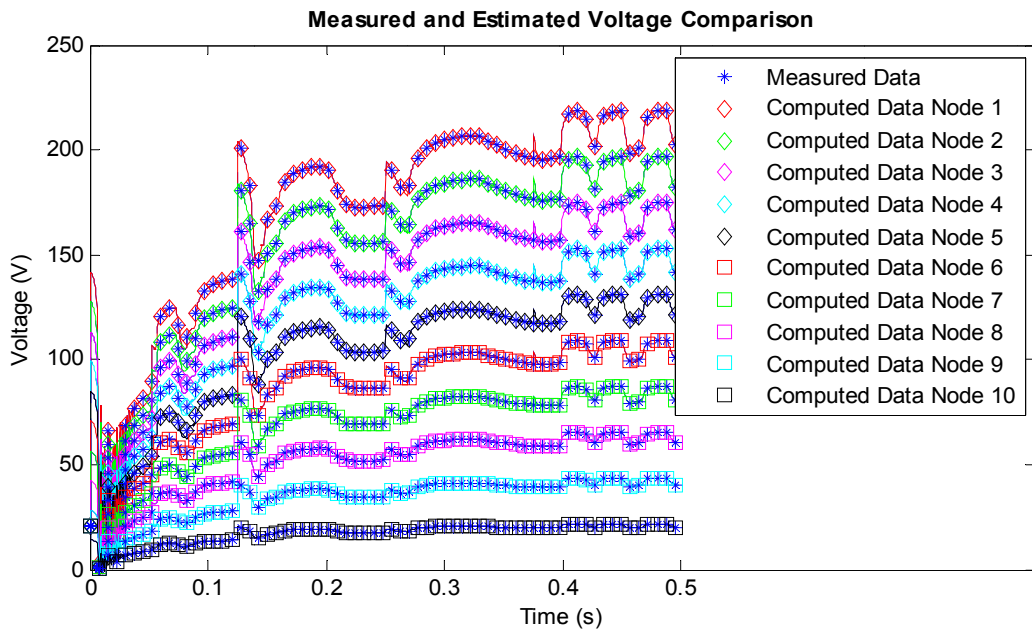
Figure F.27: Computed and measured voltage plots comparison for nodes 1 to 10.
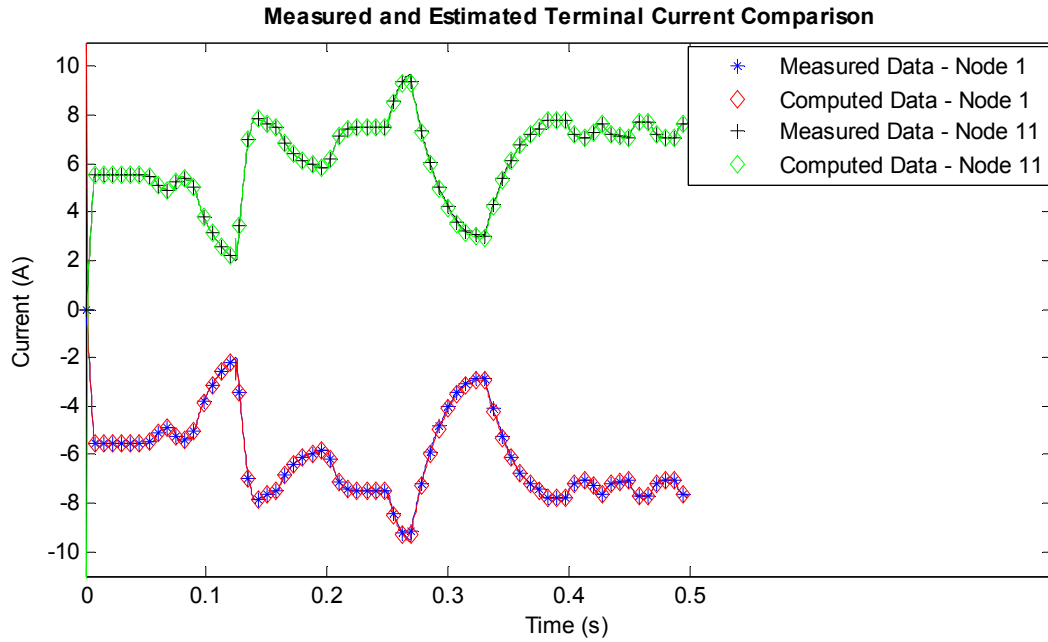
Figure F.28: Computed and measured terminal current plots comparison for nodes 1 and 11.
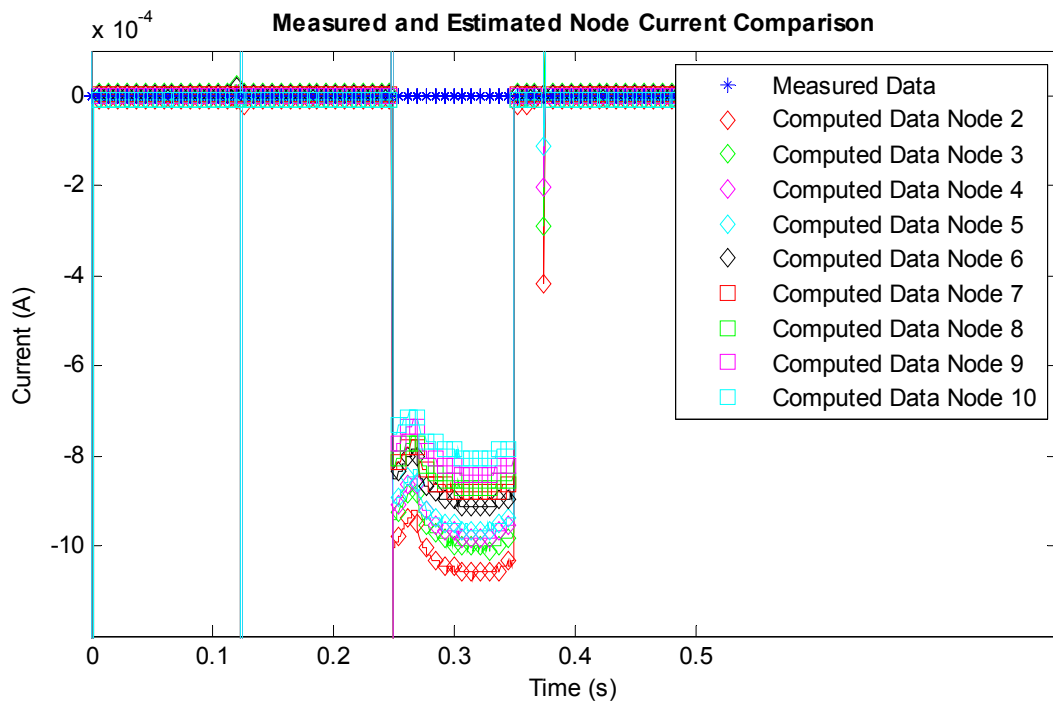
Figure F.29: Computed and measured current plots comparison for nodes 2 through 10.

Figure F.30: Voltage residual plots for photovoltaic module 2 shorted.
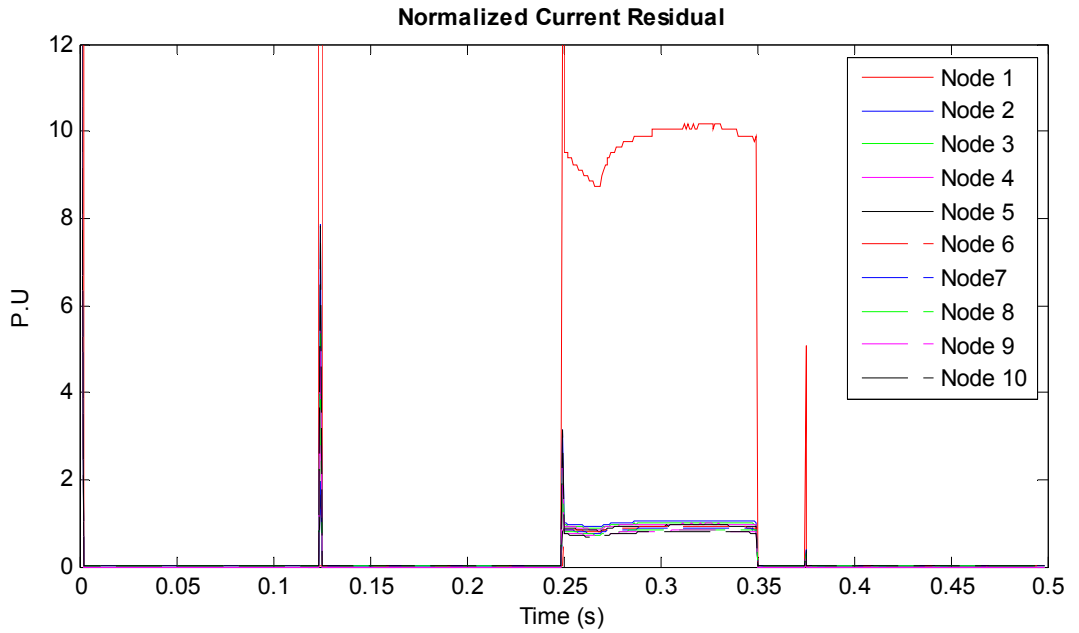
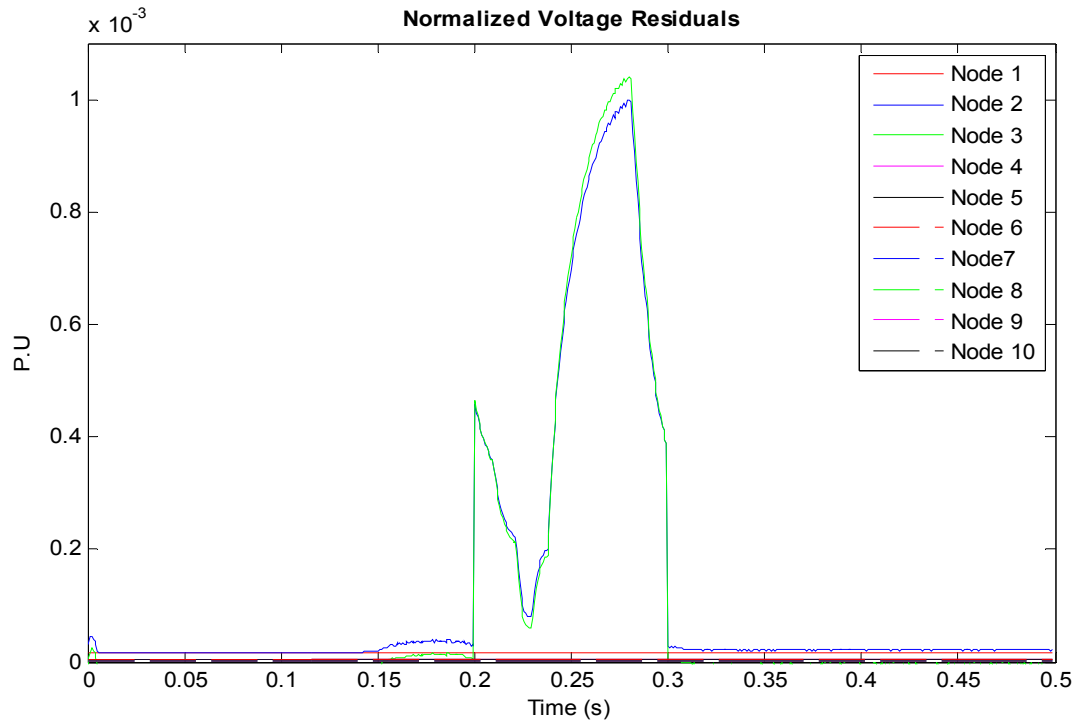**Figure F.31: Current residual plots for photovoltaic module 2 shorted.**

F.6. Simulation Result for a High Impedance Fault from Photovoltaic Module number 2 cell to Ground with Blocking Diode

Figure F.32: Confidence level and cost function plots during a high impedance fault on the photovoltaic cell of module 2.
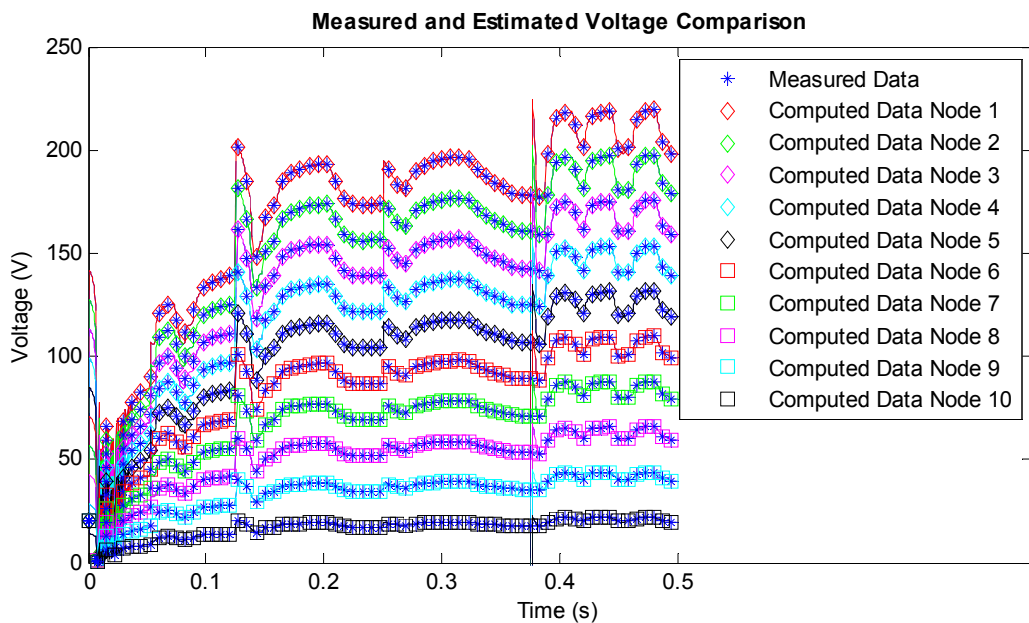
Figure F.33: Computed and measured voltage plots comparison for nodes 1 to 10.
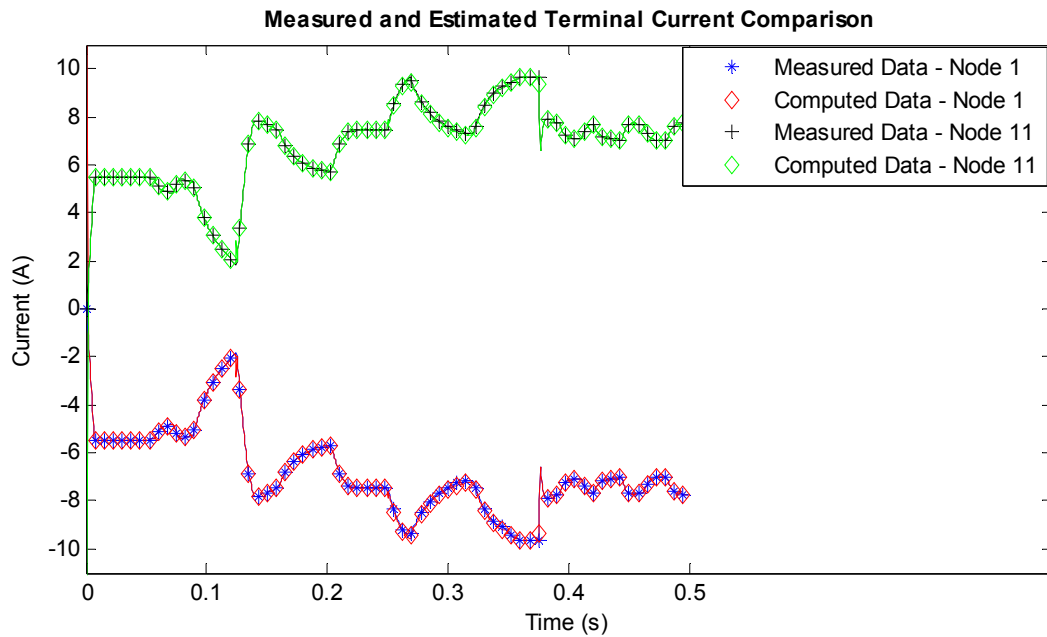
Figure F.34: Computed and measured terminal current plots comparison for nodes 1 and 11.

Figure F.35: Computed and measured current plots comparison for nodes 2 through 10.
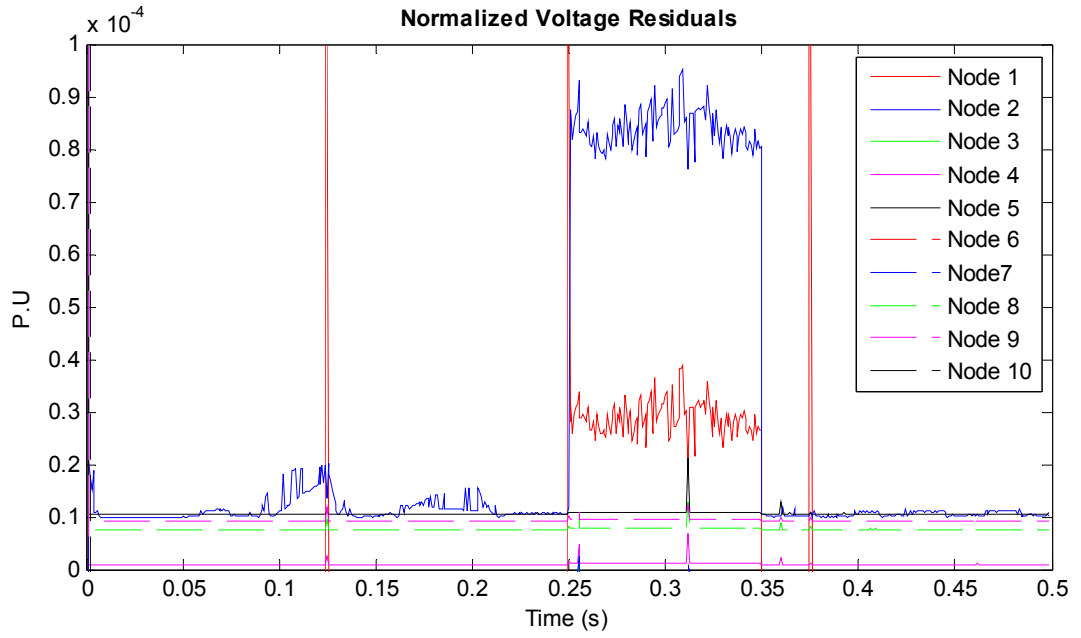
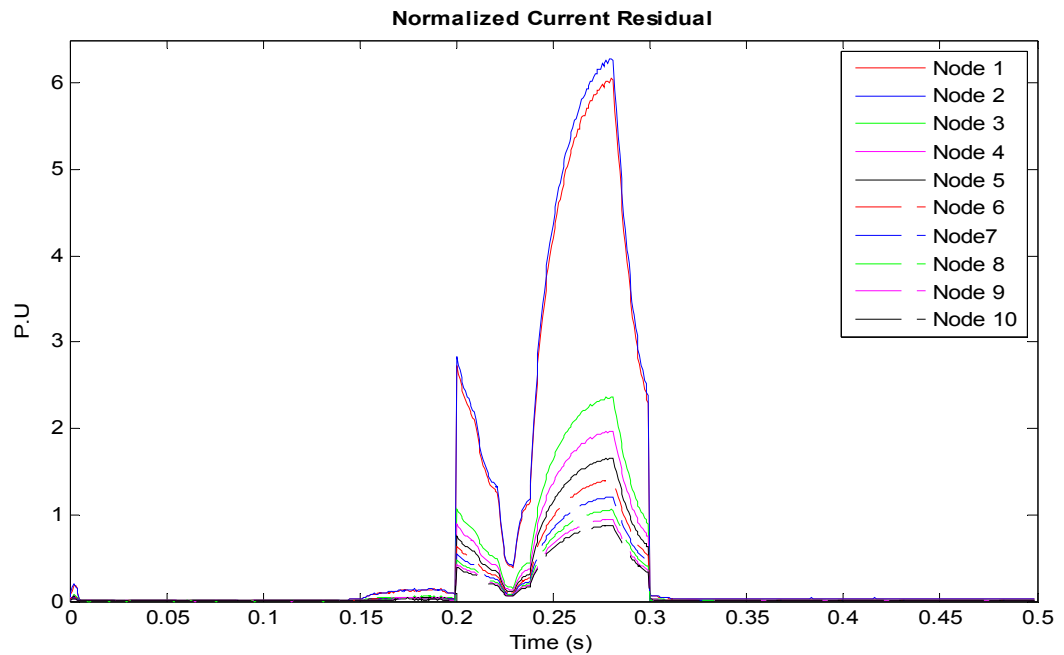**Figure F.36: Voltage residual plots for photovoltaic module 2 shorted.**
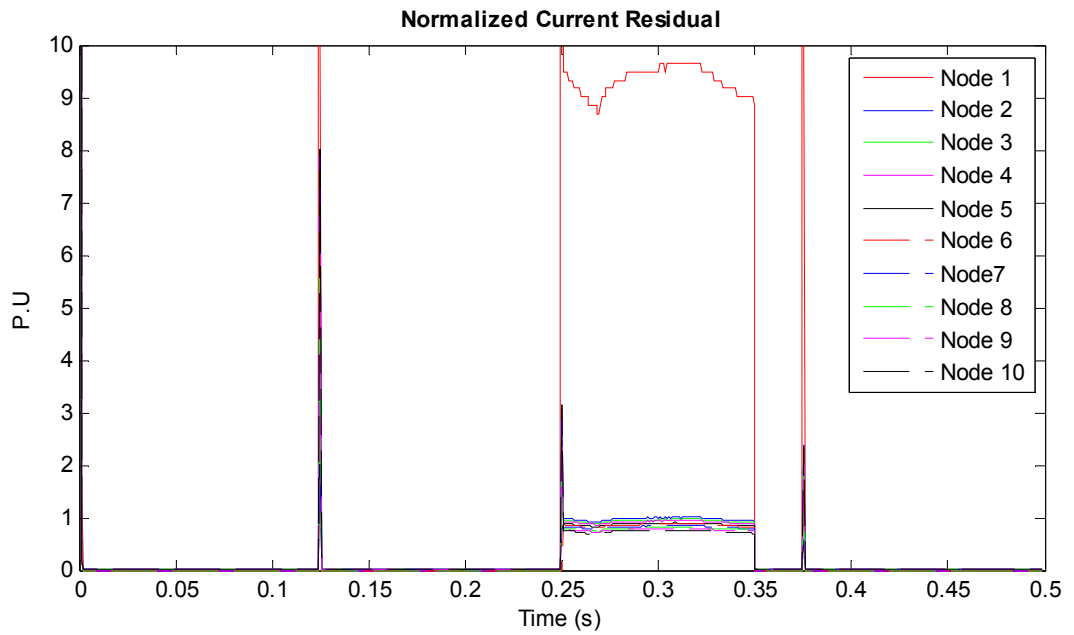
Figure F.37: Current residual plots for photovoltaic module 2 shorted.

F.7. Simulation result with four photovoltaic cells of Module 2 shorted, and with blocking diode
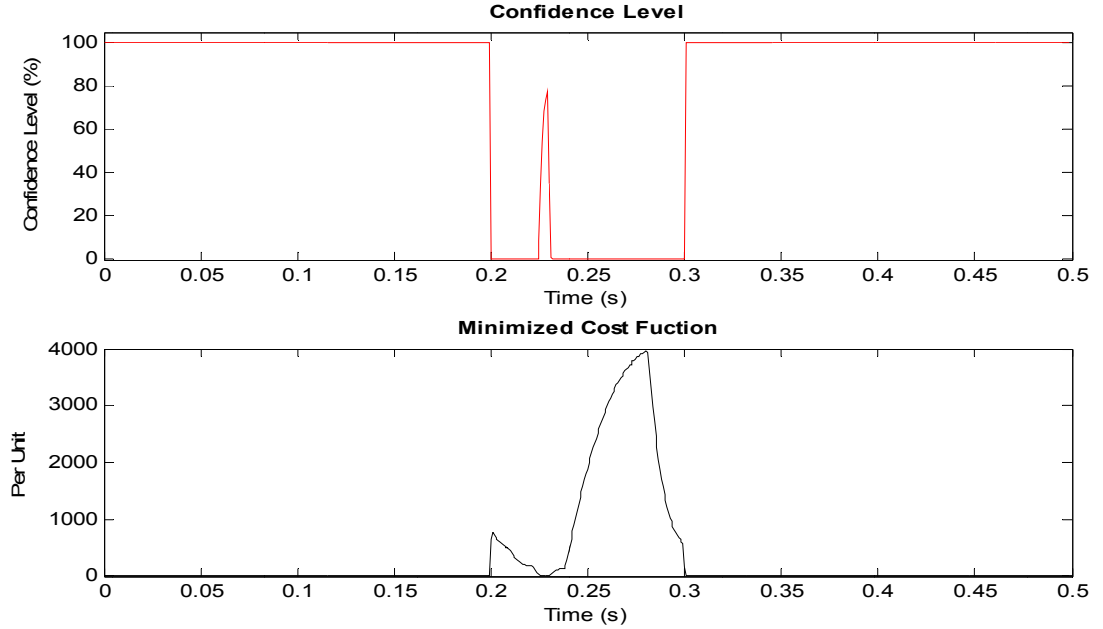
Figure F.38: Confidence level and cost function plots with photovoltaic cells shorted.
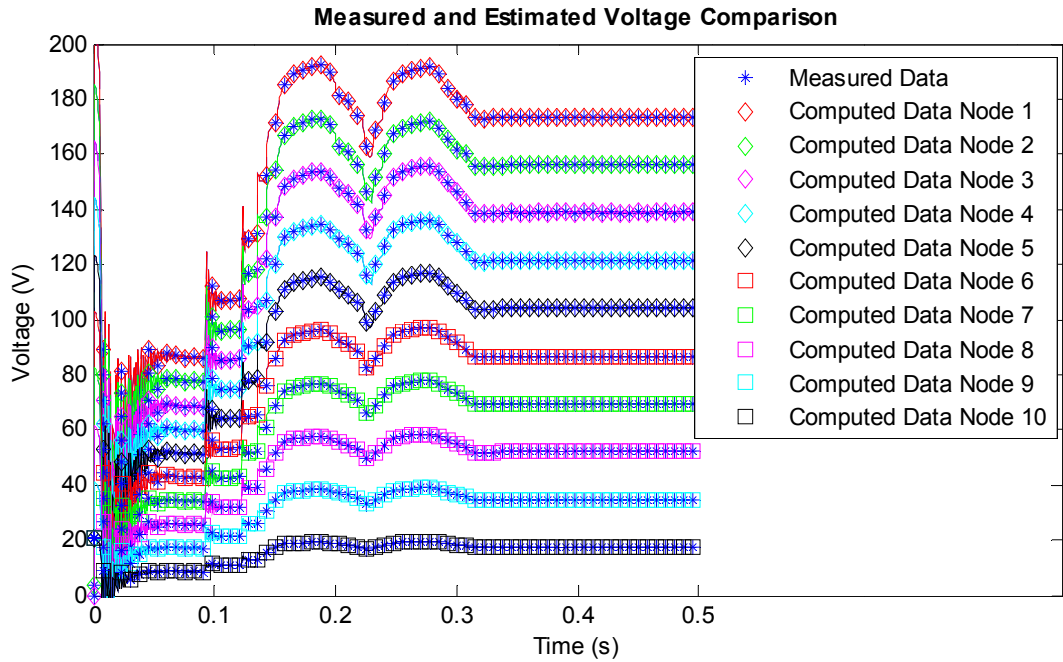
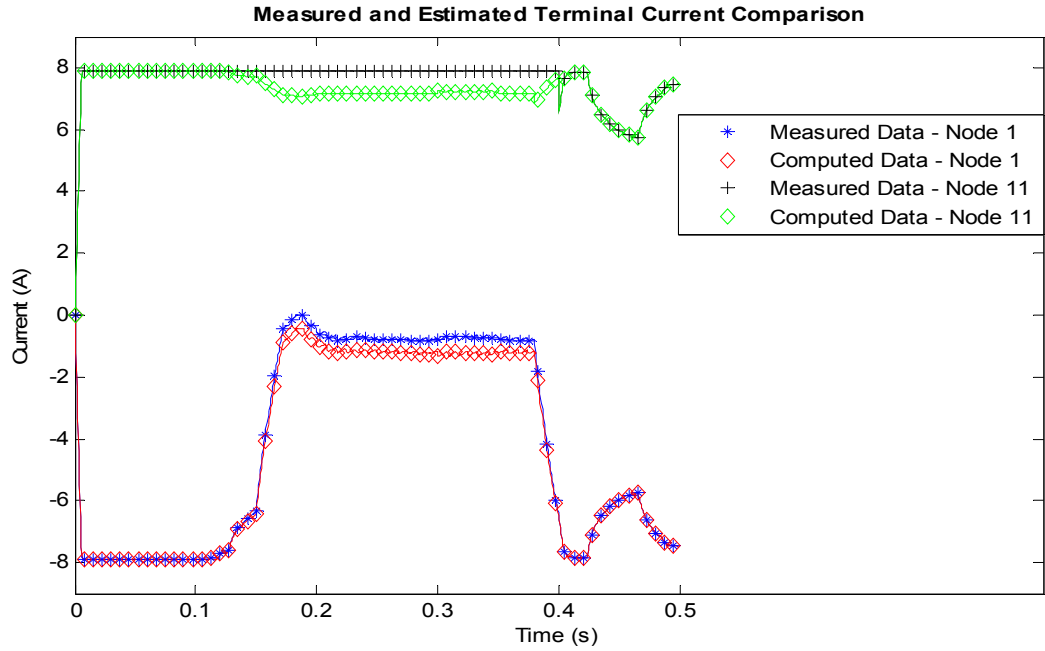**Figure F.39: Computed and measured voltage plots comparison for nodes 1 to 10.**
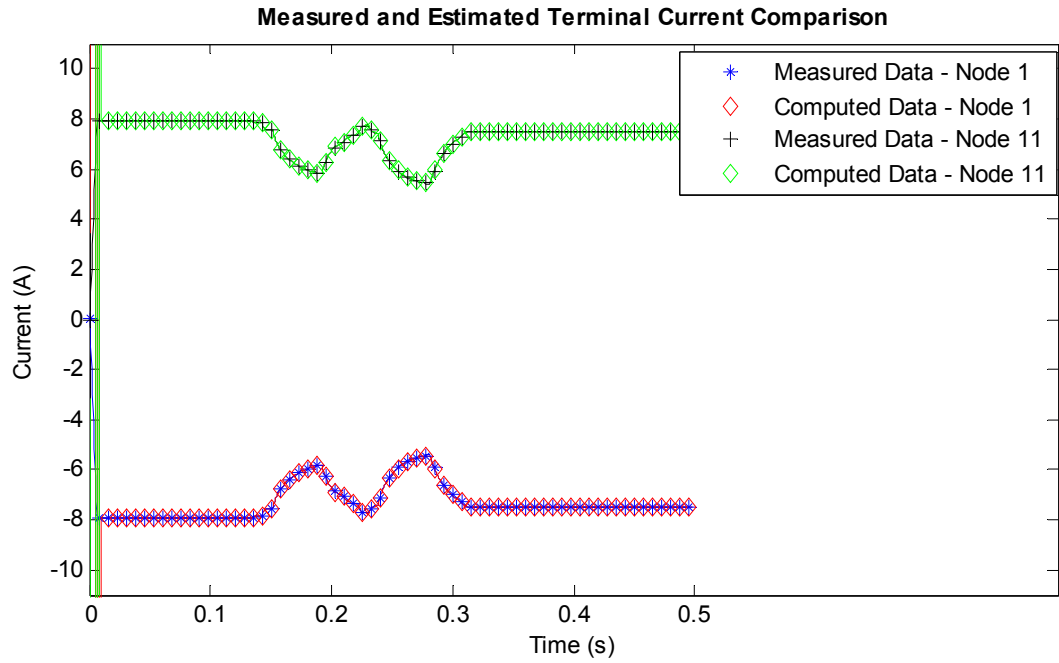
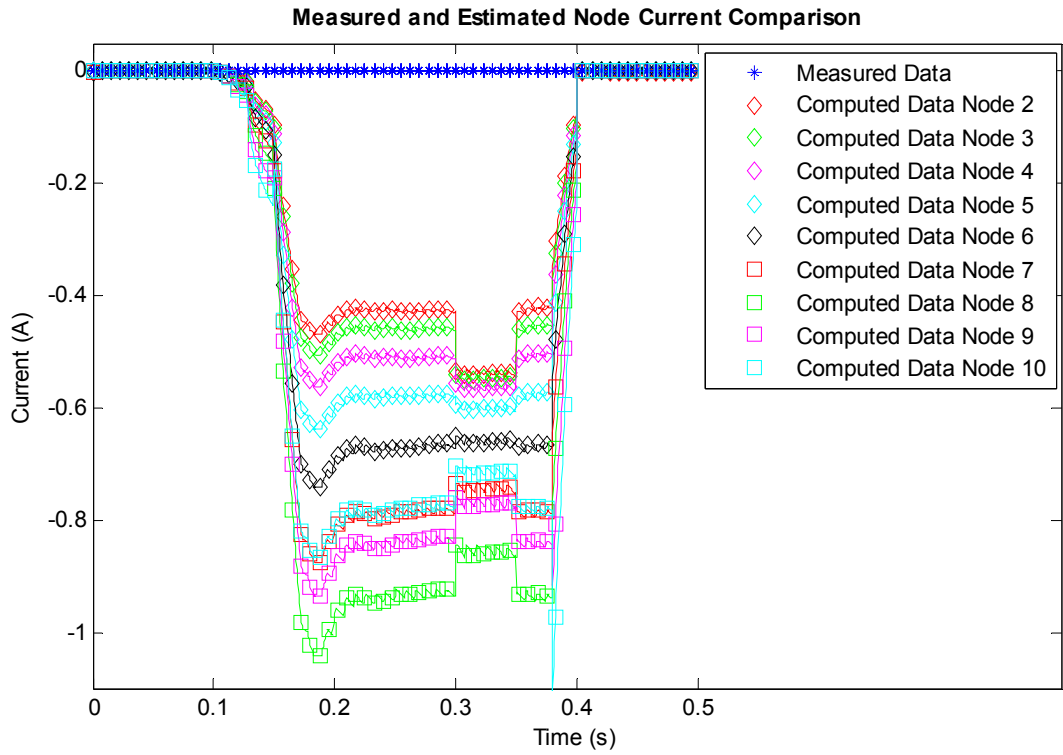**Figure F.40: Computed and measured terminal current plots comparison for nodes 1 and 11.**
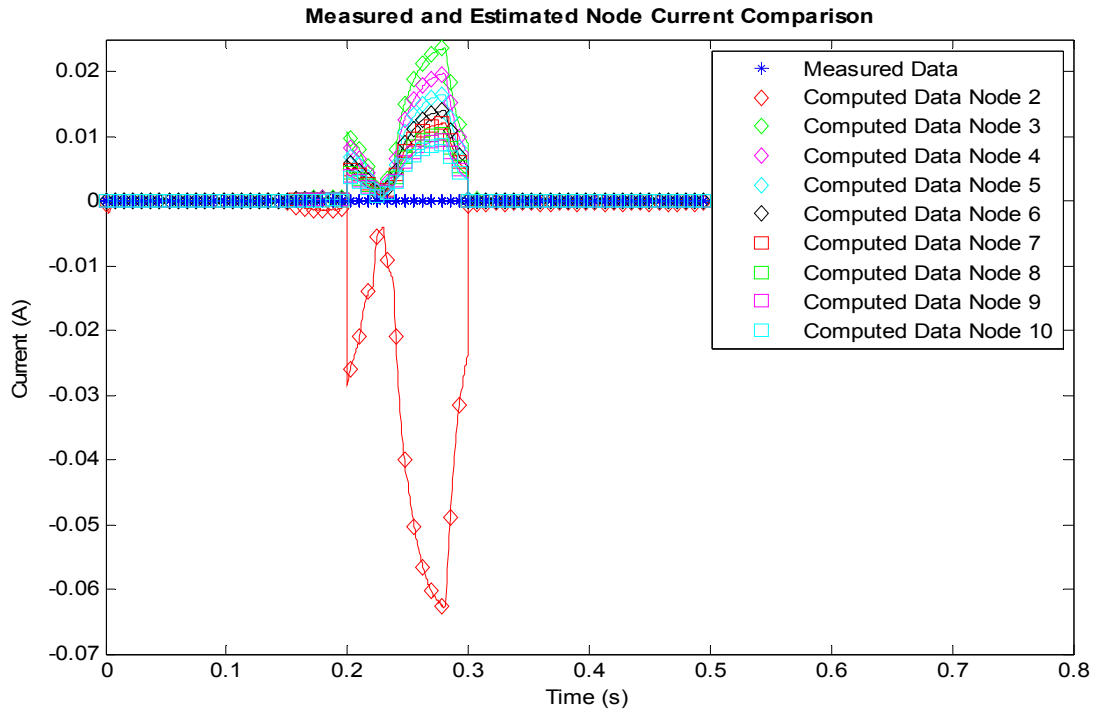
Figure F.41: Computed and measured current plots comparison for nodes 2 through 10.
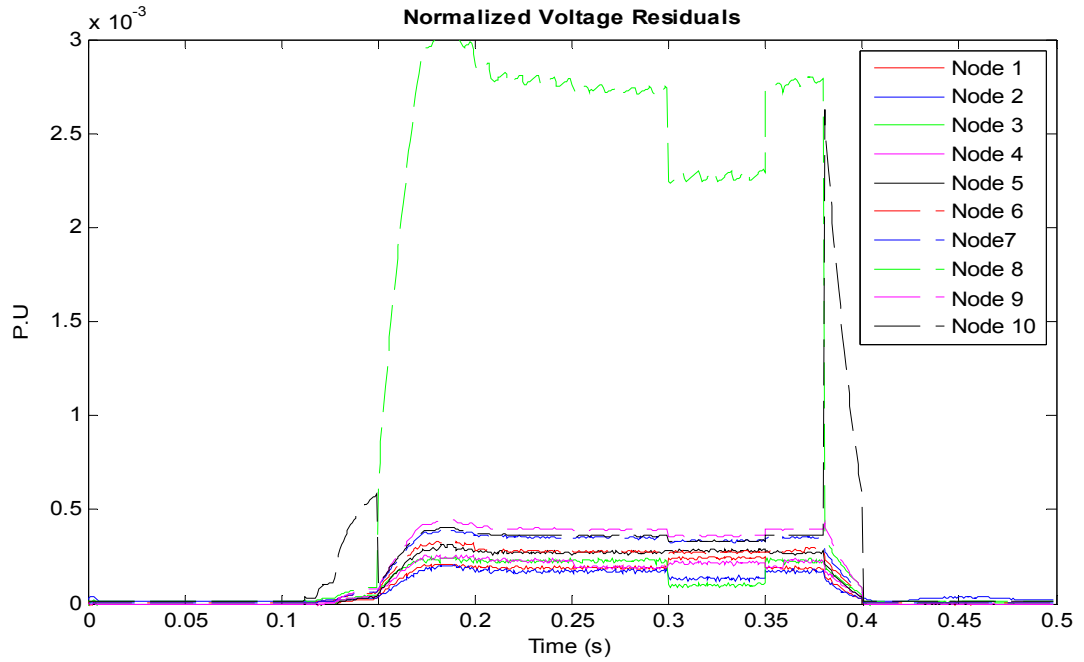
246

Figure F.42: Voltage residual plots for the event with photovoltaic cells shorted.

Figure F.43: Current residual plots for the event with photovoltaic cells shorted.

F.8. Simulation result with photovoltaic cells of Module 2 shorted to ground, with blocking diode and in the presence of multiple ground faults
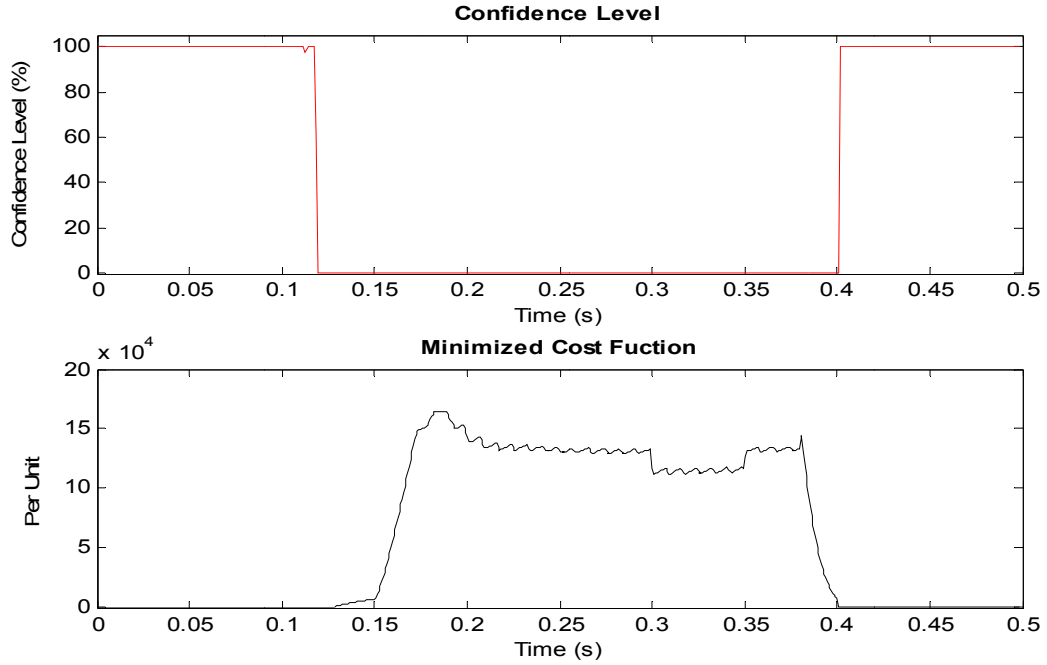
Figure F.44: Confidence level and cost function plots with multiple ground faults.
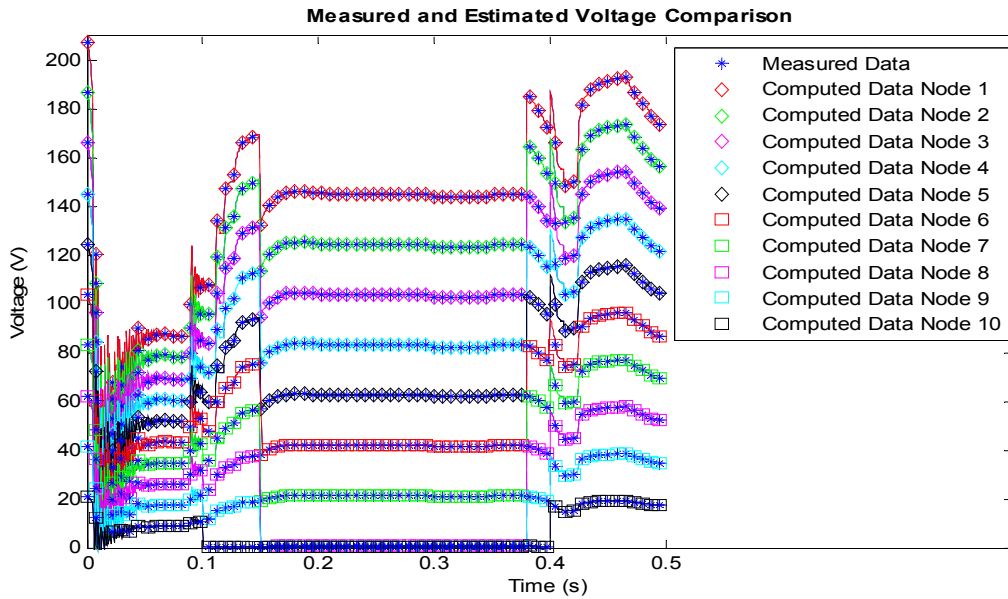
Figure F.45: Computed and measured voltage plots comparison for nodes 1 to 10.

248

Figure F.46: Computed and measured terminal current plots comparison for nodes 1 and 11.

Figure F.47: Computed and measured current plots comparison for nodes 2 through 10.

Figure F.48: Voltage residual plots for the event with photovoltaic cells shorted.
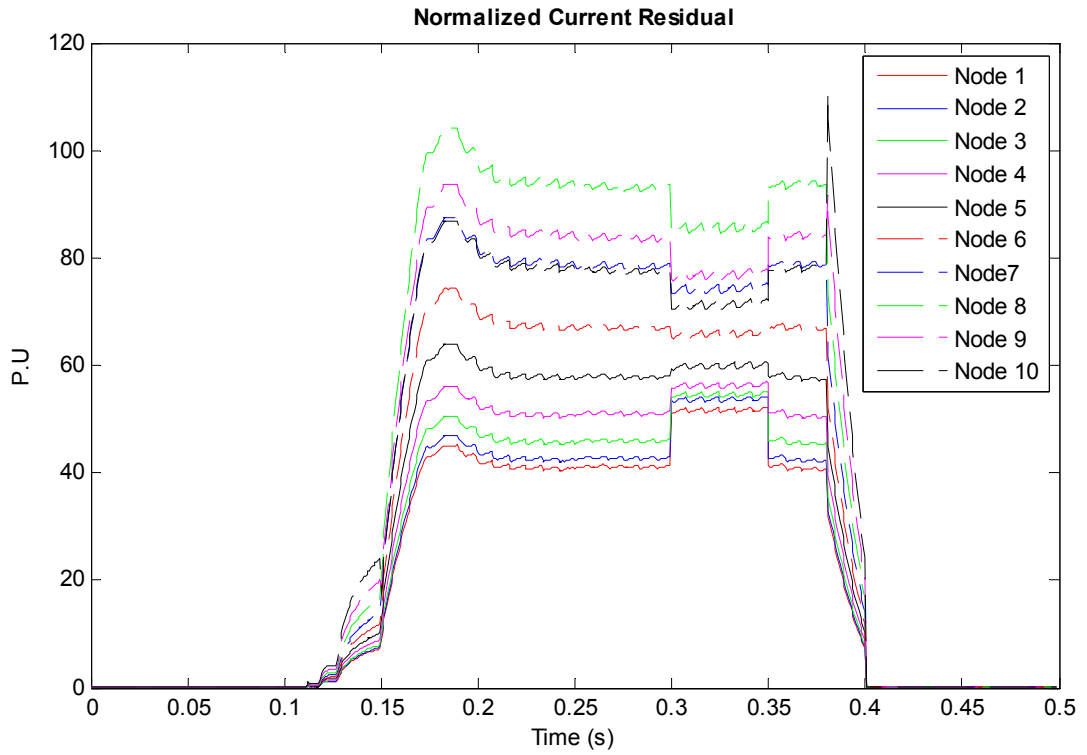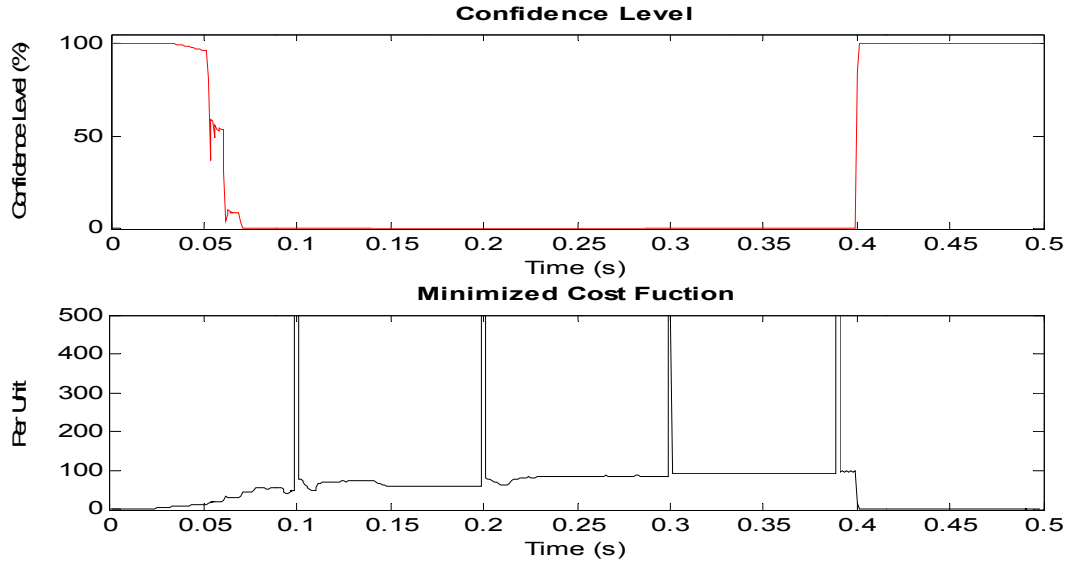

**Figure F.49: Current residual plots for the event with photovoltaic cells shorted.**

F.9. Simulation result with a Fault on a Photovoltaic Cell during low irradiance, with the Irradiance Gradually Increased to the Nominal Value, and with Blocking Diodes
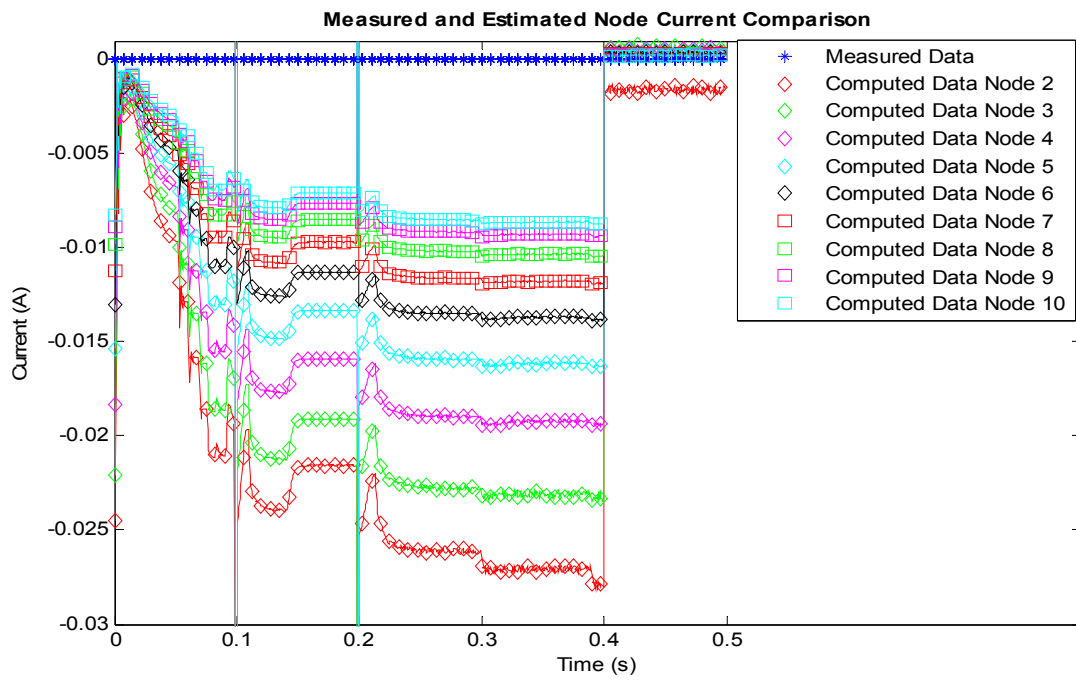

Figure F.50: Confidence level and cost function plots with gradually increasing solar irradiance during a fault on a photovoltaic cell.
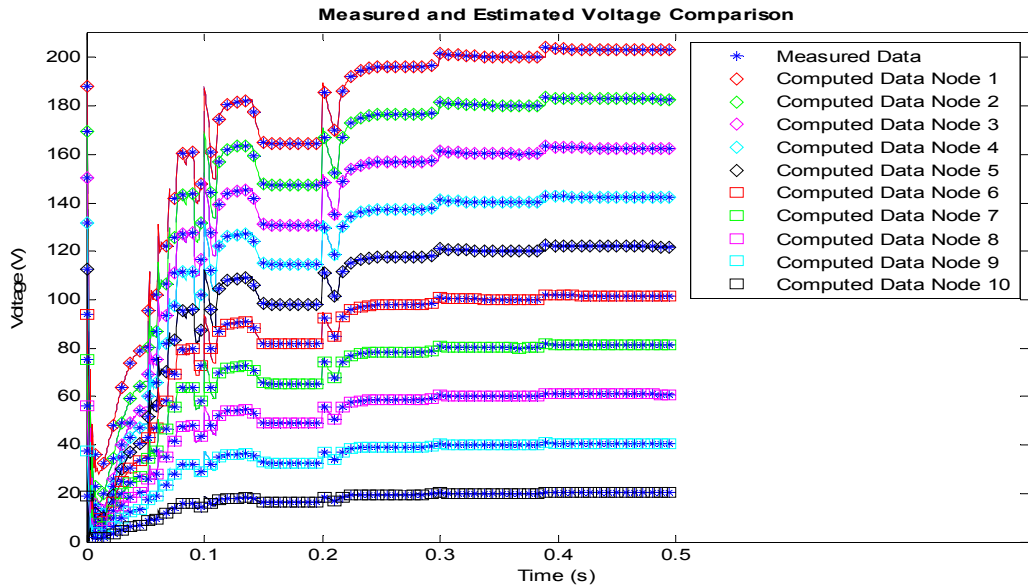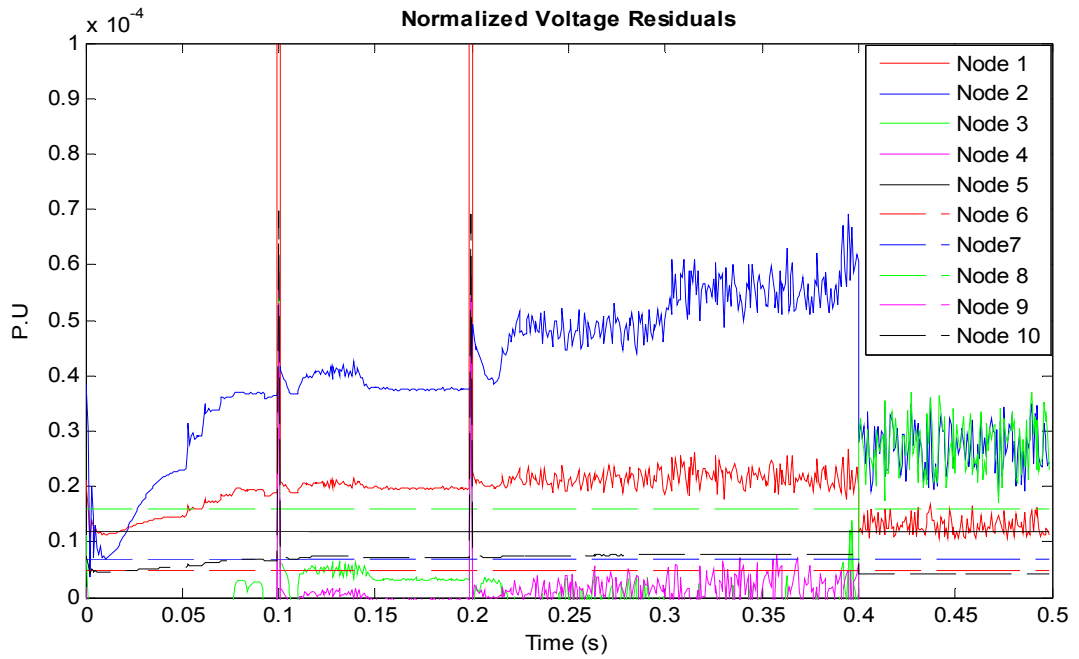

Figure F.51: Computed and measured voltage plots comparison for nodes 1 to 10.

251
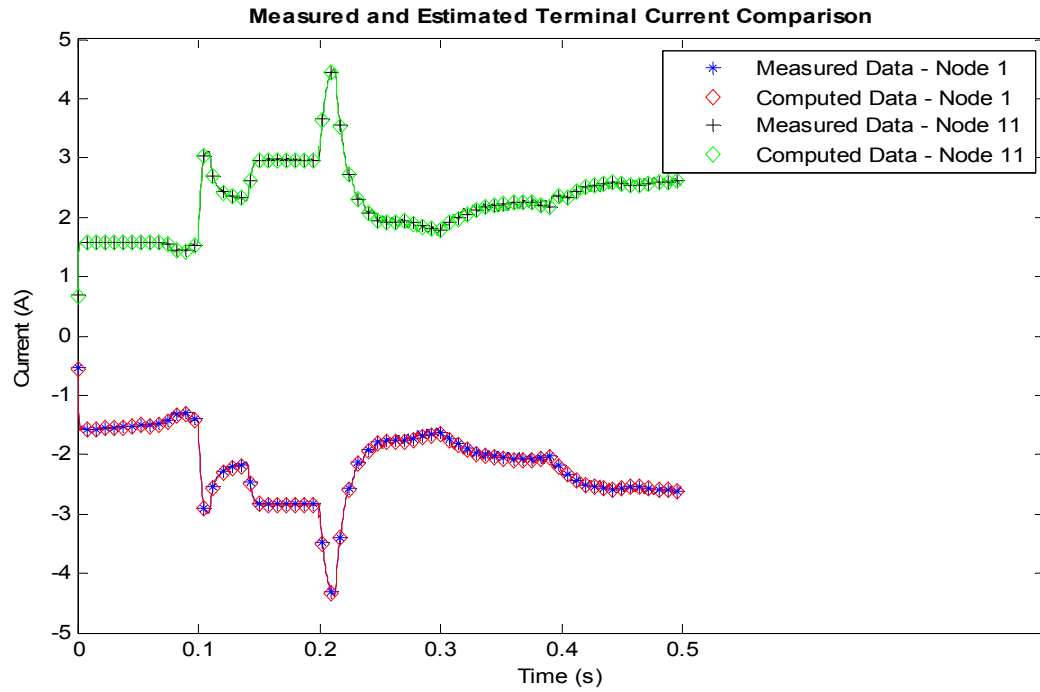
Figure F.52: Computed and measured terminal current plots comparison for nodes 1 and 11.

Figure F.53: Computed and measured current plots comparison for nodes 2 through 10.

Figure F.54: Voltage residual plots during a gradually increasing solar irradiance with a fault on a photovoltaic cell.
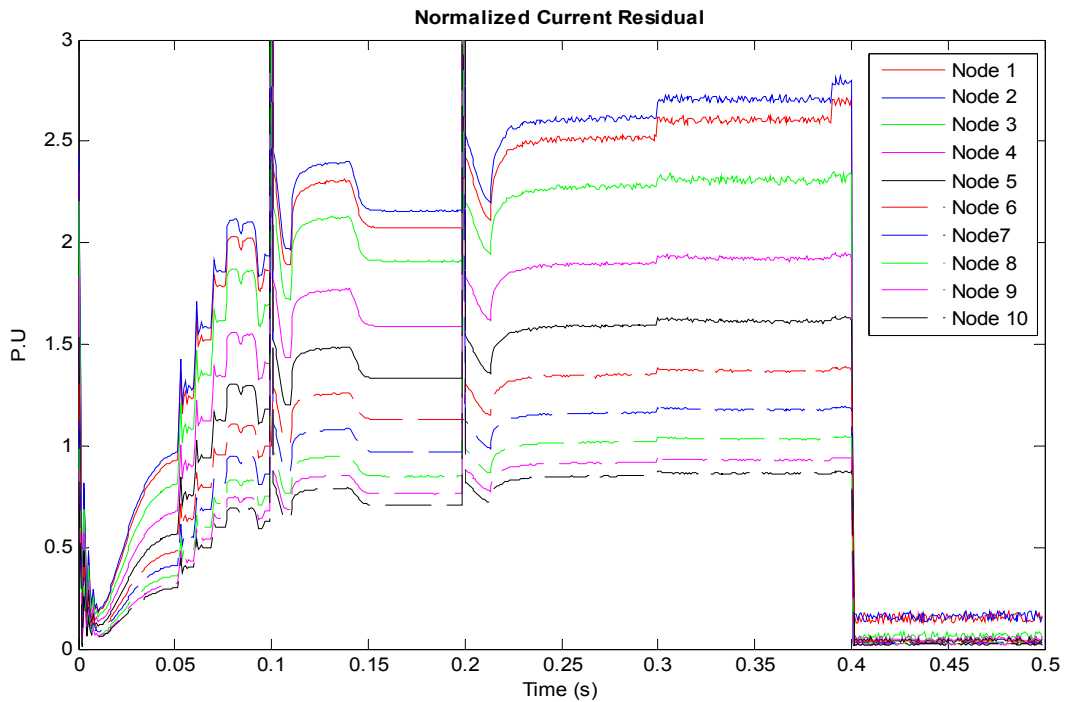
Figure F.55: Current residual plots during a gradually increasing solar irradiance with a fault on a photovoltaic cell.

253

REFERENCES

[1] L. Bin, Y. Yue, W. Lei, "Research on relay protection of grid-connected photovoltaic power station in the Plateau," *International conference on Advanced Power System Automation and Protection,* 2011, Vol 3, pp. 1814-1818.

[2] Y. Weidong, Z. Xia, X. Feng, "Impacts of large scale and high voltage level photovoltaic penetration on the security and stability of power system," *IEEE Power and Energy Engineering Conference,* 2010.

[3] B. Brooks (2011) The Bakersfield fire – A lesson in ground-fault protection, Solarpro Magazine, pp. 62 – 70.

[4] A. Meliopoulos, G. Cokkinides, R. Huang, E. Polymeneas, P. Myrda, "Grid modernization: Seamless integration of protection, optimization & control," *IEEE 47th Hawaii Conference on System Sciences,* 2014, pp 2463-2474.

[5] A. Meliopoulos, G. Cokkinides, G. Stefopoulos, "Improved numerical integration method for power/power electronic systems based on three-point collocation," *IEEE 44th Conference on Decision and Control,* 2005, pp 6780-6787.

[6] Y. Cho, G. Cokkinides, A. Meliopoulos, "Modeling methodology suitable for converters integrating renewables: The QMQI method," *IEEE Journal of Emerging and Selected Topics in Power Electronics,* Vol 1, No. 4, 2003 pp 269 – 276.

[7] D. Collier, T. Key, "Electrical fault protection for a large photovoltaic power plant inverter*," IEEE Photovoltaic Specialists Conference,* 1988, pp. 1035-1042.

[8] Y. Zhao, B. Lehman, J.-F de Palmer, J. Mosesian, R. Lyons, "Challenges to overcurrent protection devices under line-line faults in solar photovoltaic arrays*," IEEE Energy Conversion Congress and Exposition,* 2011, pp. 20-27.

[9] Y. Zhao, B. Lehman, J.-F de Palmer, J. Mosesian, R. Lyons, "Line-line fault analysis and protection challenges in solar photovoltaic array," *IEEE transactions on Industrial Electronics,* 2013, Vol. 60, Issue 9, pp 3784-3795.

[10] M. Nthontho, S.P Chowdhury, S. Winberg, S. Chowdhury, "Protection of domestic solar photovoltaic based microgrid," *11th International Conference on Developments in Power Systems Protection,* 2012.

[11] J. Wiles, D. King, "Blocking diodes and fuses in low-voltage PV systems," *26th IEEE Photovoltaic Specialist Conference,* 1997, pp. 1105-1108.

[12] S. Durand, D. Bowling, V. Risser, "Lessons learned from testing utility connected PV systems," *21st IEEE Photovoltaic Specialist Conference,* 1990, vol 2, pp. 909-913.

[13] W. Bower, J. Wiles, "Investigation of ground-fault protection devices for photovoltaic power systems applications," *28th IEEE Photovoltaic Specialist Conference,* 2000, pp. 1378-1383.

[14] J. Hastings, M. Juds, C. Luebke, B. Pahl, "A study of ignition time for materials exposed to DC arching in PV systems," *37th IEEE Photovoltaic Specialist Conference,* 2011, pp. 003724-003729.

[15] H. A. Siddique, P. Xu, R. De Doncker "Parameter extraction algorithm for one-diode model of PV panels based on datasheet values," *37th IEEE International Conference on Clean Electrical Power*, 2013, pp. 7-13.

[16] Y. Mahmoud, W. Xiao, H. Zeineldin, "A parameterization approach for enhancing PV model accuracy," *IEEE Transaction on Industrial Electronics,* 2013, Vol 60, No. 12, pp. 5708-5716.

[17] M. G. Villalva, J. R. Gazoli, E. R. Filho, "Comprehensive approach to modeling and simulation of photovoltaic arrays," *IEEE Transactions on Power Electronics,* Vol 24, May 2009, pp. 1198-1208.

[18] G. Yordanov, O. Midtgard, T. Saetre, "Two-diode model revisited: Parameters extraction from semi-log plots of I-V data," *25th European Photovoltaic Solar Energy Conference and Exhibition,* 2010, pp. 4156-4163.

[19] Z. Ran, X. Hui-jun, Z. Zhi-ying, Z. Shun-hua, "A simplified double-exponential model of photovoltaic module in Matlab," *IEEE Conference on Energy and Environment Technology,* 2009, pp. 157-160.

[20] Z. Salam, K. Ishaque, H. Taheri, "An improved two-diode photovoltaic (PV) model for PV system," *IEEE Conference on Power Electronics, Drives and Energy Systems*, 2010.

[21] P. Bhatnagar, R. Nema, "Control techniques analysis for dc-dc converter for photovoltaic application using SIMSCAPE," *5th IEEE India International Conference on Power Electronics,* 2012.

[22] A. Khalifa, E. El-Saadany, "Control of three phase grid-connected photovoltaic arrays with open loop maximum power point tracking," *IEEE Power and Energy Society General Meeting,* 2012.

[23] G. Pandove, M. Singh, "High-frequency dc-dc boost converter for residential PV system with power factor correction," *5th IEEE India International Conference on Power Electronics,* 2012.

[24] A. Barchowsky, J. Parvin, G. Reed, M. Korytowski, B. Grainger, "A comparative study of MPPT methods for distributed photovoltaic generation," *IEEE PES Innovative Smart Grid Technologies*, 2012.

[25] T. Esram, P. Chapman, "Comparison of photovoltaic array maximum power point tracking techniques," *IEEE Transactions on Energy Conversion,* Vol. 22, Issue 2, 2007.

[26] G. Stefopoulos, G. Cokkinides, A. Meliopoulos, "Quadratic integration method for transient simulation and harmonic analysis," *IEEE 13th Conference on Harmonics and Quality of Power,* 2008.

[27] A. Umana, A. Meliopoulos, "The modeling of a two-diode photovoltaic module for power system simulations," *47th North American Power Symosium,* 2015.

[28] A. Umana, A. Meliopoulos, "Protection and monitoring of the photovoltaic array system," *IEEE Journal on Photovoltaics,* To be published.

[29] A. Umana, A. Meliopoulos, "The extraction of photovoltaic module parameters using Fibonacci and Steepest Descent methods," *47th North American Power Symosium,* 2015.

[30] J. Faires, R. Burden, "Numerical method," Thomson-Brooks/Cole California, 2003, Third Edition, pp. 435-439.

[31] L. Cooper, D. Steinberg, "Introduction to methods of optimization," W. B. Saunders Company, Philadelphia, 1970, pp. 147-151.

[32] S, Wenham, M. Green, M Watt, R. Corkish, "Applied photovoltaics," Earthscan, Virginia, 2007, pp. 37-39.

[33] A. Meliopoulos, G. Cokkinides, Z. Tan, S. Choi, Y. Lee, "Setting-less protection: feasibility study," *IEEE 46th Conference on System Sciences,* 2013, pp 2345-2353.

[34] A. Umana, A. Meliopoulos, "Detection of cell-level fault conditions within a photovoltaic array system," *IEEE PES Transmission and Distribution Conference and Exposition, 2016.* In Press.

[35] N. Jantharamin, L. Zhang, "A new dynamic model for lead-acid batteries," *4th IET Conference on Power Electronics, Machines and Drives,* 2008, pp. 86-90.

[36] A. Khalifa, E. El-Saadany, "Control of three phase grid-connected photovoltaic arrays with open loop maximum power point tracking," *IEEE Power and Energy Society General Meeting,* 2012.

[37] N. Mohan, T Undeland, W. Robbins, "Power electronics, converters, cpplications and design," John Wiley & Sons, New York, 2006, pp. 211-212.

[38] M. Rashid, "Power electronics, circuits, devices, and applications," Pearson Prentice Hall, NJ, 2004, Third Edition, pp. 186-204.